
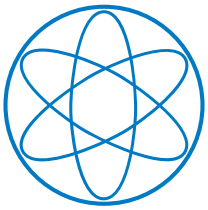

Non-equilibrium Phase Transitions in Systems with long-range Interactions

Dissertation

vorgelegt von

Johannes Andreas Lang

Januar 2019

Physik Department T34
Technische Universität München

Technische Universität München

Physik Department
Lehrstuhl T34, Prof. Dr. Wilhelm Zwerger

Non-equilibrium Phase Transitions in Systems with long-range Interactions

Johannes Andreas Lang

Vollständiger Abdruck der von der Fakultät für Physik der Technischen Universität München zur Erlangung des akademischen Grades eines

Doktors der Naturwissenschaften (Dr. rer. nat)

genehmigten Dissertation.

Vorsitzender:	Prof. Jonathan J. Finley, Ph.D.
Prüfer der Dissertation:	1. Prof. Dr. Wilhelm Zwerger
	2. Prof. Dr. Michael Hartmann (Heriot-Watt University, Edinburgh)

Die Dissertation wurde am 29.01.2019 bei der Technischen Universität München eingereicht und durch die Fakultät für Physik am 01.03.2019 angenommen.

Abstract

In this thesis, we investigate many-body systems with long-range interactions, that frequently arise as a consequence of strong light-matter interactions. Because of the advanced experimental control over the lossy nature of the photons, these systems can be studied in and out of equilibrium. We first consider an infinite range spin chain at finite temperatures and study its dynamical phase diagram by means of the Loschmidt echo and the late-time dynamics of the order parameter. It turns out, that both dynamical phase diagrams are identical. Using a semiclassical analysis of the return rate based on the spin WKB wave function, an intuitive interpretation for this concurrence is found. Then, notivated by the recent experiments at ETH [1, 2], we study the symmetry breaking associated with the Dicke-Hepp-Lieb transition of bosons in two crossed optical cavities. We find, that in the presence of atom-mediated scattering between the two cavities the $U(1)$ invariance with respect to redistribution of the cavity field intensity I between the two resonators is broken, giving rise to an effective Goldstone mass $\sim \sqrt{I}$. Next, we turn to open systems and investigate the steady state of interacting polaritons in photonic crystal waveguides or tapered fibers, for which we develop a controlled diagrammatic expansion in the inverse interaction range between quasiparticles. This is then used to describe the phenomenon of *interaction induced transparency* (IIT), where dissipative interactions between EIT polaritons drive a first order phase transition between an opaque and a transparent phase. In the latter a high density of polaritons can compensate losses forced onto the quasiparticles by external laser fields. Finally, we address the late-time dynamics in the open Dicke model near the Dicke-Hepp-Lieb transition by a self-consistent diagrammatic approximation. It turns out, that the phase transition following a small quench is not the result of a diverging quasiparticle lifetime, but rather a proliferation of overdamped excitations. Consequently, the phase transition to a condensate in the interacting system is not captured by the single-particle spectrum.

Zusammenfassung

Den Fokus dieser Arbeit bilden Vielteilchensysteme mit langen Wechselwirkungsreichweiten, wie sie häufig durch starke Licht-Materie Wechselwirkungen entstehen. Dank der zunehmenden experimentellen Kontrolle über Photonverluste, können diese Systeme heutzutage sowohl im, wie auch außerhalb des Gleichgewichts untersucht werden. Wir untersuchen zuerst das dynamische Phasendiagramm einer Spinkette mit unendlicher Reichweite bei endlichen Temperaturen mit Hilfe des Loschmidt-Echos und der Langzeitdynamik des Ordnungsparameters. Dabei stellt sich heraus, dass beide Methoden das gleiche Phasendiagramm liefern. Eine intuitive physikalische Erklärung für diese Beobachtung ergibt sich aus einer semiklassischen Analyse der Rückkehrrate basierend auf der Spin-WKB-Wellenfunktion. Motiviert durch aktuelle Experimente an der ETH [1, 2], untersuchen wir die Symmetriebrechung am Dicke-Hepp-Lieb Ãœbergang von Bosonen in zwei gekreuzten optischen Resonatoren. Es zeigt sich, dass die Streuung zwischen den Resonatoren, wie sie durch Atome vermittelt wird zu einer Brechung der $U(1)$-Invarianz bezüglich der Umverteilung der Lichtfeldintensität I zwischen den beiden Resonatoren führt, was eine effektive Masse der Goldstone-Mode $\sim \sqrt{I}$ nach sich zieht. Anschließend wenden wir uns offenen Systemen zu und untersuchen den stationären Zustand wechselwirkender Polaritonen in photonischen Kristallwellenleitern oder in verjüngten Glasfasern. Dazu entwickeln wir eine kontrollierte diagrammatische Entwicklung in der inversen Wechselwirkungsreichweite zwischen Quasiteilchen. Diese wird dann benutzt, um eine neue Form von *wechselwirkungsinduzierter Transparenz* zu beschreiben. Diese Transparenz wird durch dissipative Wechselwirkungen zwischen EIT-Polaritonen hervorgerufen und ist durch einen Phasenübergang erster Ordnung von einer trüben Phase mit hohen Verlusten getrennt. In der transparenten Phase kompensiert eine hohe Dichte aus Polaritonen Verluste, die den Quasiteilchen durch äußere Laserfelder aufgezwungen werden. Abschließend wird die Langzeitdynamik im offenen Dicke-Modell nahe des Dicke-Hepp-Lieb Phasenübergangs mit einer selbstkonsistenten diagrammatischen Näherung behandelt. Dabei stellt sich heraus, dass der Phasenübergang nach einer kleinen Störung des Systems nicht, wie naiv erwartet, durch eine verschwindende Zerfallsrate der Quasiteilchen hervorgerufen wird, sondern durch die Anhäufung überdämpfter Anregungen. Folglich ist eine Beschreibung des Kondensationübergangs basierend auf dem Ein-Teilchen-Spektrum nicht möglich.

Contents

List of Figures

Chapter 1

Introduction

It is no coincidence that light has been the preferred method of communicating information for several decades. This is mostly owed to the fact, that in transparent media photons hardly interact and can propagate with a group velocity close to the speed of light for almost unlimited distances. However, for quantum information processing strong interactions are required. Thus, the possibility to selectively implement interactions between photons in the quantum regime is recently attracting a lot of interest [3, 4]. Interacting photons are also promising for the creation of synthetic quantum matter, like superfluids [5], or crystalline like states of light [6, 7, 8, 9] and even topological [10] phases.

In recent years a lot of progress in this direction has been made in a number of vastly different experimental platforms. Among them are trapped ions [11, 12, 13], coupled arrays of microcavities [6, 14, 15], photonic crystal waveguides [16, 17], polaritons in Rydberg gases [18, 19, 20, 21], tapered fibers [22, 23, 24, 25], optomechanical systems [26, 27, 28] and Bose-Einstein condensates in optical resonators [29, 30, 31, 32]. All of these are many-body systems, controlled by methods from quantum optics. This gives rise to a common feature: The interactions are photon mediated and therefore long ranged. As opposed to solid state systems, interactions in these hybrid light-matter experiments can be adjusted via external laser fields. Furthermore, the photons naturally possess loss channels, the control over which lies at the heart of the experimental advances towards the exceptional authority required for example in quantum computers.

Apart from the lofty goal of a scalable quantum computer, there are many concrete applications already within reach of the latest generation of experiments, for example quantum simulators [11, 33] and single photon gates [34, 35, 36]. Given the fast progress towards larger and more complex systems and especially the promising technical opportunities these platforms provide, there is an urgent need for reliable, quantitative theoretical descriptions. However many well established methods from solid state physics are unable to deal with quantum systems far from equilibrium. The typically quickly growing entanglement entropy limits the use of matrix product states (MPS) or density matrix renormalization group (DMRG) and recent experiments have attained system sizes beyond the reach of exact diagonalization [11, 33].

Compared to the well-established description of phase transitions in equilibrium

the treatment of open systems and dynamical phase transitions is therefore still in its infancy. In particular, the description of quantum phase transitions, be they dynamical [37, 38] or towards novel phases of matter [39, 40, 41, 42, 10, 43] has proven difficult [44] because important concepts from equilibrium physics, like detailed balance or a thermodynamic potential do not apply. Nevertheless, recently ideas to generalize these notions to dynamical systems have attracted a lot of attention [45] and subsequently also have met with some success [37, 46]. Furthermore, important advances towards the classification of dynamical phase transition have been made [44, 47]. The combination of many remaining open theoretical challenges and abundant experimental realizations creates the opportunity to discuss fundamentally new physical concepts in concrete applications. With the easy access to many observables via the emitted photons, precision measurements enable a quantitative comparison between theory and experiment. Consequently, we focus in this thesis on the quantitative description of long-range systems far from equilibrium, realizable in quantum optical systems with ions and ultracold bosonic atoms in optical cavities and near photonic crystal waveguides.

We begin in chapter 2 with the description of dynamical quantum phase transitions by means of the Loschmidt echo. In particular, in section 2.1, we consider very long spin chains with infinite range interactions that can be realized with trapped ions [11] and investigate the connection between the long-time order parameter dynamics and the non-analyticities of the return rate. This extends a recent investigation [48] to finite temperatures and allows us to identify the proper generalization of the Loschmidt echo to mixed states. The long-range nature of the interactions then enables us in section 2.3 to perform a semiclassical analysis based on the spin WKB wave function and find a geometric interpretation of the return rate at arbitrary temperatures. Connections to an effective Ginzburg-Landau description and extensions to finite interaction ranges are discussed. In chapter 3 we consider a recent experiment at ETH [1, 2] which found supersolid behavior in a Bose-Einstein condensate trapped in two crossed cavities. We investigate the symmetries of the experiment including higher order scattering processes. With a focus on the stationary state of the atomic cloud, the photon losses can be mostly neglected. Consequently, a quantitative finite temperature mean-field analysis is used to determine the mass and lifetime of the associated Goldstone and Higgs mode in the symmetry broken phase beyond the Dicke-Hepp-Lieb transition. We then turn our attention to dissipative systems. In chapter 4, we develop a controlled diagrammatic expansion in the inverse interaction range between EIT polaritons. Given its non-perturbative nature this out-of-equilibrium field theory is suitable for the quantitative description of phase transitions. We therefore use it to investigate the novel predicted phenomenon of interaction-induced transparency in photonic crystal waveguides. Furthermore, corrections due to finite interaction ranges are detailed in Sec. 4.8 and the application to Rydberg atoms is outlined in Sec. 4.9. Finally, the late-time dynamics of the open Dicke model is discussed in chapter 5. Using a self-consistent Hartree-Fock approximation in the Keldysh path integral

formalism for finite system sizes, a scaling form of the Green's function is found and compared to an extensive numerical simulation. Utilizing this result, the peculiar nature of the superradiance instability in an open system with overdamped excitations is explained.

Chapter 2

Loschmidt echo in infinite range spin chains

For most of this thesis, we will focus on atomic and photonic one-particle Green's functions as a tool to characterize the non-equilibrium phases of matter. There are, however, several disparate approaches to detect dynamical phase transitions (DPT), for example from the dynamics [49, 50, 51] or asymptotic long-time limit of observables and correlation functions [52, 53, 54, 55, 56, 57], which has recently been measured experimentally with trapped ions [11]. In the following these will collectively be referred to as DPT-I. An alternative concept, referred to as DPT-II, is based on the so-called Loschmidt echo, which was introduced by Heyl and Kehrein [45] and has attracted a lot of interest in recent years (for a topical review see [37]). Contrary to the aforementioned DPT-I it is defined already at intermediate time-scales, however – at least in principle – it requires measurements that are exponential precise in the system size.

In this chapter, we will discuss the Loschmidt echo for semiclassical spin models at finite temperature and compare the arising dynamical phase diagram to that obtained from the late-time behavior of the magnetization. In the thermodynamic limit we find a concurrence of the DPT-I and DPT-II phase diagrams. Moreover, in Sec. 2.3 we develop an intuitive, geometric picture based on the spin WKB wave function, that allows an interpretation similar to the Ginzburg-Landau theory of equilibrium phase transitions as well as a connection to entanglement witnesses, that have been used to detect dynamical phase transitions, like the spin squeezing [58, 59] and the quantum Fisher information [60, 61]. Beyond the significant numerical advantages this method presents, it also clarifies the connection between DPT-I and DPT-II in mean-field like systems and paves the way for the calculation of Loschmidt echos or entanglement witnesses within the more general framework of the truncated Wigner approximation, potentially even in generic non-integrable systems. Section 2.2 is based on the publication [62] resulting in some text overlap. Also most figures are taken from there. The latter half of this chapter is derived from the paper [63] with which it partially overlaps in text and figures.

2.1 The Loschmidt echo as a measure for dynamical quantum phase transitions

In equilibrium phase transitions are well understood both classically and quantum mechanically [64, 65]. The main reason behind this is, that the partition function Z contains the full information about the thermodynamics of the system. For example for a system in contact with a heat bath one has

$$Z = \mathrm{Tr}\, \mathrm{e}^{-\beta H}\,, \tag{2.1}$$

where $\beta = 1/T$ is the inverse temperature with the Boltzmann constant set to unity and H the Hamiltonian of the system. Phase transitions can then be detected and classified in terms of non-analyticities of the free energy

$$F = -T \ln Z\,. \tag{2.2}$$

Far from equilibrium however, equivalent concepts are missing, raising many fundamental questions, regarding universality or the existence of an ordering principle, similar to the minimization of the free energy.

One possibility to find non-analytic behavior in a quantity, which is closely related to a free energy in equilibrium, is the Loschmidt echo, which we will consider in more detail now. Assuming that a system is prepared in the ground state $|\Psi_0\rangle$ of some initial Hamiltonian H_i we perform a sudden quench to the final Hamiltonian H_f, exciting the system in the process. In this simplest of all quench protocols the Loschmidt echo $\mathcal{L}$ can be defined as the return probability of the time-evolved state $|\Psi(t)\rangle$ to the initial state:

$$\mathcal{L}(t) = |G(t)|^2 = |\langle\Psi_0|\Psi(t)\rangle|^2 = |\langle\Psi_0|\mathrm{e}^{-iH_\mathrm{f}t}|\Psi_0\rangle|^2\,. \tag{2.3}$$

Formally the Loschmidt amplitude G is equivalent to a boundary partition function with the boundary states $|\Psi_0\rangle$ and the imaginary inverse temperature $\beta \to it$. Thus, we can introduce the real and positive return rate $r(t)$ as an analog to the thermodynamic limit of the free energy density in equilibrium via

$$r(t) = -\lim_{N\to\infty} \frac{1}{N} \ln \mathcal{L}(t)\,. \tag{2.4}$$

Note, that the absolute value in the definition of $\mathcal{L}(t)$ is purely for convenience as the corrections due to the phase of $G(t)$ would anyways be suppressed by $1/N$. Similar to the free energy, the expression $\ln \mathcal{L}(t)$ is typically extensive. As is the case for F, proving this for interacting systems is a highly nontrivial task, that due to the imaginary exponent in Eq. (2.3), however, has to rely on the large deviation scaling [66] of the overlaps between the eigenstates of H_i and H_f. In the following, we will not concern ourselves with this and instead simply note, that for infinite

range spin chains the return rate defined by Eq. (2.4) is properly normalized and of order one[1]. Continuing along the same lines as in equilibrium, we can now define a non-equilibrium phase transition as a non-analyticity in $r(t)$, which one then has to connect to some more practical observations in the dynamics of the system. This has for example been achieved by Trapin and Heyl for the revivals of the superfluid state after a quench of the Bose-Hubbard model to the Mott insulator [67, 46]. Following the standard notation, the instances of the periodically appearing non-analyticities in $r(t)$ will be called critical times t_{c_n}, sorted in time by the index $n \in \mathbb{N}$.

Typically for systems with degenerate ground states the Loschmidt echo is calculated as the overlap with the entire ground state manifold [68, 69, 70, 71]. As we will see in the case of the $U(1)$ symmetric, infinite range XX-model, this can result in an artificial suppression of cusps in the return rate, rendering the Loschmidt echo meaningless. Consequently, we will avoid using any such construction.

We note, that the Loschmidt echo is exponentially sensitive to the overlap between initial and time-evolved state. It is therefore not entirely unreasonable to suspect some rigorous relation between the return rate and infinite-time expectation values. A well known case, where a similar exponentially weighted expectation value taken shortly after a quench predicts the final equilibrium properties (more precisely the free energy) is the Jarzynski-Crooks fluctuation relation [72, 73, 74, 75]. There, the difference between the initial and final free energy $\Delta F = F_\mathrm{f} - F_\mathrm{i}$ in equilibrium is expressed via fluctuations of the ensemble average of the work W performed during the quench:

$$\mathrm{e}^{-\beta \Delta F} = \langle \mathrm{e}^{-\beta W} \rangle \ . \tag{2.5}$$

Despite the fact, that the Loschmidt amplitude $G(t)$ can be identified with the characteristic function of the work distribution [76], currently no rigorous statements relating DPT-I and DPT-II are known. In fact, only few generic statements can be made regarding cusps in $r(t)$. For a finite system $G(z)$ is an entire function (with $z \in \mathbb{C}$) that can be rewritten with the Weierstrass factorization theorem [77] as

$$G(z) = \mathrm{e}^{f(z)} \prod_j (z_j - z) \ . \tag{2.6}$$

Here $f(z)$ is an entire function and thus any non-analyticity in $r(t)$ originates from the zeros z_j in the complex plane. In the thermodynamic limit these isolated zeros accumulate into lines or areas of the complex plane [37]. If any such structure is intersected by the real axis the return rate $r(t)$ will exhibit a cusp at the entry and the exit point [78]. These are closely related to the non-analyticities of the free energy that are fully determined by zeros of the partition function which were

[1] A simple proof can be constructed by means of the spin WKB wave function treated in Sec. 2.3.

first studied by Lee and Yang [79]. However, due to the presence of two distinct Hamiltonians H_i and H_f the determination of the Lee-Yang zeros for quenched systems is even harder than in equilibrium.

Despite the lack of generic results, some remarkable advances have been made for specific systems. In particular we distinguish between non-interacting, fermionic many particle systems and interacting or many-body systems. In the former case the Hamiltonian turns into a sum over single-particle Hamiltonians

$$H = \sum_k H_k = \sum_k \hat{\mathbf{c}}_k^\dagger h_k \hat{\mathbf{c}}_k \tag{2.7}$$

with vectors $\hat{\mathbf{c}}_k$ and $\hat{\mathbf{c}}_k^\dagger$ of fermionic creation and annihilation operators. In this case the ground state $|\Psi_0\rangle = \prod_k |\Psi_k\rangle$ factorizes into a product of single-particle ground states $|\Psi_k\rangle$, entailing the same property for the Loschmidt echo:

$$G(t) = \prod_k \langle \Psi_k | \mathrm{e}^{-iH_k t} | \Psi_k \rangle = \prod_k G_k(t) \tag{2.8}$$

and therefore

$$r(t) = \lim_{N\to\infty} \frac{1}{N} \sum_k r_k(t) = -\lim_{N\to\infty} \frac{1}{N} \sum_k \ln |G_k(t)|^2 \,. \tag{2.9}$$

Examples for Hamiltonians of this type include, among others, topological band insulators, Bogoliubov-de Gennes superconductors or the one-dimensional nearest-neighbor transverse Ising model, for each of which k denotes the quasi-momentum and the product in $G(t)$ runs over the Brillouin zone. Clearly $G_k(t)$ is a finite sum and consequently an analytic function, which implies that the only origin of a singularity in the return rate is if $G_k(t_{c_n}) = 0$ for some k. Interacting systems on the other hand do not factorize and in the thermodynamic limit $G(t)$ is an infinite sum, that can itself be non-analytic. For one and two-dimensional non-interacting topological two-band systems, i.e. where h_k is a 2×2 matrix, $G_k(t)$ contains only two terms, most results can be obtained analytically.

A particularly simple picture arises through the use of the relative Bloch sphere, that is by expressing the time-evolved state $|\Psi_k(t)\rangle$ in the basis $\{|\Psi_{k-}\rangle, |\Psi_{k+}\rangle\}$ of the initial Hamiltonian

$$|\Psi_k(t)\rangle = \cos(\theta_k(t)/2)|\Psi_{k-}\rangle + \mathrm{e}^{i\phi_k(t)} \sin(\theta_k(t)/2)|\Psi_{k+}\rangle \,. \tag{2.10}$$

Initially, for every k the Bloch vector points to the north pole $\{\theta_k(0) = 0, \phi_k(0) = 0\}$. However, the DPT-II condition $G_k(t_{c_n}) = 0$ is only satisfied, if $|\Psi_k(t_c)\rangle$ becomes orthogonal to the initial state, thus pointing to the south pole. This will happen if and only if the initial and final Hamiltonian $h_k^{\mathrm{i,f}} = \alpha_{\mathrm{i,f}} \mathbb{1}_{2\times 2} + \mathbf{d}_k^{\mathrm{i,f}} \cdot \boldsymbol{\sigma}$, with $\boldsymbol{\sigma}$ the vector of Pauli matrices, have orthogonal eigenstates, i.e. if $\mathbf{d}_k^\mathrm{i} \cdot \mathbf{d}_k^\mathrm{f} = 0$. In 1D

for a quench between systems with different Zak phase in the ground state, this is guaranteed, thereby relating the equilibrium topological phase with the existence of cusps in the Loschmidt echo [80]. In two dimensions the weaker statement that a quench between systems with different modulus of the Chern number results in non-analyticities in the return rate has been found by Vajna and Dóra [80].

Note however, that these relations between dynamical and equilibrium phase transitions can be lifted by dynamical constraints to the dynamics [81]. Furthermore, there is also the possibility of accidental dynamical phase transitions that are not related to a change in topology [81, 82]. As opposed to the topological transitions these are neither connected to equilibrium transitions nor protected by symmetry and require fine-tuning. For the case of the 1D transverse field Ising model a simultaneity between the sign change in the order parameter and cusps in the return has been established [45]. A similar behavior has also been found in the non-interacting $N \to \infty$ limit of the $\mathcal{O}(N)$-model [71]. These relations between the equilibrium topological phase and the Loschmidt echo can be generalized to any finite number of bands [83], however calculations quickly become very cumbersome and already for three bands the critical times are not analytically known.

By removing the dynamical component $\phi_k^{\mathrm{dyn}}(t) = -\int_0^t ds \langle \Psi_k(s)|H_f|\Psi_k(s)\rangle$ from the phase $\phi_k(t)$ of the Loschmidt amplitude $G_k(t) = |G_k(t)|\mathrm{e}^{i\phi_k(t)}$ Budich and Heyl have been able to identify the geometric Pancharatnam phase $\phi_k^P(t) = \phi_k(t) - \phi_k^{\mathrm{dyn}}(t)$ [84] as a topological, dynamical order parameter [85]. Cusps in the return rate of one-dimensional topological insulators are necessarily accompanied by simultaneous jumps in the Pancharatnam phase [85].

For interacting systems typically no one-to-one correspondence between DPT-II and an equilibrium transition exists [86, 87, 70]. However, in the case of long-range transverse field Ising models it has been found that the time t_{c_1} is correlated with the infinite time expectation value of the magnetization [48, 87, 88]. In case that both the initial and the steady-state magnetization are finite, the so-called anomalous phase, where t_{c_1} appears only after the first minimum of $r(t)$, has been found. This differs from the quench between a ferromagnetic and a paramagnetic state, where the first cusp in the return rate appears before the first minimum. Therefore, as opposed to the non-interacting case, the critical times cannot coincide with sign changes in the magnetization.

Lacking a consensus on the proper generalization of the Loschmidt echo to finite temperatures, pure, excited initial states have been studied instead [89]. In analogy to the quantum critical regime in equilibrium a similar effect has been observed for small systems and strong quenches [68, 69]: The energy resolved order parameter, which experiences a sudden change near the critical times, becomes increasingly smooth as the energy is increased. The instance of the jump in the order parameter in the time-evolved system upon projection to the ground state manifold was then identified with the critical time of the return rate, thus linking DPT-I and DPT-II. However, as mentioned above, careful numerical investigations of large systems call

these results into question, as zeros of the order parameter and the critical times are not perfectly synchronous [48], prohibiting the identification of the discontinuity in the energy resolved order parameter with the critical time.

In the case of a 2D topological insulator and a short spin chain with long-range interactions the Loschmidt echo has recently been measured in experiments with ultracold atoms and trapped ions [90, 69]. Recently, further observations of DQPTs by means of the Loschmidt echos have been reported in photonic quantum walks [91, 92], nanomechanical oscillators [93] and superconducting qubits [94]. In the case of the infinite-range transverse field Ising model (IR-TFIM) one has furthermore observed a connection between the Loschmidt echo and the Kitagawa-Ueda spin-squeezing parameter [58, 69], raising the question of a possible relation between entanglement witnesses and the Loschmidt echo.

2.2 Finite-temperature Loschmidt echo for large spin chains

As the vast majority of the results mentioned above has been obtained in non-interacting systems initialized in the ground state, it is only natural to ask, which of these statements carry over to interacting systems, where singularities in the Loschmidt echo are not related to orthogonal initial and final states. In fact, only very little is known for non-integrable systems with exponentially large Hilbert spaces, as these require a lot of numerical effort to reliable resolve any connection between the Loschmidt echo and the order-parameter dynamics, as is evidenced by the discrepancy between the recent studies [70] and [87]. Beyond significant quantitative contradictions, there are also qualitative disagreements: While the former finds cusps in the return rate only for quenches of a ferromagnetic initial state to a paramagnetic phase as $t \to \infty$, the latter finds an *anomalous* phase – characterized by cusps in all but the first few periods of the return rate – for quenches where the magnetization remains finite. The situation becomes even worse, at finite preparation temperatures, where no consensus between the different proposed generalizations of the return rate has been achieved [95, 96, 97, 98, 99, 100] (see Sec. 2.2.3).

In the following, we will thus focus on the simplest case of an interacting many-body system, realized in the form of infinite range spin chains, where reliable, numerical results can be obtained. More specifically, we will mostly focus on the transverse field Ising model, but also show extensions to the $\mathcal{O}(2)$-symmetric XX chain. While these systems are integrable in the sense that the explored Hilbert space is only linear in system size, their dynamics is not exactly known and the Loschmidt echo cannot be classified in the same way as is the case for non-interacting systems (see Sec. 2.3.1). Nevertheless, the relatively simple structure renders the exact diagonalization (ED) of very large systems possible. Furthermore, the existence of a finite temperature phase transition in equilibrium allows to investigate dynamical

phase transitions by means of the Loschmidt echo also at $T \neq 0$.

2.2.1 Model and quench protocol

The IR-TFIM is described by the Hamiltonian

$$H(\Gamma) = -\frac{J}{2N} \sum_{i \neq j=1}^{N} s_i^z s_j^z - \Gamma \sum_{j=1}^{N} s_j^x - \Lambda \sum_{j=1}^{N} s_j^z \,, \tag{2.11}$$

with (ferromagnetic) coupling constant $J > 0$ and system size N. The Kac normalization factor [101] $1/N$ in the interaction term is introduced to ensure extensivity in the thermodynamic limit. The variables $s_j^{z(x)}$ denote the projection of the spin operator of site j onto the z (x) direction. For quenches starting in a paramagnetic state the small longitudinal field proportional to $\Lambda \ll \Gamma$ is needed to seed the symmetry breaking in case of an ordered long-time steady state. This procedure will be described in more detail in Sec. 2.2.4. Thus, unless otherwise specified, we set $\Lambda = 0$. The result is the usual IR-TFIM, which has a finite-temperature equilibrium phase diagram [102, 103] depicted in Fig. 2.1 with ordered and disordered phases separated by the equilibrium critical line

$$T_{\mathrm{c}}^{\mathrm{e}}(\Gamma) = \Gamma \left[\ln\left(\frac{J + 2\Gamma}{J - 2\Gamma} \right) \right]^{-1} , \tag{2.12}$$

with zero-field thermal critical point $T_{\mathrm{c}}^{\mathrm{e}}|_{\Gamma \to 0} = \lim_{\Gamma \to 0} T_{\mathrm{c}}^{\mathrm{e}}(\Gamma) = J/4$, and zero-temperature quantum critical point $\Gamma_{\mathrm{c}}^{\mathrm{e}}(T = 0) = J/2$, where $\Gamma_{\mathrm{c}}^{\mathrm{e}}(T)$ is the inverse of $T_{\mathrm{c}}^{\mathrm{e}}(\Gamma)$.

We note here that the IR-TFIM is a special case of the Lipkin-Meshkov-Glick (LMG) model, which was introduced originally to analyze shape phase transitions in nuclei [104, 105, 106]. The LMG model describes the infinite-range anisotropic XY model in a transverse magnetic field along the z direction. Despite its simple structure, it exhibits a finite-temperature phase transition [107, 108], and can be experimentally realized in quantum-optical settings either in an optical resonator [109] or with Rydberg atoms [33] or trapped ions [110, 111, 11, 112]. Since its introduction, it has been extensively studied in statistical physics, and even its spectrum in the thermodynamic limit has been analytically calculated by Ribeiro et al. [113].

We prepare our system at temperature $T = 1/\beta$ in the thermal state

$$\rho_{\mathrm{i}} = \frac{\mathrm{e}^{-\beta \mathcal{H}(\Gamma_{\mathrm{i}})}}{\mathrm{Tr}\, \mathrm{e}^{-\beta \mathcal{H}(\Gamma_{\mathrm{i}})}} \,, \tag{2.13}$$

and set the Planck constant as well as J to unity. Here, $\mathcal{H}$ refers to the full (mean-field) Hamiltonian when ρ_{i} is in the paramagnetic (ferromagnetic) equilibrium phase and we define the partition function as $Z = \mathrm{Tr} \exp\left(-\beta \mathcal{H}(\Gamma_{\mathrm{i}})\right)$. Due to the infinite-

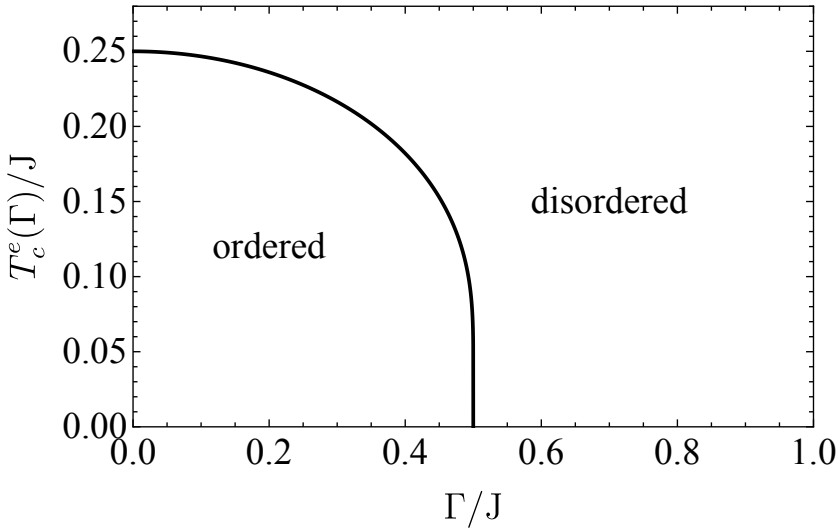

Figure 2.1: Equilibrium phase diagram of the infinite-range transverse field Ising model. The critical temperature $T_c^e(\Gamma)$ determined by Eq. (2.12) separates the ordered (ferromagnetic) phase from a disordered (paramagnetic) regime at high temperatures or large fields.

range nature of the interactions, the exact Hamiltonian (2.11) may be replaced by the mean-field Hamiltonian

$$H_{\mathrm{MF}} = \sum_{i=1}^{N} \left(m s_i^z - \Gamma s_i^x \right) \ , \tag{2.14}$$

with the equilibrium mean-field magnetization $m = \sum_i \langle s_i^z \rangle / N$ determined self-consistently by solving

$$2\sqrt{\Gamma^2 + m^2} = \tanh\left(\frac{\beta}{2} \sqrt{\Gamma^2 + m^2} \right) . \tag{2.15}$$

As opposed to Eq. (2.11) the $\mathbb{Z}_2$-symmetry is explicitly broken in the mean-field Hamiltonian. This procedure therefore allows to enforce a finite magnetization in the initial state in the ferromagnetic phase.

At time $t = 0$, we abruptly switch the transverse-field strength from Γ_{i} to $\Gamma_{\mathrm{f}} \neq \Gamma_{\mathrm{i}}$, thereby initiating the dynamics of our system, which is always evolved by the full Hamiltonian (2.11).

2.2.2 Classical dynamics

We now derive the classical dynamics of our model. As we will see, this suffices to find the finite-temperature DPT-I phase diagram. We begin by rewriting the

Hamiltonian (2.11) in the form

$$\begin{aligned} H =& -\frac{1}{2N} S_z S_z - \Gamma S_x - \Lambda S_z \\ \simeq& -\frac{S^2}{2N} \cos^2\theta - \Gamma S \sin\theta\cos\phi - \Lambda S\cos\theta \\ \equiv& H(\theta,\phi)\ , \end{aligned} \tag{2.16}$$

for the total spin vector $\boldsymbol{S} = (S_x, S_y, S_z)^\intercal = \sum_i \boldsymbol{s}_i$, with conserved spin length $S^2 = S_x^2 + S_y^2 + S_z^2$. The first equality in (2.16) is, up to an irrelevant constant, an exact reformulation of (2.11), while the second uses the classical continuous representation $\boldsymbol{S} = S\,(\cos\phi\sin\theta, \sin\phi\sin\theta, \cos\theta)^\intercal$ and thus neglects intensive terms arising from the non-commutativity of the spin operators. Consequently, the classical description is identical to the $S \to \infty$ limit. The system of coupled equations of motion for $\boldsymbol{S}$ is given by

$$\frac{\mathrm{d}\boldsymbol{S}}{\mathrm{d}t} = -\mathrm{i}\,[\boldsymbol{S}, H]\,. \tag{2.17}$$

In the classical formulation, where the commutator is replaced by the Poisson bracket, these turn into

$$\begin{aligned} \frac{\mathrm{d}\theta}{\mathrm{d}t} &= \Gamma\sin\phi, \\ \frac{\mathrm{d}\phi}{\mathrm{d}t} &= \Gamma\cos\phi\cot\theta - \frac{S}{N}\cos\theta - \Lambda\ , \end{aligned} \tag{2.18}$$

which show no relaxation, such that $m(t \to \infty) \neq 0$. In fact the latter is a consequence of dephasing and thus a purely quantum mechanical effect, that is beyond the reach of a fully classical description. We will briefly revisit this point in a semiclassical approximation in Sec. 2.3.3.

The (conserved) energy of the initial state after the quench (measured by the final Hamiltonian) can be written as a weighted integral over all classical configurations

$$E = \frac{1}{Z}\int_0^{2\pi}\mathrm{d}\phi\int_0^{\pi}\mathrm{d}\theta\int_0^1 \mathrm{d}s\ s^2\sin\theta\ \mathrm{e}^{-\beta H_\mathrm{i}(s,\theta,\phi)} D(sN/2) H_\mathrm{f}(s,\theta,\phi)\ , \tag{2.19}$$

with $s = 2S/N \in [0,1]$, and where $H_{\mathrm{i(f)}}$ corresponds to (2.16) with $\Gamma = \Gamma_{\mathrm{i(f)}}$. Note, that we omit any normalization constant for the integrals, as it is entirely inconsequential. The degeneracy factor of the subspace with fixed value of S can simply be constructed from rotational invariance: Obviously the configuration with S_z-projection $m_S = N/2$ is unique and by rotational symmetry the same has to be true for any other value of m_S in the subspace of maximal spin length. Of the N configurations with $m_S = N/2-1$, one has thus already been used and only $N-1$ have spin length $S = N/2-1$. Repeating this argument, one finds that $D(S)$ is

given by

$$D(S) = \binom{N}{\frac{N}{2} - S} - \binom{N}{\frac{N}{2} - S - 1}. \tag{2.20}$$

As usual

$$Z = \int_0^{2\pi} \mathrm{d}\phi \int_0^{\pi} \mathrm{d}\theta \int_0^1 \mathrm{d}s \; s^2 \sin\theta \; \mathrm{e}^{-\beta H_\mathrm{i}(s,\theta,\phi)} D(sN/2) \tag{2.21}$$

is the partition function. The limit $N \to \infty$ allows for a saddle-point expansion around the maximum of the product $D(sN/2) \exp\left(-\beta H_\mathrm{i}(s,\theta,\phi)\right)$, which fixes $s = \bar{s}$, $\theta = \bar{\theta}$, and for $\Gamma_\mathrm{i} \neq 0$ also ϕ to exact values. Thermal fluctuations around these values are suppressed by factors of $\exp\left(-\beta N\right)$ and can thus be neglected. This implies that the partition function and all thermal expectation values are simply given by the evaluation at the saddle point of $D(sN/2) \exp\left(-\beta H_\mathrm{i}(s,\theta,\phi)\right)$. Consequently, the integrals in (2.19) collapse and one finds

$$E = H_\mathrm{f}(\bar{s}, \bar{\theta}, \bar{\phi}). \tag{2.22}$$

Since $D(S)$ has no angular dependence, one has

$$\theta_\mathrm{i} = \bar{\theta} = \arcsin \frac{2\Gamma_\mathrm{i}}{\bar{s}} \tag{2.23}$$

and if $\Gamma_\mathrm{i} \neq 0$

$$\phi_\mathrm{i} = \bar{\phi} = 0 \tag{2.24}$$

directly by minimizing $H_\mathrm{i}(s,\theta,\phi)$. Clearly this solution is only real and thus physical, if $\Gamma_\mathrm{i} \leq \bar{s}/2$, otherwise the system is initialized in the $\mathbb{Z}_2$ symmetric state with $\theta_\mathrm{i} = \bar{\theta} = \pi/2$. By expanding the binomial factors in $D(S)$ by means of Stirling's formula, one obtains the additional saddle point equation

$$\frac{\beta\bar{s}}{4} \cos^2\bar{\theta} + \frac{\beta\Gamma_\mathrm{i}}{2} \sin\bar{\theta} = \operatorname{arctanh}\bar{s}\,, \tag{2.25}$$

which, together with $\Gamma_\mathrm{i} = \bar{s}/2$, immediately leads to the equilibrium phase transition (2.12). In the case of a $\mathbb{Z}_2$ symmetry-broken initial state one has

$$E(\bar{s}) = -N\left[\frac{\bar{s}^2}{8} + \Gamma_\mathrm{i}\left(\Gamma_\mathrm{f} - \frac{1}{2}\Gamma_\mathrm{i}\right)\right]. \tag{2.26}$$

The long-time-averaged magnetization in the z-direction can vanish only if the classical spin vector can overcome the equator of the Bloch sphere. Thus a phase transition in the sense of DPT-I occurs if the initial state is prepared such that its

energy after the quench is sufficiently large. This allows us to use the equation

$$E(\bar{s}) = -\Gamma_\mathrm{f}\frac{N\bar{s}}{2} \,. \tag{2.27}$$

to find the dynamical critical temperature in the thermodynamic limit $N \to \infty$, which reads

$$T_\mathrm{c}^\mathrm{d}(\Gamma_\mathrm{i}, \Gamma_\mathrm{f}) = \frac{2\Gamma_\mathrm{f} - \Gamma_\mathrm{i}}{2\,\mathrm{arctanh}\,(4\Gamma_\mathrm{f} - 2\Gamma_\mathrm{i})} \,. \tag{2.28}$$

For a $\mathbb{Z}_2$-symmetric initial state the classical system shows no dynamics if $\Gamma_\mathrm{f} > \Gamma_\mathrm{i}$ since the system is initialized in the ground state (for fixed s) of both the initial and final Hamiltonians. Dynamics is only induced by a quench if the ground state of the final system at $s = \bar{s}$ is ferromagnetic. In this case $\langle S_z \rangle$ will average to a finite value (given an infinitesimal seed). As the effective spin length s is not the same as in the equilibrium phase corresponding to Γ_f, but rather to that of the equilibrium phase at Γ_i, the resulting critical final field strength is given by

$$\Gamma_\mathrm{c}^\mathrm{d} = \frac{\bar{s}}{2} = \frac{1}{2}\tanh\frac{\Gamma_\mathrm{i}}{2T} \,, \tag{2.29}$$

for $\Gamma_\mathrm{i}(T) > \Gamma_\mathrm{c}^\mathrm{e}(T)$, as immediately follows from the condition

$$\left.\frac{\mathrm{d}^2 H(\theta, 0)}{\mathrm{d}\theta^2}\right|_{\theta=\frac{\pi}{2}} \stackrel{!}{=} 0 \,. \tag{2.30}$$

It is important to note that the collapse of the partition function in the thermodynamic limit is also true for the quantum-mechanical treatment of the problem, where it is therefore also allowed to fix s according to (2.25) as $N \to \infty$. We will confirm these predictions in Sec. 2.2.4 with numerical results obtained from the exact diagonalization of large systems.

2.2.3 Loschmidt echos at finite temperatures

There are several distinct generalizations of the ground-state Loschmidt echo to finite temperatures. However, not all of them are equally suited to distinguish dynamical phases in interacting systems. Using the IR-TFIM, we demonstrate that the so-called interferometric Loschmidt echo is in general ill-suited for this task. However, we find a relative of the more useful fidelity Loschmidt echo, that can be efficiently evaluated and produces the same phase-diagram.

Interferometric Loschmidt-echo return rate

One straightforward extension of Eq. (2.3) to thermal states is the interferometric Loschmidt amplitude, which has recently been defined as [97, 96]

$$G_{\mathrm{I}}(t) = \mathrm{Tr}\left\{\rho_{\mathrm{i}} \mathrm{e}^{-\mathrm{i}H(\Gamma_{\mathrm{f}})t}\right\}, \tag{2.31}$$

where H refers to the full Hamiltonian (2.11). In the limit of zero temperature this reduces to the original Loschmidt amplitude [45] $G(t) = \langle\psi_{\mathrm{i}}| \exp(-\mathrm{i}H(\Gamma_{\mathrm{f}})t)|\psi_{\mathrm{i}}\rangle$, with $|\psi_{\mathrm{i}}\rangle$ the ground state of the pre-quench Hamiltonian $H(\Gamma_{\mathrm{i}})$. In (2.31), the evolution time t takes the place of the complex inverse temperature, making it a weighted sum of dynamical analogs of a boundary partition function. Consequently, the corresponding dynamical analog of the thermal free energy density in equilibrium is the Loschmidt-echo return rate

$$r_{\mathrm{I}}(t) = -\lim_{N\to\infty} \frac{1}{N} \ln |G_{\mathrm{I}}(t)|^2 . \tag{2.32}$$

At $T = 0$, the DPT-II is connected to non-analytic cusps in (2.32) and has previously been investigated in the non-integrable one-dimensional long-range [70, 87, 88] and the fully connected transverse-field Ising models [57, 48]. Unlike the DPT-I, which for infinite-range spin chains in the absence of a meaningful notion of distance is limited to the late-time behavior of the order parameter, and thus has only two phases (vanishing or finite order parameter), the DPT-II exhibits three distinct dynamical phases [87, 88, 48]. Starting from an ordered ground state, quenches across a dynamical critical point give rise to regular cusps (i.e. cusps in every oscillation) in the Loschmidt-echo return rate. On the other hand, for quenches below this dynamical critical point, the return rate displays no cusps when the interactions are short range, while for sufficiently long-range interactions [87], a new kind of *anomalous* cusps (i.e. cusps appearing only after a certain number of smooth oscillations) have been shown to emerge in numerical studies [87, 48, 88]. Moreover, the DPT-I and DPT-II seem to be intimately connected, at least for long-range interactions [70, 87, 48].

For the infinitely connected model, however, even trivial quenches from $\Gamma_{\mathrm{i}} \to \Gamma_{\mathrm{i}}$, that at $T = 0$ result in $r_{\mathrm{I}}(t) \equiv 0$, can show a rich non-analytic behavior of the return rate at finite temperatures. To understand this in some more detail, let us consider the easiest case without a transverse field. The associated Hamiltonian is diagonal in S_z and given by

$$H = -\frac{1}{2N} S_z^2, \tag{2.33}$$

where each eigenstate of S_z has degeneracy

$$D_z(S_z) = \binom{N}{S_z + \frac{N}{2}}. \tag{2.34}$$

While the return rate, even for this simple system, cannot be calculated exactly for arbitrary system sizes N, we can obtain the thermodynamic limit for short times analytically. For large systems and short times, the sum in the return rate for $\Gamma_\mathrm{i} = \Gamma_\mathrm{f}$, which is given by

$$r_\mathrm{I}(t) = -\frac{2}{N} \ln \left| \sum_{S_z} D_z(S_z) \exp\left[(\beta + \mathrm{i}t) \frac{S_z^2}{2N} \right] \right| + \frac{2}{N} \ln Z, \tag{2.35}$$

can be replaced by an integral. With $s_z = \frac{S_z}{N} + \frac{1}{2}$ we obtain

$$\begin{aligned} r_\mathrm{I}(t) = -\frac{2}{N} \ln \Bigg| \int_0^{1/2} \mathrm{d}s_z \, \exp\Bigg\{ N \Bigg[(\beta + \mathrm{i}t) \frac{1}{8}(1-2s_z)^2 \\ - s_z \ln s_z - (1-s_z)\ln(1-s_z) - \ln 2 \Bigg] \Bigg\} \Bigg| + A \,, \end{aligned} \tag{2.36}$$

to leading order in N, where the constant A ensures the normalization $r(t=0) = 0$. Its value $A = \frac{1}{4}\left[\beta - 4s_0^2\beta - 8\ln(2-2s_0)\right]$ is determined by the evaluation of the integrand in (2.36) at the non-trivial saddle point $s_0 \in (0, 1/2)$, which solves

$$\beta\left(s_0 - \frac{1}{2}\right) = 2\,\mathrm{arctanh}\,(1-2s_0)\,. \tag{2.37}$$

For finite $t > 0$, however, the first term of the return rate $r_\mathrm{I}(t)$ will be dominated by the values of s_z near $1/2$, where the exponent converges quadratically to zero. Yet, in the thermodynamic limit the integral over this region yields only a vanishing contribution to $r_\mathrm{I}(t)$ such that the return rate is bounded by A from above. For short times in the sense of $t \cdot \Delta\epsilon \ll 1$, where $\Delta\epsilon$ is the typical energy difference between the discrete levels around the saddle point s_0, one can still use (2.36) as an approximation to $r_\mathrm{I}(t)$. Performing again a saddle point expansion around s_0, the ensuing Gaussian integral and the limit $N \to \infty$ yields

$$r_\mathrm{I}(t) = \frac{s_0\,(1-s_0)\,(1-2s_0)^2\,[1 + s_0\,(s_0-1)\,\beta]\,t^2}{4\,\{1 + s_0\,(s_0-1)\,[2\beta + s_0\,(s_0-1)\,(t^2+\beta^2)]\}}\,. \tag{2.38}$$

By comparing the result for A and (2.38) we realize that for sufficiently small temperatures the unrestricted Gaussian integral used in (2.38) allows $r_\mathrm{I}(t)$ to quickly grow beyond its allowed bound. This is not possible for the original expression (2.35) or (2.36), involving a *restricted* sum or integral instead. Consequently, one has a sharp transition from the short-time behavior to the limiting value.

In summary we obtain in the thermodynamic limit a sharp signature in the short-time return rate,

$$r_{\mathrm{I}}(t) = \frac{1}{4}\min\left\{\frac{\left(s_0^2 - s_0\right)\left(1-2s_0\right)^2\left[1+\left(s_0^2-s_0\right)\beta\right]t^2}{1+\left(s_0^2-s_0\right)\left[2\beta+\left(s_0^2-s_0\right)\left(t^2+\beta^2\right)\right]}, \beta - 4s_0^2\beta - 8\ln\left(2-2s_0\right)\right\}, \tag{2.39}$$

where s_0 solves (2.37).

This result compares well with the full, numerically evaluated expression for inverse temperatures $\beta < 5.5$. Further numerical investigation shows that the sharp cutoff in the first peak survives for temperatures as low as $\beta \approx 5.9$, which is deep inside the ferromagnetic phase. Fig. 2.2 shows a comparison of exact interferometric return rates $r_{\mathrm{I}}(t)$ for finite systems with the analytical expression (2.39). One clearly sees the convergence for $N \to \infty$ of the numerical data toward the analytical plateau, creating an increasingly sharp thermal cusp in the first peak in the process. In addition to the cutoff in the first peak, numerical simulations for system sizes of up to $N = 1 \times 10^6$ show further cusps appearing at late times, reminiscent of the anomalous phase previously investigated in the IR-TFIM at $T = 0$ in Refs. [87, 48] (see Fig. 2.3). For the trivial quench at finite temperatures, where $G_{\mathrm{I}}(t) = \mathrm{Tr}\left\{\exp\left[-(\beta+it)H\right]\right\}$, these cusps are nothing else but the Lee-Yang zeros in the complex plane of the partition function [79] and clearly not related to any dynamical phase transition.

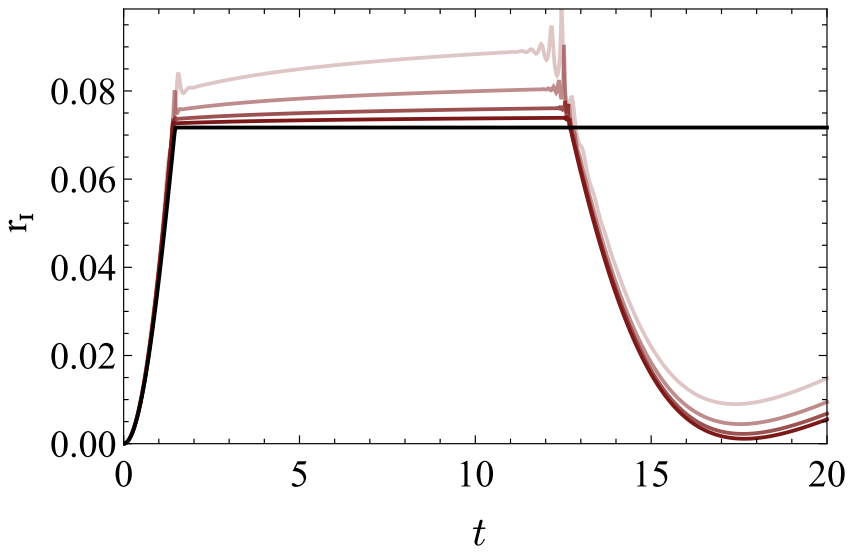

Figure 2.2: Comparison of exact finite-size results with the analytical expression (2.39), shown in black, for the return rate (2.32) at short times with inverse temperature $\beta = 5$ and a trivial quench $\Gamma_{\mathrm{i}} = \Gamma_{\mathrm{f}} = 0$. System size from light to dark red is $N = 201$, 401, 801, and 1601.

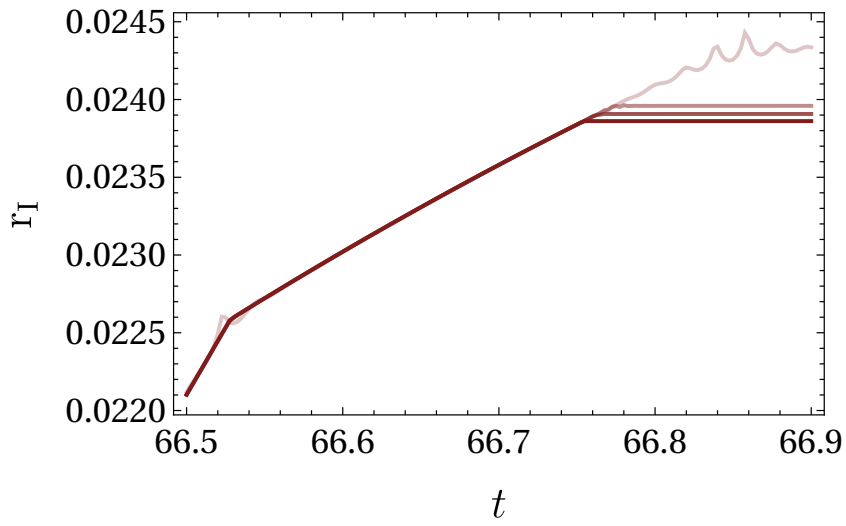

Figure 2.3: Non-analytic features in the interferometric return rate $r_\mathrm{I}(t)$ at low temperature $\beta = 10$ and late times following a trivial quench $\Gamma_\mathrm{i} = \Gamma_\mathrm{f} = 0$. System sizes from light to dark red are $N = 2 \times 10^4$, $N = 1 \times 10^5$, $N = 2 \times 10^5$ and $N = 1 \times 10^6$.

Turning to the case of a finite quench distance, we now give a few examples of how the behavior of this return rate gets even more convoluted once the system is actually excited out of its equilibrium configuration.

The anomalous behavior of $r_\mathrm{I}(t)$ for trivial quenches quickly turns into a regular behavior with very pronounced cusps in every peak for short quench distances beginning and ending in an ordered state. An example for the same parameters that will be used again in Fig. 2.7(b) is illustrated in Fig. 2.4(a). As a representative example for a quench through the dynamical phase transition we present the same quench as in Fig. 2.9(b) in Fig. 2.4(b). While there are clearly more cusps visible in Fig. 2.4(b) than in Fig. 2.4(a) these additional cusps do not appear all at the same value of T or Γ_f and cannot be linked to any particular behavior of the magnetization vector. Finally, we note that even a quench at very high temperature and very deep within the disordered phase, as shown in Fig. 2.4(c), exhibits cusps in every peak of $r_\mathrm{I}(t)$. This happens despite the absence of any dynamics in the magnetization vector and in a regime where not even $T = 0$ would support ferromagnetic order.

Fidelity Loschmidt-echo return rate

In a quantum quench setup one is interested in the time evolution governed by a Hamiltonian H_f, where the system is initially prepared in a thermal equilibrium

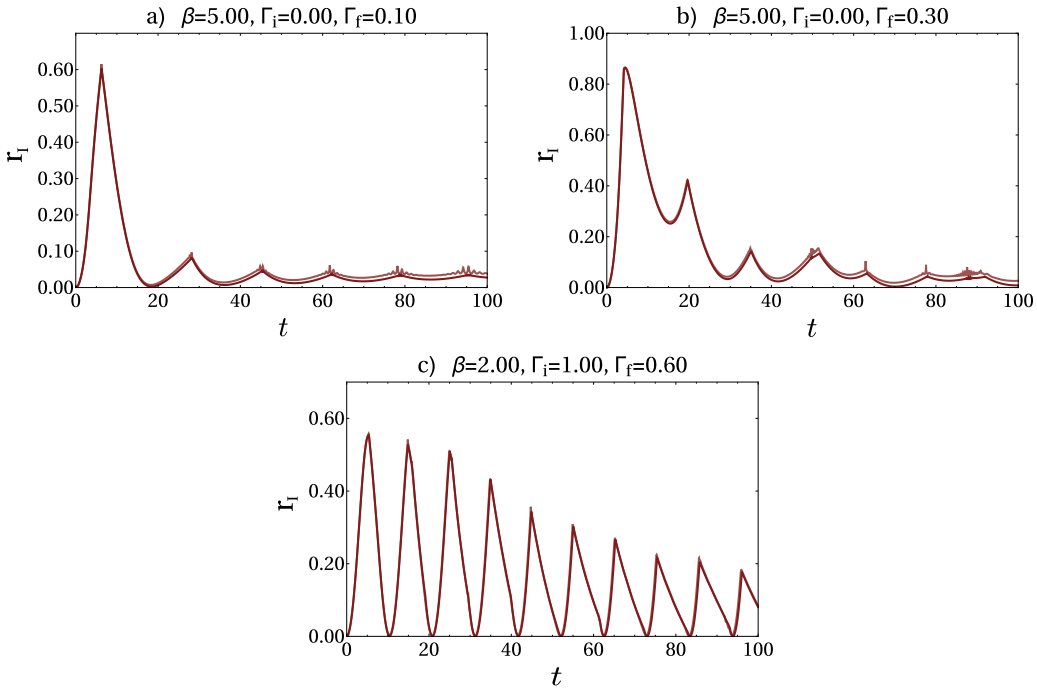

Figure 2.4: Behavior of the interferometric return rate $r_{\mathrm{I}}(t)$ as defined in (2.32) for different quenches, which also shown in the main text for $r_{\mathrm{q}}(t)$, with system sizes $N = 201$ and $N = 1001$ for the light and dark line respectively. The quench in panel (a) is identical to the one depicted in Fig. 2.7(b). Here $r_{\mathrm{I}}(t)$ exhibits pronounced non-analyticities in all peaks. The same is true for the quench in (b), which is the same as in Fig. 2.9(b), and for the quench in panel (c) that is deep within the paramagnetic phase and also shown in Fig. 2.11(b).

state ρ_i. Under the condition that ρ_i is not diagonal in the eigenbasis $\{|\Phi_\mathrm{f}\rangle\}$ of H_f, the Loschmidt return function $r_\mathrm{I}(t)$ can show non-analytic behavior due to the nontrivial overlap of the states making up ρ_i with the eigenstates of H_f. However, starting with a genuine density matrix and not a pure state can give rise to a type of non-smooth features in $r_\mathrm{I}(t)$ that we are not interested in and that would already appear in a trivial quench $\Gamma_\mathrm{i} \to \Gamma_\mathrm{i}$, as discussed in detail in Sec. 2.2.3. Therefore, a particularly interesting choice of the finite-temperature Loschmidt amplitude is given by the fidelity of the initial and time-evolved density matrices [98, 99]

$$G_\mathrm{F}(t) = \mathrm{Tr}\sqrt{\sqrt{\rho(0)}\rho(t)\sqrt{\rho(0)}}\,. \tag{2.40}$$

As with the interferometric definition (2.31), (2.40) reproduces the zero-temperature Loschmidt echo. The advantage of this definition is, however, that it forms a metric, measuring the distance over which the density matrix has evolved during the time t. This also implies that the corresponding fidelity return rate

$$r_\mathrm{F}(t) = -\lim_{N\to\infty}\frac{2}{N}\ln G_\mathrm{F}(t) \tag{2.41}$$

vanishes identically in case of any trivial quench, as then $G_\mathrm{F}(t) \equiv 1$. Furthermore, r_F is also applicable to open systems. Nevertheless, these advantages come at a high price: Introducing the symmetric interference matrix

$$A_{ij}(t) = \frac{1}{Z}\sum_l \mathrm{e}^{-\frac{\beta}{2}\epsilon_i^\mathrm{i}}\langle\Psi_i|\Phi_l\rangle\,\mathrm{e}^{-\mathrm{i}\epsilon_l^\mathrm{f}t}\langle\Phi_l|\Psi_j\rangle\,\mathrm{e}^{-\frac{\beta}{2}\epsilon_j^\mathrm{i}}\,, \tag{2.42}$$

where $\{|\Psi_i\rangle\}$ ($\{|\Phi_i\rangle\}$) are the eigenstates of the initial (final) Hamiltonian with eigenenergies $\epsilon_i^{\mathrm{i(f)}}$, allows us to represent the Loschmidt amplitudes (2.31) and (2.40) in a unified form. While the interferometric Loschmidt amplitude $G_\mathrm{I}(t) = \mathrm{Tr}\{A(t)\}$ is easily evaluated, its fidelity counterpart $G_\mathrm{F}(t) = \mathrm{Tr}\{\sqrt{A(t)\cdot A(t)^*}\}$ is numerically far more expensive, because it requires calculating the square root of a large matrix at every time step.

Quantum Loschmidt-echo return rate

Since on the one hand the interferometric definition $r_\mathrm{I}(t)$ already shows cusps for a trivial quench, where it probes the complex Lee-Yang zeros, and on the other hand computation of the fidelity return rate $r_\mathrm{F}(t)$ entails an undesirably large numerical effort, we shall introduce a third finite-temperature return rate. While this choice will be specific to integrable systems like our infinitely connected model, it reconciles a simple physical motivation with a numerically efficient evaluation, and, furthermore, resolves the same phases as $r_\mathrm{F}(t)$.

Due to the fact that in the infinite range Ising model $[H, S^2] = 0$, we conserve the total angular momentum independent of the initial and final values of $\Gamma_\mathrm{i,f}$. The

ability to numerically treat system sizes of the order of several thousand sites relies directly on this fact. On the other hand, our quench protocol only allows for states within a fixed S-subspace to interfere during the time evolution. However, in the standard $r_{\mathrm{I}}(t)$ we compute interferences of arbitrary S-subspaces:

$$r_{\mathrm{I}}(t) = -\frac{2}{N} \ln \left| \sum_S G_S(t) \right| , \tag{2.43}$$

with

$$G_S(t) = \mathrm{Tr} \left\{ \mathrm{e}^{-\mathrm{i}H_{\mathrm{f}}t} \rho_{\mathrm{i}}^S \right\} \tag{2.44}$$

the Loschmidt amplitude obtained for the subspace with total spin length $S \in \{1/2, 3/2, \ldots, N/2\}$ for odd N without loss of generality. Here,

$$\rho_{\mathrm{i}}^S = \frac{\mathrm{e}^{-\beta \mathcal{H}(\Gamma_{\mathrm{i}})}\big|_S}{\mathrm{Tr}\, \mathrm{e}^{-\beta \mathcal{H}(\Gamma_{\mathrm{i}})}} , \tag{2.45}$$

denotes the partial density matrix restricted to the spin subspace with spin length S. Obviously, in $r_{\mathrm{I}}(t)$ all spin sectors interfere and can give rise to cusps despite the fact that the quench in Γ cannot mix any states of different S.

Additionally, for a finite quench distance, $r_{\mathrm{I}}(t)$ will show quite a rich behavior that is related only to the integrability of the infinite range model and is not expected to be found in a more generic system. If we expand $r_{\mathrm{I}}(t)$ in a spectral representation

$$r_{\mathrm{I}}(t) = -\frac{2}{N} \ln \left| \int \mathrm{d}\epsilon \; g(\epsilon) \mathrm{e}^{-\mathrm{i}\epsilon t} \right| , \tag{2.46}$$

we see that it is simply the Fourier transform of the overlap density of states $g(\epsilon)$ that is given by

$$g(\epsilon) = \sum_S \frac{D(S)}{Z} \sum_{i,j} \left| \langle \Phi_j^S | \Psi_i^S \rangle \right|^2 \mathrm{e}^{-\beta \epsilon_i^{\mathrm{i},S}} \delta(\epsilon - \epsilon_j^{\mathrm{f},S}) , \tag{2.47}$$

where again $\{|\Psi_i^S\rangle\}$ $\left(\{|\Phi_i^S\rangle\}\right)$ denote the eigenstates in the spin sector S of the initial (final) Hamiltonian with energies $\epsilon_i^{\mathrm{i(f)},S}$. Like any ordinary density of states, $g(\epsilon)$ contains a superposition of Dirac distributions located at the actual final-Hamiltonian eigenvalues $\epsilon_i^{\mathrm{f},S}$, but, importantly, here they carry weights proportional to the degeneracy factor $D(S)$ of the corresponding subspace. Due to its binomial behavior, see (2.20), $D(S)$ varies over several orders of magnitude between the different spin sectors. As such, we have to compute the Fourier transform of a very rough function that does not become smooth even in the thermodynamic limit, as the average level spacing remains of order one. In contrast, in a non-integrable

model, the huge degeneracies vanish and the typically exponentially small energy distances in the spectrum smoothen both g and r_{I}. Thus, in order to investigate features that do not depend too crucially on the full permutation invariance of the model and to focus on cusps that are indeed related to the S-conserving quench protocol, we define a generalized Loschmidt echo $r_{\mathrm{q}}(t)$ that sums all subspaces in phase

$$r_{\mathrm{q}}(t) = -\frac{2}{N} \ln \sum_S |G_S(t)| \,. \tag{2.48}$$

Quite importantly, this choice treats the mixing of eigenstates by the quench and the resulting interferences on an equal footing. Furthermore, the sum here is always dominated by the subspace with the largest combination of the degeneracy factor $D(S)$ times the thermal weight of its ground state. This space can be found analytically in mean-field theory (2.25). As a consequence, thermal broadening disappears in the thermodynamic limit and all cusps in the Loschmidt echo become sharp signatures if they are for the system with $\Gamma^{\mathrm{eff}}_{\mathrm{i(f)}} = \Gamma_{\mathrm{i(f)}}/\bar{s}$ for the quench at $T = 0$, with $\bar{s}$ a solution of (2.25).

Within the dominant subspace, like in every other subspace, all states have the same $D(S)$, cf. Sec. 2.2.2, so the importance of a certain state during a quench depends only on its thermal weight factor and the overlaps with the eigenstates of the final Hamiltonian, giving rise to a much smoother density of states and Fourier transform compared to the situation discussed in Sec. 2.2.3. Finally, in a trivial quench, $r_{\mathrm{q}}(t)$ will be a smooth function, as the sum is now dominated by a single state, which cannot give rise to interferences. This latter is given by the ground state of the most important S-subspace.

Taking into account that the total spin is conserved, the interference matrix A from (2.42) decouples into block diagonal form with a block A^S for every spin sector. As a result both

$$r_{\mathrm{q}}(t) = -\frac{2}{N} \ln \sum_S \left|\mathrm{Tr}\, A^S(t)\right| \,, \tag{2.49}$$

as well as

$$r_{\mathrm{F}}(t) = -\frac{2}{N} \ln \sum_S \mathrm{Tr} \sqrt{A^S(t) \cdot A^{S*}(t)}, \tag{2.50}$$

sum over all spin spaces in phase. Consequently, neither of these signals shows the large number of cusps which are present in $r_{\mathrm{I}}(t)$ and not associated with a physical phase. Clearly $r_{\mathrm{q}}(t)$ and $r_{\mathrm{F}}(t)$ are closely related with the former involving a sum over the eigenvalues of A^S compared to a sum over singular values in the latter. Without loss of generality, we sort the eigenstates $\{|\Psi_i^S\rangle\}$ in the fixed-S subspace of H_{i} by their energy such that the ground state is $|\Psi_1^S\rangle$. At $t = 0$, the matrix A^S is diagonal, and due to the thermal weights, its maximal element is

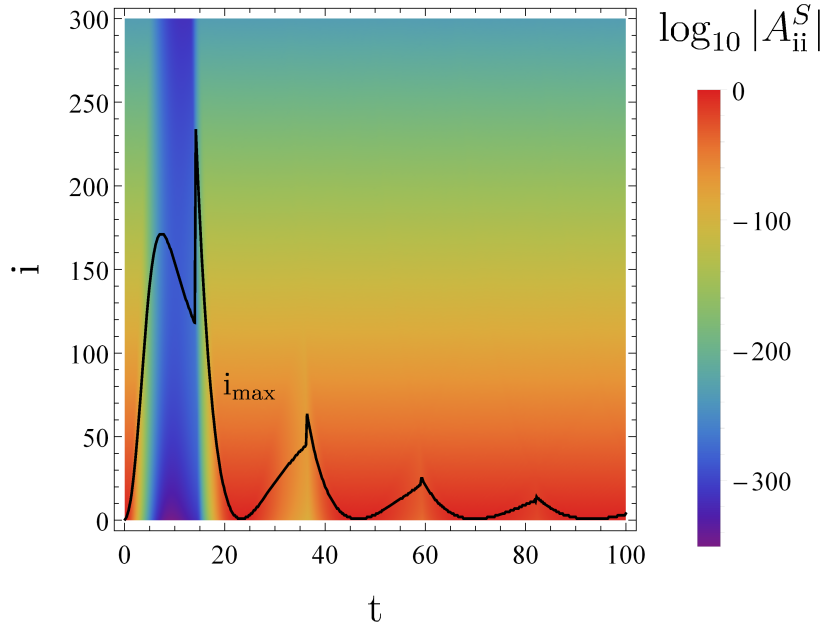

Figure 2.5: Decadic logarithm of the modulus of the diagonal elements A^S_{ii} of the interference matrix (2.42) in the dominant spin subspace S, set by the classical saddle point (2.25), as a function of time. Initially the largest component is given by A^S_{11}, however during the time evolution the index $i_{max}(t)$ is a nontrivial function that exhibits discontinuities, which coincide with the cusps in $r_F(t)$. Parameters for the quench are $\Gamma_i = 0$ and $\Gamma_f = 0.3$ at $\beta = 5$ for a system of size $N = 4001$.

A^S_{11}. At later times, the overlaps between different initial states remain suppressed, and, therefore, A is still dominated by its diagonal elements. However, during the time evolution, interferences between the final states result in an oscillation of all elements A^S_{ii} with a frequency that is given by the mean level spacing between those eigenstates of the final Hamiltonian with which the initial state $|\Psi^S_i\rangle$ has the largest overlaps. Since the spectrum of the final Hamiltonian is not perfectly linear, these oscillations are damped. For any S-subspace in the thermodynamic limit, we now define the function $i_{max}(t) \in (0, 1]$ by requiring that $|A^S_{i_{max}(t)L, i_{max}(t)L}(t)| \geq |A^S_{ii}(t)|$ for all $i \in \mathbb{N}$ and $i \leq L = \dim(A^S)$. Since A^S is symmetric, with a narrow maximum, the largest value of $M = A^S \cdot A^{S*}$ will also be near $M_{i_{max}L, i_{max}L}$ with an uncertainty that vanishes in the thermodynamic limit. Consequently, after a discontinuous change in i_{max} the time evolution of A^S is governed by a new maximum, that in general evolves with a different slope, resulting in a discontinuity of the first derivative of the return function $r_F(t)$. Such a jump in the function $i_{max}(t)$ for a typical quench is presented in Fig. 2.5. While $r_q(t)$ contains only

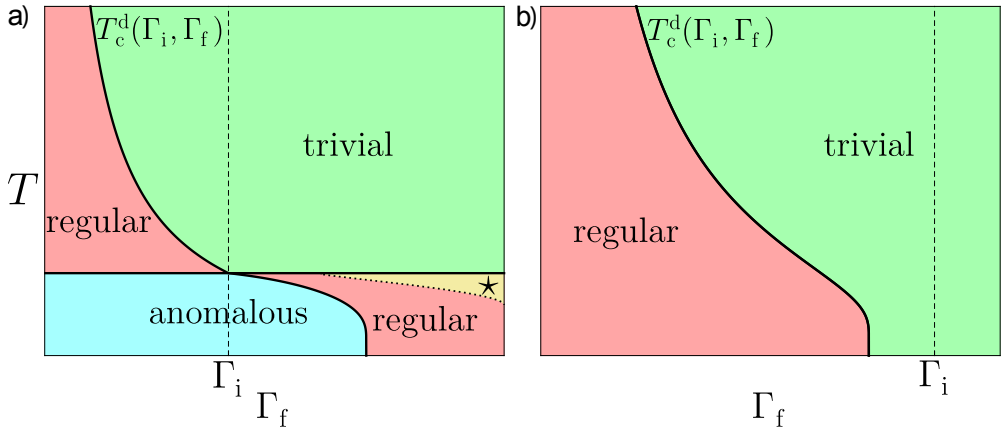

Figure 2.6: Finite-temperature dynamical phase diagram of the fully connected transverse-field Ising model. In (a) the system is initialized with $\Gamma_i < \Gamma_c^e(T = 0)$ whereas the quench in (b) starts always in a paramagnetic state. The full lines indicating the critical lines are analytical results. The dotted line separates the area where the Loschmidt-echo return rate exhibits a thermal cutoff ($\star$) from the rest of the regular phase, but this is not a separate phase in itself and is still within the latter.

the trace of A^S, and, therefore, also probes discontinuous changes in the diagonal elements of A^S, interferences between these can shift the cusp in time. However, after the first period of the return rate, the sum within the trace is once again evaluated with all terms almost completely in phase. Thus, before the end of the period, the corresponding cusp will also be visible in $r_q(t)$ and, consequently, $r_F(t)$ and $r_q(t)$ will always indicate the same dynamical phases. Larger quenches result in broader overlaps $\langle \Psi_i^S | \Phi_l^S \rangle$, whereas higher temperatures reduce the suppression of highly excited pre-quench eigenstates. Both effects lead to more destructive interferences in A^S. Based on this discussion, it becomes clear that larger quenches and higher temperatures give rise to earlier and more pronounced cusps in both return rates $r_F(t)$ and $r_q(t)$. Since the computation of the latter is several orders of magnitude faster, we will in the following exclusively focus on the quantum return rate $r_q(t)$.

2.2.4 Equivalence of DPT-I and DPT-II in infinite range spin chains

Using ED, we calculate the return rate (2.48) and magnetization for several quenches of thermal initial states at various temperatures in order to construct the finite-temperature dynamical phase diagram shown in Fig. 2.6 for the IR-TFIM.

Quenches from the ferromagnetic phase

We shall first present our results for quenches from a ferromagnetic thermal initial state, examples of which are shown in Figs. 2.7, 2.8, and 2.9. At low temperatures and for short quench distances, the final state will still exhibit ferromagnetic order (see discussion in Sec. 2.2.2). Following the quench, the initial magnetization vector, which for $\Gamma_\mathrm{i} = 0$ points along the positive z-direction with length $\bar{s}/2$ fixed by (2.25), starts to precess within the upper hemisphere around a tilted mean magnetization. However, the equator will never be crossed, and, while dephasing will damp the precession, the mean magnetization m cannot relax to zero. As our numerical investigation shows, this behavior is always accompanied by an anomalous phase in the return rate, where cusps appear only after its first minimum at finite time. The anomalous phase has previously been reported on in the IR-TFIM and one-dimensional transverse-field Ising model with power-law interactions for quenches starting from a ferromagnetic ground state in the case of an ordered final steady state [48, 87]. For the short quench distance $\Gamma_\mathrm{i} = 0 \to \Gamma_\mathrm{f} = 0.1$ and the low temperature $T = 0.1$ in Fig. 2.7(a), the return rate shows a strongly anomalous behavior characterized by many smooth periods before the appearance of the first cusp. The inset demonstrates the finite-size scaling of the curvature $|\ddot{r}_\mathrm{q}(t)|$ of the first two cusps, which is clearly consistent with the algebraically divergent model $\propto L^\alpha$ with $\alpha > 0$ used in the fit. Preparing our initial state at $T = 0.2$, on the other hand, we see in Fig. 2.7(b) that the same quench leads to a return rate where only the first peak is smooth, and thereafter every period of the return rate contains one cusp. This indicates that the higher the preparation temperature, the *closer* we are to a regular phase. Indeed, upon further increasing the preparation temperature to $T = 1/4.1$, which is very close to the equilibrium thermal critical point $T_\mathrm{c}^\mathrm{e}|_{\Gamma\to 0} = 1/4$, the anomalous phase disappears and is replaced by its regular counterpart, as shown in Fig. 2.7(c). At the same time the ferromagnetic order, which is already reduced by thermal fluctuations in the initial state, is lost completely in the final state. A closer investigation of the behavior for temperatures between $T = 0.2$ and $T = 1/4.1$ shows that, within our numerical precision, DPT-I and DPT-II coincide perfectly.

For the larger quench distance $\Gamma_\mathrm{i} = 0 \to \Gamma_\mathrm{f} = 0.2$ and at small temperatures, we observe an anomalous phase as shown in Fig. 2.8(a). However, in accordance with the DPT-I, the regular behavior of the return rate with cusps in every peak (see Fig. 2.8(b)) appears at smaller temperatures than in the smaller quench of Fig. 2.7. At even higher temperatures, but still below $T_\mathrm{c}^\mathrm{e}|_{\Gamma\to 0}$, something unexpected happens in the return rate: whereas the quench ends up in a state that is deep within the paramagnetic phase, where one expects a regular behavior of the return rate, a chipped-off first peak is observed. This can be explained by noting that for high preparation temperatures in the ferromagnetic phase the dominant subspace becomes very short. This in turn implies that the contribution of the short S-subspaces with $S \sim \mathscr{O}(1)$ instead of $S \sim \mathscr{O}(N)$ can become large enough to

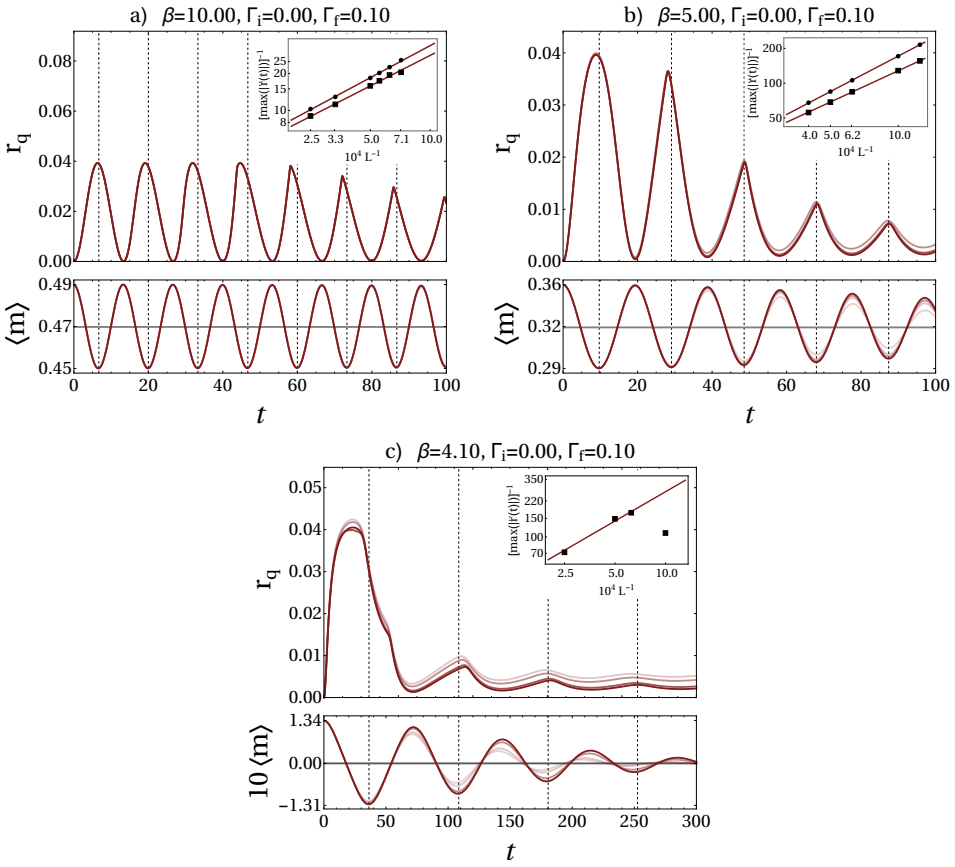

Figure 2.7: Quantum quench in the IR-TFIM from $\Gamma_\mathrm{i} = 0$ to $\Gamma_\mathrm{f} = 0.1$ with initial ferromagnetic thermal state at inverse temperatures $\beta = 10$, 5, and 4.1 ((a) through (c)) for various system sizes (light to dark red with increasing size) showing convergence. Even though at zero temperature this quench gives rise to an anomalous phase [48], as the temperature of the initial state is raised the anomalous phase transitions into its regular counterpart at temperatures above $T_\mathrm{c}^\mathrm{d}(\Gamma_\mathrm{i} = 0, \Gamma_\mathrm{f} = 0.1)$, cf. (2.28). Corresponding magnetization plots show the agreement between the anomalous (regular) phase and the long-time ordered (disordered) Landau-type phase. The gray constant represents the time-averaged magnetization obtained from the classical equations of motion to which $\langle m(t) \rangle$ must converge in the long-time limit. The grid lines fixed at the minima of the magnetization are almost synchronous with the maxima of $r_\mathrm{q}(t)$. Insets show the inverse curvature of each of the first two anomalous cusps in (a,b) and the first regular cusp in (c) in the return rate vanishing algebraically with system size, thereby indicating their sharpness, and thus true non-analyticity. For the sake of plot clarity, we only include the return-rate and magnetization plots for the four largest system sizes: in (a) $N = 1401, 2001, 3001, 4001$, (b) $N = 1001, 1601, 2001, 2501$, and (c) $N = 801, 1001, 1601, 2001$.

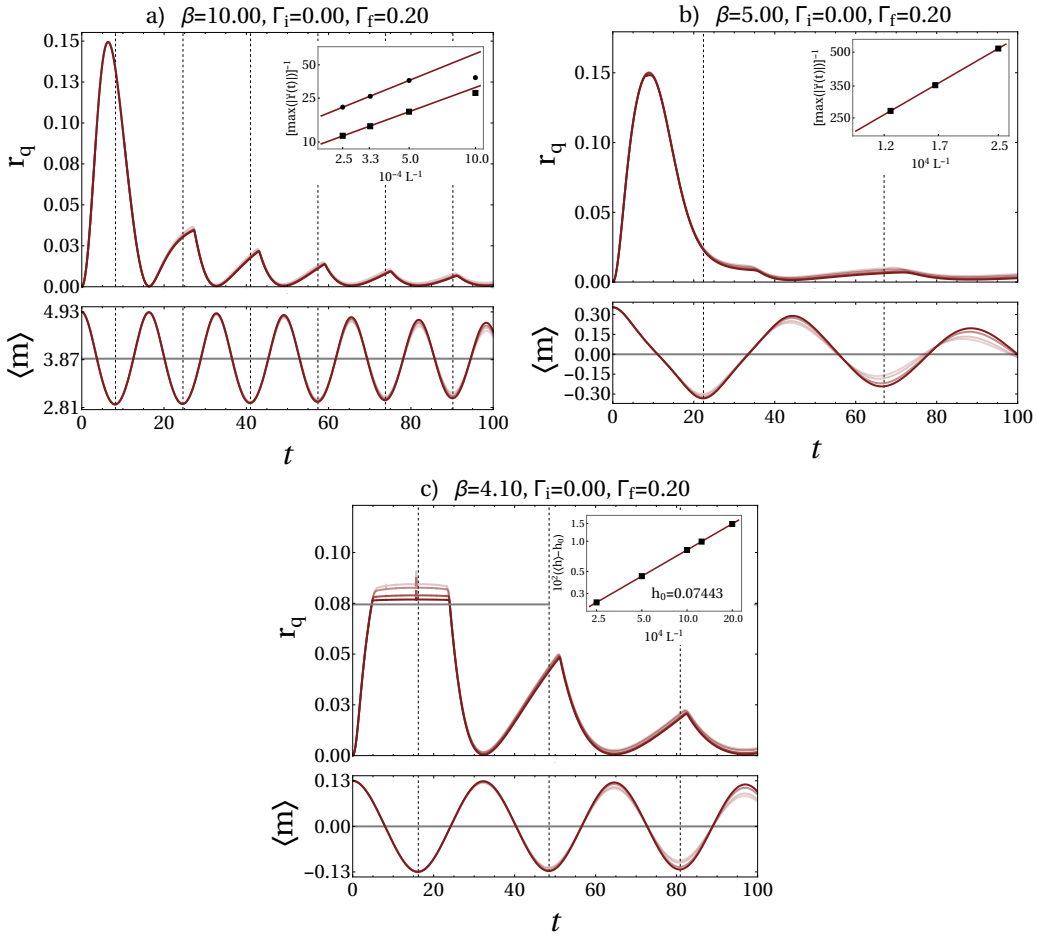

Figure 2.8: Same as Fig. 2.7 but with $\Gamma_\mathrm{f} = 0.2$. At low temperatures we again see an anomalous phase in (a), but now already at $T = 0.2$ the phase is regular, which coincides with a zero infinite-time average of the magnetization. At the even higher temperature of $T = 1/4.1$, where the return rate is even deeper in the regular phase, a thermal cutoff appears in the first peak occluding the cusp therein. In the thermodynamic limit it approaches the value $r_\mathrm{q}^\mathrm{max}$ indicated by the grey line. Insets in (a) and (b) illustrate the divergence of the curvature of the first two anomalous cusps in (a) and the first regular cusp in (b), while the inset in panel (c) shows the algebraic convergence of the thermal cutoff height towards the analytical result for infinite system size as obtained from (2.51). System sizes are in (a) $N = 1001, 2001, 3001, 4001$, in (b) $N = 801, 1001, 1501, 2001$, and in (c) $N = 801, 1001, 2001, 4001$.

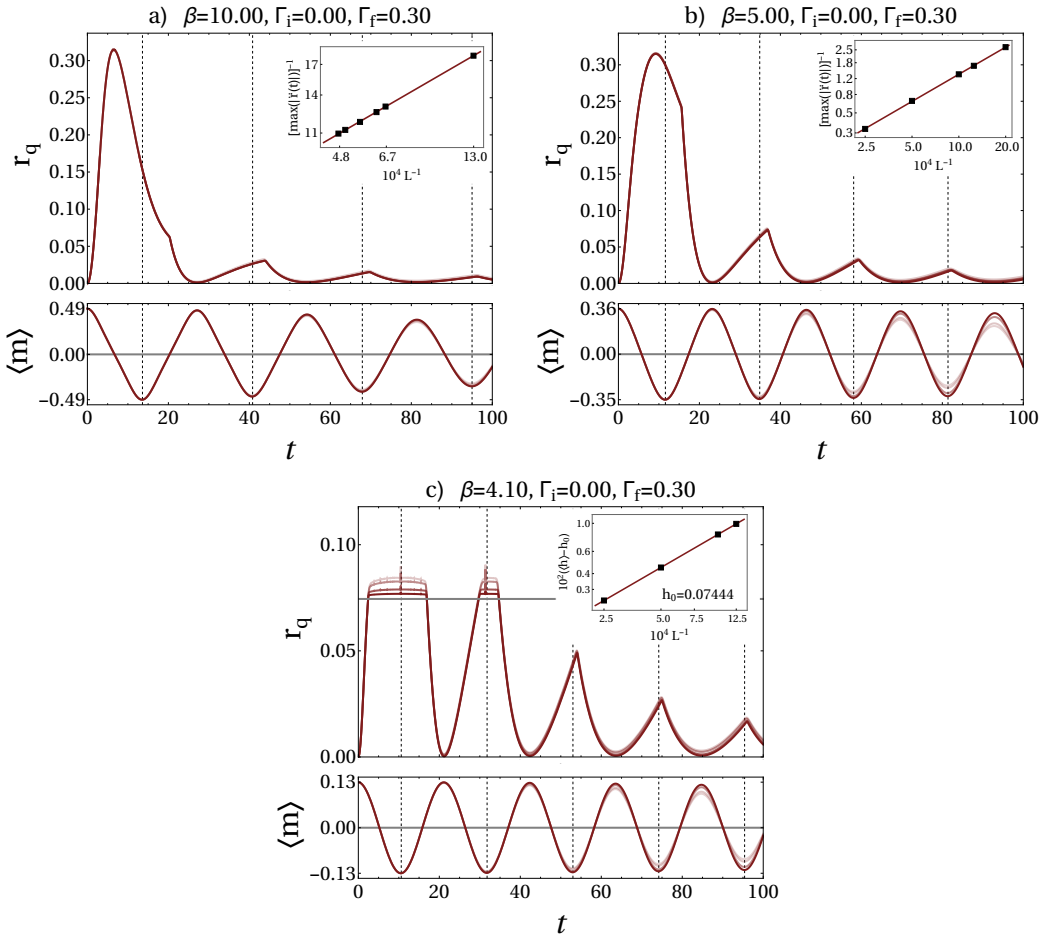

Figure 2.9: Same as Fig. 2.7 but with $\Gamma_\mathrm{f} = 0.3$. This quench gives rise to a regular phase even at $T = 0$. At higher temperatures below $T_\mathrm{c}^\mathrm{e}|_{\Gamma\to 0} = 0.25$, the phase is therefore also regular. In (c) a thermal cutoff is visible in the first two peaks of the return rate. Insets are the same as in Fig. 2.8, but here only the curvature of the first cusp, that is relevant for the classification as a regular phase, is analyzed. The presented system sizes are $N = 801, 1501, 1601, 1801$ in (a), $N = 501, 801, 1001, 2001$ in (b), and $N = 801, 1001, 2001, 4001$ in (c).

be resolved in the return rate. However, within these subspaces, no contributions to the Loschmidt echo that are exponentially small in system size can be generated due to the absence of enough interfering terms in the sum. Instead, these manifest as sharp (logarithmically divergent) signatures on top of the return rate that vanish $\propto 1/N$. As a result, the return rate is limited at (almost) all times by a maximal value $r_{\mathrm{q}}^{\max}$, for which one obtains in the thermodynamic limit

$$r_{\mathrm{q}}^{\max} = 2\ln\left[\cosh\left(\frac{\beta}{2}\sqrt{m^2+\Gamma_{\mathrm{i}}^2}\right)\right]. \tag{2.51}$$

The argument behind this result follows the same lines as Sec. 2.2.3. Since we initialize the system with a mean-field Hamiltonian the ground state of each spin sector has energy $E_{\min} = -S\sqrt{m^2+\Gamma_{\mathrm{i}}^2}$. Consequently, the partition function is approximately given by

$$\begin{aligned} Z &\approx \sum_{\{s_i^\tau\}} \mathrm{e}^{\beta\sqrt{m^2+\Gamma_{\mathrm{i}}^2}\sum_i s_i^\tau} = \sum_{\{s_i^\tau\}} \mathrm{e}^{\beta\sqrt{m^2+\Gamma_{\mathrm{i}}^2}S_i^\tau} \\ &= \sum_{L=0}^{N} \binom{N}{L} \mathrm{e}^{\beta\sqrt{m^2+\Gamma_{\mathrm{i}}^2}(N-2L)/2} = \left[\cosh\left(\frac{\beta}{2}\sqrt{m^2+\Gamma_{\mathrm{i}}^2}\right)\right]^N, \end{aligned} \tag{2.52}$$

where the contributions of excited states in each sector of fixed spin length has been neglected and the quantization axis τ was chosen such that it diagonalizes H_{MF}. The maximal value the return rate can take, is obtained if within each S-subspace $G_S(t) = 0$. For an even number of spins this is, however, not possible, as the smallest value $S = 0$ allows no interference. Instead this subspace always contributes $G_0(t) = 2^N/Z$ to leading order in N. For an odd number of spins on the other hand, interference in every subspace is possible. In the thermodynamic limit the contribution of the subspace with the minimal length $S = 1/2$ for $\Gamma_{\mathrm{i}} \neq 0$ is given by $G_{1/2}(t) = 2^N/Z$. If on the other hand $\Gamma_{\mathrm{i}} = 0$, the eigenvectors of the initial and final Hamiltonians are orthogonal. Hence, as discussed in the introduction, this two-level system can interfere destructively, giving rise to $G_{1/2}(t) = 2^N \cos[\Gamma_{\mathrm{f}} t/2]/Z$, which oscillates with the same period π/Γ_{f} as the magnetization of that subspace. Except for a time interval that is exponentially short in system size N, where $G_{1/2}(t)$ can thus exhibit a logarithmic divergence, the contribution of the subspaces with the shortest spins to the return rate is identical for even and odd system sizes. Furthermore, by the same argument, by which the integral in (2.36) vanishes at finite times, the contributions of other subspaces cause only subleading corrections to $r_{\max}$, such that we can conclude $r_{\mathrm{q}}^{\max} = -2\ln(2/Z^{1/N})$, which simplifies to (2.51). This expression can be confirmed numerically by the finite-size scaling in the insets of Figs. 2.8(c) and 2.9(c). These are performed by fitting a constant h_0 plus an algebraic decay to the average height of the plateau on top of the first peak. The obtained values for h_0 agree very well with $r_{\mathrm{q}}^{\max} \approx 0.07445$.

For quenches within the anomalous phase, the classical magnetization vector never crosses the equator of the Bloch sphere and our numerical simulations show that the return rate never grows to a value sufficiently large so as to resolve $r_{\mathrm{q}}^{\mathrm{max}}$. Consequently, the thermal cutoff can only be seen for quenches from a ferromagnetic to a paramagnetic state, i.e. only in the regular phase. At the same time not every quench will be affected by $r_{\mathrm{q}}^{\mathrm{max}}$, but rather predominantly those involving large quench distances where the overlap between initial and final state is generally smaller, as can be witnessed in Figs. 2.7, 2.8, and 2.9, where the latter shows the large quench from $\Gamma_{\mathrm{i}} = 0 \to \Gamma_{\mathrm{f}} = 0.3$. Despite the cutoff, the underlying phase is still regular in both of Figs. 2.8(c) and 2.9(c), as can be seen by decreasing the preparation temperature. For lower temperatures in the regular phase, the cusp is located on the shoulder of the first maximum. Upon varying the temperature, it moves up the trailing slope until it reaches the simultaneously decreasing value of $r_{\mathrm{q}}^{\mathrm{max}}$. From this point onwards it will be hidden by the thermal cutoff as illustrated in Fig. 2.10, where we present an example of the emergence of a thermal cutoff in the regular phase. In particular, this illustrates why we do not attribute this behavior to a dynamical phase transition. Beginning at a temperature $\beta = 4.7$ we quench from $\Gamma_{\mathrm{i}} = 0$ to $\Gamma_{\mathrm{f}} = 0.2$, obtaining regular behavior where the first cusp appears shortly before the first minimum at finite time. Increasing the temperature to $\beta = 4.5$, the cusp appears earlier in time at a larger value of the return rate. Finally, at $\beta = 4.2$ the thermal cutoff is almost small enough to affect the first peak and the cusp that is now located almost at the top of the peak. Actually, in the thermodynamic limit the cutoff will be small enough to affect the very top of the first maximum of the return rate. However, for the system size shown in Fig. 2.10(c) this is not yet the case. Furthermore, the order-parameter average is zero at infinite time indicating the equivalence of DPT-I and DPT-II. Note that the quench of Fig. 2.9 already at zero temperature gives rise to the regular phase,[48] and, as such, all temperatures $T < 1/4$ result in a regular phase.

As has been established in previous analytical [45] and numerical [70, 87, 88, 48] studies at $T = 0$, the late-time periodicity of the return rate coincides with that of the magnetization, whether the underlying phase is ordered ($\equiv$ anomalous) or disordered ($\equiv$ regular), as can be seen in the magnetization panels in Figs. 2.7, 2.8, and 2.9. Naively, the smallest overlap between final and initial states is obtained whenever the classical magnetization vector is furthest from its original orientation. This happens for times $t = \omega_{\mathrm{mag}}^{-1} n\pi/2$, where n is an odd positive integer and ω_{mag} is the frequency of the precession of the magnetization. However, at short times, we observe significant deviations from this simple picture, the origin of which will be elucidated in Sec. 2.3.

We summarize the discussion of quenches of the IR-TFIM starting from the ferromagnetic phase, by observing that beyond the representative examples shown here, our extensive numerical simulations indicate that the DPT-I and DPT-II dynamical critical lines, to high precision, fully coincide in the $T-\Gamma_{\mathrm{f}}$ phase diagram for $\Gamma_{\mathrm{i}} < \Gamma_{\mathrm{c}}^{\mathrm{e}}(T)$. Moreover, this dynamical critical line can be directly connected to

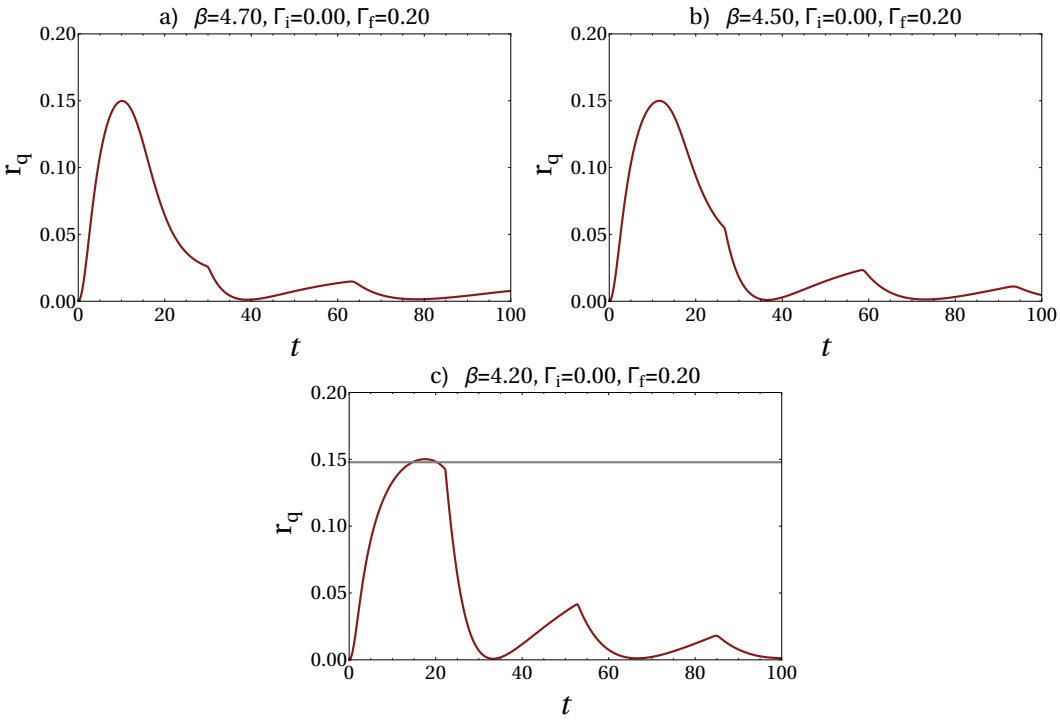

Figure 2.10: Disappearance of the first cusp underneath the thermal cutoff with increasing temperature. The temperature grows form $\beta = 4.7$ in (a) through $\beta = 4.5$ in panel (b) to $\beta = 4.2$ in (c). While these quenches reach deeper and deeper into the regular phase the simultaneously decreasing value of the thermal cutoff will eventually crop the first cusp. The constant indicated by the gray line in (c) represents $r_{\mathrm{q}}^{\max}$ as given by (2.51), thus the signal will be cut off in the thermodynamic limit. The system size is $N = 2001$.

the equilibrium critical line. In fact, it exactly reproduces the equilibrium critical line if, at a temperature $T < T_c^e|_{\Gamma\to 0}$, the ferromagnetic thermal state is prepared at $\Gamma_i = \Gamma_c^e(T) - \delta$, with $\delta \to 0^+$.

Quenches from the paramagnetic phase

As we shall see in the following, the DPT-I and DPT-II dynamical critical lines also coincide when starting with paramagnetic thermal initial states, albeit their shape will be qualitatively different from the case of ferromagnetic initial conditions.

For the system to be able to detect the possible preference for ferromagnetic order in the final state following a purely unitary time evolution, we have to introduce a finite seed in the form of a magnetic field along the z-direction with strength $\Lambda > 0$. This is not a finite-size effect and even the thermodynamic system will not exhibit spontaneous symmetry breaking. Instead the inability of the system to dissipate energy forces the final magnetization in the ferromagnetic phase to depend on the initial magnetization. Given an initial state with $\langle S_z\rangle = \langle S_y\rangle = 0$, the thermodynamic system will not show any dynamics at all, independent of the final value Γ_f. Therefore, for all the plots presented in Figs. 2.11, 2.12, and 2.13, we set $\Lambda_i = \Gamma_i/20$. The motion of the magnetization will be determined by the angles $\bar{\theta}_i$ and $\bar{\theta}_f$ that minimize the pre- and post-quench classical Hamilton function. This angular dependence leads to the following consequence: Every finite difference $\bar{\theta}_i - \bar{\theta}_f$ gives rise to a non-stationary magnetization, e.g. we can set $\Lambda_f = 0$, which for quenches where the final state is still paramagnetic results in the long-time average $\langle S_z\rangle = 0$ in contrast to $\langle S_z\rangle \neq 0$ for quenches to a ferromagnetic state. On the other hand, whenever the classical spin expectation value changes in time, we find a return function that does not scale to zero in the thermodynamic limit. Within the paramagnetic phase such a classical motion of the total magnetization vector, which is purely caused by the need of a small explicit symmetry breaking in the initial state, can be avoided by choosing the final external field Λ_f such that the angles $\bar{\theta}_{i,f}$, coincide. The absence of classical motion yields an entirely smooth return rate that scales to zero in the thermodynamic limit. Quenches that remain in the paramagnetic phase in the DPT-I sense can therefore be classified as *trivial* in the DPT-II sense. In general, the resulting trigonometric equation for Λ_f has to be solved numerically, as is done for Figs. 2.11, 2.12, and 2.13. For small values of $\Lambda_{i,f}/\Gamma_{i,f}$, however, this reduces to the simple expression

$$\Lambda_f = \Lambda_i \frac{\bar{s} - 2\Gamma_f}{\bar{s} - 2\Gamma_i} \,. \tag{2.53}$$

The important difference for a quench to the ferromagnetic phase is that (2.53) has no solution. Even setting $\Lambda_f = 0$ results in a final magnetization along the z-direction that is larger than that of the initial state. The unavoidable classical motion of the magnetization vector results in a finite return rate with regular cusps as $N \to \infty$, which indicates the same dynamical phase transition as characterized

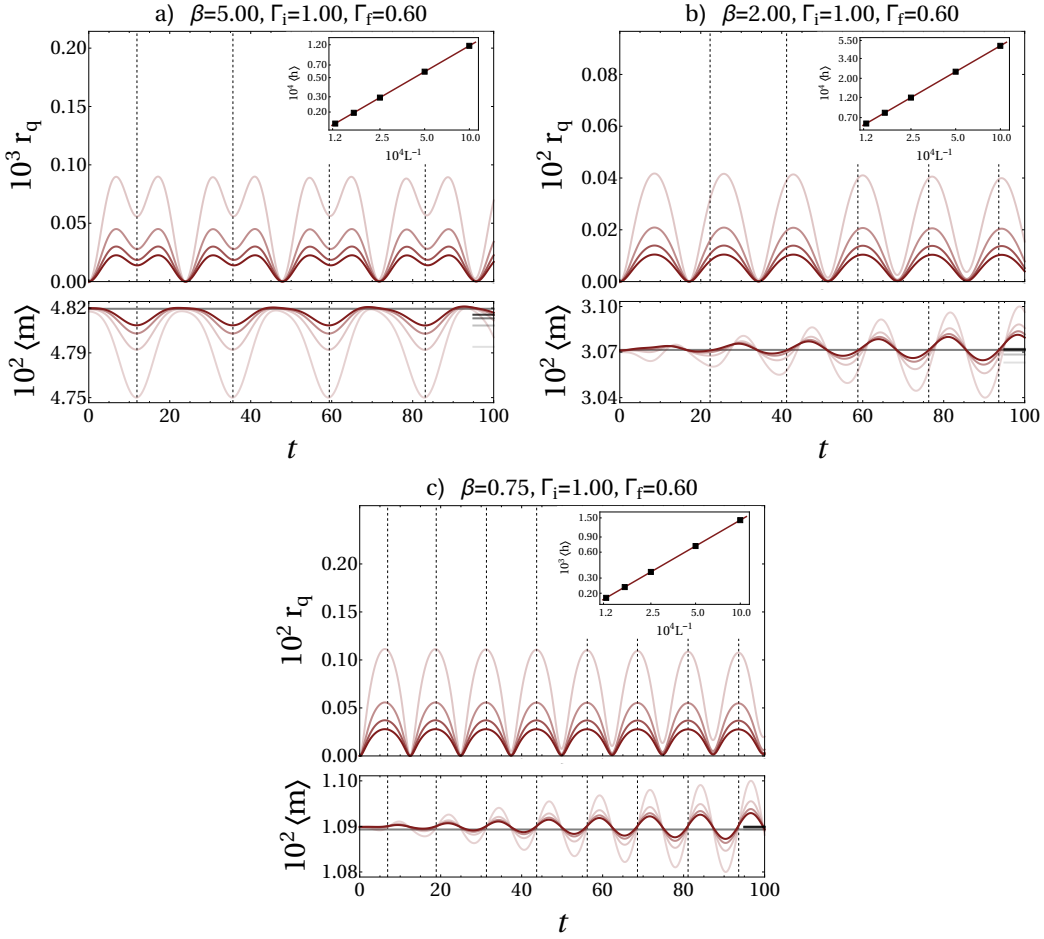

Figure 2.11: Quantum quench in the IR-TFIM from $\Gamma_\mathrm{i} = 1$ to $\Gamma_\mathrm{f} = 0.6$ at inverse temperatures $\beta = 5$, 2, and 0.1 for $N = 2001, 4001, 6001, 8001$. This quench is within the paramagnetic phase at any temperature, and thus the return rate exhibits the trivial phase which scales to zero in the thermodynamic limit. The insets show the average amplitude of $r_\mathrm{q}(t)$ over the first period as a function of system size, showing clear algebraic decay. The infinite-time magnetization of an infinite system is constant at the seeding value, indicating a disordered infinite-time steady state (see Sec. 2.2.4). The convergence of the infinite-time magnetization with increasing system size towards this value is indicated with increasingly opaque gray lines at the right edge of the magnetization plot.

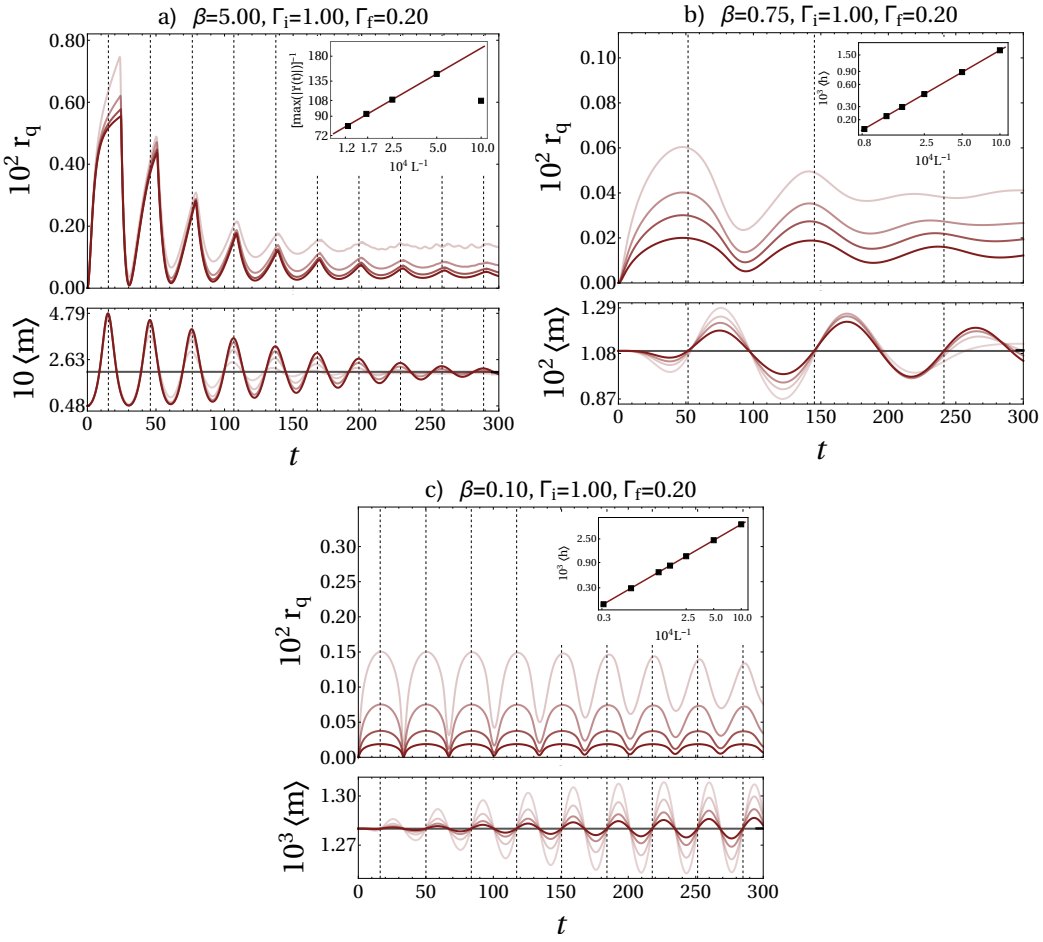

Figure 2.12: Same as Fig. 2.11 but for $\Gamma_f = 0.2$. At the temperature $T = 0.2$, a regular phase emerges in (a) coinciding with an ordered infinite-time steady state. The inset in (a) shows the finite-size scaling of the curvature of the first cusp, indicating its algebraic divergence with system size, and, therefore, the true non-analyticity of the cusp in the thermodynamic limit. The depicted system sizes are: (a) $N = 2001, 4001, 6001, 8001$, (b) $N = 4001, 6001, 8001, 12001$, (c) $N = 4001, 8001, 16001, 32001$.

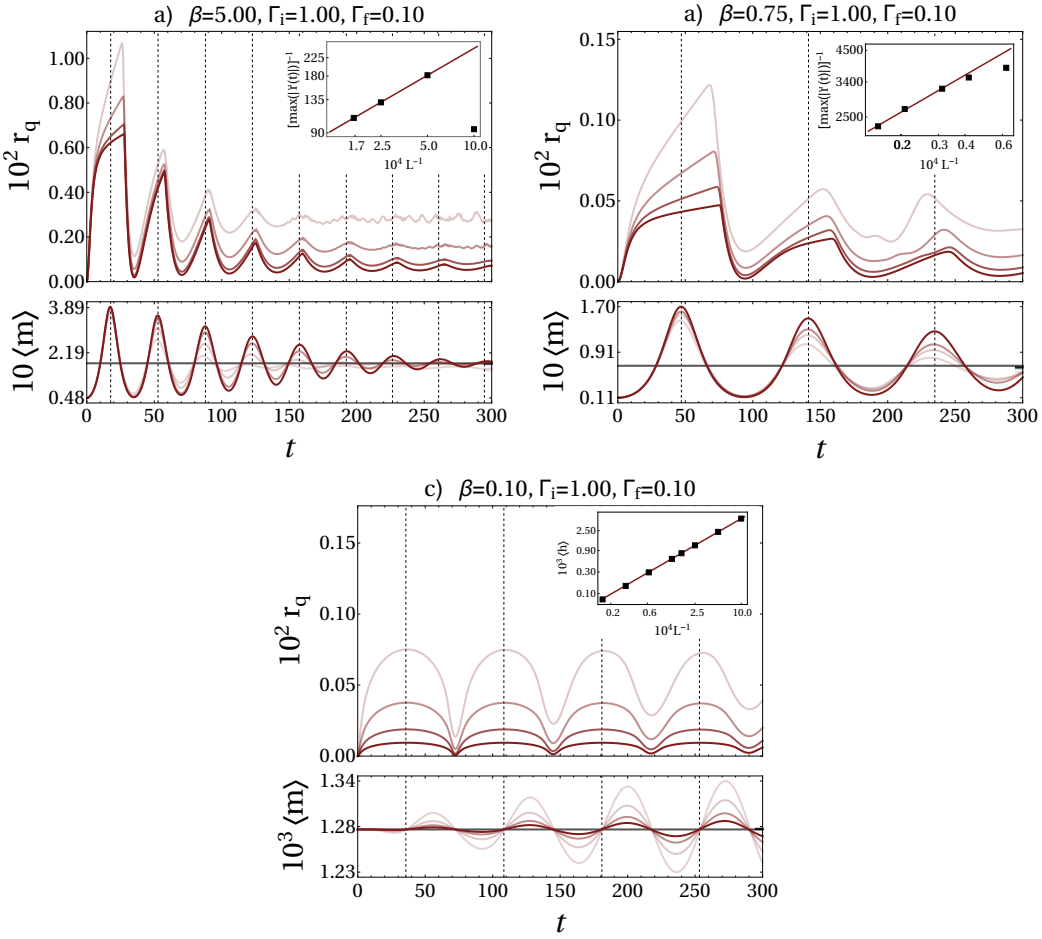

Figure 2.13: Same as Fig. 2.11 but with $\Gamma_f = 0.1$. Even though in equilibrium $T = 4/3$ corresponds to a paramagnetic state at any value of the transverse field, for this quench it is already low enough to give rise to a regular phase in the return rate, which coincides with an ordered infinite-time steady state. The insets in panels (a) and (b) show the finite-size scaling of the curvature of the first cusp, which diverges algebraically with system size, while the inset in (c) depicts how the average height of the first peak decays to zero algebraically as the system size is increased. The plots show system sizes of $N = 1001, 2001, 4001, 6001$ in (a), as well as $N = 8001, 16001, 32001, 64001$ in (b,c).

by the DPT-I. Apart from the relaxation due to dephasing, the time evolution and mean value of the magnetization are again well-described by the classical equations of motion.

In Fig. 2.11, we show ED results for a paramagnetic thermal initial state at $\Gamma_\mathrm{i} = 1$ that is subsequently subjected to a quench in the transverse-field strength to the value $\Gamma_\mathrm{f} = 0.6$ at temperatures $T = 0.2$, $T = 4/3$ and $T = 10$. Each of the return rates shows a trivial phase [45, 87] and scales to zero in the thermodynamic limit. Since we break the $\mathbb{Z}_2$ symmetry explicitly by a small external magnetic field along the z direction in both the initial and final Hamiltonian, with the value of Λ_f chosen appropriately, the initial and final magnetization after the decay of the induced oscillations are the same. This value of the magnetization in the thermodynamic limit can be easily found from the classical model introduced in Sec. 2.2.2.

Fig. 2.12 shows the same analysis for the quench from $\Gamma_\mathrm{i} = 1 \to \Gamma_\mathrm{f} = 0.2$. At a sufficiently low temperature $T = 0.2$, we see in Fig. 2.12(a) that the dynamics gives rise to a ferromagnetic steady state with infinite-time average of the magnetization greater than the seeding value. This ordered infinite-time steady state coincides with a regular phase in the return rate characterized by a cusp in each period of $r_\mathrm{q}(t)$. Corresponding insets show how the curvature of $r_\mathrm{q}(t)$ at the first cusp diverges algebraically with system size, indicating clear non-analytic behavior in the thermodynamic limit. Upon further increasing the temperature to $T = 4/3$ or even $T = 10$, the dynamics no longer leads to an ordered steady state and the regular phase is replaced by the trivial phase, where the return rate goes to zero in the thermodynamic limit, as shown in Fig. 2.12(b,c).

Fig. 2.13 repeats this analysis but at an even larger quench from $\Gamma_\mathrm{i} = 1 \to \Gamma_\mathrm{f} = 0.1$. While the magnetization and return rate for panels (a) and (c) are qualitatively similar to the corresponding temperatures in Fig. 2.12, the regular phase now also replaces the trivial quench at $T = 4/3$. The finite-size scaling in Fig. 2.13(b), on which we base this claim, requires much larger systems than the other quenches. This is because at high temperatures and close to the critical field strength the dynamics governing the system is slow and fluctuations that introduce dephasing are enhanced. The combination of both lead to unusually strong finite-size effects. Consequently, both the magnetization and return rate converge much more slowly towards the thermodynamic limit. At first sight, a regular phase for this quench is surprising, since in equilibrium there is no ferromagnetic phase at these high temperatures. However, the conserved spin length S for these quenches starting from deep within the paramagnetic phase is longer than the equilibrium value at Γ_f, which in turn increases the system's susceptibility to ferromagnetic order. Indeed, we find, that no matter how high the temperature of the thermal initial state is, there is always a small enough Γ_f, a quench to which would give rise to a ferromagnetic infinite-time steady state that coincides with a regular phase. For a system that is weakly connected by local couplings to its environment this has the interesting consequence that there exists a timescale in the relaxation from a

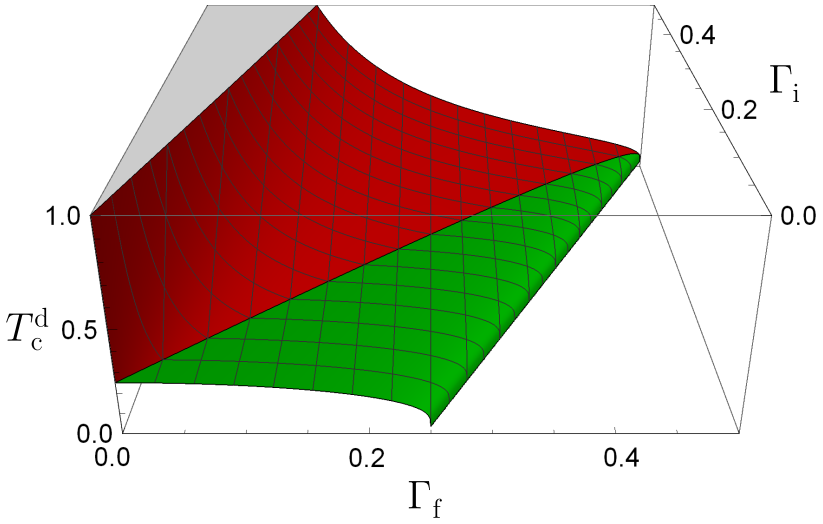

Figure 2.14: Finite-temperature dynamical phase diagram of the fully connected transverse-field Ising model for ferromagnetic (green) and paramagnetic (red) initial states. The analytical results from (2.28) and (2.29) coincide with numerical results for the return rate, for which no error bars are shown, since they are in most cases too small to be resolved in the plot.

paramagnetic thermal initial state to a paramagnetic long-time steady state during which the system can spontaneously break the $\mathbb{Z}_2$ symmetry and thus evolve through a ferromagnetic quasi-stationary state. Here, energy dissipation due to the local contact to the environment allows for relaxation of the length of the magnetization vector. Consequently, this enables the system to evolve from a ferromagnetic state, which would be the infinite-time steady state in the case of a closed system, to a paramagnetic equilibrium final state.

Also in the case of quenches from a paramagnetic thermal state, the return rate and the magnetization profile exhibit the same periodic relation as has been shown in the literature. For quenches that end up in the paramagnetic phase, the largest deviation between $\langle m(t)\rangle$ and $\langle m(0)\rangle$ coincides with times when $\langle S_z(t)\rangle$ takes its initial value; however, the deviation in the azimuthal angle becomes maximal.

Within our numerical precision, we find from our ED simulations that for quenches beginning from a paramagnetic thermal state an ordered (a disordered) infinite-time steady state always coincides with a regular (trivial) phase in the return rate (2.48), and thus again, as for quenches from the ordered phase, the DPT-I and DPT-II share the same critical line. Unlike for quenches from a ferromagnetic thermal initial state, the dynamical critical line here cannot be directly connected to its equilibrium counterpart. Finally, we summarize our findings with regards to the dynamical critical line for all initial conditions in Fig. 2.14.

Quenches in the infinite range XX model

So far, we have focused exclusively on the infinite-range transverse field Ising model, which below the critical temperature $T_c^{\mathrm{e}}(\Gamma)$ set by (2.12) breaks a $\mathbf{Z}_2$-symmetry. This is in line with the predominant discussion of Loschmidt echos, which apart from few examples [114, 115, 71, 116] is limited to discrete symmetries. While for low-dimensional systems with short-range interactions continuously broken symmetries at finite temperatures are prohibited by the Mermin-Wagner theorem [117], this is not the case for the presently discussed setup with infinite-range interactions. By the same argument as in Sec. 2.2.1, one finds, that the infinite range XX model

$$H_{XX}(\Gamma) = -\frac{J}{2N}\sum_{i\neq j=1}^{N}\left(s_i^x s_j^x + s_i^y s_y^y\right) - \Gamma\sum_{j=1}^{N} s_j^z;, \tag{2.54}$$

shares the same finite temperature phase transition, as the transverse field Ising model. However, below the critical temperature the system breaks a continuous $O(2)$-symmetry. As opposed to the equilibrium properties, dynamically the XX-model behaves completely different from the IR-TFIM as any quench results in a disordered state. Furthermore, a quench of the transverse field Γ conserves the corresponding magnetization $\langle S_z\rangle$. To illustrate this behavior, we show a set of quenches at different temperatures, initialized in the symmetry broken phase in Fig. 2.15. To enforce this symmetry breaking explicitly we again use the mean-field Hamiltonian (2.14), however with s_i^z and s_i^x exchanged. Note, that the Loschmidt echo for each of these quenches is regular in agreement with the vanishing long-time average of the magnetization. In fact, the return rate looks almost identical for all displayed temperatures, a property, that can be understood with the semiclassical ansatz developed in the next section. We thus find, that even for a continuous symmetry, independent of the temperature, DPT-I and DPT-II coincide, if the latter is defined through either the quantum or fidelity return rate. Finally, we point out, that this concurrence would be absent, if the overlap in the return rate was calculated with the ground-state manifold (or a generalization thereof at finite temperatures), as the return rate would vanish identically. This will become apparent in the geometric interpretation of Sec. 2.3.3.

2.2.5 Finite size scaling for large systems

The numerically exact diagonalization of sufficiently large systems, that allow a proper finite size scaling as presented in Sec. 2.2.4 requires some optimization of the matrix operations involved. This section is devoted to these techniques.

As we have already mentioned above, the Hamiltonian conserves the spin length S and is therefore block diagonal with blocks of size $2S+1$. Furthermore, within these blocks the Hamiltonian expressed in the basis of S_z eigenstates is a tridiagonal matrix (pentadiagonal for the XX model), which can be diagonalized fairly

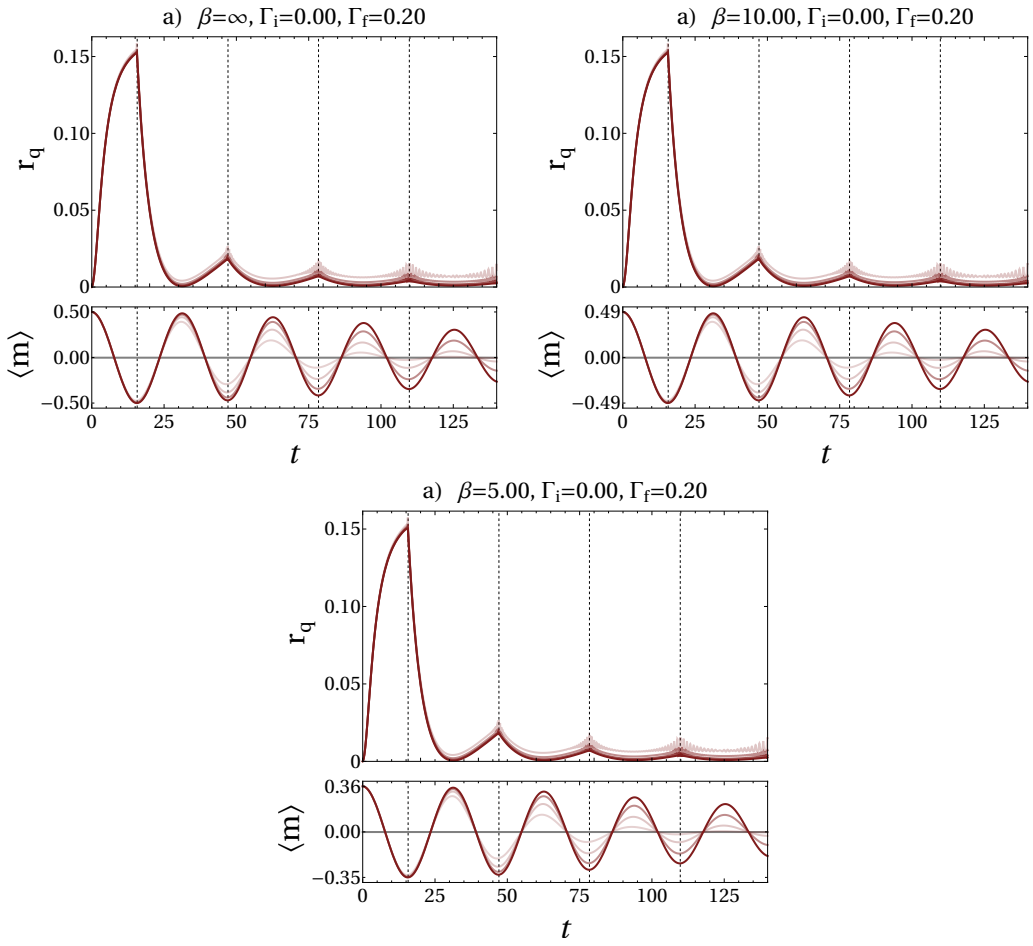

Figure 2.15: Quenches of the infinite range XX model, beginning in the symmetry broken phase with $\Gamma_i = 0$ and ending at $\Gamma_f = 0.2$. All quenches are regular with sharp cusps that require no finite size scaling and in fact are beyond the resolution of the finite time steps at all system sizes. Correspondingly for long times the magnetization relaxes to a paramagnetic state. The plots show system sizes of $N = 501, 1001, 2001, 4001$.

efficiently with a computational complexity of $\mathcal{O}(N^2)$. However, one can do even better and use the $\mathbb{Z}_2$ symmetry of the Hamiltonian to build symmetric and antisymmetric eigenvectors: Assume, as we will throughout the rest of this section, that N is odd and define the reduced Hamiltonian matrices

$$H^{\pm}_{\mathrm{red}} = H|_{S_z>0} \pm \sum_{n,m=1}^{N} \langle n/2|H|-m/2\rangle |m/2\rangle\langle n/2|, \tag{2.55}$$

where n and m are odd and the states $|n\rangle$ satisfy the eigenvalue equation $S_z|n\rangle = n|n\rangle$. Clearly, as the reduced matrices $H^{\pm}_{\mathrm{red}}$ have only size $(N+1)/2$ and the same number of bands as H, they can be diagonalized a lot faster. The normalized symmetric (+) and antisymmetric (-) eigenvectors $|v_{\pm}\rangle$ of the full system are then found according to the condition

$$\langle -n|v_{\pm}\rangle = \pm\langle n|v_{\pm}\rangle = \frac{1}{\sqrt{2}}\langle n|v^{\pm}_{\mathrm{red}}\rangle. \tag{2.56}$$

While this procedure is helpful, much larger gains in efficiency can be made by noting that $D(S)\mathrm{e}^{-\beta E_n}$ for large systems is a sharply peaked function. Additionally the return rate in the thermodynamic limit is bounded from above by some value $r_{\max}$, that can for example be estimated from the results of small systems. Consequently, no eigenstate with an initial weight

$$\frac{D(S)\mathrm{e}^{-\beta E_n}}{\max_{S,n} D(S)\mathrm{e}^{-\beta E_n}} < \mathrm{e}^{-N r_{\max}/2} \tag{2.57}$$

will be resolved. Using the classical approximation of the mean-field energy one can significantly reduce the number of eigenvectors per S-subspace to be found and, especially at high temperatures, the number of these subspaces that have to be diagonalized. If the number of eigenvectors per S-subspace that have to be found is smaller than $S/5$ a Krylov subspace method is used for the diagonalization of the initial Hamiltonian.

As the allowed error $\simeq \mathrm{e}^{-N r_{\max}/2}$ decreases exponentially in system size N, a calculation with machine precision fails for most results presented above, where in some cases a precision of 10^{-320} had to be used. This is problematic, as calculations with precisions exceeding the internal floating point accuracy in high level programming languages are typically far less optimizable. We thus aim to reduce the number of operations that have to be performed with high accuracy as much as possible. A direct diagonalization of $H^{\pm}_{\mathrm{red}}$ at the desired precision is clearly not advisable. Instead, we use the readily available machine precision eigenvectors to iteratively determine improved eigenstates: Using the eigenstate $|v_{\mathrm{old}}\rangle$ with eigenenergy ϵ_{old} we solve the matrix equation

$$\left(H^{\pm}_{\mathrm{red}} - \epsilon_{\mathrm{old}}\mathbb{1}\right)|v_{\mathrm{new}}\rangle = |v_{\mathrm{old}}\rangle \tag{2.58}$$

in $\mathcal{O}(N)$ time to find an improved accuracy of $32 \cdot 3^{j-1}$ digits after j iterations beginning with machine precision input. The simultaneously updated eigenenergy

$$E_{\text{new}} = \langle v_{\text{new}} | H^{\pm}_{\text{red}} | v_{\text{new}} \rangle \tag{2.59}$$

is then known to an accuracy of $64 \cdot 3^{j-1}$, as the normalization of $|v_{\text{new}}\rangle$ is unperturbed. Especially for the diagonalization of the final Hamiltonian, this iterative method is advantageous as a priori it is not known, which eigenvectors of H_{f} have sufficient overlap with the initial state that they need to be included in the time evolution. However, as this overlap is a smooth function of the eigenenergy ϵ^{f}_n the machine precision results can be used to extrapolate the necessary interval of eigenenergies of H_{f} to be considered.

Having diagonalized both the initial and final Hamiltonians, the time evolution is still not entirely straight forward. As we aim to resolve cusps at unknown times in the return rate, a large number m of time-steps (of size Δt) have to be evaluated. However, finding $\mathrm{e}^{-i\epsilon^{\text{f}}_n m \Delta t}$ to the prescribed accuracy for each time-step individually is very time consuming. Fortunately the much faster evaluation of the m-th time step from the previously calculated $m-1$-th step according to

$$\mathrm{e}^{-iE^{\text{f}}_n m \Delta t} = \mathrm{e}^{-i\epsilon^{\text{f}}_n \Delta t} \mathrm{e}^{-i\epsilon^{\text{f}}_n (m-1) \Delta t} \tag{2.60}$$

does not suffer from exponentially growing round-off errors, as the norm remains constant.

With all of the ingredients in place, it is then a simple task to determine the trace of the reduced interference matrix A^S_{red}, involving only those initial and final states that contribute to r_{q} or r_{I} below $r_{\max}$. For r_{F} however, one still has to diagonalize $M_{\text{red}} = A^S_{\text{red}} \cdot A^{S\ *}_{\text{red}}$, which at high temperatures scales as $\mathcal{O}(N^3)$ and requires a high precision. As a result it is typically orders of magnitude slower than any of the previous calculations.

2.3 Geometric Interpretation of the Loschmidt echo

Armed with the numerically exact Loschmidt echos for large spin chains with infinite range interactions, we will now derive an approximation valid for systems well described by mean-field theory that correctly captures the return rate dynamics and reproduces the phase diagram Fig. 2.6. Beyond the obvious advantage of providing a simple and physically intuitive, geometric interpretation, it also opens a potential avenue towards an understanding of Loschmidt echos in non-integrable models, i.e. systems with an exponentially large Hilbert space. In the following we will briefly discuss this aspect, thereby also contextualizing the role of fully connected spin chains.

2.3.1 Approaching DQPTs in non-integrable models

As we have already seen above for the fairly restrictive class of infinite range spin chains, the Loschmidt echo has a complicated analytical structure and rich phenomenology, which we fully understand only in the simplest of cases. Comprehending its behavior in generic non-integrable models requires such detailed knowledge of the system, that, if there is to be any hope for a deeper understanding than mere numerical experiments can provide, an approach from either of the well-understood cases has to be attempted. On the one hand one can try to generalize the results for two-band models, the properties of which we will briefly discuss for arbitrary dimensions and geometries in the following subsection. On the other hand weak finite range interactions can be added to the previously discussed spin chains, thereby breaking the conservation of the total spin length S.

Non-interacting two-band models

For two-band models, i.e. systems that map to a 2×2 Bloch Hamiltonian the condition for cusps in the interferometric Loschmidt echo can be formulated as the simple temperature independent condition

$$p_e(\mathbf{k}) = p_g(\mathbf{k}) \ , \tag{2.61}$$

where $p_{e(g)}(\mathbf{k}) = \mathrm{Tr}\{|\Psi_{e(g)(\mathbf{k})}\rangle\langle\Psi_{e(g)}(\mathbf{k})|\rho_\mathrm{i}\}$ is the projection of the density matrix of the initial state ρ_i onto the excited (ground) state of the final Hamiltonian. The fact that we can write a necessary *equation* is specific to this simplest case of systems supporting non-zero Loschmidt echos. In general one is limited to the necessary but not sufficient inequality

$$\max_i p_i < \sum_{j \neq i} p_j \ , \tag{2.62}$$

where i and j run over all available eigenstates of the final Hamiltonian. In this more generic case the complex Loschmidt amplitude follows a chaotic trajectory that allows only statistical statements [83] that are considerably weaker than those for the exactly solvable two-band case.

In the following we will investigate the behavior of any two-band system in d dimensions in the vicinity of the critical time t_c. Introducing the level spacing

$$\epsilon(\mathbf{k}) \equiv \frac{1}{2}\left(\epsilon_e(\mathbf{k}) - \epsilon_g(\mathbf{k})\right) \tag{2.63}$$

between the eigenenergies $\epsilon_{e(g)}$ of the final Hamiltonian and utilizing $p_g(\mathbf{k}) + p_e(\mathbf{k}) \equiv 1$ allows to write the interferometric Loschmidt echo for translation invariant two-

state systems as

$$\begin{aligned} r_{\mathrm{I}}(t) &= \int_{\mathrm{BZ}} \frac{d^d k}{(2\pi)^d} \log \left| p_e(\mathbf{k}) \mathrm{e}^{-i\varepsilon_e(\mathbf{k})t} + p_g(\mathbf{k}) \mathrm{e}^{-i\varepsilon_g(\mathbf{k})t} \right|^2 \\ &= \int_{\mathrm{BZ}} \frac{d^d k}{(2\pi)^d} \log \left(\cos^2\left(\epsilon(\mathbf{k})t\right) + f(\mathbf{k}) \sin^2\left(\epsilon(\mathbf{k})t\right) \right) \end{aligned} \tag{2.64}$$

with

$$f(\mathbf{k}) = \left(1 - 2p_g(\mathbf{k})\right)^2 . \tag{2.65}$$

We clearly see that the integrand, evaluated at critical momenta $\mathbf{k}_c$, which are defined by $f(\mathbf{k}_c) = 0$, diverges at critical times $t_c = \pi(n + 1/2)/\epsilon(\mathbf{k}_c)$ with $n \in \mathbb{N}$. This, however, does not directly imply that the return rate also shows a cusp at these critical times. Instead, if the integrand varies too quickly near k_c the signal might appear smooth and will in fact be differentiable. It is therefore necessary to investigate the properties of the return rate near t_c in some more detail. We first simplify notation by shifting time and momentum according to $\tau = t - t_c$ and $\boldsymbol{\kappa} = \mathbf{k} - \mathbf{k}_c$.

Assuming that the non-negative functions $f(\boldsymbol{\kappa})$ and $\epsilon(\boldsymbol{\kappa})$ are isotropic for small $\boldsymbol{\kappa}$ we expand these around the critical momentum

$$\begin{aligned} f(\boldsymbol{\kappa}) &\sim |\boldsymbol{\kappa}|^\alpha \\ \epsilon(\boldsymbol{\kappa}) &\sim e(\boldsymbol{\kappa}) + |\boldsymbol{\kappa}|^\gamma , \end{aligned} \tag{2.66}$$

with some analytic function $e(\boldsymbol{\kappa})$ that either satisfies $e(0) \neq 0$ or at least $e(\boldsymbol{\kappa}) \sim \kappa^{2m}$ with $\gamma/2 < m \in \mathbb{N}$. Since we are only interested in the nature of the divergence, we can neglect all non-vanishing prefactors and constants. This leaves an integral of the form

$$r_I \sim \int d\kappa \, \kappa^{d-1} \log\left(\tau^2 + \kappa^\beta\right) , \tag{2.67}$$

where $\beta = \alpha - 2\gamma$ for $e(0) = 0$ or $\beta = \alpha$ else[2]. An expansion for small τ now yields

$$r_I \sim \tau^2 + |\tau|^{2d/\beta}, \tag{2.68}$$

which has a leading non-analytic behavior for any $\beta > d$ but a cusp only for $\beta \geq 2d$.

In case of an anisotropic behavior of $\epsilon(k)$ or $f(k)$ around a critical point $\mathbf{k}_c$, we

[2]Note, that for $e(0) \to 0$ the critical times diverge.

can write

$$\begin{aligned} f(\boldsymbol{\kappa}) &\sim \prod_{i=1}^{d} |\kappa_i|^{\alpha_i} \\ \epsilon(\boldsymbol{\kappa}) &\sim e(\boldsymbol{\kappa}) + \prod_{i=1}^{d} |\kappa_i|^{\gamma_i} \ . \end{aligned} \tag{2.69}$$

A similar analysis as the one before yields a leading non-analytic behavior if $\sum 1/\beta_i < 1$ and a cusp for $\sum 1/\beta_i \leq 1/2$, where $\beta_i = \alpha_i - 2\gamma_i$ for $e(0) = 0$ and $\beta_i = \alpha_i$ else.

As a simple example, we consider a tight binding model with a two atomic basis in any dimension reduces to a 2×2 Bloch Hamiltonian. We can thus write

$$H = \mathbf{d}(\mathbf{k}) \cdot \boldsymbol{\sigma} \ , \tag{2.70}$$

where $\boldsymbol{\sigma}$ is the vector of Pauli matrices and $\mathbf{d}(\mathbf{k})$ is an arbitrary three dimensional vector of real functions. For $d = 1$ and $\mathbf{d}(k) = (t_1 + t_2 \cos k, t_2 \sin k, 0)^T$ this is the tight binding formulation of the well-known Su-Schrieffer-Heeger (SSH) model [118] with intrabasis hopping amplitude $t_1 = 1$ and interbasis hopping t_2 as well as lattice constant $a = 1$. As we have explained in Sec. 2.1 for any two 2×2 matrices $H_\mathrm{i} = \mathbf{d}_\mathrm{i}(\mathbf{k}) \cdot \boldsymbol{\sigma}$ and $H_\mathrm{f} = \mathbf{d}_\mathrm{f}(\mathbf{k}) \cdot \boldsymbol{\sigma}$ the criticality condition $f(\mathbf{k}) = 0$ is satisfied iff $\mathbf{d}_\mathrm{i} \cdot \mathbf{d}_\mathrm{f} = 0$. In case of the SSH model this is equivalent with $k_c = \arccos\left(-\frac{1+t_2^\mathrm{i} t_2^\mathrm{f}}{t_2^\mathrm{f}+t_2^\mathrm{i}}\right)$, which is real only if $|t_2^\mathrm{i}| < 1 \leq |t_2^\mathrm{f}|$ or $|t_2^\mathrm{f}| < 1 \leq |t_2^\mathrm{i}|$. Furthermore, $f(\kappa) \sim \kappa^2$, such that cusps in the interferometric return rate are present only for quenches across the equilibrium topological transition. In a similar manner any two-band system in any dimension can be discussed.

The generalization of the return rate to finite temperatures is once again not unique. If, instead of the temperature-independent interferometric return rate, the fidelity return rate is used, any finite temperature yields a smooth signal [100].

As we have seen, the Loschmidt echo of two-band models can be classified by the dimensions of the time-dependent nodal surface, that in topological insulators and superconductors is symmetry protected. It is therefore an interesting open question, whether in these systems a classification of dynamical phase transitions in close analogy to nodal surfaces in Weyl semimetals [119, 120] can be achieved.

All of this simplicity of two-band models comes at a price, however, as these non-interacting systems are quite special. In particular the factorizability into a continuum of independent two-dimensional systems is broken by any interaction. As these effects would have to be described with exponential precision no perturbative expansion in weak interactions around a non-interacting two-band system will help to understand the Loschmidt echo of non-integrable models.

Semiclassical systems

Semiclassical systems in the thermodynamic limit constitute exactly the opposite limit of only a few (possibly coupled) degrees of freedom, each with a continuum of available states. This dense spectrum of quantum states is essential to the applicability of a semiclassical approximation. However, the number of coupled degrees of freedom is not. As such the generalization of these systems to fully non-integrable models with many (strongly) coupled degrees of freedom, each with many accessible quantum states – while potentially demanding from a computational perspective – is at least conceptually straight forward.

With this motivation we will now develop an intuitive picture of the return rate in fully connected spin chains, which in the thermodynamic limit constitute a long – and thus almost classical – rotor with self-interactions. In terms of the classification of semiclassical models this constitutes the simplest case of just one quasiparticle. The method we present, however, is more general, as it solely relies on the initial WKB wave function and classical time evolution. In fact, a closely related analysis has already successfully explained the collapse and revival of the time-of-flight interference patterns following a quench to the deep lattice limit of the Bose-Hubbard model [67]. We will discuss the possibility of generalizations to more degrees of freedom in Sec. 2.3.5.

2.3.2 Construction of the initial wave function

To ensure comparability, we perform the same quench protocol as in Sec. 2.2.1, that is an instantaneous quench of the transverse field. In this case, the DPT-I phase diagram based on the order parameter $m_z = \langle S_z \rangle / N$ is completely determined by mean-field theory [54], which is equivalent to the leading order of a $1/N$-expansion (see Sec. 2.2.2). It is based on the Bloch sphere representation of the spin in terms of the continuous classical vector $\mathbf{S} = S(\sin\theta\cos\phi, \sin\theta\sin\phi, \cos\theta)$ that contributes the highest weight to the free energy arising from the pre-quench Hamilton function

$$H_{\mathrm{i}}(\theta, \phi) = -\frac{S^2}{2N}\cos^2\theta - \Gamma_{\mathrm{i}} S \sin\theta\cos\phi \,. \tag{2.71}$$

The short-time evolution is then governed by the classical equations of motion (EOM) derived from the post-quench Hamiltonian $H_{\mathrm{f}}(\theta, \phi)$; see (2.85) below. As the Loschmidt echo typically shows its characteristic signatures also at short times, it is natural to use mean-field theory as the starting point for the semiclassical treatment of the Loschmidt echo and the DPT-II phase diagram, the construction of which we will now discuss in detail. For simplicity, we restrict ourselves to $\Gamma_{\mathrm{i}} = 0$ in the rest of this chapter, which – due to the increased symmetry – significantly simplifies the construction of the initial wave function. For the moment we focus on the zero-temperature case and deal with thermal states later.

Similar to the procedure applied in Sec. 2.2.2 at $T = 0$, one first finds the vector

$\mathbf{S}_{\mathrm{cl}}$ minimizing $H_{\mathrm{i}}(\theta,\phi)$, which we choose, due to the spontaneously broken $\mathbb{Z}_2$ symmetry, to be fully polarized along the positive z-axis. In other words, $\mathbf{S}_{\mathrm{cl}}$ has angular variables $\theta_{\mathrm{cl}}=0$, ϕ_{cl} arbitrary, and the maximal possible length $S_{\mathrm{cl}}=N/2$. For convenience we will again use the relative spin length $s=2S/N\in[0,1]$, so here $s_{\mathrm{cl}}=1$.

Clearly a purely classical theory will not allow to calculate overlaps between different states, which inherently arises from quantum mechanics. We thus have to quantize the theory by assigning to $\mathbf{S}_{\mathrm{cl}}$ the WKB wave function [121, 122] adapted to large spins [123, 124, 125] for the initial Hamiltonian

$$H_{\mathrm{i}}=-\frac{1}{2N}S_z^2\,. \tag{2.72}$$

At first glance, it may seem as a complete technical overkill to create a semiclassical approximation to the eigenstates of the exactly solvable H_{i}. However, the spin WKB wave functions $\Psi(q)$ can both be easily mapped onto the Bloch sphere, and, when expressed in terms of the $2S{+}1$ eigenstates of S_x with $q\in\{-S,-S{+}1,\ldots,S\}$, they reproduce the correct leading fluctuations expressed by the expectation values of the quadratic spin operators $\langle S^2_{\{x,y,z\}}\rangle$. This is to be contrasted with the obvious, direct representation in the eigenbasis of S_z, which as it diagonalizes H_{i} results in a vanishing width of the WKB wave functions and is thus unable to yield finite fluctuations. While a classical wave function cannot reproduce the quantum mechanical result $\langle S_x^2+S_y^2+S_z^2\rangle=S(S+1)$, it is nevertheless important to capture the correct variance in the directions orthogonal to the initial polarization, as these determine the overlap between states. The initial fluctuations in the S_z direction on the other hand are subleading to the polarization in that direction, which is correctly described already on the fully classical level. As a result the unavoidable error of a classical wave function has to be fully projected onto the initial magnetization vector. We thus choose the quantization axis along the x-direction, transforming the Hamiltonian to $H_{\mathrm{i}}=-\frac{1}{8N}(S_+ + S_-)^2$, where $S_{+(-)}$ denotes the spin raising (lowering) operator. The stationary Schrödinger equation for $\Psi(q)$ with eigenenergy E then becomes the finite-difference equation

$$-\frac{a^2(q)}{8N}\left[\Psi(q+2)+2\Psi(q)+\Psi(q-2)\right]=E\Psi(q)\,, \tag{2.73}$$

with boundary condition $\Psi(|q|>S)=0$. Here, we have omitted corrections of order $1/S$ from the exact prefactors of the raising and lowering operators and instead approximated them by $a(q)=\sqrt{S(S+1)-q^2}$. For the wave function, we use the WKB ansatz

$$\Psi(q)=\mathcal{N}\,\mathrm{e}^{\mathrm{i}\mathcal{A}(q)}\,, \tag{2.74}$$

where $\mathcal{N}$ denotes the normalization. Inserting this ansatz into the Schrödinger

equation (2.73) and making use of the fact that in the semiclassical limit $S \to \infty$ the argument of $\Psi(q)$ can be treated as a continuous variable, one obtains to lowest order in $1/S$

$$\mathcal{A}'(q) = \frac{1}{2} \arccos\left(-\frac{4NE}{a^2(q)} - 1\right) , \tag{2.75}$$

where the prime indicates the derivative with respect to q. Similar results have previously been derived by van Hemmen and Sütő for several, related spin models [123, 125]. With Eq. (2.75) the boundary between the classically allowed and forbidden spin orientations is given by $B = \sqrt{2NE + S(S+1)}$, which behaves as $B \simeq \sqrt{S}$ for small energies. This is inaccurate and will significantly overestimate the spin fluctuations and we are thus forced to include further corrections. As we are interested in overlaps between spin wave functions, we can focus on the imaginary part of $\mathcal{A}'(q)$, which vanishes at B with divergent slope. Therefore, the next corrections to be included are higher order derivatives of $\mathcal{A}$, whereas corrections to the approximation made in (2.73) can be neglected. While $|\mathcal{A}''|$ is typically suppressed by $1/S$ compared to $|\mathcal{A}'|$, this is obviously not the case near the boundary to the classically allowed region, which in turn implies, that

$$\frac{4NE}{a^2(q)} + 1 = -\cos(2\mathcal{A}')\mathrm{e}^{2\mathrm{i}\mathcal{A}''} \tag{2.76}$$

has to be solved self-consistently together with the condition that $\mathcal{A}''$ is a good approximation to the derivative of $\mathcal{A}'$. Expecting the result to be mainly reflected in a shift to B, we parametrize the solution as

$$\mathcal{A}'(q) = \frac{1}{2} \arccos\left(-\frac{4NE}{a^2(q)} - 1 + \mathcal{B}(q)\right) . \tag{2.77}$$

The correction term has to satisfy the condition

$$\mathcal{B}(q) = (\mathrm{e}^{2\mathrm{i}\mathcal{A}''} - 1)\cos\left(2\mathcal{A}'(q)\right) , \tag{2.78}$$

which follows from the inclusion of the second derivative of $\mathcal{A}(q)$ in the continuum limit of the difference equation (2.73) when acting on the ansatz (2.74) with modified exponent (2.77). In the region, where $|\mathcal{A}'(q)| \gg |\mathcal{A}''(q)|$, already the initial guess (2.75) was a good approximation to the exact wave function. One thus has to expand $\mathcal{B}$ around its minimum obtained for spin projections $q \sim S$ deep within the classically forbidden region on the northern hemisphere (our choice for the broken $\mathbb{Z}_2$ symmetry), where successively higher derivatives are suppressed by increasing powers of $1/S$. For energies close to the ground state energy $E_0 = -S^2/(2N)$ one

obtains

$$\mathcal{B}(q) \simeq \frac{2S}{a^2(q)}\,, \tag{2.79}$$

showing that $\mathcal{B}(q)$ is indeed a $1/S$ correction to the leading terms. With this addition,

$$\mathcal{A}'(q) = \frac{1}{2}\arccos\left(-\frac{4NE-2S}{a^2(q)}-1\right) \tag{2.80}$$

is now consistent with the Schrödinger equation expanded up to the second derivative at all possible values of q.

We can check, that at this level our approximation is sufficiently precise, as the boundary between classically allowed and forbidden spin orientations now takes the far more accurate value

$$B = \sqrt{2NE+S^2}\,, \tag{2.81}$$

which vanishes for the ground state as all higher-energy spin projections can only be reached via quantum tunneling through the classically forbidden region. To obtain the final expression for $\Psi(q)$ that will be used for the determination of the Loschmidt return rate, one has to integrate (2.74) with fixed lower boundary B. Expanding $\mathcal{A}'(q)$ around $q \simeq B$ and using the asymptotics $\arccos(z) \simeq \mathrm{i}\sqrt{2}\sqrt{z-1}$ in the vicinity of $z \simeq 1$, results in

$$\begin{aligned}&\Psi(\mathcal{E},q) = \\ &\mathcal{N}\exp\left[\frac{\sqrt{2B(S-\mathcal{E})+\mathcal{D}(q-B)}\sqrt{q-B}}{2}\left(\frac{q-B}{\mathcal{E}-S}-\frac{B}{\mathcal{D}}\right)\right. \\ &\qquad\left.-\frac{B^2(\mathcal{E}-S)}{\mathcal{D}^{3/2}}\ln\frac{\sqrt{\mathcal{D}(q-B)}+\sqrt{2B(S-\mathcal{E})+\mathcal{D}(q-B)}}{\sqrt{2B(S-\mathcal{E})}}\right].\end{aligned} \tag{2.82}$$

Here, we have introduced the abbreviations $\mathcal{E} = 2NE$ and $\mathcal{D} = 3\mathcal{E} + S + 4S^2 \gg S$, and the normalization $\mathcal{N}$ is actually irrelevant for the determination of the Loschmidt return function. Quite importantly, $\Psi(q)$ shows the proper scaling of the spin expectations values, i.e. for the ground state $\langle S_x^2\rangle = S/2 = \langle S_y^2\rangle$ and $\langle S_z^2\rangle = S^2$ with subleading corrections. For the geometric interpretation it is necessary to place these wave functions on the Bloch sphere, which is simply done by substituting $q = S\sin\theta$, where θ is the polar angle on the Bloch sphere. Note that a resolution of the azimuthal angle is not necessary as the rotational symmetry of the Hamiltonian will be recovered in any eigenfunction. Using the definitions for $\mathcal{E}$ and $\mathcal{D}$ and

neglecting subleading corrections, $\Psi(q)$ can be further simplified into the expression

$$\Psi(\theta, E_n) = \mathcal{N} \exp\left[\frac{E_n b^2}{d^{3/2}}\big(\sinh(4y) - 4y\big)\right]. \tag{2.83}$$

Here $d = 24E_n/N + 4s_{\mathrm{cl}}^2$, $b = \sin\theta_n$, and $y = \operatorname{arcsinh}\sqrt{Nd\,(b - \sin\theta)\,/\,(16bE_n)}$ are functions of θ and θ_n, where the latter separates the classically allowed ($\theta < \theta_n$) from the forbidden region as it determines the eigenenergy $E_n = -s_{\mathrm{cl}} S_{\mathrm{cl}} \cos^2(\theta_n)/4$. At $T = 0$, one has $B = 0$ and $\mathcal{E} = -S^2 \ll -S$ yielding

$$\Psi_0(\theta) = \mathcal{N} \mathrm{e}^{-\frac{1}{2} S_{\mathrm{cl}} \sin^2\theta}\ . \tag{2.84}$$

To enforce $\mathbb{Z}_2$ symmetry breaking, we restrict θ in all initial wave functions to the northern hemisphere.

2.3.3 Time evolution and saddle-point approximation

Having set up the semiclassical state at time $t = 0$, we now incorporate the time evolution with H_{f} by first determining the classical trajectories of the angular variables $(\vartheta(\theta, \phi\,|t), \varphi(\theta, \phi\,|t))$, which result from the classical EOM

$$\frac{\mathrm{d}\vartheta}{\mathrm{d}t} = \Gamma_{\mathrm{f}} \sin\varphi, \qquad \frac{\mathrm{d}\varphi}{\mathrm{d}t} = \Gamma_{\mathrm{f}} \cot\vartheta \cos\varphi\ , \tag{2.85}$$

with initial conditions $(\vartheta(\theta, \phi|0), \varphi(\theta, \phi|0)) = (\theta, \phi)$. These derive from the Heisenberg equations for the total spin operators $S_{\{x,y,z\}}$ by neglecting all commutators that are suppressed by at least $1/N$ (see Sec. 2.2.2). In close analogy to the time evolution in a truncated Wigner approximation [126], the initial amplitude $\Psi_0(\theta)$ is then transported along the classical trajectory, which implies that $\Psi_0(\vartheta(\theta, \phi\,|t))$ depends on both initial angles θ and ϕ. Due to the absence of any dephasing within this description the magnetization, however, will never relax. Higher-order corrections can be treated by more faithfully representing the Schrödinger equation on the Bloch sphere, which will then include derivatives acting on the wave function (2.84) [54]. Here we take no effects beyond (2.85) into account, which will turn out to determine the critical times accurately. In this limit the Loschmidt return function at $T = 0$, defined in (2.4), reads

$$\begin{aligned} r(t) &= -\frac{1}{N} \ln\left|\int \mathrm{d}\Omega\ \Psi_0^*\big(\vartheta(\theta, \phi\,|t)\big)\Psi_0\big(\theta\big)\right|^2 \\ &= \frac{1}{2}\left(\sin^2\vartheta(\bar\theta, \bar\phi\,|t) + \sin^2\bar\theta\right) + \mathcal{O}\left(N^{-1}\right)\ , \end{aligned} \tag{2.86}$$

where the integral sums over the surface of the Bloch sphere with measure $\mathrm{d}\Omega = \mathrm{d}\phi\ \mathrm{d}\theta \sin\theta$. The simple expression in the second line results from the limit $N \to \infty$, where, due to the extensive scaling of the exponent of the wave function (2.84), at

every moment in time the integral is determined by the Loschmidt vector $\mathbf{v}_{\max}(t) = (\vartheta(\bar{\theta}, \bar{\phi}\,|t), \varphi(\bar{\theta}, \bar{\phi}\,|t))$ corresponding to the saddle-point trajectory that minimizes the exponent.

Note that, as depicted in Fig. 2.16 for the quench also used in Fig. 2.17 and the top panel of Fig. 2.21, the initial coordinates $(\bar{\theta}, \bar{\phi})$ are themselves time dependent. In Fig. 2.16 we illustrate the initial orientation $(\bar{\theta}, \bar{\phi})$, which is found when one evolves $\mathbf{v}_{\max}(t)$ backwards in time. In agreement with the jump of the Loschmidt vector, we observe a sudden change of $(\bar{\theta}, \bar{\phi})$ at the critical time.

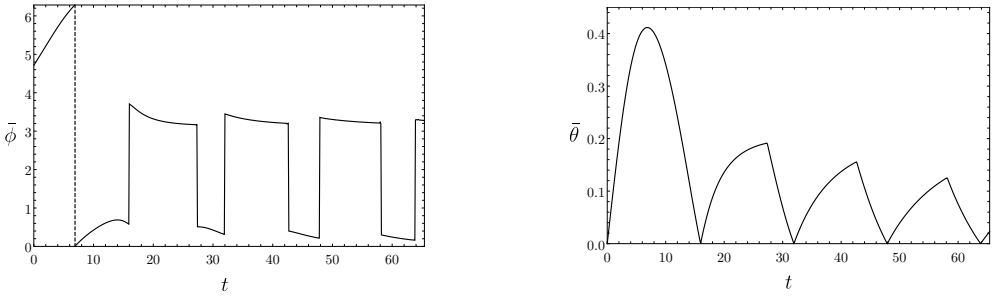

Figure 2.16: Initial angles that at time t coincide with the Loschmidt vector $\mathbf{v}_{\max}(t) = (\vartheta(\bar{\theta}, \bar{\phi}\,|t), \varphi(\bar{\theta}, \bar{\phi}\,|t))$. At the first critical time $t_c = 27.4$ a jump in $\bar{\phi}$ from $3.18 \to 0.51$ occurs at fixed $\bar{\theta}$. In general, non-analyticities in $r(t)$ appear only when $\bar{\phi}$ decreases. Its sudden growths by π in turn, are observed at times when the classical magnetization passes through the north pole, corresponding to zeros in $\bar{\theta}$ and ill-defined $\bar{\phi}$. The dashed line in the left panel is no non-analyticity, but rather a result of the 2π periodicity of the azimuthal angle, due to which $\phi = 0$ and $\phi = 2\pi$ have to be identified.

The result (2.86) allows for a simple geometric interpretation:

The classical trajectory with smallest arithmetic mean of initial and time-evolved WKB distances

$$A_0 = -2\Re \ln(\Psi_0/\mathcal{N})/N = \sin^2\theta/2$$

from the classical initial state determines the Loschmidt echo.

Figures 2.17 and 2.18 illustrate our results for the spin dynamics in case of quenches to $\Gamma_{\rm f} = 0.2$ and $\Gamma_{\rm f} = 0.3$ shortly after the first critical time. The corresponding return rates can be found in the two top panels of Fig. 2.21. Movies of the spin dynamics can be found under the links [127, 128, 129]. The first quench lies within the anomalous phase (see Fig. 2.8), whereas the latter gives rise to a regular signal [87] (see Fig. 2.9a).

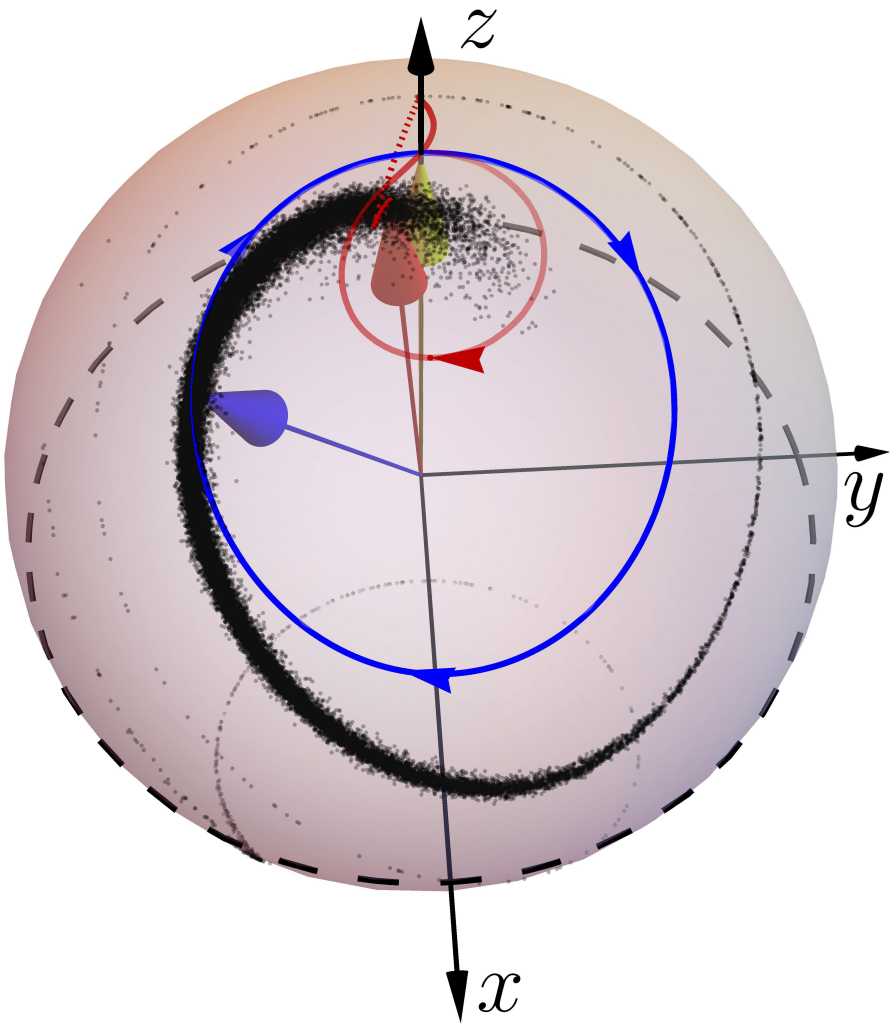

Figure 2.17: Semiclassical representation of the return rate on the Bloch sphere of the zero-temperature anomalous quench $\Gamma_\mathrm{i} = 0 \to \Gamma_\mathrm{f} = 0.2$ shortly after the first critical time. The initial state pointing to the north pole is depicted by a yellow vector. The time-evolved classical initial state (blue vector) $\mathbf{v}_\mathrm{cl}(t) = (\vartheta_\mathrm{cl}(0,\phi\,|t), \varphi_\mathrm{cl}(0,\phi\,|t))$ that governs the dynamics of the magnetization order parameter and thus determines the DPT-I phase, moves along the blue trajectory. The cloud of black dots indicates the distribution of the wave function that initially was centered symmetrically around the north pole. Finally the red arrow, which follows the red line, marks the orientation of the Loschmidt vector $\mathbf{v}_\mathrm{max}(t) = (\vartheta(\bar{\theta},\bar{\phi}\,|t), \varphi(\bar{\theta},\bar{\phi}\,|t))$. At the critical time the sudden jump (dashed red line) of this saddle point orientation from the trailing to the leading edge of the time-evolved quantum amplitude results in a cusp in the return rate.

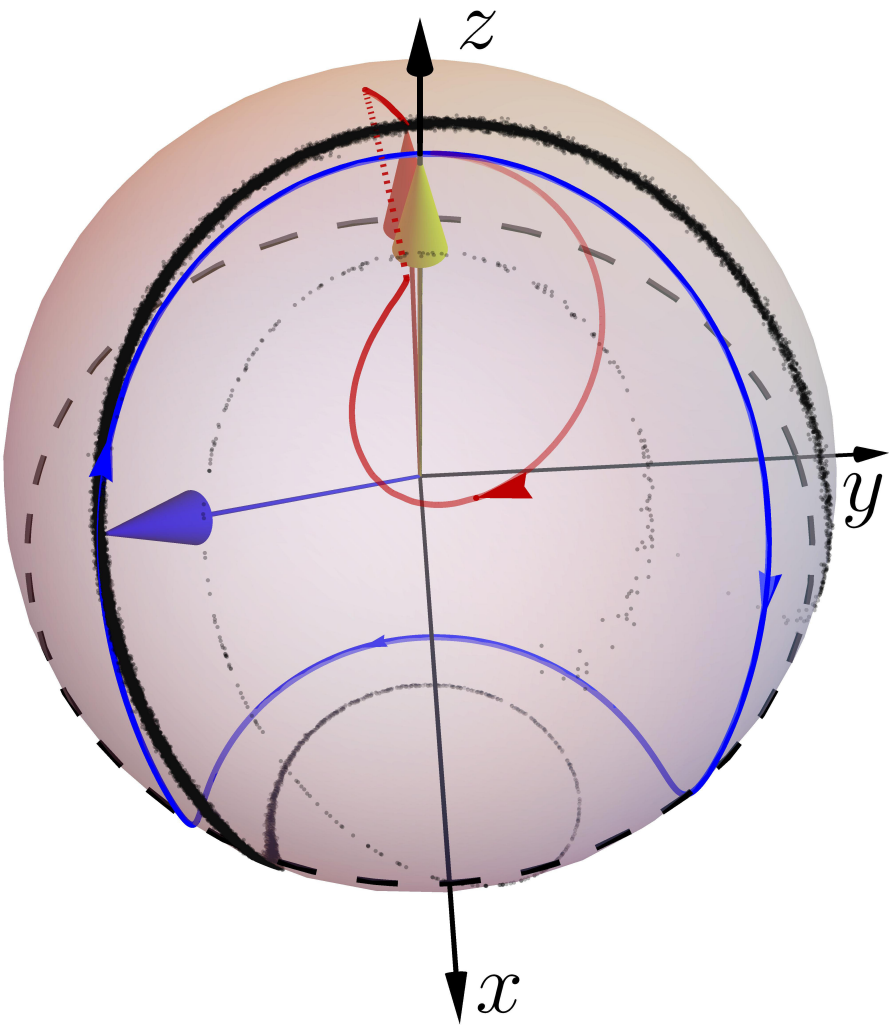

Figure 2.18: Depiction of the semiclassical spin configuration of the regular quench $\Gamma_\mathrm{i} = 0 \to \Gamma_\mathrm{f} = 0.3$ at $T = 0$ shortly after the first cusp. The color coding is the same as in Fig. 2.17.

In the anomalous quench to $\Gamma_\mathrm{f} = 0.2$ [127], the classical state

$$\mathbf{v}_\mathrm{cl}(t) = (\vartheta_\mathrm{cl}(0, \phi\,|t), \varphi_\mathrm{cl}(0, \phi\,|t)) \tag{2.87}$$

moves only in the upper hemisphere yielding a positive m_z at all times. Consequently, its trajectory returns so quickly to the initial state that the wave packet remains sufficiently concentrated around the classical state to prevent any discontinuous movement of the Loschmidt vector $\mathbf{v}_\mathrm{max}(t)$ (obtained from (2.86)) during the first period. The first jump of $\mathbf{v}_\mathrm{max}(t)$, and therefore cusp in $r(t)$, appears only in the second period in agreement with the results obtained by ED calculations (see Fig. 2.21). At very late times the initial wave packet has spread so far over the Bloch sphere that the Loschmidt vector always points near the north pole, resulting in a very small $r(t)$.

For the regular quench to $\Gamma_\mathrm{f} = 0.3$ on the other hand [128], the classical vector crosses the equator of the Bloch sphere where the increased fluctuations in S_z result in a fast squeezing of the wave packet. This gives rise to a jump of the dominant orientation already during the first period of the motion, and thus to a regular LE.

In summary the semiclassical evolution allows for a very intuitive understanding of the relation between the order parameter dynamics and the return rate.

Let us now consider finite temperatures where the initial classical state for $\Gamma_\mathrm{i} = 0$ minimizes the mean-field free energy

$$F = -T \ln \left[\int \mathrm{d}\Omega \int_0^1 \mathrm{d}s\; s^2 D(Ns/2) \mathrm{e}^{-\beta H_\mathrm{i}(\theta)} \right] , \tag{2.88}$$

where $D(S)$, given by (2.20), denotes the degeneracy of the spin subspace of length S. These two equations specify the mean-field pre-quench state in terms of S_cl with $\theta_\mathrm{cl} = 0$ and ϕ_cl arbitrary (see Sec. 2.2.2). The exact initial density matrix

$$\rho_\mathrm{i} = Z^{-1} \sum_n \exp\left(-\beta E_n\right) |E_n\rangle\langle E_n| \tag{2.89}$$

in the eigenbasis $|E_n\rangle$ of H_i in our semiclassical description becomes

$$\rho_\mathrm{i}(\theta, \theta') = \frac{S_\mathrm{cl}^2}{Z} \int \mathrm{d}\Omega \int_{-1}^1 \mathrm{d}\cos\theta_n \Psi^*(\theta, E_n) \Psi(\theta', E_n) \mathrm{e}^{-\beta E_n} , \tag{2.90}$$

where the wave function is defined by (2.83). In close analogy to the interference matrix A (see Eq. (2.42)), in the thermodynamic limit the off-diagonal terms in (2.90) are suppressed by factors exponentially large in the system size and thus we can set $\theta' = \theta$.

Using this diagonal form of ρ_i and the fact that the truncated time evolution acts only on the coordinates $(\vartheta(\theta, \phi\,|t), \varphi(\theta, \phi\,|t))$, we can write for the fidelity Loschmidt

echo (cf. (2.41))

$$r_{\mathrm{F}}(t) = -\lim_{N\to\infty} N^{-1} \ln |\operatorname{Tr} \sqrt{\rho(0)}\sqrt{\rho(t)}|^2 \,. \tag{2.91}$$

In the thermodynamic limit the remaining integrals in this expression once again reduce to their saddle-point values.

The semiclassical Loschmidt echo at finite temperatures is therefore determined by the minimization problem over all starting points (θ, ϕ) in

$$r_{\mathrm{F}}(t) = \min_{(\theta,\phi)} \left\{ \mathrm{dist}(\vartheta(\theta,\phi\,|t)) + \mathrm{dist}(\theta) \right\} \tag{2.92}$$

and all classical angles θ_n in the combined thermal and WKB distance measure

$$\mathrm{dist}(\theta) = \min_{\theta_n} \left\{ \frac{\beta s_{\mathrm{cl}}^2}{8} \sin^2\theta_n + \Re A\,(\theta,\theta_n) \right\} . \tag{2.93}$$

The geometric interpretation of (2.92) remains the same as in (2.86), but now $\mathrm{dist}(\theta)$ first finds the saddle point of the density matrix, i.e. the largest product of the wave function $\Psi(E_n) = \mathcal{N} \exp(-NA(\theta,\theta_n)/2)$ and the corresponding Boltzmann factor $\exp(-\beta E_n)$, which are also the states dominating the calculation of the free energy.

We illustrate the dynamics on the Bloch sphere for a quench to $\Gamma_{\mathrm{f}} = 0.2$ at $\beta = 5$ in Fig. 2.19 (for the video see [129]) and the corresponding Loschmidt echo in the bottom panel of Fig. 2.21. The initial state shows a finite magnetization m_z but the radius of the Bloch sphere has decreased to $s_{\mathrm{cl}} \approx 0.71$. Due to the thermal fluctuations the quench is now regular and, in contrast to the $T = 0$ case, shows the same features as Fig. 2.18. This can be explained by the decreased spin length $s_{\mathrm{cl}} < 1$ which effectively renders the transverse field in the Hamiltonian more relevant compared to the S_z^2-term. As a result, the ground state of the final Hamiltonian is paramagnetic and the quench crosses the ferro- to paramagnetic transition in the DPT-I picture as well.

Finally, note that for high temperatures close to the equilibrium critical temperature $T_c = 1/4$ the initial distribution on the Bloch sphere becomes fully determined by thermal fluctuations. Hence, r_{F} in (2.92) can then be replaced by the completely thermal distance measure

$$r_{\mathrm{F}}(t) = \frac{\beta s_{\mathrm{cl}}^2}{8} \min_{\theta_n,\phi} \left\{ \sin^2\vartheta(\theta_n,\phi\,|t) + \sin^2\theta_n \right\} . \tag{2.94}$$

As evidenced in Fig. 2.21c) this simplification already produces decent results for the quench considered in Fig. 2.19, where we are thus calculating an essentially

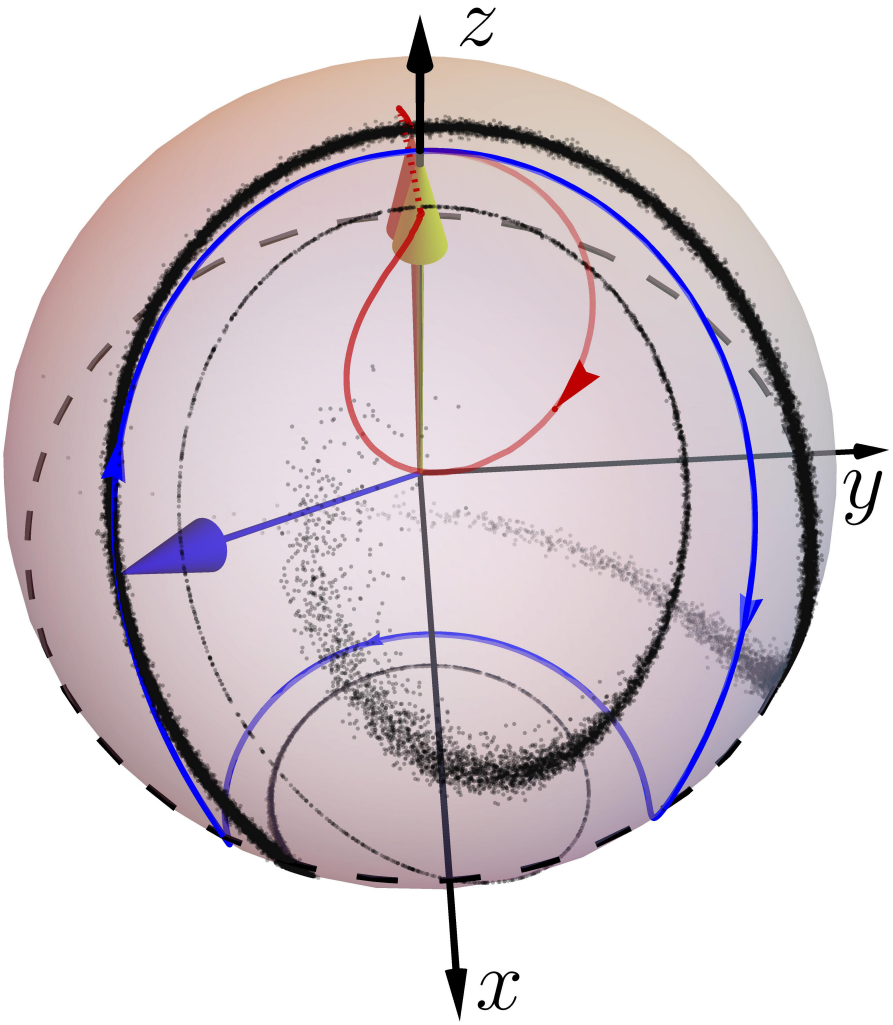

Figure 2.19: Illustration of the Bloch sphere in case of the regular quench $\Gamma_{\mathrm{i}} = 0 \to \Gamma_{\mathrm{f}} = 0.2$ at the finite inverse temperature $\beta = 5$. The color coding is the same as in Figs. 2.17 and 2.18.

classical return rate.

We now return to the discussion of a quench in the XX model described by the Hamiltonian

$$H_{\mathrm{XX}} = -\frac{1}{2N}\left(S_x^2 + S_y^2\right) - \Gamma S_z \tag{2.95}$$

which is identical to Eq. (2.54) except for a constant. When starting from a symmetry broken state we claimed every quench to be regular, independent of the distance between Γ_i and Γ_f. To test this statement requires an initial state at $T = 0$ that explicitly breaks the $O(2)$-symmetry and so we again employ (2.84). However, as the initial magnetization shall be oriented along the x-axis, we rotate the arguments of (2.84) according to

$$\begin{aligned} \theta &\to \arccos\left(\sin\theta\cos\phi\right) \\ \phi &\to \operatorname{sign}\left(\sin\phi\right)\arccos\left(\frac{\cos\theta}{\sqrt{1-\sin\theta\cos\phi}}\right). \end{aligned} \tag{2.96}$$

Starting from this rotated initial state the semiclassical calculation, the result of which is shown in Fig. 2.20 and as a video in Ref. [130], is identical to that for the infinite range transverse-field Ising model. The only difference lies in the equations of motion, which for the XX model are given by

$$\frac{\mathrm{d}\varphi}{\mathrm{d}t} = \Gamma_\mathrm{f} - \frac{s}{2}\cos\vartheta \quad \text{and} \quad \frac{\mathrm{d}\vartheta}{\mathrm{d}t} = 0\,. \tag{2.97}$$

We observe, that for any non-trivial quench ($\Gamma_\mathrm{f} \neq \Gamma_\mathrm{i}$), the classical magnetization vector begins to precess along a circle of latitude, the latter being non-zero if $\Gamma_\mathrm{i} \neq 0$. As the wave function on the northern hemisphere stays to the west and on the southern hemisphere to the east of the classical trajectory, the early-time return rate will be determined by the northern (southern) hemisphere for quenches with $\Gamma_\mathrm{f} \overset{>}{(<)} \Gamma_\mathrm{i}$. However, at some point before the magnetization vector returns to the initial orientation, the faster parts of the wave function in the other hemisphere will determine the return rate, thus always creating a regular signal. In fact, since the dynamics of the initial wave function is independent of the temperature that only affects the radius of the Bloch sphere, the shape of the return rate, as well as the critical times are mostly unaffected by finite temperature, as long as the initial phase is ferromagnetic. Note however, that this would not be the case, had we chosen to calculate the Loschmidt echo as the overlap between the time evolved state and the entire ground state manifold, which in the example in Fig. 2.20 is the entire equator. In that case any quench would result in a trivially vanishing return rate, as the classical vector never leaves the equator.

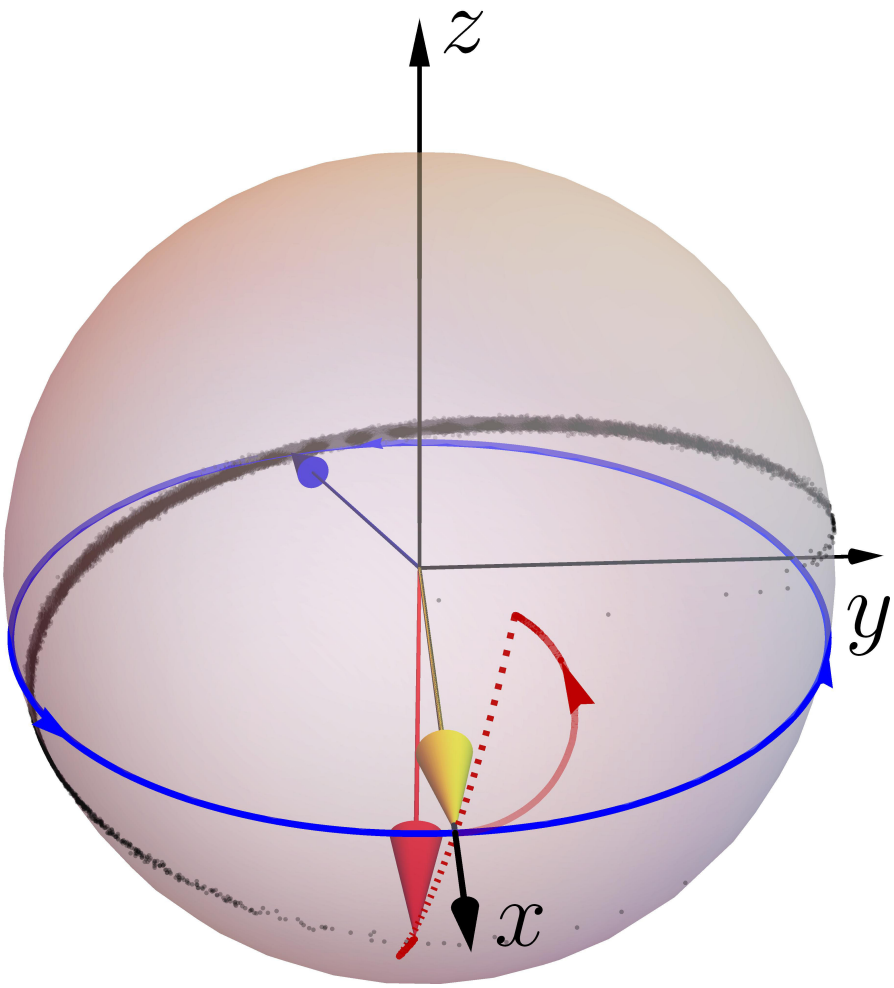

Figure 2.20: Illustration of the Bloch sphere for the quench $\Gamma_{\mathrm{i}} = 0 \to \Gamma_{\mathrm{f}} = 0.2$ in the XX model at vanishing temperature $T = 0$. The color coding is the same as in Figs. 2.17, 2.18 and 2.19.

2.3.4 Comparison with exact numerical results

In order to compute $r(t)$ according to (2.86), we cover the Bloch sphere with a Fibonacci lattice consisting of several million points, assigning to each the corresponding WKB amplitude of (2.84). This lattice is then evolved in time, by numerically solving (2.85) and finally extracting the site that yields the largest contribution to $r(t)$. In Fig. 2.21, the results are then compared with the fully numerical (quantum) return rate obtained with the algorithm detailed in Sec. 2.2.5. While the critical times and the DPT-II phases are well captured, there are significant discrepancies for large values of the return rate. As these are not at all symmetric between the rising and falling slopes of each peak, they are not related to inaccuracies in the initial wave function, but rather a consequence of the crude time evolution. In particular the slope $A'(q)$ of the exponent of the initial state becomes large at values relevant only for large return rates. These strongly suppressed parts of the wave function are thus not well captured by the purely classical equations of motion and spatial derivatives acting during the evolution would have to be incorporated, which will be left to future work.

We also provide a similar comparison between semiclassical and finite-size results for the XX model in Fig. 2.22. Note that the simple precession dynamics following a quench of the transversal field are captured much better by the semiclassical equations of motion, resulting in a significant reduction in the discrepancy with the fully numerical calculation.

2.3.5 Interpretation and robustness

If one views the semiclassical Bloch sphere discussed here as a non-trivial generalization of the relative Bloch sphere discussed for 2×2 Hamiltonians in Sec. 2.1, one can draw a number of conclusions. First one notices, that cusps in the return rate of the semiclassical model are not related to any orthogonality condition between the initial and time-evolved state. Moreover, as the Loschmidt vector $\mathbf{v}_{\max}$ is largely unrelated to the classical trajectory, the cusps in the return rate are independent of sign changes in the magnetization. This becomes particularly apparent in the anomalous phase, where the magnetization always remains in the northern hemisphere and the return rate is thus identical to that obtained for overlaps with the entire ground state manifold. The origin of cusps in $\mathrm{r}(t)$ as a result of a deformation of the wave function under time evolution is to be considered as a general feature that is absent only in non-interacting models [45, 131, 85, 96, 71], where in the case of two-band systems, the wave function is a point on the Bloch sphere that obviously has no internal dynamics. Similarly the coherent state in the $N \to \infty$ limit of the $\mathcal{O}(N)$ model experiences no non-trivial deformation following a quench, thus rigorously synchronizing the magnetization and the return rate in these systems. The importance of these internal dynamics in the form of spin squeezing is captured in Fig. 2.23, where the time-evolved polar angle $\vartheta(\theta, \phi|t)$ near the critical time is

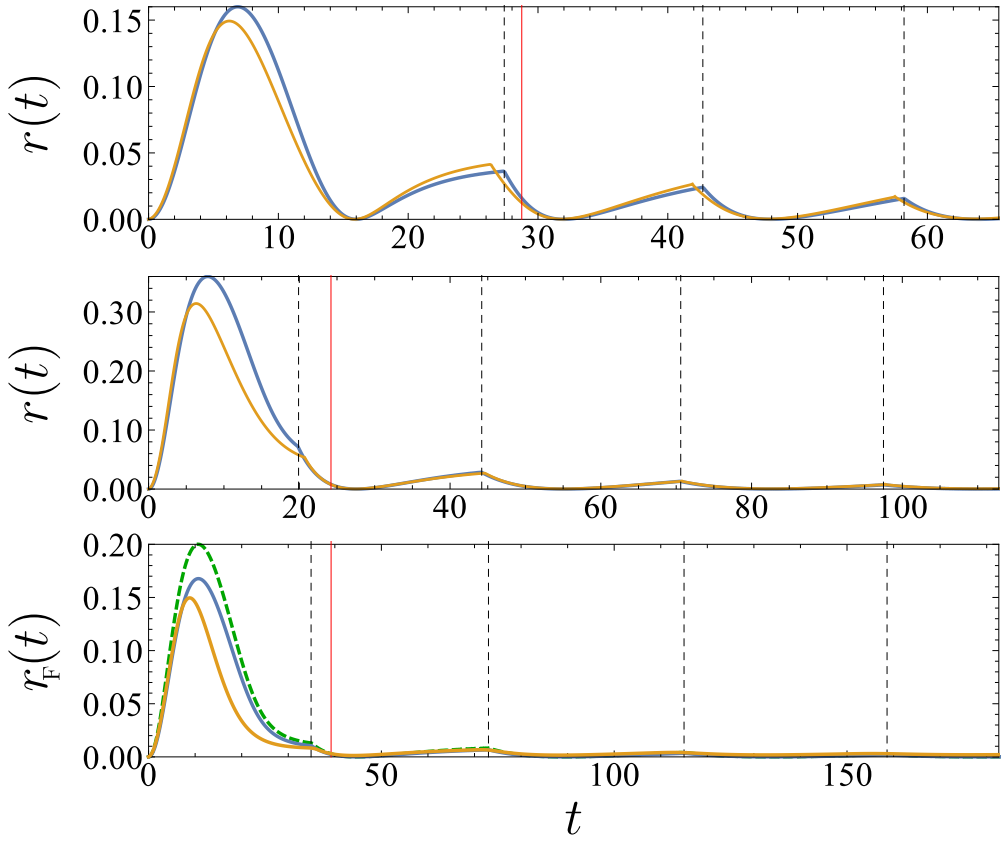

Figure 2.21: Comparison between the return rate calculated numerically for a system of size $N = 4001$ in yellow and the semiclassical results obtained from (2.86) and (2.92) in blue. Panels from top to bottom correspond to the parameters in Figs. 2.17 through 2.19 in that order. The red line indicates the time, depicted in those figures, while the black dashed lines mark the positions of cusps in the semiclassical return rate. The dashed green line in the bottom panel was calculated using the purely classical return rate from (2.94).

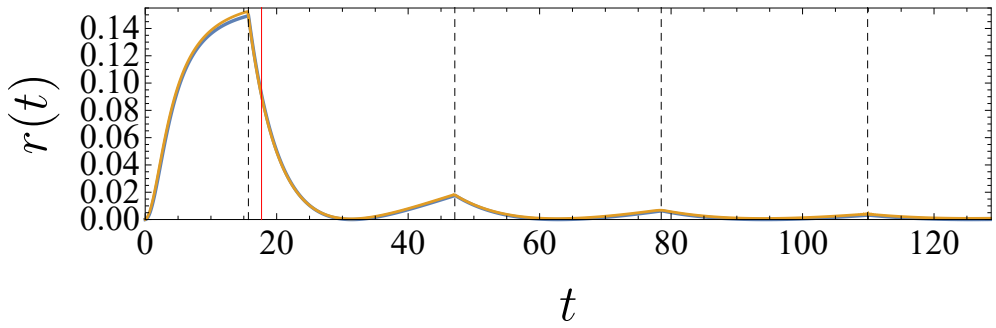

Figure 2.22: Comparison between the quantum return rate calculated numerically for a system of size $N = 4001$ in yellow and the semiclassical result obtained from (2.86) in blue for a quench of the XX model from $\Gamma_\mathrm{i} = 0$ to $\Gamma_\mathrm{f} = 0.2$ at $T = 0$. The time indicated by the red line corresponds to the instance depicted in Fig. 2.20, while the black dashed lines mark the positions of cusps in the semiclassical return rate.

shown to depend in a very complicated manner on the initial polar angle θ. Given the different origin of cusps in generic systems as compared to the non-interacting case, it is also not to be expected, that the attempts to classify dynamical phase transitions by Vajna and Dóra [81, 80] will be relevant and applicable to interacting systems.

However, the geometric picture presented here, also provides a macroscopic description of the return rate and therefore allows to draw an analogy to Ginzburg-Landau theory. In Sec. 2.3.3 we have argued that the Loschmidt return rate is dominated by a single trajectory on the Bloch sphere, namely the Loschmidt vector $\mathbf{v}_\mathrm{max}$, which can be obtained by minimizing a semiclassical distance measure. Interpreting this distance as the equivalent of a time-dependent free energy landscape, the cusp in the return rate becomes the dynamical analog of a first order phase transition. We make this more explicit, by discussing the specific example of the anomalous quench from $\Gamma_\mathrm{i} = 0$ to $\Gamma_\mathrm{f} = 0.2$ at zero temperature. We show the angular distribution of the corresponding distance measure $\left(\sin^2\vartheta(\bar{\theta},\bar{\phi}\,|t) + \sin^2\bar{\theta}\right)/2$ in Fig. 2.24, just before and after the critical time $t_c = 27.4$, when the first cusp in $r(t)$ occurs (cf. Fig. 2.21 in the main text). At this time one of the local minima (blue regions) becomes the new global one, which causes a jump of $\mathbf{v}_\mathrm{max}$ (red dot). This discontinuous movement is directly related to the non-analyticity of $r(t)$. We emphasize, that the more conventional effective free energy construction in Ref. [46] relies on the concurrence of sign changes in the magnetization and cusps in the return rate and is thus neither applicable here, nor in more general non-integrable systems.

From the perspective of the quantum mechanical calculation, which required an enormous precision in the eigenenergies and eigenstates, it is very surprising,

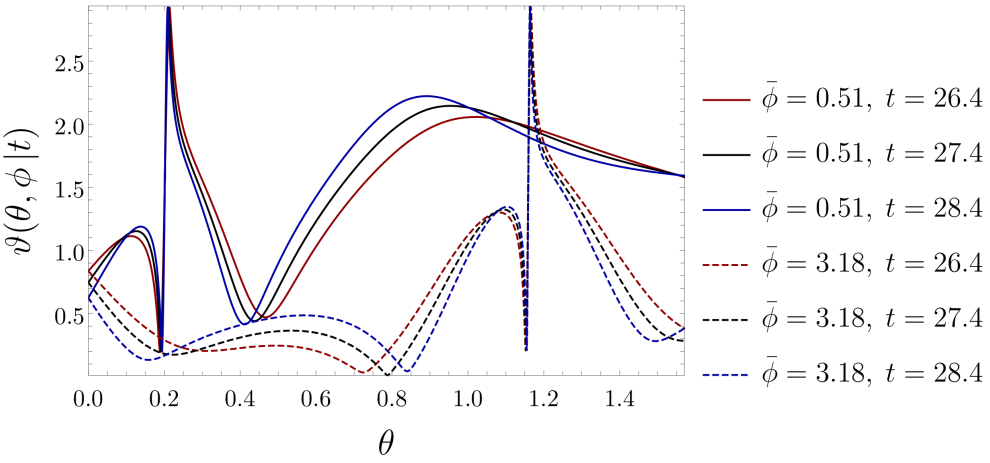

Figure 2.23: Plot of the time evolved polar angle $\vartheta(\theta, \phi|t)$ for the anomalous quench $\Gamma_\mathrm{i} = 0 \to \Gamma_\mathrm{f} = 0.2$ as a function of the initial polar angle θ at fixed azimuthal angle ϕ in the proximity of the critical time. The values of ϕ are chosen to coincide with those minimizing the WKB-distance at times infinitesimally before and after the jump of the Loschmidt vector. The strong spin squeezing near the equator separate close by initial angles to such an extent, that they can end up in different hemispheres. This is evidenced by the sharp signatures visible in the time evolved polar angle. At the critical time the Loschmidt trajectory changes from the solid to the dashed black line at fixed $\bar{\theta} \approx 0.2$. However, due to the explicit nonlinear dependence of the WKB-distance on *both* the initial and time-evolved angle, it is not possible to use this plot to determine the return rate directly.

that the crude approximation applied in Sec. 2.3.3 suffices to capture all essential features of the return rate. This is because any inaccuracy in the numerical procedure of Sec. 2.2 is expressed as a perturbation that usually corresponds to an operator involving arbitrary powers of spin operators that varies quickly between adjacent eigenstates and thereby destroys the phase coherence between states of comparable energies. In the semiclassical description these unphysical and therefore non-classical operators are not even possible to include properly as they contradict the condition of applicability, namely the suppression of higher order commutators in the equations of motion. Instead only semiclassical, i.e. smooth perturbations on the Bloch sphere that typically preserve coherent dynamics can be added to the picture. In other words, semiclassical dynamics actually describes the physics we are interested in by discarding all unphysical perturbations. Considering the dynamics of the Wigner function in such a formulation is thus ideally suited to determine Loschmidt echoes in more complicated systems.

Let us for example consider the case, where the eigenenergy of a single state is shifted by some small amount. This state will then no longer fully participate in the coherent evolution and is trapped in the semiclassical picture. The Loschmidt echo vector will therefore behave as it did without the defect until $r(t) > r_{\mathrm{pert}}$, where r_{pert} is given by the overlap of the initial state with the perturbation. Due to the trapped state the maximal value of the return rate is then fixed to r_{pert} as well, exactly reproducing the well-known errors in numerical calculations [70].

Finally, we can return to the question, regarding the connection between DPT-I and DPT-II in general models. If the order parameter of the model under consideration exhibits a dynamical phase transition (DPT-I), part of the initial wave function (or in general the Wigner function) will inevitably move through a 'critical' regime of strong squeezing in the phase space, which favors cusps in the Loschmidt echo. In the case of a quench across the DPT-I the center-of-mass will run around the 'critical' regime, making early cusps more likely. Nevertheless, there seems to be no argument for a direct and universal connection between DPT-I and DPT-II and for finite quenches one would in general expect different critical values for DPT-I and DPT-II, which thus have to be determined for each model individually.

2.3.6 Quantum Fisher Information

Quantum entanglement is an important resource for quantum computing [132, 133, 134] and quantum metrology [135, 136]. However, it is difficult to access experimentally [137], because the required precision per measurement grows exponentially in the system size N. In equilibrium the closely related quantum Fisher information F_Q, instead, can be measured directly by means of the dynamical susceptibilities [138]. This is particularly useful, since the quantum Fisher information density $f_Q = F_Q/N$ is a lower bound for multipartite entanglement. In fact, if m is a divisor of N and $f_Q > m$, the system must be in a state with $m+1$-partite entanglement [139, 140]. Furthermore, F_Q is a measure for the sensitivity of the system

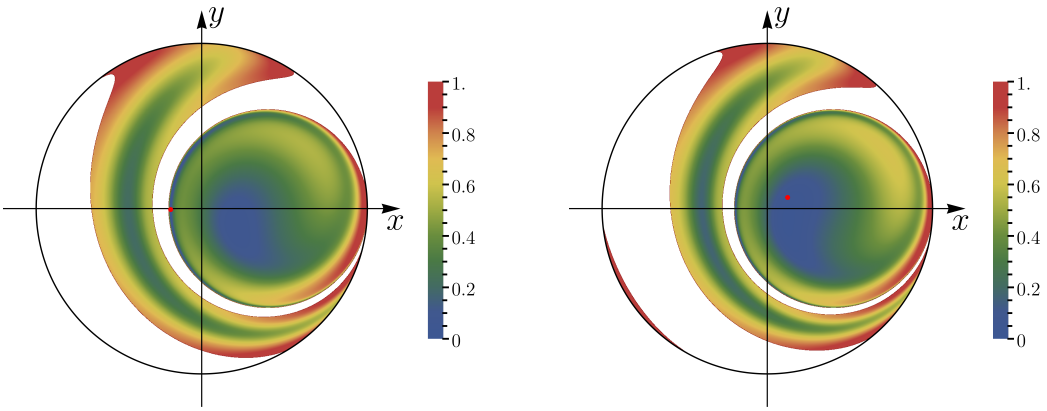

Figure 2.24: Representation of the zero-temperature distance measure (2.86) for the anomalous quench $\Gamma_\mathrm{i} = 0 \to \Gamma_\mathrm{f} = 0.2$ on the Bloch sphere. The absolute minimum determines the Loschmidt vector $\mathbf{v}_\mathrm{max}$ which is indicated by the red point. At the critical time $t_c = 27.4$ it jumps discontinuously. The left panel shows the configuration at $t = t_c - 1$, while the right one is taken at $t = t_c + 1$. The white regions are covered by points that initially where located within the lower hemisphere. Therefore, they carry negligible semiclassical weight and have not been taken into account for the numerics.

to perturbations, which in turn sets a bound for the measurability of these via the quantum Cramér-Rao bound: If a parameter α is to be estimated, based on M independent measurements, its variance is limited by [141]

$$\mathrm{Var}(\alpha) \geq \frac{1}{MF_Q} \,. \tag{2.98}$$

Therein lies the importance of highly entangled states for quantum enhanced measurements. However, preparation of these states is difficult, due to their sensitivity to decoherence [142, 143, 144]. Recently, Fiderer and Braun have therefore proposed to use driven, quantum chaotic systems to increase the sensitivity of a measurement from the standard quantum limit $\mathrm{Var}(\alpha) \propto 1/N$ to the Heisenberg limit $\mathrm{Var}(\alpha) \propto N^{-2}$ [145]. A similar quantum enhancement can also be achieved in the transverse field Ising model following a quench close to the dynamical critical point $\Gamma_c^d(T)$ given by Eq. (2.28).

To show this, we first define the quantum Fisher information [146]

$$F_Q(\alpha, t) = \lim_{\delta \to 0} \frac{8}{\delta^2} \left(1 - \mathrm{Tr} \sqrt{\sqrt{\rho(0)} \rho_\alpha(t) \sqrt{\rho(0)}} \right) \,, \tag{2.99}$$

where ρ_0 is the density matrix of the initial state and $\rho_\alpha(t)$ that of the system

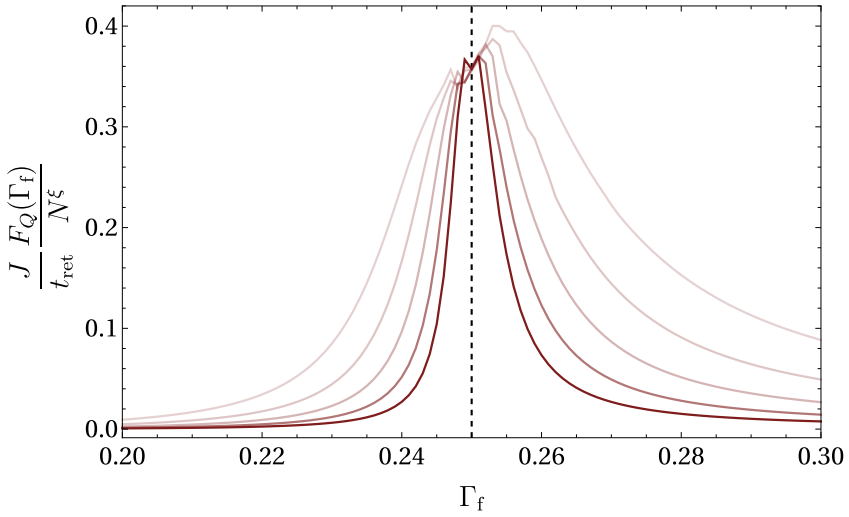

Figure 2.25: Finie size scaling of the quantum Fisher information in a quench of the infinite range transverse field Ising model at $T = 0$ and initial transverse field $\Gamma_\mathrm{i} = 0$. To compensate for the slowly increasing return time t_ret near criticality we divide by t_ret. Near the critical point $\Gamma_\mathrm{f} = 0.25$ indicated with a dashed line, the quantum Fisher information is then approximately proportional to N^ξ with $\xi = 1.92$ very close to the Heisenberg limit of $\xi = 2$. System sizes used in order of increasing saturation are $N = 2001, 4001, 8001, 16001, 32001$.

time-evolved forward with parameter α until time t and then evolved backwards to $t = 0$ with $\alpha + \delta$. It is easy to show via second order perturbation theory, that this definition is identical to

$$F_Q(\alpha, t) = 2 \sum_{\lambda,\lambda'} \frac{(p_\lambda - p'_\lambda)^2}{p_\lambda + p'_\lambda} \left| \langle \lambda | \hat{\mathcal{O}} | \lambda' \rangle \right|^2 , \tag{2.100}$$

where $\rho_0 = \sum_\lambda p_\lambda |\lambda\rangle\langle\lambda|$ and $\rho_\alpha = \sum_{\lambda'} p_{\lambda'} |\lambda'\rangle\langle\lambda'|$ have been expanded in their eigenbases and $\hat{\mathcal{O}}$ is the part of the Hamiltonian proportional to α (i.e. $\hat{H} = \hat{H}_0 + \alpha\hat{\mathcal{O}}$ with $\hat{H}_0 = \hat{H}|_{\alpha=0}$).

Using the numerical approach of section 2.2, it is straight forward to evaluate Eq. (2.99)[3]. We implement a protocol, where $t = t_\mathrm{ret}$ is fixed to the time of the first minimum of the return rate and $\alpha = \gamma_\mathrm{f}$. With the methods described in Sec. 2.2.5 and for $T = 0$, very large systems can be treated, that enable a finite size scaling. Far from the critical point, we find the standard quantum limit $F_Q \sim N$,

[3]In fact, F_Q can be calculated with machine precision for all system sizes and for finite temperatures the matrix root is to be taken over the initial, thermal states, where the number of relevant states is typically much smaller than after the quench.

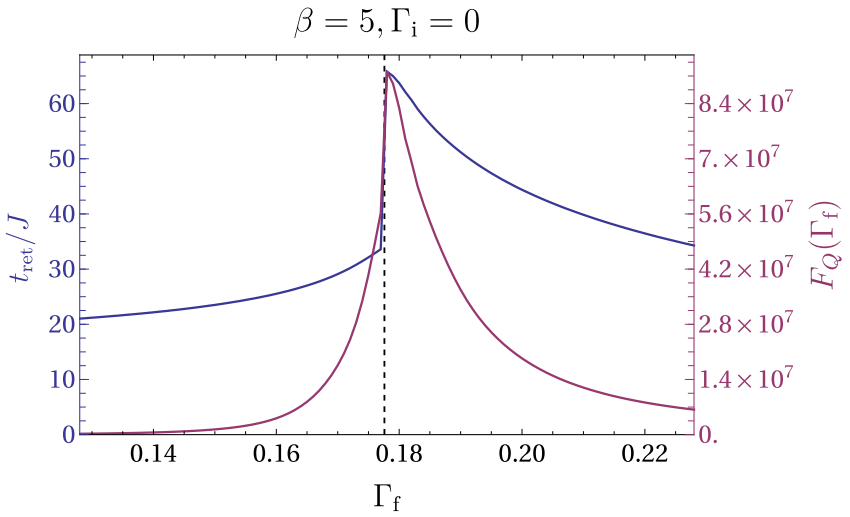

Figure 2.26: The qualitative behavior of the return time t_{ret} and F_Q are unaffected by finite temperatures in the initial state. However, quantitative corrections are observed, in particular the maximal value of the quantum Fisher information near the critical point at $\Gamma_f \approx 0.1776$ is reduced by a factor of approximately 2 for the plotted system size $N = 4001$ with $\beta = 5$ and $\Gamma_i = 0$ when compared to the maximal F_Q for the same system size and $T = 0$.

however at the critical point, we find $F_Q \sim tN^{\xi}$ with $\xi \approx 1.92$, which is very close to the Heisenberg limit reported for quantum chaotic systems in Ref. [145] (see Fig. 2.25). Surprisingly, a similar enhancement of the quantum Fisher information also happens at finite temperatures (see Fig. 2.26), where, however, a proper finite size scaling becomes numerically prohibitively expensive.

Nevertheless, the thermodynamic limit can be determined with the semiclassical method. Following the same arguments as before, we identify

$$F_Q(\alpha, t) = \frac{8}{\delta^2}\left(1 - \exp\left[-\frac{L}{2}\min_{(\theta,\phi)}\left\{\mathrm{dist}(\vartheta(\theta,\phi\,|t)) + \mathrm{dist}(\theta)\right\}\right]\right) , \tag{2.101}$$

where now, contrary to the notation used for the discussion of the return rate, $\vartheta(\theta, \phi\,|t)$ is evolved forward in time with Γ_f until time t and then back to $t = 0$ with $\Gamma_f + \delta$ with $\delta = 10^{-5}$. Evaluating Eq. (2.101) we find that in the thermodynamic limit the quantum Fisher information density collapses to a temperature independent scaling near the dynamical phase transition at $\Gamma_f^c(T)$ (see Fig. 2.27). Sufficiently far from the critical point, where the finite size scaling in Figs. 2.252.26 are already converged, the results obtained via Eq. (2.101) agree very well with the fully quantum mechanical calculation.

With the help of the semiclassical picture a qualitative understanding of the

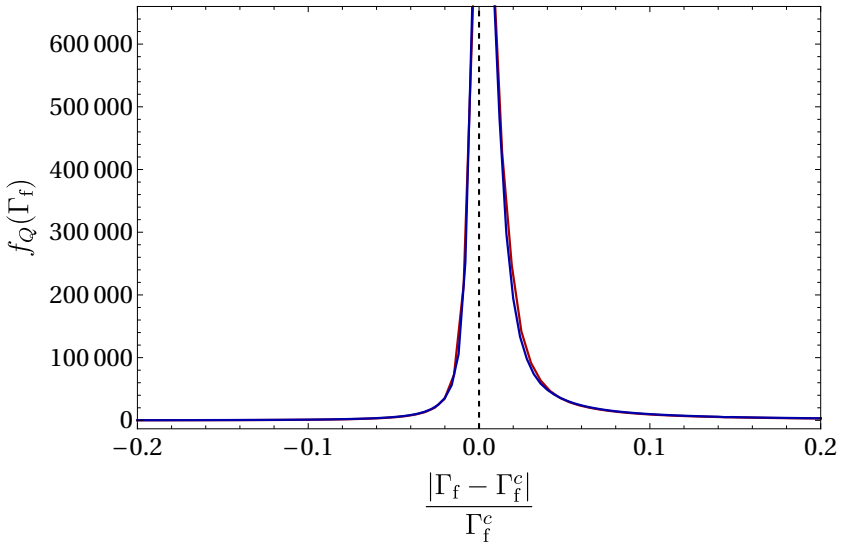

Figure 2.27: Thermodynamic limit of the quantum Fisher information density $f_Q(\Gamma_f)$ determined by Eq. (2.101) at $T = 0$ (red line) and $T = 1/5$ (blue line) for a quench from $\Gamma_i = 0$ to the vicinity of the critical point $\Gamma_f^c(T)$.

change in scaling behavior near Γ_f^c observed in Fig. 2.25 can be developed. While the definition (2.99) looks very similar to that of the fidelity return rate in Eq. (2.41), no direct connection exists. However, the change in behavior of the Loschmidt echo near the phase transition is a consequence of the deformation of the wave function, which entails a large spin squeezing and quantum Fisher information. Instead of a ballistic transport of the wave function across the Bloch sphere, that dominates the time evolution far away from the critical point, the wave function disperses strongly near the critical point, which gives rise to the mostly diffusive scaling observed in Fig. 2.25.

Interestingly, the description by means of the semiclassical wave function works exceptionally well, despite the large amount of multipartite entanglement built-up during the time evolution. We also emphasize that, opposed to the equilibrium scenario [138], F_Q diverges along the critical line $\Gamma_c^d(T)$ for all temperatures, making quantum quench enhanced measurements a real possibility in trapped ion experiments [11].

Chapter 3

Supersolidity in systems with long-range interactions

Following a short review of the search for the elusive supersolid phase in ^{4}He, we summarize recent proposals and experimental advances in systems with cold atoms. Most of these attempts, that aim to find different generalizations of supersolidity, rely on lasers or cavity fields to create long-range interactions between atoms, which suppress fluctuations and thereby help in stabilizing long-range correlations. They are therefore accessible to a quantitative mean-field analysis, which we apply to the recent experiment at ETH [1, 2], where supersolid behavior was observed in a gas of cold atoms trapped in two crossed cavities. We will also discuss, to what extent this experiment can be considered a 'true' supersolid.
This chapter is largely based on the publication [147], with some minor modifications and additions.

3.1 The hunt for the supersolid

Literally, a supersolid is a material, that simultaneously is crystalline and superfluid [148]. The coexistence of these two concepts is in fact so counterintuitive, that Onsager and Penrose, in the first publication on this topic, already concluded that it was likely non-existent [149]. However, the argument discussed there actually only states that a 'classical' crystal of atoms localized at fixed lattice positions is irreconcilable with superfluidity (which is correct). Obviously, this was not the end of story, as it was quickly realized, that diagonal and off-diagonal long-range order can indeed coexist [150, 151].

Let us clarify this statement: A crystal is a material, that breaks continuous translation invariance and leaves only a discrete symmetry, i.e. the density $\rho(\mathbf{r}) = \langle\hat{\psi}^\dagger(\mathbf{r})\hat{\psi}(\mathbf{r})\rangle$ is not constant, but satisfies $\rho(\mathbf{r}) = \rho(\mathbf{r}+\mathbf{T})$ for any lattice vector $\mathbf{T}$[1]. This is equivalent to the existence of Bragg peaks in the static structure factor accessible in neutron or X-ray scattering. A superfluid is defined by its property of supporting dissipationless flow. In three dimensions, superfluidity requires Bose-Einstein condensation, which is a property of the one-particle density matrix

[1] For simplicity we assume a simple Bravais lattice. Also, if zero point or thermal fluctuations are included, $\rho(\mathbf{r})$ has to be understood as the equilibrium expectation value.

$\rho(r,r') = \langle\hat{\psi}^\dagger(\mathbf{r})\hat{\psi}(\mathbf{r}')\rangle$. If for a system of volume V the averaged density matrix takes the finite expectation value $V^{-1}\int d^3r'\rho(\mathbf{r},\mathbf{r}+\mathbf{r}') \to \rho_0 \neq 0$ as $|\mathbf{r}| \to \infty$, the system is condensed and thus in a superfluid state, with condensate density ρ_0. As opposed to crystalline order, condensation affects the off-diagonal entries of the density matrix in position space. One therefore often refers to it as off-diagonal long-range order. In a supersolid both of these orders have to coexist. Simply put, the system has to condense and spontaneously form a mass density wave, which is not that hard to envision. However, it has many peculiar experimental consequences, for example a duct clogged by a supersolid will be impermeable for any other substance, but permit dissipationless flow of a superfluid of the particles forming the obstruction [148, 152, 153].

Note, that the presence of *two* simultaneously broken continuous symmetries clearly distinguishes supersolids from the Fulde-Ferrell-Larkin-Ovchinnikov state [154, 155], where the superfluid order parameter is spatially periodic, put the density remains homogeneous. Furthermore, a state shall be classified as supersolid only if it breaks two continuous symmetries spontaneously, thereby explicitly excluding any system, where a symmetry is broken externally, which would, for example, be the case for the interface layer of a condensate on the surface of a crystal.

Among conventional condensed matter systems, the most promising candidate to exhibit supersolidity is solid ^{4}He, where, because of the large ratio between kinetic and interaction energy, at low temperatures, the system is not necessarily so deeply frozen, that the crystal becomes essentially classical, thereby preventing superfluidity. It has been argued by Andreev and Lifshitz [156], and independently by Chester [157], that highly mobile zero-point defects can flow dissipationless through solid ^{4}He. In fact this is the only possible origin of superfluidity in a clean sample of solid ^{4}He, as states with off-diagonal long-range order are necessarily Bose-Einstein condensates [158], in which particles can be added or removed without expending energy. Therefore supersolid ^{4}He is not to be understood as a perfect, commensurate crystal of delocalized atoms, but rather an incommensurate crystal, in which vacancies or interstitials form a superfluid gas. Encouraged by these predictions, most early experiments focused on solid ^{4}He, but returned negative results [159]. This changed in 2004, when Kim and Chan performed an experiment [160, 161] that had long before been suggested by Leggett [162], where a sample of solid Helium is placed in a torsional oscillator (a device similar to a balance wheel in a pocket watch). Upon lowering the temperature, the authors noted a reduction of the oscillation period, indicating a decrease in the moment of inertia. This was interpreted as part of the sample turning superfluid, thereby disengaging from the rotation.

However, the situation in Helium has turned out to be much more complicated than initially anticipated. In fact unbiased quantum Monte Carlo calculations find a large energy gap for vacancies and interstitials, which furthermore attract one another [163]. Instead it has been hypothesized, that dissipationless flow can occur along extended lattice defects like domain walls or dislocations [164]. Although

these imperfections are absent in thermal equilibrium, they are frozen in during the crystallization of the sample. If the melting transition is only weakly first order, these defects can be very mobile, which would allow for superfluid behavior. However in this case they can also be removed from the crystal fairly easily by annealing the sample. Experiments searching for this effect have produced inconsistent results [165, 166, 167] and without a smoking gun many possible microscopic explanations for the non-classical rotational inertia found by Kim and Chan have been brought forward, some of which, like ^{3}He flowing through imperfection in the solid ^{4}He or sudden changes in the crystal structure require no superfluidity [148].

In general a strong short-range repulsion reduces the quantum degeneracy of the high density solid phase since the amount of overlap between the bosonic single-particle wave functions is reduced. While hard-core potentials are unavoidable in solid state experiments, where at short distances the Fermi character of the electrons stabilizes the material, softer repulsive potentials can be engineered with Rydberg atoms [40] or dipolar gases [39]. While the possibility of supersolidity in ^{4}He remains an open question, calculations by Henkel et al. indicate that Rydberg atoms show a roton instability that gives rise to a first-order phase transition towards a supersolid phase at low temperatures [40]. In the case of two-dimensional dipolar gases Spivak and Kivelson have speculated about the coexistence of a Wigner crystal with superfluid droplets [168].

Although neither of these proposed experiments has yet been realized, ultracold gases have made significant advances. Especially the possibility to create photon mediated interactions of arbitrary range between atoms proves expedient for stabilizing the necessary density wave, without impairing the condensate. Several proposed and realized experiments of 'supersolids', all of which in some sense rely on a broadening of the original definition, have emerged.

A lot of public interest has been generated by the experiment at MIT [169], where spin-orbit coupling was used to create a stripe phase of condensed ^{23}Na atoms with supersolid properties. In this state both the spin-wave and lattice phonons are expected to be gapless at $\mathbf{q} = 0$ with a linear dispersion [41]. As opposed to solid state materials the periodicity of the stripes is fixed externally by the wavelength of the lasers required to create the pseudospin.

A setup without this caveat has been proposed by Ostermann et al. [42] and was subsequently realized by the group at MIT [170]. In this case the lattice is formed by collective scattering between a BEC and counterpropagating non-interfering laser beams. Since the refractive index of the cloud depends on its spatial configuration, so does the lattice constant. However in this case, due to the long-range interactions the phonon spectrum is gapped. Very similar properties, however with an externally fixed lattice spacing have been proposed in the closely related system of a BEC in a ring cavity [171, 172]. A different system in which long-range positional order coexists with superfluid behavior has been realized in recent years by studying ultracold atoms in a high finesse cavity. In the presence of a transverse laser field there is an induced interaction between the atoms which is mediated

by the cavity photons [41]. The interaction is long-ranged and, beyond a critical strength λ_c of the drive, the atoms spontaneously arrange in a periodic lattice, allowing to scatter the light of the transverse field coherently into the cavity. This superradiant state was first observation by Black et al. with a cloud of thermal atoms [173] and was repeated several years later by Baumannn et al. in the same group with a BEC [29]. It is an example of the classic Dicke-Hepp-Lieb transition [174, 175, 176, 177], described in detail – including a finite photon loss rate – in Chap. 5, and results in a two-fold degeneracy of the periodic arrangement of the atoms. More precisely, the $\mathbf{Z}_2$ symmetry which is broken at the Dicke-Hepp-Lieb transition is associated with the sign of the two degenerate wave-vectors $\mathbf{q} = \pm\mathbf{k}_0$ which appear with equal weight in the standing periodic density wave described by a non-vanishing expectation value $\langle\hat{\rho}_{\mathbf{k}_0}\rangle \neq 0$, where $\mathbf{k}_0$ is the externally fixed cavity wave vector. From the point of view of off-diagonal long-range order, which characterizes Bose-Einstein condensation in its most general form [158], the phase beyond λ_c is one in which extensive eigenvalues of the one particle density matrix appear not only at $\mathbf{q} = 0$ but also at arbitrary multiples of $\mathbf{q} = \pm\mathbf{k}_0$, forming a fragmented condensate with a self-generated optical lattice [178, 179]. The system therefore possesses simultaneously both diagonal and off-diagonal long-range order. Despite the fact that periodic order is now generated through light-field mediated interactions between the atoms, it is not a supersolid in the standard sense because the superradiant transition does not break a continuous symmetry: With the Fabry-Pérot interferometer fixed in position the translational symmetry that is broken is reduced to a discrete $\mathbb{Z}_2$ symmetry by the periodic coupling strength between the induced dipole moments of the atoms and the cavity light field. Furthermore, due to the long-range interactions the system is effectively zero-dimensional and therefore the acoustic phonons near reciprocal lattice vectors $\mathbf{q} \simeq \mathbf{G}$, which are the Goldstone modes usually associated with the breaking of a continuous translation symmetry [180], are gapped. Equivalently the system does not sustain dissipationless particle currents e.g. of the $\mathbf{q} = 0$ part of the condensate with respect to the fixed periodic density wave pattern associated with the $\pm\mathbf{k}_0$ components[2].

Recently, a major step towards the realization of supersolid behavior with dissipationless particle transport has been taken by Léonard and coworkers at ETH in a setup involving ultracold atoms in *two crossed* cavities [1]. In this setup, a cloud of Bose-condensed atoms is enclosed in a configuration involving two optical cavities which are at a 60° angle with respect to each other. Tuning the parameters such that the atoms couple symmetrically to both cavities, this system allows to realize light-induced crystallization of the atoms which involves an arbitrary superposition of both cavity wave vectors. Within a simple two-mode description, the two discrete symmetries $\mathbf{Z}_2$ of the individual cavities can thus be combined to a

[2]Within a hydrodynamic description, such dissipationless currents would be associated with a fourth sound-like mode with linear dispersion, see [181].

continuous $U(1)$ symmetry, allowing to observe a continuous shift of the crystallization pattern [1]. Our aim is to analyze a fully microscopic model for this setup in order to study the detailed structure of the broken symmetries and the resulting spectrum of collective excitations. In particular, we will derive the associated effective dynamic Ginzburg-Landau functional for the light field in the cavity and discuss the limits in which the system indeed exhibits the breaking of a continuous translation symmetry. Beyond a detailed discussion of symmetry breaking and the subtle issue of supersolidity in this context, our results also provide a quantitative understanding of the recent measurements of the effective Goldstone and Higgs mode frequencies [2].

3.2 Supersolid behavior in two crossed cavities

In the following we will discuss the nature of symmetry breaking and the associated collective excitations. We will show, that in the absence of direct intercavity scattering the accidental $U(1)$ symmetry holds asymptotically for vanishing cavity field intensity and provide an estimate for the associated effective Goldstone mass. Finally we compute the spectral distribution of the cavity light field and show that both the Higgs and Goldstone mode acquire a finite lifetime due to Landau damping at non-zero temperature.

3.2.1 Model and symmetries

We begin with a description of the setup used for the recent experiments at ETH [1, 2]. It consists of a three dimensional cloud of bosonic atoms trapped at the intersection of the TEM_{00}-modes of two optical cavities. The system is driven transversally by a laser in the same plane as the cavities and all photons couple the atomic ground state to the same excited state. We create (destroy) an atom in the ground state at position $\mathbf{r}$ by the field operator $\hat{\psi}^\dagger(\mathbf{r})$ ($\hat{\psi}(\mathbf{r})$) and in the excited state by $\hat{\psi}_e^\dagger(\mathbf{r})$ ($\hat{\psi}_e(\mathbf{r})$). For atoms with mass m and excitation energy ω_e, the purely atomic system is described by (note that we use units in which $\hbar = 1$)

$$H_a = \int d^3r \left[\hat{\psi}^\dagger(\mathbf{r}) \left(-\frac{\nabla^2}{2m}\right) \hat{\psi}(\mathbf{r}) + \hat{\psi}_e^\dagger(\mathbf{r}) \left(-\frac{\nabla^2}{2m} + \omega_e\right) \hat{\psi}_e(\mathbf{r})\right] . \tag{3.1}$$

The single-mode cavities are of high quality, such that losses can be neglected. Using $\hat{a}_i$ as the bosonic annihilation operator of a photon with frequency ω_i in cavity i, the cavities are simply described by

$$H_c = \sum_{i=1,2} \omega_i \hat{a}_i^\dagger \hat{a}_i . \tag{3.2}$$

Neglecting counterrotating terms and using the dipole approximation, the classical laser field with energy ω_p and mode function $\eta_p(\mathbf{r}) = \cos(k_0 y + \frac{\pi}{2})$ rotates the

atomic states with Rabi frequency Ω:

$$H_{p/a} = -\Omega \int d^3r \, \left(\eta_p(\mathbf{r}) \hat{\psi}^\dagger(\mathbf{r}) \hat{\psi}_e(\mathbf{r}) \mathrm{e}^{-i\omega_p t} + \mathrm{h.c.} \right) . \tag{3.3}$$

The same process is also possible with the quantized cavity fields:

$$H_{c/a} = -\sum_{i=1,2} g_i \int d^3r \, \left(\eta_i(\mathbf{r}) \hat{a}_i \hat{\psi}^\dagger(\mathbf{r}) \hat{\psi}_e(\mathbf{r}) + \mathrm{h.c.} \right) , \tag{3.4}$$

where g_1 and g_2 are the single photon Rabi couplings for the two cavities with the corresponding mode functions $\eta_1(\mathbf{r})$ and $\eta_2(\mathbf{r})$. To get rid of the explicit time-dependence in $H_{p/a}$, we go to the rotating frame, where the complete system is then described by

$$\begin{aligned} H = & \int d^3r \, \left[\hat{\psi}^\dagger(\mathbf{r}) \left(-\frac{\nabla^2}{2m} \right) \hat{\psi}(\mathbf{r}) + \hat{\psi}_e^\dagger(\mathbf{r}) \left(-\frac{\nabla^2}{2m} - \Delta_A \right) \hat{\psi}_e(\mathbf{r}) \right] \\ & - \sum_{i=1,2} \Delta_i \hat{a}_i^\dagger \hat{a}_i - \Omega \int d^3r \, \left(\eta_p(\mathbf{r}) \hat{\psi}^\dagger(\mathbf{r}) \hat{\psi}_e(\mathbf{r}) + \mathrm{h.c.} \right) \\ & - \sum_{i=1,2} g_i \int d^3r \, \left(\eta_i(\mathbf{r}) \hat{a}_i \hat{\psi}^\dagger(\mathbf{r}) \hat{\psi}_e(\mathbf{r}) + \mathrm{h.c.} \right) , \end{aligned} \tag{3.5}$$

with the convention $\Delta_A = \omega_L - \omega_e < 0$, $\Delta_i = \omega_L - \omega_i < 0$. We note, that the excited atomic state appears at most quadratically and can thus be integrated out exactly. Note that in the experiment under consideration [1, 2] the laser drive is far detuned ($\Omega/|\Delta_A| \approx 3 * 10^{-4}$). We can therefore simplify the inverse propagator of the excited state as

$$G_e^{-1}(\omega, k) = \omega + \Delta_A - \frac{k^2}{2m} \approx \Delta_A \, , \tag{3.6}$$

which implies that the retardation of the induced interaction is negligible. This adiabatic elimination leads to an effective Hamiltonian that takes the following form:

$$\hat{H} = -\sum_{i=1,2} \Delta_i \hat{a}_i^\dagger \hat{a}_i + \int d\mathbf{r} \, \hat{\psi}^\dagger(\mathbf{r}) \left(-\frac{\nabla^2}{2m} + \hat{V}(\mathbf{r}) \right) \hat{\psi}(\mathbf{r}) \, . \tag{3.7}$$

Assuming equal dipole couplings $g_1 = g_2 = g$ in both cavities, the associated single-particle potential – which still depends on the quantum state of the cavity field – is given by

$$\hat{V}(\mathbf{r}) = V_L(y) + \sum_{i=1,2} V_i(\mathbf{r}) \left(\hat{a}_i + \hat{a}_i^\dagger \right) + \sum_{i,j=1,2} V_{i,j}(\mathbf{r}) \hat{a}_i^\dagger \hat{a}_j \, , \tag{3.8}$$

where V_L accounts for the pump potential while the V_i result from the interference between one cavity and the pump. The last term in Eq. (3.8) describes the effects of direct inter- and intracavity scattering. In terms of the mode functions, these potentials take the form

$$\begin{aligned} V_L(\mathbf{r}) &= \frac{\Omega^2}{\Delta_A}\eta_p(\mathbf{r})^2 \\ V_i(\mathbf{r}) &= g\frac{\Omega}{\Delta_A}\eta_p(\mathbf{r})\eta_i(\mathbf{r}) \\ V_{i,j}(\mathbf{r}) &= \frac{g^2}{\Delta_A}\eta_i(\mathbf{r})\eta_j(\mathbf{r}) \ . \end{aligned} \tag{3.9}$$

In the experiment under consideration [1], one has

$$\eta_1(\mathbf{r}) = \cos(\frac{\sqrt{3}}{2}k_0 x + \frac{1}{2}k_0 y) \quad \text{and} \quad \eta_2(\mathbf{r}) = \cos(\frac{\sqrt{3}}{2}k_0 x - \frac{1}{2}k_0 y) \ , \tag{3.10}$$

which correspond to the configuration shown in Fig. 3.1, where the cavity axes form a 30° angle with the x axis and lie in the $x-y$ plane i.e. $\mathbf{k}_{1,2} = k_0(\mathbf{n}_x \cos(30°) \pm \mathbf{n}_y \sin(30°))$. The pump axis is along the y direction i.e. $\mathbf{k}_p = k_0\mathbf{n}_y$ and the standing wave obtained by retroreflection has a phase-shift $\pi/2$. Due to the small detuning $|\Delta_i| \ll \omega_L$ the pump and cavity modes can be taken to have the same wavelength $\lambda_0 = 2\pi/k_0$. In the following discussion we will include the leading contribution of the direct intracavity processes $\propto \eta_i(\mathbf{r})\eta_i(\mathbf{r})$ as a dispersive shift to the cavity detuning

$$0 < \delta_{c_i} = -\Delta_i + \frac{g^2}{\Delta_A}\int d^3r \ \left\langle \hat{\psi}^\dagger(\mathbf{r})\eta_i^2(\mathbf{r})\hat{\psi}(\mathbf{r})\right\rangle \approx -\Delta_i + \frac{Ng^2}{2\Delta_A} \ . \tag{3.11}$$

where the approximation is valid for a shallow density wave, which is experimentally well realized, since $\alpha_i^2 g\Omega \ll \Delta_A E_R$, where $\alpha_i = \langle \hat{a}_i \rangle$ and $E_R = k_0^2/(2m)$ is the recoil energy. Since furthermore $\Delta_i\Delta_A \gg Ng^2$ the mapping between δ_{c_i} and Δ_i is actually trivial. We will however neglect contributions quadratic in $V_{i,j}(\mathbf{r})$, which are of order g^4. This is valid in the experimentally realized regime where fourth order processes due to V_1 and V_2 are more important than second order effects in $V_{i,j}$. Since intermediate states in this perturbation series carry energies $\sim E_R$ (in the superradiant phase creation of cavity photons costs very little energy), this reduces to the condition $\Omega \gg \sqrt{|\Delta_A E_R|}$, which is well satisfied in the experiment (see below). As the critical Rabi amplitude $\Omega_c \propto |\Delta_A|$ is decreased, close to the onset of superradiance, direct intercavity scattering will eventually be the dominant effect. Their role, together with different choices of the retroreflection phase-shift, have been theoretically investigated in [182, 183].

As discussed in [1], assuming small (in a sense that will become clear later) light field intensities, so that multiple scattering is suppressed, we can restrict the Hilbert

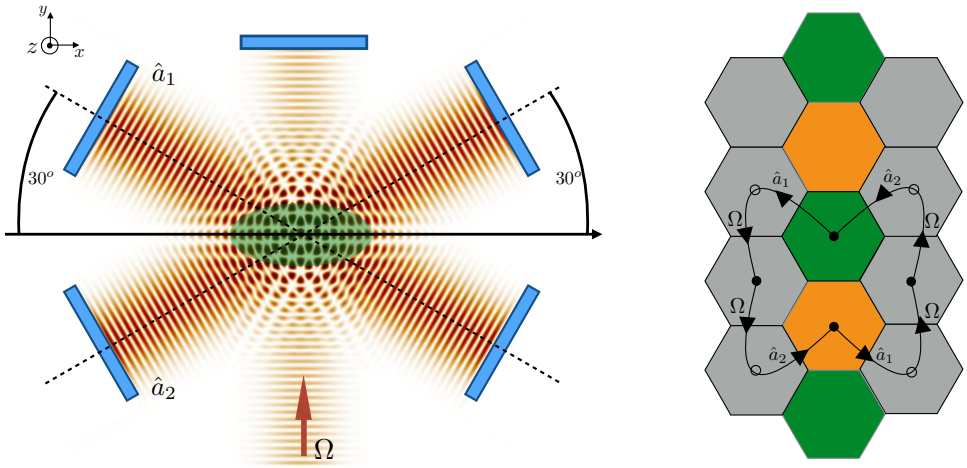

Figure 3.1: Left: sketch of the setup considered as implemented in the experiments of Refs. [1]. Right: momentum space in the repeated-zone scheme, where each hexagon indicates the Brillouin zone for a given band. Green zones are occupied even without cavity fields and in particular their center (Γ-point) is the only state occupied at $T = 0$. Gray zones are occupied via cavity-photon scattering and correspond to the truncation used in the $U(1)$-symmetric Hamiltonian (3.12). The closed curve indicates a scattering path involving two photons from each cavity. This scattering process, for which we need to include the orange zones in our Hilbert-space truncation, explicitly breaks the $U(1)$ symmetry in the full Hamiltonian (3.7).

space to the lowest nine momentum states $|k_x, k_y\rangle = |0,0\rangle, |\pm\mathbf{k}_i \pm \mathbf{k}_p\rangle$ (see also Fig. 3.1) and truncate the Hamiltonian (3.7) as follows [1]:

$$\begin{aligned}\hat{H}_{\text{trunc}} = \sum_{i=1,2} \Big[& \delta_{c_i} \hat{a}_i^\dagger \hat{a}_i + E_+ \hat{c}_{i+}^\dagger \hat{c}_{i+} + E_- \hat{c}_{i-}^\dagger \hat{c}_{i-} \\ & + \frac{g\Omega}{2\sqrt{2}\Delta_A} (\hat{a}_i^\dagger + \hat{a}_i)(\hat{c}_{i+}^\dagger \hat{c}_0 + \hat{c}_{i-}^\dagger \hat{c}_0 + \text{h.c.}) \Big] \ ,\end{aligned} \tag{3.12}$$

where $\hat{c}_{i\pm}^\dagger$ excites an atom into a standing wave of wave vector $\mathbf{k}_i \pm \mathbf{k}_p$ with energy $E_\pm = (2 \pm 1)E_R$ and $\hat{c}_0$ removes an atom at $\mathbf{k} = 0$. Here $g\Omega/|\Delta_A|$ is the effective cavity pump strength. The truncated Hamiltonian (3.12) has in general a $\mathbf{Z}_2 \otimes \mathbf{Z}_2$ symmetry corresponding to the following transformation

$$(\hat{a}_1, \hat{c}_{1\pm}) \to -(\hat{a}_1, \hat{c}_{1\pm}) \tag{3.13}$$

$$(\hat{a}_2, \hat{c}_{2\pm}) \to -(\hat{a}_2, \hat{c}_{2\pm}) \ . \tag{3.14}$$

The spontaneous breaking of either one of these discrete symmetries corresponds to a superradiant phase transition characterized by the order parameter $\langle \hat{a}_i^\dagger + \hat{a}_i \rangle$ or equivalently $\langle \hat{c}_{i+}^\dagger \hat{c}_0 + \hat{c}_{i-}^\dagger \hat{c}_0 + \text{h.c.} \rangle$. In the full model in real space given by Eq. (3.7), the above $\mathbf{Z}_2 \otimes \mathbf{Z}_2$ symmetry corresponds to the transformations

$$(\hat{a}_1, \mathbf{r}) \to (-\hat{a}_1, \mathbf{r} + \pi \frac{\mathbf{k}_1}{|\mathbf{k}_1|^2}) \tag{3.15}$$

$$(\hat{a}_2, \mathbf{r}) \to (-\hat{a}_2, \mathbf{r} + \pi \frac{\mathbf{k}_2}{|\mathbf{k}_2|^2}) \,, \tag{3.16}$$

which involve a discrete spatial translation along a cavity axis. In this sense, the superradiant transition corresponds to a self-ordering of the atoms into a spatial pattern which scatters constructively into the cavity [32].

As pointed out in [1], for a symmetric choice of cavity detunings $\Delta_1 = \Delta_2$ there is an accidental $U(1)$ symmetry in the truncated Hamiltonian (3.12):

$$\begin{aligned} &\left(\hat{a}_1, \hat{c}_{1\pm}, \hat{a}_2, \hat{c}_{2\pm}\right) \\ &\to \left(\hat{a}_1 \cos\theta - \hat{a}_2 \sin\theta, \hat{c}_{1\pm} \cos\theta - \hat{c}_{2\pm} \sin\theta, \hat{a}_1 \sin\theta + \hat{a}_2 \cos\theta, \hat{c}_{1\pm} \sin\theta + \hat{c}_{2\pm} \cos\theta\right) . \end{aligned} \tag{3.17}$$

The signatures of the spontaneous breaking of this continuous symmetry, which corresponds to a fixed value of the relative phase θ of the two coherent cavity fields, varying randomly between different realizations, have been experimentally investigated in Refs. [1, 2]. In particular, it has been shown that the symmetry broken state possesses a collective excitation with a frequency below the experimental resolution of 100kHz. Correspondingly the cavity fields have been observed at randomly distributed relative amplitudes with a fixed overall output intensity. Both these signatures have been interpreted as the Goldstone mode of the broken $U(1)$ symmetry.

As discussed in [1], the transformations (3.17) can be translated into an invariance of the potential (3.8) in real space. Indeed, by examining the potential (3.8) we see that by restricting to the subspace X defined by $k_0 y + \pi/2 = n\pi, n \in \mathbb{Z}$, the potential is invariant under:

$$\begin{aligned} &\left(\hat{a}_1, \hat{a}_2, x, y = \pi(n - 1/2)/k_0\right) \\ &\to \left(\hat{a}_1 \cos\theta - \hat{a}_2 \sin\theta, \hat{a}_1 \sin\theta + \hat{a}_2 \cos\theta, x \pm 2\theta/(\sqrt{3}k_0), y = \pi(n - 1/2)/k_0\right) , \end{aligned} \tag{3.18}$$

where the $-(+)$ sign applies for even (odd) values of n. The continuous symmetry of the Hamiltonian under rotations of the cavity field by an angle θ and a simultaneous shift of the atoms along the x-direction by $\pm 2\theta/\left(\sqrt{3}k_0\right)$ thus leads to supersolid-like behavior with no restoring force for translations of the atoms along the x-direction.

Now, the fact that the $U(1)$ symmetry (3.18) in the full model (3.7) is restricted

to the subspace X of discretely spaced values of the y coordinate implies that this symmetry holds only approximately. The fundamental reason is that the potential (3.8) has no minimum on the $U(1)$-symmetric lines $y = \pi(n - 1/2)/k_0$, but rather at a position which is shifted by an amount inversely proportional to the amplitude of the state-independent ac-Stark shift V_L in the effective potential. This shift appears due to interference between the two cavity fields and is therefore present for any finite number of photons in *both* cavities. The corresponding lowest-order scattering processes are depicted in Fig. 3.1 as a closed path involving two photons for each cavity, which for equal intensities $I_1 = I_2 = I$ implies that the lowest order of the explicit breaking of the $U(1)$ symmetry is proportional to I^2. It is important to note that the description of these scattering processes requires the inclusion of momentum states that are absent in the truncation used to obtain the Hamiltonian (3.12) (see Fig. 3.1). In the following we will discuss the consequences of the explicit $U(1)$ symmetry breaking for the supersolid-like features, which will turn out to be still approximately present in the limit of intense laser driving Ω.

To understand the physics beyond the deviations from a perfect $U(1)$-symmetry, it is convenient to use a simple effective Hamiltonian obtained by adiabatically eliminating the photons from (3.7). Assuming deep lattices such that we can neglect the kinetic term as well as all terms beyond $\mathcal{O}(g^2)$ from the contribution $V_{i,j}(\mathbf{r})$, the resulting effective Hamiltonian

$$\hat{H} = \int d\mathbf{r}\ \hat{\psi}^\dagger(\mathbf{r})\hat{\psi}(\mathbf{r}) \left(V_L(\mathbf{r}) - \sum_i \frac{V_i(\mathbf{r})}{\delta_{c_i}} \int d\mathbf{r}'\ V_i(\mathbf{r}')\hat{\psi}^\dagger(\mathbf{r}')\hat{\psi}(\mathbf{r}') \right) \tag{3.19}$$

for the atoms alone contains an instantaneous, cavity field induced, attractive density-density interaction of the form $-\sum_i V_i(\mathbf{r})V_i(\mathbf{r}')/\delta_{c_i}$ which does not decay as a function of the separation $|\mathbf{r} - \mathbf{r}'|$. Since we neglect direct intercavity scattering, there are no interactions of higher order in the density. In the case that only a single cavity is superradiant the ground state is given by a density distributed solely within the high symmetry subspace X

$$\rho(\mathbf{r}) = \rho_0 \frac{2\pi^2}{\sqrt{3}} \delta\left(k_0 y - \frac{\pi}{2} + n\pi\right) \delta\left(k_0 x - \frac{\mp\pi + 4\pi m}{2\sqrt{3}}\right),\ n, m \in \mathbb{Z} \tag{3.20}$$

with $\rho_0 = N/V$. Here, the minus sign implies superradiance in cavity 1 ($\alpha_1 = \langle \hat{a}_1 \rangle \neq 0$) while the plus sign corresponds to a finite expectation value of $\alpha_2 = \langle \hat{a}_2 \rangle$. The energy density of both states is given by $\epsilon = \frac{\Omega^2}{\Delta_A}(1+c)$, with $c = Ng^2/\delta_{c_i}|\Delta_A|$ a dimensionless positive constant which is much less than one for typical experimental parameters. For two identical cavities $\delta_{c_i} = \delta_c$ and therefore $\alpha = \alpha_i$, this is, however, not in the ground state manifold which instead contains for example the

density profile

$$\rho(\mathbf{r}) = \rho_0 \frac{2\pi^2}{\sqrt{3}} \delta(k_0 x - \frac{2n\pi}{\sqrt{3}}) \sum_{\sigma=\pm} \delta\left(k_0 y + 2\sigma \arcsin\left(\sqrt{\frac{1+4c-d(c)}{6c}} \right) + 2\pi m \right), \tag{3.21}$$

with $n, m \in \mathbb{Z}$ and $d(c) = \sqrt{1+2c+4c^2}$. This density distribution slightly frustrates the potential V_L induced by the ac-Stark shift of the atoms and shifts the densities away from the X subspace. It therefore slightly breaks the $U(1)$ invariance in the atomic density and locks the relative cavity phases. The small energy difference between state (3.21) and state (3.20) is given by

$$\begin{aligned} \Delta\epsilon &= -\frac{\Omega^2}{\Delta_A}\left[1 + c + \frac{1}{27c^2}\left(1+4c-d(c)\right)\left(1-2c-d(c)\right)\left(2+2c+d(c)\right) \right] \\ &\approx \frac{\Omega^2 c^2}{4\Delta_A} < 0 \quad \text{for} \;\; c \ll 1 \, . \end{aligned} \tag{3.22}$$

As will be discussed below, this energy determines the scale of the effective Goldstone mass. Resubstituting either one of these density profiles into the cavity equations of motion we obtain $|\alpha| = \sqrt{I} \approx N\Omega g/|\Delta_A|\delta_c$ to leading order in c, which shows that in the deep lattice limit the critical coupling strength λ_c vanishes. Since kinetic energy contributions have been neglected, the Goldstone mass has an upper bound

$$m_G = \frac{\sqrt{-\Delta\epsilon}}{\alpha} \lesssim \frac{\delta_c \sqrt{-\Delta_A I}}{\Omega N} = \frac{g}{\sqrt{-\Delta_A}} \, . \tag{3.23}$$

Physically the Goldstone mass m_G arising from the finite energy scale $\Delta\epsilon$ associated with the breaking of the $U(1)$ symmetry describes the azimuthal curvature of the Ginzburg-Landau potential, which will be discussed in more detail in section 3.2.3. As expected according to the argument based on the scattering processes illustrated in Fig. 3.1, $\Delta\epsilon \propto |\alpha^4| = I^2$. The explicit symmetry breaking $\Delta\epsilon$ due to the latter scattering processes has actually the same scaling with intensity as the one which would result from direct intercavity scattering (not involving the pump Ω), which we neglected in our model (3.7). As mentioned before, this is justified in the experimentally realized limit $\Omega/\sqrt{|\Delta_A E_R|} \gg 1$, where direct intercavity scattering is suppressed with respect to the processes shown in Fig. 3.1. In particular, the fact that we can neglect all contributions from the last term in (3.8) beyond the simple dispersive shift has no influence on the $U(1)$ invariance in subspace X. Even including all contributions from the last term in (3.8), the explicit breaking of the $U(1)$ symmetry is still caused by the fact that the global potential minimum for the atoms lies outside the subspace X.

3.2.2 Effective action and phase diagram

In order to compute the phase diagram and the experimentally accessible spectrum of the cavity light field, we extend the effective equilibrium path-integral approach developed by Piazza et al. [178] for a single-cavity configuration. We derive an effective action for the cavity degrees of freedom by exactly integrating out the atoms. The action splits into a mean-field (MF) plus a fluctuation (FL) part. The latter will be discussed in detail in section 3.2.4 below. As was shown in Ref. [178], this action becomes exact in the thermodynamic limit due to the infinite-range interactions. By separating the coherent part of cavity fields $\alpha_i = \langle \hat{a}_i \rangle$ as well as the atom field $\phi(\mathbf{r}) = \langle \hat{\psi}(\mathbf{r}) \rangle$ (which corresponds to the condensate fraction) we obtain the effective action

$$S_{\text{eff}}[a^*_{1,2}, a_{1,2}] = S^{(MF)}_{\text{eff}} + S^{(FL)}_{\text{eff}}[a^*_{1,2}, a_{1,2}] \, . \tag{3.24}$$

The leading MF action reads

$$S^{(MF)}_{\text{eff}} = -\sum_{i=1,2} \Delta_i |\alpha_i|^2 + \text{Tr} \ln \left[G^{-1} \right] + \int d\mathbf{r} \; \phi^*(\mathbf{r}) \left[-\frac{\nabla^2}{2m} + V_{\text{sp}}(\mathbf{r}) - \mu \right] \phi(\mathbf{r}) \, . \tag{3.25}$$

It involves an effective c-number single-particle potential $V_{\text{sp}}(\mathbf{r}) = \hat{V}(\mathbf{r})\big|_{\hat{a}_i \to \alpha_i}$ felt by the atoms in which the light field operators are replaced by their coherent state expectation values. The atom propagator is defined by

$$G^{-1}_{n,n'}(\mathbf{r}, \mathbf{r}') = \left[-i\omega_n - \frac{\nabla^2}{2m} + V_{\text{sp}}(\mathbf{r}) - \mu \right] \delta_{n,n'} \delta(\mathbf{r} - \mathbf{r}') \, , \tag{3.26}$$

where the integers n, n' label the Matsubara space with frequencies $\omega_n = 2\pi n k_B T$, k_B is the Boltzmann constant and T the temperature of the system. In Eq. (3.25) the trace $\text{Tr} = \int d\mathbf{r} \sum_n$ is taken over coordinate and Matsubara space and μ is the atomic chemical potential.

The saddle point associated with the mean-field action defines a closed system of equations:

$$\begin{aligned} -\Delta_i \alpha_i + \int d\mathbf{r} \; \frac{\partial V_{\text{sp}}(\mathbf{r})}{\partial \alpha_i^*} \left[|\phi(\mathbf{r})|^2 + \rho(\mathbf{r}) \right] &= 0 \, , \quad i = 1, 2 \\ \left(-\frac{\nabla^2}{2m} + V_{\text{sp}}(\mathbf{r}) - \mu \right) \phi(\mathbf{r}) &= 0 \\ \int d\mathbf{r} \; \left(|\phi(\mathbf{r})|^2 + \rho(\mathbf{r}) \right) &= N \, , \end{aligned} \tag{3.27}$$

with the condensed $\rho_0(\mathbf{r}) = |\phi(\mathbf{r})|^2$ and non-condensed $\rho(\mathbf{r}) = \langle \hat{\psi}^\dagger(\mathbf{r}) \hat{\psi}(\mathbf{r}) \rangle - \rho_0(\mathbf{r}) = \sum_\ell n_{\text{b}}(\epsilon_\ell - \mu) |v_\ell(\mathbf{r})|^2$ atom density. Here $v_\ell(\mathbf{r})$ are the eigenvectors of

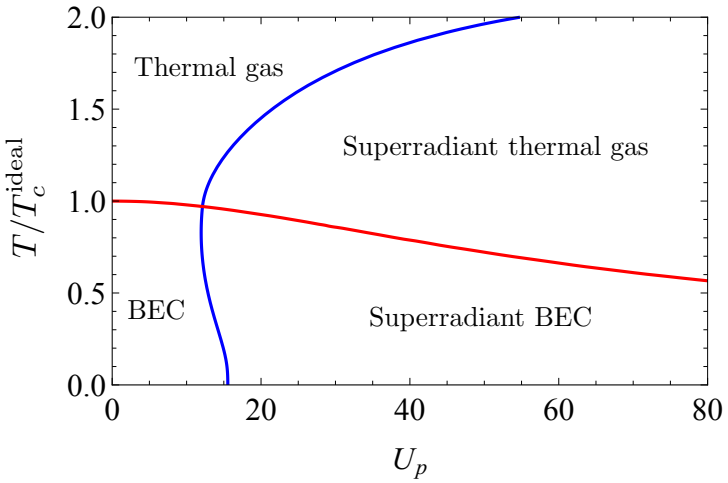

Figure 3.2: Phase diagram in the $U_p - T$ plane for parameters $\Delta_2 = \Delta_1$, $\epsilon_{\mathrm{R}} = 8$, $n = 1$, $\lambda = 2.8$. To the right of the blue line the system is in a superradiant state with equal intensity in both cavities, below the red line a finite fraction of the atoms is condensed.

the single-atom Hamiltonian with potential $V_{\mathrm{sp}}(\mathbf{r})$ with eigenvalue ϵ_ℓ, and $n_b(x) = (\exp(x/k_BT)-1)^{-1}$ is the Bose-Einstein distribution. The second equation in (3.27) is the Gross-Pitaevskii equation for the condensate wave function while the third equation fixes the chemical potential. We stress that both $\rho(\mathbf{r})$ and $V_{\mathrm{sp}}(\mathbf{r})$ depend on the cavity coherent parts $\alpha_{1,2}$.
It is convenient to introduce dimensionless quantities, which we define by

$$\delta_c = \min_i (\delta_{c_i}) , \ f = \frac{\rho_0}{(m\delta_c)^{3/2}}, \ U_p = \frac{\Omega^2}{|\Delta_A|\delta_c}, \ \lambda = \frac{\Omega g\sqrt{N}}{|\Delta_A|\delta_c}, \ \epsilon_R = \frac{E_R}{\delta_c} . \qquad (3.28)$$

Moreover, we measure temperatures in units of the critical temperature of an ideal Bose gas $T_c^{\mathrm{ideal}} = 2\pi\delta_c \left(f/\zeta(3/2)\right)^{2/3}$ at the given average filling fraction f and with ζ the Riemann zeta function. We furthermore rescale $\alpha \to \alpha/\sqrt{N}$ in the remainder of this chapter and in all figures.

As discussed in the previous section, the Hamiltonian (3.7) possesses the $\mathbf{Z}_2 \otimes \mathbf{Z}_2$ symmetry defined by Eq. (3.15). The corresponding order parameters are the two real quantities

$$X_{1,2} = \langle \hat{\mathrm{X}}_{1,2} \rangle = \langle \hat{a}_{1,2} + \hat{a}_{1,2}^\dagger \rangle = 2\mathrm{Re}(\alpha_{1,2}) . \qquad (3.29)$$

A finite expectation value $X_i \neq 0$ creates the effective one-body potential V_i, which results in an atomic density wave. Thus, equivalent order parameters can be defined

by the density components

$$\begin{aligned}\rho_{1,2} &= \int d\mathbf{r}\ \cos(\mathbf{k}_p\cdot\mathbf{r})\cos(\mathbf{k}_{1,2}\cdot\mathbf{r})\langle\hat{\psi}^\dagger(\mathbf{r})\hat{\psi}(\mathbf{r})\rangle \\ &= \int d\mathbf{r}\ \cos(\mathbf{k}_p\cdot\mathbf{r})\cos(\mathbf{k}_{1,2}\cdot\mathbf{r})\left(|\phi(\mathbf{r})|^2+\rho(\mathbf{r})\right)\ . \end{aligned} \tag{3.30}$$

Additionally, we have the Bose-Einstein condensation transition described by the $U(1)$ order parameter $\phi(\mathbf{r})$.

We first investigate the interplay between the superradiant transition and the Bose-Einstein condensation by solving the mean-field equations (3.27) as a function of temperature T and driving strength U_p (for details see appendix A). The corresponding phase diagram Fig. 3.2[3] is qualitatively the same as the one for the single-cavity case considered in Ref. [178]. With growing values of the coupling strength U_p the atomic gas becomes increasingly confined to the minima of the effective single-particle potential, which results in an enhancement of the kinetic energy and therefore a reduction of the critical temperature for Bose-Einstein condensation T_c. Beyond a critical coupling strength U_{p_c} (or equivalently λ_c) the atoms spontaneously arrange into a spatially ordered configuration, resulting in a superradiant backscattering of light into the cavity. This Dicke-Hepp-Lieb transition, as indicated by the blue line in Fig. 3.2, can be found both with and without a condensate fraction. Additionally, a finite, but small, temperature can enhance the tendency towards superradiance, which can be seen from the decrease of the critical driving strength resulting in a reentrance of the superradiant phase for increasing temperatures at $T \lesssim T_c^{\text{ideal}}$.

The phase diagram of Fig. 3.2 is computed for a symmetric cavity configuration i.e. for equal detunings $\Delta_1 = \Delta_2$, implying that in the superradiant phase both cavities are equally occupied with order parameters $\alpha_1 = \alpha_2$. For a comparison with the experimental results we also compute the zero temperature phase diagram in the $\delta_{c_1} - \delta_{c_2}$ plane, which is shown in Fig. 3.3. Apart from the superradiant phases with only one nonzero cavity field i.e. $\alpha_{1,2} \neq 0, \alpha_{2,1} = 0$ we observe a narrow region around the diagonal $\Delta_1 = \Delta_2$ where both $\mathbf{Z}_2$ symmetries are broken i.e. $\alpha_1 \neq 0, \alpha_2 \neq 0$. Within this small region of the phase diagram the two cavity order parameters are not equal, as quantified by the color scale in Fig. 3.3, indicating the value of the angle θ in the $\alpha_1 - \alpha_2$ plane (see also Fig. 3.4), defined as

$$\theta = \arctan\left(\frac{\alpha_1}{\alpha_2}\right)\ ,$$

which is identical with the parameter introduced in Eq. (3.18).

This region exists due to the fact that the $U(1)$ symmetry of Eq. (3.18) is not

[3] We choose $E_R = 8\delta_c$ for our computations. This is much larger than the experimental values $E_R \sim \delta_c/100$ of the recoil energies, which would increase the numerical effort considerably without changing the qualitative physics.

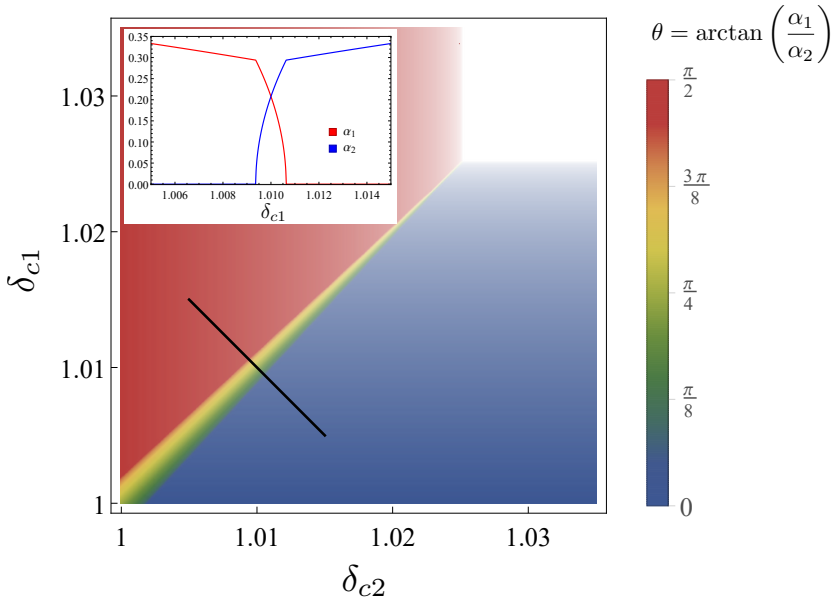

Figure 3.3: Phase diagram in the $\delta_{c_1} - \delta_{c_2}$ plane. The color scale indicates the angle in θ in the $\alpha_1 - \alpha_2$ plane. Inset: cavity amplitudes along the black line indicated on the phase diagram. The parameters used are $T = 0$, $\lambda = 2.82$, $\eta = 4$ and $\epsilon_{\mathrm{R}} = 8$.

perfectly realized. In particular, the size of the region is set by the value of the Goldstone mass. Using Eq. (3.23) and the experimental parameters $\Omega^2/|\Delta_A| = 38E_R$, $g^2/|\Delta_A| = 5 * 10^{-4}E_R$ and $|\Delta| = 10^3 E_R$ [1], one obtains $|\Delta\epsilon| \sim m_G^2\alpha^2 \sim 0.1\ E_R$, consistent with the experimental result $|\Delta\epsilon| < 10\ E_R$.

3.2.3 Ginzburg-Landau potential for the cavity fields and role of cavity losses

In order to investigate the approximate $U(1)$ symmetry of our model in more detail, we compute the full Ginzburg-Landau (GL) potential corresponding to the mean-field Eqs. (3.27). The resulting effective potential in the $\alpha_1 - \alpha_2$ plane is shown in Fig. 3.4, both for an asymmetric and the perfectly symmetric choice of detunings, at zero and also at finite temperature.

The asymmetric case for $T = 0$ is picked such that we are in the single-cavity superradiant phase and the GL potential has indeed two minima at angles $\theta = 0, \pi$ when cavity 1 is preferred, or $\theta = \pm\pi/2$ when cavity 2 is preferred. The asymmetric case for $T = 0.9T_c$ is instead picked such that we still are in the coexistence region where both cavities are occupied and where the GL potential has four minima. One of those is shown at an angle slightly below $\theta = \pi/4$, with the other three obtained by mirror symmetry with respect to the coordinate axes.

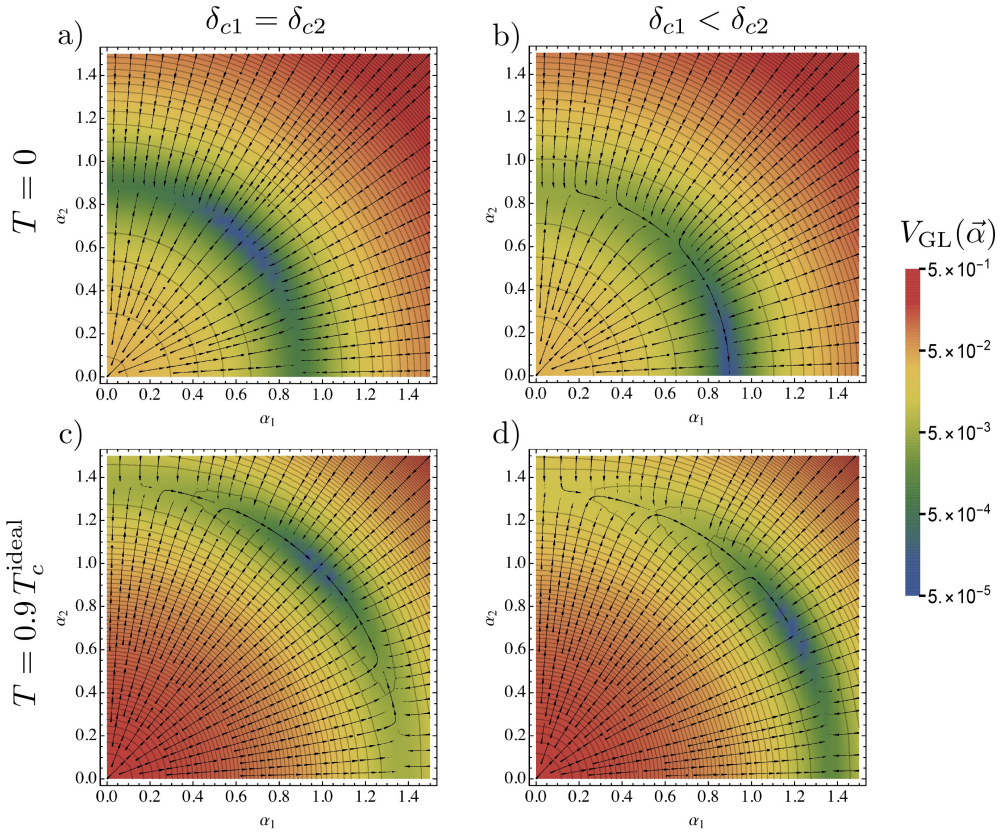

Figure 3.4: Ginzburg-Landau potential V_{GL} as a function of the cavity amplitudes. Arrows indicate the gradient. a),b) are for $T = 0$ while c),d) for $T = 0.9T_c^{\text{ideal}}$. a) and c) correspond to a symmetric configuration $\delta_{c_1} = \delta_{c_2}$, while b) and d) correspond to $\delta_{c_2} = 1.01\delta_{c_1}$. The remaining parameters are $\eta = 10$, $\epsilon_{\text{R}} = 8$ as well as $\lambda = 3$ in a), b) and $\lambda = 2.7$ in c),d). Notice the small curvature along the azimuthal direction.

On the contrary, for $\Delta_1 = \Delta_2$ the GL potential shows four degenerate minima at $\theta = \pm\pi/4, \pm 3\pi/4$. Since a $U(1)$ symmetric potential would show a degenerate minimum on a whole circle, we see that the extent to which this symmetry is explicitly broken is measured by the azimuthal curvature of the potential about any one of the four minima, which determines the square of the effective Goldstone mass. The latter, together with the associated effective Higgs mass, which corresponds to the square root of the curvature in the radial direction, is shown in Fig. 3.5 across the superradiant phase transition at zero and at finite temperature. In the disordered phase there is only a single collective mode in the radial direction with a mass vanishing at the critical point. Beyond this point Goldstone and Higgs mass separate, the latter growing much faster while the former remains at least

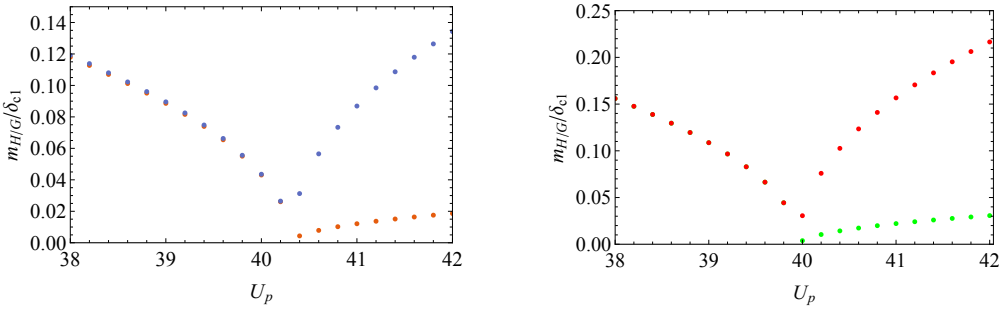

Figure 3.5: Goldstone and Higgs mass across the superradiant transition at $T = 0$(left) and $T = 0.5T_c^{\text{ideal}}$ (right). Parameters are the same as in Fig. 3.2 apart from $\lambda = 2.278$.

one order of magnitude smaller. By expanding the GL potential one can show that the Goldstone mass close to the critical point is proportional to $\sqrt{\alpha_1\alpha_2}$, in accordance with the arguments discussed in section 3.2.1. Moreover, the ratio between Goldstone mass and Higgs mass is inversely proportional to the drive strength, so that for the strong drive employed in experiment and considered in Fig. 3.5 we find a large separation between the Higgs and the Goldstone mass.

The qualitative behavior and the ratio of the Goldstone to Higgs mass shown in Fig. 3.5 is consistent with the experimental results of [2]. By contrast, the presence of a well-defined minimum in the GL potential in the range $0 < \theta < \pi/2$ of Fig. 3.4 is not compatible with the experimental finding [1] that θ is homogeneously distributed in this range. However, we can reconcile our prediction with the experiment by adding the noise induced by cavity losses to the picture. The probability of escaping the minimum and delocalizing across the circle in Fig. 3.4 is given by $P_{\text{deloc}} \approx \exp(-\sqrt{N_{\text{ph}}}\Delta V/\kappa)$, where $\Delta V \propto \alpha^4 \propto |\lambda - \lambda_c|^2$ is the depth of the minimum while κ is the cavity loss rate. Note that the noise is suppressed by a factor $1/\sqrt{N_{\text{ph}}}$ if we assume a coherent cavity field. With the experimental value $\kappa/2\pi \sim 200\,\text{kHz}$ and with $\Delta V \simeq |\Delta\epsilon|$ which is determined by the square of the Goldstone mass according to the first equality in Eq. (3.23), typical values $N_{\text{ph}} = |\alpha|^2 \sim 100$ lead to an escape probability of $P_{\text{deloc}} \simeq \exp(-0.02) \simeq 0.98$. We stress that our estimate for ΔV is an upper bound and thereby our escape probability provides a lower bound. A critical test for this scenario of a restoration of the $U(1)$ symmetry by cavity loss induced noise, is that with an increasing number of intracavity photons the escape probability is expected to decrease exponentially like

$$P_{\text{deloc}} \propto \exp(-N_{\text{ph}}^{5/2}) \,. \tag{3.31}$$

3.2.4 Effective action for low-energy excitations

In this final section we will discuss the nature of the low-energy excitations of the cavity field in the superradiant phase. For this purpose, we expand the effective action derived in section 3.2.2 up to quadratic order around the minima of the mean-field potential discussed in section 3.2.3. The resulting time-dependent deviations $a_i(\tau)$ can be expanded in terms of discrete Fourier-coefficients $a_{i,n}$ which determine the spectrum of light field fluctuations in the cavity. Thus, the effective Goldstone and Higgs mode appear explicitly, allowing to compute both their masses discussed above and - moreover - their damping or inverse lifetime which appears at finite temperature.

As described in section 3.2.2, in the thermodynamic limit the action (3.24) can be expanded up to quadratic order in the fluctuations. Since the coupling between atoms and the imaginary part of the cavity fields results solely in a dispersive shift, we can integrate out the imaginary part, generating only even powers in ω_n. At zero temperature the fluctuation part in dimensionless units is given by

$$S_{\text{eff}}{}^{(FL)}[a^R_{1,2}]\Big|_{T=0} = \sum_{n\neq 0}\sum_{i=1,2}\Bigg\{ \left(\omega_n^2+1\right) a^R_{i,n}a^R_{i,-n} + 4\sum_{j=1,2}\sum_{l}\frac{1}{i\omega_n-\epsilon_l(0)}\langle\Psi_0(0)|\frac{\partial V_{\text{sp}}}{\partial\alpha_i^*}|\Psi_l(0)\rangle\langle\Psi_l(0)|\frac{\partial V_{\text{sp}}}{\partial\alpha_j^*}|\Psi_0(0)\rangle a^R_{i,n}a^R_{j,-n}\Bigg\}\,, \tag{3.32}$$

where a_i^R is a real part of the cavity field and $|\Psi_l(k)\rangle$ is the atomic wave function with quasi-momentum k and band index l. This expression describes the scattering of atoms from the condensate to the Γ-point of an excited band in second order perturbation theory. Since these processes are far off-resonant with respect to the low energy excitations in the photon fields, they do not give rise to damping. The associated spectral functions are thus perfectly sharp. The picture gradually changes with increasing temperature, when more and more atoms occupy states near the edge of the Brillouin zone, where low energetic photons can be scattered resonantly. This effect can be accounted for by generalizing the effective action

through the inclusion of thermally occupied states

$$\begin{aligned} S_{\text{eff}}^{(FL)}[a_{1,2}^R] =& f_0 S_{\text{eff}}^{(FL)}[a_{1,2}^R]\Big|_{T=0} \\ &+ \sum_{j=1,2}\sum_{m,l} V \int \frac{d^3k}{4\pi^3} \langle \Psi_m(k)| \frac{\partial V_{\text{sp}}}{\partial \alpha_i^*} |\Psi_l(k)\rangle \langle \Psi_l(k)| \frac{\partial V_{\text{sp}}}{\partial \alpha_j^*} |\Psi_m(k)\rangle \\ &\qquad \times \frac{n_b(\epsilon_m(k)) - n_b(\epsilon_l(k))}{i\omega_n + \epsilon_m(k) - \epsilon_l(k)} a_{i,n}^R a_{j,-n}^R \\ \equiv& \sum_{n\neq 0}\sum_{i,j} \mathcal{G}(\omega_n)_{i,j} a_{i,n}^R a_{j,-n}^R \,, \end{aligned} \tag{3.33}$$

where f_0 is the condensate fraction. An important point is that, both at $T = 0$ and at finite temperature, the action involves only the real parts of the cavity fields and is thus an even function of ω. Therefore, it contains no linear terms of the form $i\hbar a^R(t)\partial_t a^R(t)$ which is characteristic for a BEC described by Gross-Pitaevskii dynamics and would give rise to equations of motion involving a reversible first order time derivative, where no proper Higgs mode exists [184]. Since the matrix elements respect the symmetry of the mean field action, the fluctuations can be diagonalized in terms of Goldstone and Higgs modes $a_G = -\sin\theta a_1^R + \cos\theta a_2^R$ and $a_H = \cos\theta a_1^R + \sin\theta a_2^R$. Upon expanding to second order in the frequency, we thus obtain the action

$$S_{\text{eff}}^{(FL)}[a_G, a_H] \approx \left(Z_G\omega_n^2 + m_G^2\right) a_{G,n} a_{G,-n} + \left(Z_H\omega_n^2 + m_H^2\right) a_{H,n} a_{H,-n} \tag{3.34}$$

with numerical coefficients that fulfill $m_G \ll m_H$, as well as $Z_{G,H} - 1 = \mathcal{O}(m_{G,H}/\epsilon_R)$ at small temperatures. From this action the existence of a (approximately) gapless Goldstone mode together with a strongly gapped Higgs mode is apparent.

As anticipated, at finite temperatures the Goldstone and Higgs modes experience losses via resonant Landau damping processes where a photon scatters against an atom while conserving energy and momentum. The resulting lifetimes as well as the masses of both excitations can be obtained from the spectral function $A(\omega) = 2\Im\mathcal{G}(-i\omega + 0^+)$ which can be measured via pump-probe experiments. The resulting spectra are shown in Fig. 3.6 for different temperatures[4]. For finite temperatures, there is additional structure in the tails of the Goldstone and Higgs peaks, which arises from van-Hove singularities at the edges of the Brillouin zones.

As shown in Fig. 3.6, the Goldstone mass increases strongly with temperature, an effect that cannot be observed in Fig. 3.5 for the mass obtained from the curvature of the mean field action at the global minimum. This is because in our expansion in fluctuations about the potential minima we do not allow atoms to redistribute. We are therefore effectively computing the behavior of photonic excitations at "high"

[4]Note that up to leading order in the frequency expansion the lifetime of the modes is infinite and we need to use the full action (3.33) in order to introduce damping.

frequencies with respect to the timescale of atomic redistribution. The inclusion of atomic redistribution beyond mean field would require a non-equilibrium approach like the one employed in Ref. [185]. This would allow to interpolate smoothly between the high frequency mass, as determined in $A(\omega)$, and the low frequency mass, obtained from the mean-field potential. However, since the atomic redistribution time is extensive in the number of atoms [185], we expect the Goldstone mass experimentally observable in large systems to correspond to the high-frequency mass measured by the spectral function.

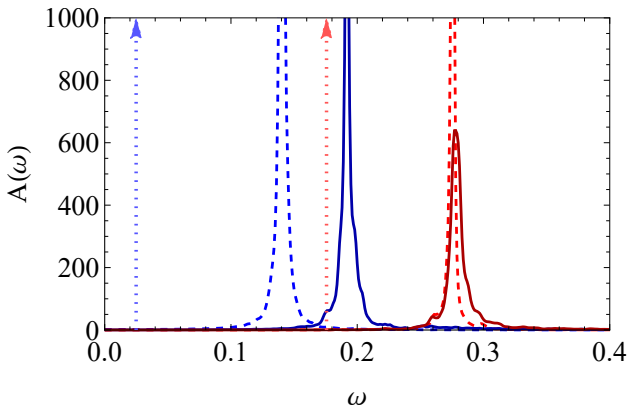

Figure 3.6: Low-energy excitation spectrum in the $\eta - \omega$ plane showing the Goldstone and Higgs peak with finite width close to the critical point. The temperatures and coupling strengths λ in order of increasing color saturation are $\{T, \lambda\} = \{0, 2.2\}$ (dotted arrows), $\{0.5, 2.3\}$ (dashed line) and $\{0.9, 2.2\}$ for the solid line.

The spectral function exhibits two distinct peaks which possess a nontrivial frequency but no momentum dependence. This is a consequence of the fact that the present double-cavity system is still an effectively zero-dimensional one. As a result, it does not give rise to a genuine spectrum of Goldstone modes usually associated with supersolids, where gauge and translation symmetry are broken simultaneously in a system with short-range interactions. For such a genuine supersolid, the total free energy can be written as an integral over a spatially varying free energy density $f(T, n, \mathbf{v}_s, \underline{u})$ which involves thermodynamic variables which vary continuously in space. In particular, the simultaneous presence of broken translation and gauge invariance leads to two additional contributions in the differential of the free energy density

$$df\big|_{T,n} = \mathbf{j}_s \cdot d\mathbf{v}_s + \mathrm{Tr}\,\underline{\sigma} \cdot d\underline{u}\,. \tag{3.35}$$

As discussed by Liu within a hydrodynamic approach [181], the term proportional to the superfluid current density $\mathbf{j}_s$ and its conjugate variable, the superfluid ve-

locity $\mathbf{v}_s = \frac{\hbar}{m}\nabla\phi$, results in a persistent mass flow for generic supersolids or dissipationless entropy flow in the absence of defects. Similarly, for the generic case of short-range interactions where the stress tensor $\underline{\sigma}$ is linearly proportional to the strain tensor $\underline{u}$, the second contribution gives rise to phonons whose frequency $\omega(\mathbf{q}) \sim |\mathbf{q}|$ vanishes linearly with the wave vector. Due to $\omega(\mathbf{q}) = \omega(\mathbf{q} + \mathbf{G})$ for regular crystals, this entails a vanishing Goldstone mass $\omega(\mathbf{q} = \mathbf{G}) = 0$ at reciprocal lattice vectors as a signature of the spontaneous breaking of translation invariance [180]. In the present system such a Goldstone mode also exists for the motion of atoms in the limit where m_G can be neglected. It is associated with the shift along the x-direction discussed in Eq. (3.18) and leads to $\omega(\mathbf{G}) = 0$ for all reciprocal lattice vectors $\mathbf{G} = n\mathbf{k}_1 + m\mathbf{k}_2$ with $n, m \in \mathbb{Z}$. In particular, the transverse acoustic phonon at $n = -m = \pm 1$ corresponds to the translation described in Eq. (3.18), which is related to the indirect exchange of a photon between the two cavities. In contrast to the standard situation, however, where the phonon frequencies approach zero continuously as $\mathbf{q}$ approaches 0, the long ranged nature of the interactions give rise to a finite energy gap at any $\mathbf{q} \neq \mathbf{G}$. The Goldstone mode thus exists only at isolated points in momentum space, with all other momenta being gapped.

3.2.5 Conclusions

In summary, we have studied the nature of broken symmetries, the effective Ginzburg-Landau potential and the spectrum of the light field in the double cavity setup realized recently at ETH [1, 2]. It has been shown that the emergent $U(1)$ invariance for symmetrically coupled cavities is slightly broken by higher order photon scattering processes. We have determined an upper bound for the resulting mass of the effective Goldstone mode which is consistent with the experimental results [2]. In addition, it has been shown that the ratio m_G/m_H between the Goldstone and Higgs mass vanishes in the limit of large driving amplitudes. As an experimentally testable prediction, we have determined the cavity noise induced escape probability from the global minimum of the effective potential as a function of the intracavity photon occupation which might be used for an indirect measurement of the Goldstone mass. Finally, the issue of dissipationless transport of particles in the double cavity supersolid has been discussed carefully and has been compared to the case of genuine supersolids, where this is associated with an additional true Goldstone mode.

Chapter 4

Interaction induced transparency

Following a short introduction into the Keldysh formalism for non-equilibrium field theories and electromagnetically induced transparency (EIT), we develop a systematic diagrammatic approach for strongly interacting photons in highly polarizable media far from equilibrium. We first discuss the limit of infinite range interactions, where we observe that the polaritons propagating under EIT conditions experience a first order phase transition between an opaque phase, characterized by high losses, and a transparent phase with long-lived excitations. We then study extensions to this approximation by inclusion of the leading corrections in the inverse interaction range. This chapter is heavily based on the recent publications [186, 187], from where most of the text and figures are taken.

4.1 Non-equilibrium field theory

Non-equilibrium quantum field theory is often viewed as exotic and exceedingly complicated. Most textbooks therefore only discuss equilibrium at finite temperatures [188, 189]. Superficially, there are good reasons to do so: The Keldysh formalism [190, 191, 192, 193], required to treat these problems, is indeed more involved than the Matsubara technique [194]. More importantly from a physical perspective, however, many solid state experiments (e.g. transport measurements) remain close to equilibrium at all times and are therefore well described by linear response theory [195]. More highly excited solid state systems, on the other hand, typically heat up and equilibrate very quickly. Thus, for a long time there was little necessity for a more involved and versatile approach. This comfortable situation changed at the latest with the advent of experiments in ultracold atomic gases [196] and mesoscopic [197] as well as optomechanical systems [198, 199]. While these systems allow to control the coupling to the environment very precisely, thereby enabling experimentalists to closely approximate equilibrium, specifically engineered non-equilibrium setups can be realized as well. Finally, beyond (non)linear response dynamics could be considered as too violent to be well described by diagrammatic quantum field theory, or at least, that only exceedingly short times are accessible. The reason behind this is secularity: If the exact solution to a simplified differential equation is known and the time evolution under an equation perturbed by some small modification $\sim \epsilon$ is sought after, the solution constructed following the

same rules as in stationary perturbation theory will, independent of the order of the expansion, only be reliable for times $t \ll 1/\epsilon$ [200, 201, 202]. Similarly, the steady state of a non-integrable system (if unique) is independent of the initial conditions (see also the eigenstate thermalization hypothesis [203, 204]). For this it is important, that the terms appearing in memory integrals during the time evolution can forget, i.e. they must be allowed to deviate from the initial state in a non-perturbative manner. Both of these issues can be dealt with by the self-consistent methods detailed below, where all corrections due to the perturbation of order ϵ are fully resummed [202]. We emphasize that these problems are by no means specific to diagrammatic quantum field theory. They are well known from the theory of differential equations and also arise in the Born approximation of the closely related Mori operator projection [205], where they have been addressed by a self-consistent approach as well [206].

4.1.1 Time contours

During the derivation of equilibrium field theory, there is a single simplification, that cannot be performed for generic out-of-equilibrium systems, thereby giving rise to the peculiarities of the Keldysh formalism. To see what goes wrong, we follow the book by Kamenev [197] and consider a system described by its density matrix $\hat{\rho}(t)$ and evolved in time from the infinite past, where $\rho(-\infty)$ is known, with the time-dependent Hamiltonian $\hat{H}(t)$ according to the von Neumann equation (throughout this chapter we set $\hbar = 1$)

$$\partial_t \hat{\rho}(t) = -i \left[\hat{H}(t), \hat{\rho}(t) \right] \ . \tag{4.1}$$

The expectation value of any operator $\hat{O}$ is calculated via

$$\langle \hat{O} \rangle(t) = \mathrm{Tr}\{ \hat{\mathcal{U}}_{-\infty,t} \hat{O} \hat{\mathcal{U}}_{t,-\infty} \hat{\rho}(-\infty) \} \ , \tag{4.2}$$

where the trace is performed over the Hilbert space and $\hat{\mathcal{U}}_{t,t'} = \mathcal{T} \exp\left(-i \int_{t'}^{t} d\tau \hat{H}(\tau) \right)$ is the time evolution operator from time t to t', with $\mathcal{T}$ denoting the time-ordering operator. Note in particular that $\hat{\mathcal{U}}_{-\infty,t}$ evolves the system backwards in time. In the zero-temperature formalism the expectation value is taken with respect to the ground state and the denominator is identical to one. In a perturbative expansion it is useful to split the Hamiltonian into a non-interacting and interacting part. Assuming a non-degenerate ground state, one can switch on the interacting part adiabatically between the distant past and the time t of the measurement. Reverting this process in the distant future, the system will return to the exactly known non-interacting ground state $|0\rangle$, picking up a phase factor e^{iL} in the process:

$$\hat{\mathcal{U}}_{+\infty,-\infty} |0\rangle = \mathrm{e}^{iL} |0\rangle \ . \tag{4.3}$$

We can use this to modify expectation values to only involve forward evolution

$$\langle \hat{O} \rangle(t) = \mathrm{e}^{-iL} \langle 0 | \hat{\mathcal{U}}_{+\infty,-\infty} \hat{\mathcal{U}}_{-\infty,t} \hat{O} \hat{\mathcal{U}}_{t,-\infty} | 0 \rangle = \frac{\langle 0 | \hat{\mathcal{U}}_{+\infty,t} \hat{O} \hat{\mathcal{U}}_{t,-\infty} | 0 \rangle}{\langle 0 | \hat{\mathcal{U}}_{+\infty,-\infty} | 0 \rangle} \,. \tag{4.4}$$

In zero-temperature field theory, this expression is then evaluated in the interaction picture, where the denominator cancels all contributions from disconnected Feynman diagrams. While the adiabatic switching of the interactions is not necessary for the derivation of the zero-temperature formalism [189], it is very useful to illustrate the limitations of equilibrium theory. Namely, if $H(t)$ itself has a non-adiabatic time-dependence, or if the system is coupled to a bath, it will not return to the non-interacting ground state in the distant future, even if adiabatic switching is used. Therefore, while (4.2) is completely general, (4.4) is highly specific. Already the slight modification of an initially degenerate state will in general not satisfy (4.3).

But what about finite-temperature field theory? Finite-temperature expectation values immediately give rise to the structure in (4.4) without any further input. For example in a canonical description one has

$$\langle \hat{O}(\tau) \rangle = \frac{\mathrm{Tr}\{ \mathcal{T}_\tau \mathrm{e}^{-\beta \hat{H}} \hat{O}(\tau) \}}{\mathrm{Tr}\{ \mathrm{e}^{-\beta \hat{H}} \}} \,, \tag{4.5}$$

where τ is an imaginary time, $\mathcal{T}_\tau$ the corresponding imaginary time-ordering operator and the evolution is restricted to the interval $0 < \tau < \beta$. Apart from this rotation in the complex plane, imaginary-time expectation values are evaluated in the same manner as in the zero-temperature formalism. In particular, the partition function $Z = \mathrm{Tr}\{\exp(-\beta \hat{H})\}$ in the denominator cancels the disconnected diagrams. While in general any density matrix can be written as a thermal state of an appropriate Hamiltonian [207], no time evolution with any other Hamiltonian is possible. In fact, real-time correlation functions have to be extracted via analytic continuation, which is only possible because of the similar functional dependence on $\hat{H}$ of the thermal statistical operator and the time evolution operator, and is a topic in its own right [208, 209].

We conclude, that any non-equilibrium system has to be evolved forward *and* backward in time. This could have been anticipated, given the same structure of the formal solution to the von Neumann equation $\hat{\rho}(t) = \hat{\mathcal{U}}_{t,0} \hat{\rho}(0) \hat{\mathcal{U}}_{0,t}$. There are, however, a few choices and generalizations suitable to treat different initial states. So far we have initialized the system in the infinite past. This so-called Schwinger-Keldysh contour $\mathcal{C}$ [190, 193] is ideal to describe stationary states and late-time dynamics, as these are largely independent of the initial state. In general, if short-time dynamics after some type of quench are of interest, it is more convenient to begin time evolution at the same time as the quench (say $t = 0$). This is simply achieved by replacing $t = -\infty$ by $t = 0$ in Eq. (4.2). The resulting path

is sometimes referred to as closed time contour [210]. Introducing this boundary, can complicate the equations of motion and therefore initial states are in practice limited to Gaussian density matrices [202]. One can however go significantly beyond this and use thermal initial states by appending a path along the negative imaginary axis to the contour. This most general contour given by

$$\langle \hat{O} \rangle(t) = \frac{\mathrm{Tr}\{\hat{\mathcal{U}}_{-i\beta,0}\hat{\mathcal{U}}_{0,t}\hat{O}\hat{\mathcal{U}}_{t,0}\}}{\mathrm{Tr}\{\hat{\mathcal{U}}_{-i\beta,0}\}} , \tag{4.6}$$

was first introduced by Kadanoff and Baym [192] and carries their names. By using an appropriate Hamiltonian along the imaginary stretch, in principle any initial state can be prepared, albeit possibly requiring an insurmountable effort [207]. For the remainder of this thesis, we will only be interested in the steady state and late-time dynamics and consequently exclusively deal with the Schwinger-Keldysh contour.

To simplify notation, we label the contour-ordered time evolution operator by $\hat{\mathcal{U}}_{\mathcal{C}} = \hat{\mathcal{U}}_{-\infty,+\infty}\hat{\mathcal{U}}_{+\infty,-\infty} = 1$ and summarize the evaluation of expectation values on the Schwinger-Keldysh contour Fig. 4.1 as

$$\langle \hat{O} \rangle(t) = \mathrm{Tr}\{\hat{\mathcal{U}}_{-\infty,+\infty}\hat{\mathcal{U}}_{+\infty,t}\hat{O}\hat{\mathcal{U}}_{t,-\infty}\hat{\rho}(-\infty)\} . \tag{4.7}$$

So far, we have focused on the comparison with equilibrium field theory and therefore have not yet considered systems in contact with a bath. However, since the derivation of the Schwinger-Keldysh contour required no approximations and instead only relied on the group property of the evolution operator

$$\hat{\mathcal{U}}_{t,t'} = \hat{\mathcal{U}}_{t,t''}\,\hat{\mathcal{U}}_{t'',t'} , \tag{4.8}$$

the same rules apply to any (deterministic) time evolution, with $\hat{\mathcal{U}}_{\mathcal{C}}$ in open systems replaced by a superoperator acting on the density matrix.

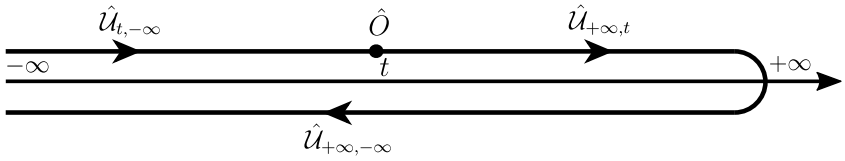

Figure 4.1: Evaluation of the expectation value $\langle \hat{O}(t) \rangle$ on the Schwinger-Keldysh contour.

4.1.2 Green's functions

On the Schwinger-Keldysh contour (see Fig. 4.1) two-point correlation functions of the field creation and annihilation operators $\hat{\phi}^\dagger(x)$ and $\hat{\phi}(x)$ with the shorthand notation $x = \{\mathbf{x}, t\}$ differ, depending on whether x is chosen on the upper or lower branch. Postponing the discussion of anomalous Green's functions to Sec. 4.7.2, we introduce the lesser and greater single-particle Green's functions or propagators

$$\begin{aligned} G^<(x,x') &= -i\langle \hat{\phi}_+(x)\hat{\phi}_-^\dagger(x')\rangle \\ G^>(x,x') &= -i\langle \hat{\phi}_-(x)\hat{\phi}_+^\dagger(x')\rangle = -[G^<(x',x)]^* \ , \end{aligned} \tag{4.9}$$

where $(\cdot)^*$ is the complex conjugation and the index $+(-)$ indicates the choice of upper – and therefore earlier – or lower and later branch. Moreover, we define the time-ordered (upper index $\mathcal{T}$) and anti-ordered (upper index $\bar{\mathcal{T}}$) Green's functions

$$\begin{aligned} G^{\mathcal{T}}(x,x') &= -i\langle \hat{\phi}_+(x)\hat{\phi}_+^\dagger(x')\rangle = \theta(t-t')G^>(x,x') + \left[1-\theta(t-t')\right] G^<(x,x') \\ G^{\bar{\mathcal{T}}}(x,x') &= -i\langle \hat{\phi}_-(x)\hat{\phi}_-^\dagger(x')\rangle = \theta(t'-t)G^>(x,x') + \left[1-\theta(t'-t)\right] G^<(x,x') \ , \end{aligned} \tag{4.10}$$

where the Heaviside theta function is chosen with $\theta(0) = 1$ [197]. The physical interpretation of these Green's functions and their relations is not very intuitive. We therefore introduce *classical* and *quantum* fields

$$\begin{aligned} \hat{\phi}_{\mathrm{cl}}(x) &= \frac{1}{\sqrt{2}}\left(\hat{\phi}_+(x) + \hat{\phi}_-(x')\right) \\ \hat{\phi}_{\mathrm{q}}(x) &= \frac{1}{\sqrt{2}}\left(\hat{\phi}_+(x) - \hat{\phi}_-(x')\right) \ , \end{aligned} \tag{4.11}$$

which allow to express the retarded Green's function in the simple form

$$G^R(x,x') = -i\theta(t-t')\left\langle\left[\hat{\phi}(x), \hat{\phi}^\dagger(x')\right]\right\rangle = \left\langle \hat{\phi}_{\mathrm{cl}}(x)\hat{\phi}_{\mathrm{q}}^\dagger(x')\right\rangle \ . \tag{4.12}$$

Additionally, we define the Keldysh Green's function by

$$G^K(x,x') = -i\left\langle\left\{\hat{\phi}(x), \hat{\phi}^\dagger(x')\right\}\right\rangle = \left\langle \hat{\phi}_{\mathrm{cl}}(x)\hat{\phi}_{\mathrm{cl}}^\dagger(x')\right\rangle \ . \tag{4.13}$$

Here, as will be the case throughout the remainder of this thesis, we restrict our discussion to Bosons, as no fermionic models will be treated. It is convenient to collect these propagators, together with the advanced component G^A in the 2×2

matrix Green's function

$$\begin{aligned}\mathcal{G}(x,x') &= -i\begin{pmatrix}\langle\hat{\phi}_{\rm cl}(x)\hat{\phi}^\dagger_{\rm cl}(x')\rangle & \langle\hat{\phi}_{\rm cl}(x)\hat{\phi}^\dagger_{\rm q}(x')\rangle\\ \langle\hat{\phi}_{\rm q}(x)\hat{\phi}^\dagger_{\rm cl}(x')\rangle & \langle\hat{\phi}_{\rm q}(x)\hat{\phi}^\dagger_{\rm q}(x')\rangle\end{pmatrix}\\ &= \begin{pmatrix}G^K(x,x') & G^R(x,x')\\ G^A(x,x') & 0\end{pmatrix}.\end{aligned} \tag{4.14}$$

We notice, that the quantum-quantum propagator vanishes. In fact, only classical field operators can have finite expectation values. The antisymmetric quantum fields then characterize the fluctuations around the classical solution. We will extend upon this argument in the context of classical stochastic models (cf. Sec. 4.1.4). Clearly the advanced propagator G^A is related to the retarded Green's function. In fact, one finds

$$G^A(x,x') = \left[G^R(x',x)\right]^* \tag{4.15}$$

as well as an antihermitian structure for the Keldysh component

$$G^K(x,x') = -\left[G^K(x',x)\right]^* . \tag{4.16}$$

While we will stick to these definitions, some authors prefer to work with the statistical function $F(x,x') = G^K(x,x')/2$ and spectral function

$$\rho(x,x') = i(G^R(x,x') - G^A(x,x')) , \tag{4.17}$$

which satisfies the normalization $\rho(x,x) = 1$ and for scalar fields also $\rho(x,x') = -2\Im(G^R(x,x'))$. We will instead use F to denote the distribution function defined as the hermitian solution to

$$G^K(x,x') = \int_{x''} G^R(x,x'')F(x'',x') - F(x,x'')G^A(x'',x') . \tag{4.18}$$

It is worthwhile to take a look back at the finite-temperature formalism. In equilibrium, the Kubo-Martin-Schwinger theorem [195, 211] relates the greater and lesser Green's functions

$$G^>(\omega,\mathbf{p}) = e^{\beta\omega}G^<(\omega,\mathbf{p}) . \tag{4.19}$$

Consequently, G^K is not independent of G^R, but rather satisfies

$$G^K(\omega,\mathbf{p}) = 2i\left(2n_B(\omega)+1\right)G^R(\omega,\mathbf{p}) , \tag{4.20}$$

where $n_B(\omega)$ is the Bose distribution. With the distribution function F fixed to $F = 2n_B + 1$, there is no need for a Keldysh contour, instead one can enforce the Kubo-Martin-Schwinger condition by using Green's functions in imaginary time

with periodicity β, which brings us back to the well-known Matsubara approach with the imaginary-time Green's function $G(\omega_m, \mathbf{p}) = \theta(m)G^R(i\omega_m, \mathbf{p}) + (1 - \theta(m))G^A(i\omega_m, \mathbf{p}) = [G(-\omega_m, \mathbf{p})]^*$ [189] defined on bosonic Matsubara frequencies $\omega_m = 2m\pi/\beta$ fixed by the periodicity $\beta = (k_B T)^{-1}$. It is in fact the Kubo-Martin-Schwinger relation that allows to prove Wick's theorem for imaginary-time Green's functions [188].

4.1.3 Diagrammatic field theory

With the basic definitions in place, we can now tackle the description of an interacting system. First of all, for any, possibly open and interacting, system we can introduce the partition function

$$Z = \mathrm{Tr}\{\hat{\mathcal{U}}_{\mathcal{C}}\hat{\rho}(-\infty)\} = 1 \,. \tag{4.21}$$

As we have mentioned before, the analogous property is not true in the standard zero-temperature formalism. Despite its simplicity, we can still use the partition function to define the generating functional as the partition function obtained from the time evolution perturbed by an operator $\hat{O}$ that couples to a field $J(t)$. Since this field can act on both branches of the Schwinger-Keldysh contour, we can split it into a symmetric (classical) and antisymmetric (quantum) part $\hat{H} \to \hat{H} + \hat{O}_+ J_+(t) - \hat{O}_- J_-(t) = \hat{H} + \hat{O}_{\mathrm{q}} J_{\mathrm{cl}}(t) + \hat{O}_{\mathrm{cl}} J_{\mathrm{q}}(t)$. Note, that the minus sign on the backward branch of the contour is an immediate consequence of the reversed direction of the time evolution. Denoting the perturbed evolution (super)operator by $\hat{\mathcal{U}}_{\mathcal{C}}[J_{\mathrm{cl}}, J_{\mathrm{q}}]$, the generating functional is simply given by

$$Z[J_{\mathrm{cl}}, J_{\mathrm{q}}] = \mathrm{Tr}\{\hat{\mathcal{U}}_{\mathcal{C}}[J_{\mathrm{cl}}, J_{\mathrm{q}}]\hat{\rho}(-\infty)\} \,. \tag{4.22}$$

It is convenient to write the generating functional as a path integral over coherent states. The procedure for doing so is very similar to that of the equilibrium coherent state path integral and we will therefore only provide a brief summary, highlighting the role of the time contour $\mathcal{C}$ and the effect of an interaction with a bath. For a more detailed derivation see Ref. [44].

Let us consider a system with Hamiltonian H coupled to a Markovian bath by a Lindblad operator L. Its time evolution is described by the Liouvillian $\mathcal{L}$, which acts on the density matrix as a superoperator:

$$\partial_t \rho = \mathcal{L}\rho = -i[H, \rho] + \left(L\rho L^\dagger - \frac{1}{2}\left\{ L^\dagger L, \rho \right\} \right) . \tag{4.23}$$

Following the same procedure as in equilibrium, we now introduce a resolution of unity in terms of coherent states $|\phi\rangle$, defined as the eigenstates of the annihilation

operator ($\hat{\phi}|\phi\rangle = \phi|\phi\rangle$), which reads

$$\mathbb{1} = \int \frac{d\phi d\phi^*}{\pi} \mathrm{e}^{-\phi^*\phi} |\phi\rangle\langle\phi| \,. \tag{4.24}$$

In this basis, the density matrix at time t_n can be expressed as

$$\rho(t_n) = \int \frac{d\phi_{+,n} d\phi^*_{+,n}}{\pi} \frac{d\phi_{-,n} d\phi^*_{-,n}}{\pi} \mathrm{e}^{-\phi^*_{+,n}\phi_{+,n} - \phi^*_{-,n}\phi_{-,n}} \langle\phi_{+,n}|\rho(t_n)|\phi_{-,n}\rangle |\phi_{+,n}\rangle\langle\phi_{-,n}| \,. \tag{4.25}$$

Note that, as opposed to the zero-temperature formalism, where a pure state is evolved in time, we had to introduce two unities, one to the left and the other to the right of the density matrix. Using that for coherent states normal ordered matrix elements are simply evaluated by replacing the operators $\hat{\phi}$ and $\hat{\phi}^\dagger$ by fields ϕ and ϕ^* – as in $\langle\phi'|f(\hat{\phi},\hat{\phi}^\dagger)|\phi\rangle = f(\phi'^*,\phi)$ – one finds the density matrix at the infinitesimally later time $t_{n+1} = t_n + \delta t$ to be given by

$$\begin{aligned} \langle\phi_{+,n+1}|\rho(t_{n+1})|\phi_{-,n+1}\rangle = \int \frac{d\phi_{+,n} d\phi^*_{+,n}}{\pi} \frac{d\phi_{-,n} d\phi^*_{-,n}}{\pi} \langle\phi_{+,n}|\rho(t_n)|\phi_{-,n}\rangle \\ \times \mathrm{e}^{i\delta t\left(-\phi_{+,n} i\partial_t \phi^*_{+,n} - \phi^*_{-,n} i\partial_t \phi_{-,n} - i\mathcal{L}(\phi_{\pm,n},\phi^*_{\pm,n})\right)} \,. \end{aligned} \tag{4.26}$$

Here, we have used Eq. (4.23) and neglected higher orders in δt, which has allowed us to reexponentiate the time evolution in the second line. Again, since the Liouvillian $\mathcal{L}$ acts on ρ from both sides, this representation requires us to define the supermatrixelement

$$\mathcal{L}(\phi_{\pm,n},\phi^*_{\pm,n}) = \langle\phi_{+,n+1}|\mathcal{L}\left(|\phi_{+,n}\rangle\langle\phi_{-,n}|\right)|\phi_{-,n+1}\rangle \,. \tag{4.27}$$

Repeating this procedure along the entire time contour with a complex field $\phi(x)$ coupled to the source $J(x)$ provides us with the path integral formulation of the generating functional

$$Z[J_{\mathrm{cl}},J_{\mathrm{q}}] = \int \mathbf{D}[\phi_{\mathrm{cl}},\phi_{\mathrm{q}}] \mathrm{e}^{iS[\phi_{\mathrm{cl}},\phi_{\mathrm{q}}] + \left(\int dx J^*_{\mathrm{cl}}(x)\phi_{\mathrm{q}}(x) + J^*_{\mathrm{q}}(x)\phi_{\mathrm{cl}}(x) + \mathrm{c.c.}\right)} \,. \tag{4.28}$$

with the Keldysh action

$$S[\phi_+,\phi_-] = \int_{-\infty}^{\infty} dt \left(\phi^*_+ i\partial_t\phi_+ - \phi^*_- i\partial_t\phi_- - i\mathcal{L}(\phi_\pm,\phi^*_\pm)\right) \,. \tag{4.29}$$

We point out the reversed time evolution along the backwards branch, evidenced

by the negative sign of the second term. Following a Keldysh rotation this becomes

$$S[\phi_{\rm cl},\phi_{\rm q}] = \int_{-\infty}^{\infty} dt \left\{ \phi^*_{\rm cl} i\partial_t \phi_{\rm q} + \phi^*_{\rm q} i\partial_t \phi_{\rm cl} - i\mathcal{L}\left[\frac{1}{\sqrt{2}}\left(\phi_{\rm cl}\pm\phi_{\rm q}\right), \frac{1}{\sqrt{2}}\left(\phi_{\rm cl}\pm\phi_{\rm q}\right)^* \right] \right\} . \tag{4.30}$$

Assuming that $\mathcal{L}$ is normal ordered a simple construction emerges: The Keldysh action is obtained by replacing operators acting from the left (right) on ρ by fields on the forward (backward) branch of $\mathcal{C}$. In particular, for the Markovian example considered in (4.23) one finds

$$\mathcal{L}(\phi_{\pm,n},\phi^*_{\pm,n}) = i\left(H_- - H_+\right) + \left[L_+ L_-^* - \frac{1}{2}\left(L_+^* L_+ + L_-^* L_- \right) \right] , \tag{4.31}$$

where $H_{+,(-)}$ and $L_{+,(-)}$ depend only on fields on the forward (backward) branch.

In any field theory, except for the highly specific case of a zero-dimensional classical field, expectation values of arbitrary operators can only be evaluated exactly for actions that are linear or quadratic in ϕ. This is to say that any interaction terms will have to be treated in some approximation. We thus split the action into a non-interacting quadratic part S_0 and an interaction part $S_{\rm int}$. In general – potentially after a suitable shift of the field $\boldsymbol{\phi}(x) = (\phi_{\rm cl}(x),\phi_{\rm q}(x))^T$ – we can parametrize the former as

$$S_0 = i\int dx \int dx' \boldsymbol{\phi}^*(x) A(x,x') \boldsymbol{\phi}(x') , \tag{4.32}$$

where $A(x,x')$ is a 2×2 matrix. The generating functional then evaluates to

$$Z[\mathbf{J}^*,\mathbf{J}] = \frac{\mathrm{e}^{\int dx \int dx' \mathbf{J}^*(x) A^{-1}(x,x') \mathbf{J}(x')}}{\det A} , \tag{4.33}$$

where we have introduced $\mathbf{J}(x) = (J_{\rm cl}(x), J_{\rm q}(x))^T$. Moreover $A^{-1}(x,x')$ denotes the inverse of $A(x,x')$ with respect to the indices $\{a,b\}\in\{\mathrm{cl},\mathrm{q}\}$ and the coordinates x and x'. Using the fact that $Z[0,0]=1$, we find that the denominator is equal to unity. This result now allows to calculate the expectation value

$$\langle \hat{\phi}_a(x) \hat{\phi}^\dagger_b(x') \rangle = \left. \frac{\delta^2 Z[J^*_{\rm cl}, J_{\rm q}]}{\delta J_a \delta J_b} \right|_{\mathbf{J}=0} = \left[A^{-1} \right]_{a,b}(x,x') . \tag{4.34}$$

Comparison with (4.14) yields the identification $A(x,x') = -i\mathcal{G}^{-1}(x,x')$. In a translational invariant system in equilibrium, the propagator will depend only on $x-x'$ and the inversion is trivial. In a general non-equilibrium setting, however, it can become a formidable (numerical) challenge. Following the same procedure, all expectation values of higher powers of the fields factorize into products of bare Green's functions as well. Of course, this is nothing else than Wick's theorem,

which therefore holds even in a non-equilibrium situation, provided the associated effective action is quadratic.

Let us, as an example, consider the contact interaction

$$\begin{aligned} S_{\text{int}} &= -\frac{g}{2}\int dx \left[\left(\phi_+^*(x)\phi_+(x)\right)^2 - \left(\phi_-^*(x)\phi_-(x)\right)^2\right] \\ &= -\frac{g}{2}\int dx \left[\phi_{\text{cl}}^*(x)\phi_{\text{cl}}^*(x)\phi_{\text{cl}}(x)\phi_{\text{q}}(x) + \phi_{\text{cl}}^*(x)\phi_{\text{q}}^*(x)\phi_{\text{q}}(x)\phi_{\text{q}}(x) + \text{c.c.}\right] . \end{aligned} \tag{4.35}$$

Note, that any unitary time evolution will in general be antisymmetric on the forward and backward branch, which becomes apparent from the relative sign in the first term in Eq. (4.31). As a consequence, there is necessarily an odd number of quantum fields involved in each scattering process. We will distinguish between *classical* vertices, involving a single quantum field, and *quantum* vertices with three or more. Following the separation of the action into S_0 and S_{int}, the propagator of the interacting system is now accessible via perturbation theory:

$$\mathcal{G}(x,x') = -i\int \mathbf{D}[\boldsymbol{\phi}^*,\boldsymbol{\phi}]\boldsymbol{\phi}^*(x)\boldsymbol{\phi}^T(x')\left(1 + iS_{\text{int}}[\boldsymbol{\phi}^*,\boldsymbol{\phi}] + \mathcal{O}(S_{\text{int}}^2)\right)\mathrm{e}^{iS_0[\boldsymbol{\phi}^*,\boldsymbol{\phi}]} . \tag{4.36}$$

The first term is just the bare propagator $\mathcal{G}_0$ and when evaluating the others, we notice, that all expectation values $\langle S_{\text{int}}^n[\hat{\boldsymbol{\phi}}^\dagger,\hat{\boldsymbol{\phi}}]\rangle_{S_0}$ with some power $n \in \mathbb{N}$ vanish. This is a direct consequence of $Z = 1$, which is true with and without interactions. Thus, we recover, that indeed Z is the generating functional of all *connected* diagrams. Clearly, this is equivalent to $W[\mathbf{J}^*,\mathbf{J}] = \ln\left(Z[\mathbf{J}^*,\mathbf{J}]\right)$, but – as opposed to equilibrium field theory – here the logarithm is not necessary. In particular, in the context of disordered systems, this is an important simplification [197] that is also found in the closely related Feynman-Vernon theory [212, 213]. We exemplify this with the one-loop correction

$$\begin{aligned} &G^R{}_{1\text{ loop}}(x,x') - G_0^R(x,x') \\ &= -\frac{g}{2}\int \mathbf{D}[\boldsymbol{\phi}^*,\boldsymbol{\phi}]\phi_{\text{cl}}(x)\phi_{\text{q}}^*(x')S_{\text{int}}[\boldsymbol{\phi}^*,\boldsymbol{\phi}]\mathrm{e}^{-iS_0[\boldsymbol{\phi}^*,\boldsymbol{\phi}]} \\ &= -g\int dy\ \langle\hat{\phi}_{\text{q}}^\dagger(x')\hat{\phi}_{\text{cl}}(y)\rangle\left[\langle\hat{\phi}_{\text{cl}}^\dagger(y)\hat{\phi}_{\text{cl}}(x)\rangle\left(\langle\hat{\phi}_{\text{cl}}^\dagger(y)\hat{\phi}_{\text{q}}(y)\rangle + \langle\hat{\phi}_{\text{q}}^\dagger(y)\hat{\phi}_{\text{cl}}(y)\rangle\right)\right. \\ &\qquad\left. + \langle\hat{\phi}_{\text{q}}^\dagger(y)\hat{\phi}_{\text{cl}}(x)\rangle\langle\hat{\phi}_{\text{cl}}^\dagger(y)\hat{\phi}_{\text{cl}}(y)\rangle\right] - \frac{g}{2}\langle\hat{\phi}_{\text{q}}^\dagger(x')\hat{\phi}_{\text{cl}}(x)\rangle\langle S_{\text{int}}\rangle \\ &= ig\int dy\ G^R(y,x')\left[G^K(x,y)\left(G^A + G^R\right)(y,y) - G^R(x,y)\left(G^K(y,y) + i\right)\right] \\ &= ig\int dy\ G^R(x,y)G^R(y,x')\left[G^K(y,y) + i\right] , \end{aligned} \tag{4.37}$$

where the second equality follows from the application of Wick's theorem and the

observation that $\langle\hat{\phi}_{\mathrm{q}}^{\dagger}\hat{\phi}_{\mathrm{q}}\rangle = 0$. Note that the prefactor can either be derived from the symmetry factors, or by directly collecting all contractions. We subsequently have used $Z = 1$ to remove the last (disconnected) term $\sim \langle S_{\mathrm{int}}\rangle$ and in the last line employed Eqs. (4.9) and (4.10) to conclude that at equal times $G^R(x,x) = -G^A(x,x)$. Note, that the commutation relations

$$\left[\hat{\phi}_\alpha(x), \hat{\phi}_\beta^{\dagger}(x')\right] = \delta_{\alpha,\beta}\delta(x,x') \tag{4.38}$$

where $\{\alpha,\beta\} \in \{\mathrm{q},\mathrm{cl}\}$ have to be considered when identifying the normal ordered expectation values with Green's functions. Here this gives rise to subtraction of the vacuum value $G^K_{\mathrm{vac}}(y,y) = 1$ and in equilibrium it is responsible for the reverse propagation direction of the Green's function in the Hartree loop. Nevertheless, this effect had not been taken into account in the initial paper using the Keldysh formalism on the open Dicke model [214]. A similar calculation as in (4.37) finds

$$\begin{aligned}
&G^K{}_{1\text{ loop}}(x,x') - G_0^K(x,x') \\
&\quad= -\frac{g}{2}\int \mathbf{D}[\boldsymbol{\phi}^*,\boldsymbol{\phi}]\phi_{\mathrm{cl}}(x)\phi^*_{\mathrm{cl}}(x')S_{\mathrm{int}}[\boldsymbol{\phi}^*,\boldsymbol{\phi}]\mathrm{e}^{-iS_0[\boldsymbol{\phi}^*,\boldsymbol{\phi}]} \\
&\quad= -g\int dy\ \Big[\langle\hat{\phi}^{\dagger}_{\mathrm{cl}}(x')\hat{\phi}_{\mathrm{q}}(y)\rangle\langle\hat{\phi}^{\dagger}_{\mathrm{cl}}(y)\hat{\phi}_{\mathrm{cl}}(x)\rangle\langle\hat{\phi}^{\dagger}_{\mathrm{cl}}(y)\hat{\phi}_{\mathrm{cl}}(y)\rangle \\
&\qquad\qquad +\langle\hat{\phi}^{\dagger}_{\mathrm{cl}}(x')\hat{\phi}_{\mathrm{cl}}(y)\rangle\langle\hat{\phi}^{\dagger}_{\mathrm{cl}}(y)\hat{\phi}_{\mathrm{cl}}(x)\rangle\left(\langle\hat{\phi}^{\dagger}_{\mathrm{q}}(y)\hat{\phi}_{\mathrm{cl}}(y)\rangle + \langle\hat{\phi}^{\dagger}_{\mathrm{cl}}(y)\hat{\phi}_{\mathrm{q}}(y)\rangle\right) \\
&\qquad\qquad +\langle\hat{\phi}^{\dagger}_{\mathrm{cl}}(x')\hat{\phi}_{\mathrm{q}}(y)\rangle\langle\hat{\phi}^{\dagger}_{\mathrm{q}}(y)\hat{\phi}_{\mathrm{cl}}(x)\rangle\left(\langle\hat{\phi}^{\dagger}_{\mathrm{q}}(y)\hat{\phi}_{\mathrm{cl}}(y)\rangle + \langle\hat{\phi}^{\dagger}_{\mathrm{cl}}(y)\hat{\phi}_{\mathrm{q}}(y)\rangle\right) \\
&\qquad\qquad +\langle\hat{\phi}^{\dagger}_{\mathrm{cl}}(x')\hat{\phi}_{\mathrm{cl}}(y)\rangle\langle\hat{\phi}^{\dagger}_{\mathrm{q}}(y)\hat{\phi}_{\mathrm{cl}}(x)\rangle\langle\hat{\phi}^{\dagger}_{\mathrm{cl}}(y)\hat{\phi}_{\mathrm{cl}}(y)\rangle\Big] - \frac{g}{2}\langle\hat{\phi}^{\dagger}_{\mathrm{cl}}(x')\hat{\phi}_{\mathrm{cl}}(x)\rangle\langle S_{\mathrm{int}}\rangle \\
&\quad= ig\int dy\ \left[G^R(x,y)G^K(y,x') + G^K(x,y)G^A(y,x')\right]\left[G^K(y,y) + i\right]\ .
\end{aligned} \tag{4.39}$$

Furthermore, the property $[\mathcal{G}_0]_{22} \equiv 0$ results in the same property for the dressed Green's function to all orders in the coupling strength g. Clearly these calculations are unpleasant because of the combinatorics related to the causality indices q and cl. The same problem also arises with anomalous Green's functions, that appear in phases with broken particle-number conservation symmetry, and so it is useful to proceed along the same lines as one would for a Nambu structure. In particular, we introduce the graphical representation in Fig. 4.2 for the Green's functions. We can then identify the one-loop result (4.37) with Fig. 4.3 and conclude simple rules relating diagrams of identical topology, but differing in internal causality indices. The resulting cancellations between diagrams, together with the Kramers-Kronig relations 4.4.3 are of paramount importance to the practical applicability of the Keldysh formalism for pen-and-paper calculations.

In general, after having canceled all disconnected diagrams, we can formally

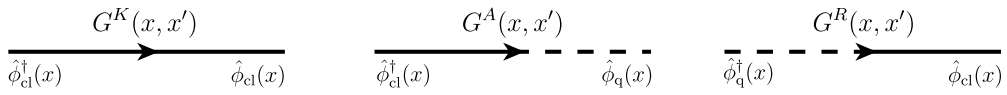

Figure 4.2: The widely used graphical representation of the non-vanishing components of the Green's function $\mathcal{G}$ is obtained by identifying classical propagators with full lines and quantum propagators with dashed lines. Both retarded and advanced Green's function change the character of the field during propagation. Note, that this notation is consistent with [188], but differs from [197].

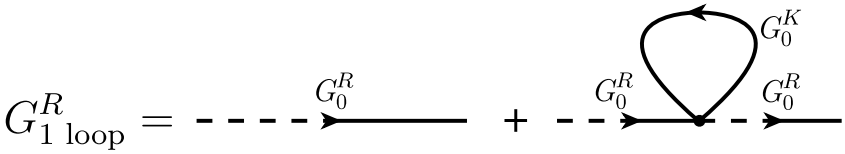

Figure 4.3: In linear order in the coupling strength g the retarded Green's function is shifted by a frequency and momentum independent Hartree shift that is proportional to the density $n(x) = (iG^K(x,x) - 1)/2$.

rearrange the perturbation series by collecting all one-particle irreducible (1PI) diagrams into a self-energy matrix

$$\Sigma(x,x') = \begin{pmatrix} 0 & \Sigma^A(x,x') \\ \Sigma^R(x,x') & \Sigma^K(x,x') \end{pmatrix} . \tag{4.40}$$

By definition it includes only those diagrams, that do not become disconnected, when cutting a single line. In our simple example, we identify

$$\Sigma^R_{1\text{ loop}}(x,x') = g\left(iG^K(x,x') - 1\right)\delta(x-x') \quad \text{and} \quad \Sigma^K_{1\text{ loop}}(x,x') = 0 . \tag{4.41}$$

One can easily confirm, that $\Sigma(x,x')$ always has the same causality structure as $\mathcal{G}(x,x')$ and consequently satisfies

$$\Sigma^R(x,x') = \left[\Sigma^A(x',x)\right]^* \sim \theta(t-t') \quad \text{and} \quad \Sigma^K(x,x') = -\left[\Sigma^K(x',x)\right]^* . \tag{4.42}$$

The full propagator can then be viewed as the sum of all chains of self-energies, joined by bare Green's functions $\mathcal{G}_0$, where, due to the 1PI construction of the self-energy, no duplicates appear. One therefore ends up with the Dyson series

$$\mathcal{G} = \mathcal{G}_0 + \mathcal{G}_0 \circ \Sigma \circ \mathcal{G}_0 + \mathcal{G}_0 \circ \Sigma \circ \mathcal{G}_0 \circ \Sigma_\circ \mathcal{G}_0 + \dots , \tag{4.43}$$

where $\circ$ denotes the convolution in space and time with a simultaneous matrix

product in the Keldysh index $\{\mathrm{cl}, \mathrm{q}\}$. Summation of this geometric series for the retarded Green's function gives the same result as in equilibrium theory

$$G^R = \left(G_0^R - \Sigma^R\right)^{-1} . \tag{4.44}$$

For the Keldysh component however one finds

$$G^K = G^R \circ \left(\Sigma^K - D_0^K\right) \circ G^A , \tag{4.45}$$

with $D_0^K = \left(\mathcal{G}_0^{-1}\right)_{2,2}$. In a perturbative treatment, one can simply plug the bare propagator $\mathcal{G}_0$ into the self-energy and obtain the dressed Green's function. However, as we had briefly mentioned before, this amounts to a step-wise augmentation of an approximate solution to a differential equation, which runs into problems with secularity and non-universal steady states. One can avoid both of these shortcomings by a self-consistent solution, where Σ becomes a functional of the dressed propagator. As a result, the two Dyson equations for G^R and G^K become coupled and have to be solved simultaneously, together with the integral equations for the self-energy.

If one is interested in relatively short time evolutions, one can simply do so, by integrating the Dyson equations forward in time, starting from a set of initial conditions at $t = 0$. To find the steady state, this procedure is impractical and instead it is much more efficient to choose some initial $\mathcal{G}$ and alternatingly find $\Sigma[\mathcal{G}]$ and $\mathcal{G}[\Sigma]$ until convergence is achieved. We will discuss this procedure and possible extensions on concrete examples in the following sections and chapter 5.

Formally, self-energies consisting of one-particle irreducible diagrams with fully dressed propagators are obtained via the two-particle irreducible (2PI) effective action, which we will briefly introduce now. Similar to the generating functional $W[\mathbf{J}]$, we can also define the generating functional for connected Green's functions by introducing the additional matrix-valued source term $R(x, y)$:

$$\begin{aligned} W[J, R] &= -i \ln Z[J, R] \\ &= -i \ln \left[\int \mathbf{D}[\boldsymbol{\phi}] \exp \left(iS[\boldsymbol{\phi}] + i \int dy \; J_{\mathrm{q}}(x)\phi_{\mathrm{cl}}(x) + J_{\mathrm{cl}}(x)\phi_{\mathrm{q}}(x) \right.\right. \\ &\qquad \left.\left. + \frac{i}{2} \int dx \; dx' \; \boldsymbol{\phi}(x') R(x', x) \boldsymbol{\phi}(x) \right) \right] . \end{aligned} \tag{4.46}$$

Note, that in order to simplify the notation we use a real field $\boldsymbol{\phi}$ and in keeping with standard notation, we do not use $Z[0, 0] = 1$ to linearize the relation between $Z[J, R]$ and $W[J, R]$. The field expectation value and the Green's function are

obtained via

$$\begin{aligned}\phi_\alpha(x) &= \frac{\delta W[\mathbf{J},R]}{\delta J_{\bar{\alpha}}(x)} \\ \mathcal{G}_{\alpha\beta}(x,x') &= 2\frac{\delta W[\mathbf{J},R]}{\delta R_{\alpha\beta}(x,x')} - \phi_\alpha(x)\phi_\beta(x') \ ,\end{aligned} \tag{4.47}$$

where $\bar{\alpha}$ is the complement of the causality index α. The two-particle irreducible effective action $\Gamma[\boldsymbol{\phi},\mathcal{G}]$ is obtained via the Legendre transform

$$\Gamma[\boldsymbol{\phi},\mathcal{G}] = W[\mathbf{J},R] - \int dx \ \frac{\delta W[\mathbf{J},R]}{\delta J_\alpha(x)} J_\alpha(x) - \int dx \ dx \ \frac{\delta W[\mathbf{J},R]}{\delta R_{\alpha\beta}(x,x')} R_{\alpha\beta}(x,x') \ . \tag{4.48}$$

The equations of motion of the field expectation value $\langle\hat{\phi}_\alpha(x)\rangle$ and the Green's function $\mathcal{G}(x,x')$ follow upon removal of the external sources:

$$\begin{aligned}\frac{\delta\Gamma[\boldsymbol{\phi},\mathcal{G}]}{\delta\phi_\alpha(x)} &= -J_{\bar{\alpha}}(x) - \int dx' R_{\alpha\beta}(x,x')\phi_\beta(x') = 0 \\ \frac{\delta\Gamma[\boldsymbol{\phi},\mathcal{G}]}{\delta\mathcal{G}_{\alpha\beta}(x)} &= -\frac{1}{2}R_{\alpha\beta}(x,x') = 0 \ .\end{aligned} \tag{4.49}$$

It is convenient to separate Γ into a one-loop contribution Γ_0 and a part resulting from interactions between dressed particles denoted by Γ_{int}

$$\begin{aligned}\Gamma[\boldsymbol{\phi},\mathcal{G}] &= \Gamma_0[\boldsymbol{\phi},\mathcal{G}] + \Gamma_{\text{int}}[\boldsymbol{\phi},\mathcal{G}] \\ &= S[\boldsymbol{\phi}] + \frac{i}{2}\,\mathrm{Tr}\ln\mathcal{G}^{-1} + \frac{i}{2}\,\mathrm{Tr}\,\mathcal{G}_0^{-1}\mathcal{G} + \Gamma_{\text{int}}[\boldsymbol{\phi},\mathcal{G}] \ ,\end{aligned} \tag{4.50}$$

where the trace is taken with respect to the space and time coordinate x as well as the causality index.

In equilibrium theory $\Gamma_{\text{int}}[\boldsymbol{\phi},\mathcal{G}]$ is known as the Luttinger-Ward functional $\Phi[\boldsymbol{\phi},\mathcal{G}]$ [215, 216]. Eventually this formalism describes the same class of self-consistently determined Green's functions that we had already introduced before. And conversely, we conclude that beyond mitigating the problems of secularity and non-universal steady states, they also form so-called conserving approximations. That is to say, that integrals of motion are not violated by any approximation that can be derived from a 2PI effective action or Luttinger-Ward functional [217, 218, 192]. Since we know how to satisfy this constraint by solving the proper classes of self-consistent self-energy diagrams, we will skip these formalities in all explicit calculations, while well aware that the resulting theory – where applicable – would be identical if we were to derive it via the 2PI effective action. As we will see in the description of interaction induced transparency, not adhering to the strict rules of the 2PI effective theory, allows us to introduce modified Feynman rules, that correctly account for the finite polarizability of neutral atoms in the limit of low polariton density with-

out the need of interaction terms in the Schwinger-Boson description and without sacrificing the universality of the steady state (see Sec. 4.4.4).

4.1.4 Classical stochastic models

Before moving on to explicit physical systems, we return to the distinction between classical and quantum vertices. We have seen in chapter 2, that systems with long-range interactions are often well described by classical approximations. It is therefore useful to examine the treatment and properties of classical models in the Keldysh path integral.

Consider the Langevin equation

$$F(X_{\rm cl}(t),t) = \xi(X_{\rm cl}(t),t) \tag{4.51}$$

of a classical stochastic model with a deterministic function $F(X_{\rm cl}(t),t)$ and an external random force $\xi(X_{\rm cl}(t),t)$ with Gaussian statistics. That is to say that all moments of its distribution are fixed by the two-point correlator

$$\begin{aligned}
&\langle \xi(X_{\rm cl}(t),t)\xi(X_{\rm cl}(t'),t')\rangle \\
&= \int \mathbf{D}[\xi]\ \xi(X_{\rm cl}(t),t)\xi(X_{\rm cl}(t'),t')\mathrm{e}^{\frac{i}{2}\int dt_1 dt_2 G_\xi^{-1}(X_{\rm cl}(t_1),t_1|X_{\rm cl}(t_2),t_2)\xi(X_{\rm cl}(t_1),t_1)\xi(X_{\rm cl}(t_2),t_2)} \\
&= iG_\xi(X_{\rm cl}(t),t|X_{\rm cl}(t'),t')\ .
\end{aligned} \tag{4.52}$$

One might for example choose F to describe the damped harmonic oscillator

$$F(X_{\rm cl}(t),t) = \ddot{X}_{\rm cl} + \gamma\dot{X}_{\rm cl} + \frac{dV(X_{\rm cl})}{dX_{\rm cl}}\ , \tag{4.53}$$

with $X_{\rm cl}$ the deflection from the equilibrium position and friction force $-\gamma\dot{X}_{\rm cl}$. Arguably the simplest random force is obtained in case of white noise

$$G_\xi(X_{\rm cl}(t),t)|X_{\rm cl}(t'),t') = -2i\gamma T\delta(t-t')\ , \tag{4.54}$$

where the normalization ensures that the classical limit of the fluctuation-dissipation theorem is satisfied. Note, that the classical model has only one time-dependent variable $X_{\rm cl}(t)$ that evolves forward in time, and, without any backward evolution, no quantum field exists. Furthermore, the energy conserving potential $V(X_{\rm cl})$ and the corresponding force $-V'(X_{\rm cl}) = -dV(X_{\rm cl})/dX_{\rm cl}$ can remain completely general. We can express (4.51) as a functional integral by rewriting the delta function

$$\delta(f(X_{\rm cl},\xi)) = \int \mathbf{D}[X_{\rm q}]\mathrm{e}^{-2i\int dt X_{\rm q} f(X_{\rm cl},\xi)}\ . \tag{4.55}$$

The suggestive choice to name the auxiliary field $X_{\rm q}$ will soon become apparent.

With the help of the Hubbard-Stratonovich transformation

$$\begin{aligned} &\mathrm{e}^{-2i\int dtdt'\, G_\xi(X_{\mathrm{cl}}(t),t|X_{\mathrm{cl}}(t'),t')X_{\mathrm{q}}(t)X_{\mathrm{q}}(t')} \\ &\quad = \int \mathbf{D}[\xi]\mathrm{e}^{\frac{i}{2}\int dtdt' G_\xi^{-1}(X_{\mathrm{cl}}(t),t|X_{\mathrm{cl}}(t'),t')\xi(X_{\mathrm{cl}}(t),t)\xi(X_{\mathrm{cl}}(t'),t')+2i\int dt\, \xi(X_{\mathrm{cl}}(t),t)X_{\mathrm{q}}(t)} \end{aligned} \tag{4.56}$$

one immediately finds for any expectation value

$$\langle \hat{O}[X_{\mathrm{cl}}]\rangle = \int \mathbf{D}[X_{\mathrm{cl}},X_{\mathrm{q}}]O[X_{\mathrm{cl}}]\mathrm{e}^{iS[X_{\mathrm{cl}},X_{\mathrm{q}}]}\,, \tag{4.57}$$

with the classical action

$$S[X_{\mathrm{cl}},X_{\mathrm{q}}] = -2\int dt\left[X_{\mathrm{q}}F(X_{\mathrm{cl}}) + \int dt'\, G_\xi(X_{\mathrm{cl}},t|X_{\mathrm{cl}},t')X_{\mathrm{q}}X_{\mathrm{q}}\right]\,. \tag{4.58}$$

For the choices (4.53) and (4.54) this action simplifies to

$$S[X_{\mathrm{cl}},X_{\mathrm{q}}] = \int dt\left\{-2X_{\mathrm{q}}\left[\ddot{X}_{\mathrm{cl}} + \gamma\dot{X}_{\mathrm{cl}} + V'(X_{\mathrm{cl}})\right] + 4i\gamma T\,(X_{\mathrm{q}})^2\right\}\,. \tag{4.59}$$

The procedure of transforming a Langevin equation into a path integral was introduced by Onsager and Machlup [219] and later extended to fields by Martin, Siggia and Rose as what came to be known as the MSR method [220]. It makes classical stochastic equations accessible to the powerful tool set of diagrammatic perturbation theory, while conversely the reverse mapping is often more favorable for numerical evaluations.

At first glance the MSR action takes the same causal form as the generic action of a quantum system discussed in Sec. 4.1.3. There is however one important difference, namely the interaction consists only of classical vertices. In fact, if we demand, that the MSR action (4.58) is independent of the reduced Planck constant $\hbar$, we find $X_{\mathrm{q}} \sim \hbar$ and consequently in the classical limit $\hbar \to 0$ only classical vertices survive. In quantum systems with long-range interactions, we therefore expect classical vertices to dominate the interaction.
We can thus conclude, that beyond the very intuitive causal structure, the Keldysh rotation has the additional advantage of making the classical limit of a quantum field theory particularly clear. Vice versa, a system will only retain its quantum character on all length scales, if the quantum vertices remain relevant [47].

4.2 Electromagnetically induced transparency

We now introduce the concept of electromagnetically induced transparency (EIT), which will serve as the foundation to the treatment of interacting polaritons by means of the Keldysh formalism. We will especially focus on the modified propagation properties of photons under EIT conditions and the influence of noise and

decay. We will briefly revisit this subject in Sec. 4.5 to demonstrate that the Keldysh approach with modified Feynman rules (cf. Sec. 4.4.4) exactly reproduces the limit of low polariton densities.

EIT is typically studied in atomic gases, where narrow transition linewidths are easily accessible, but extensions to solid state systems have been reported as well [221]. In its essence EIT is quantum interference between two optical pathways [222]. It is therefore enough to consider three energy levels of the medium, which we will label by $|g\rangle$, $|s\rangle$ and $|e\rangle$, where the first two have the same parity, therefore forbidding an electric dipole transition. The energies of these states are of no relevance and we therefore choose the most common, so-called Λ-scheme (cf. Fig. 4.4). For the moment, we will assume, that the ground-state level $|g\rangle$ is coupled to the

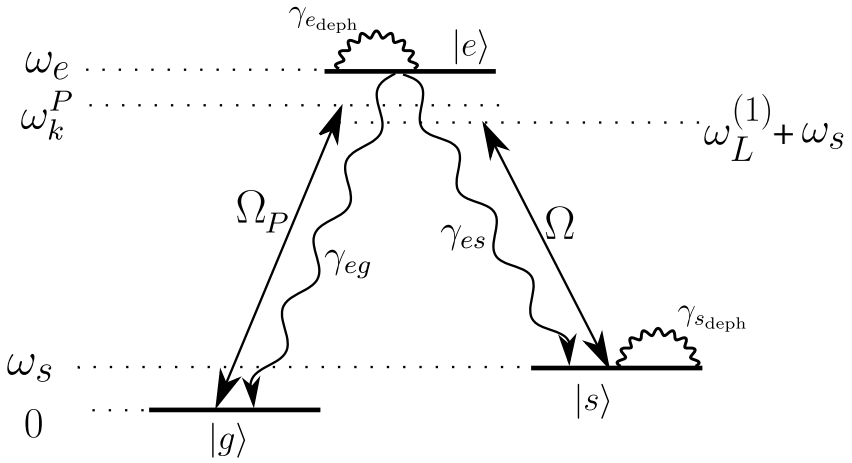

Figure 4.4: The prototypical Λ-scheme for EIT. Transitions between the ground state $|g\rangle$ and the excited, decaying state $|e\rangle$ as well as between $|e\rangle$ and $|s\rangle$ are driven by coherent light fields of amplitude Ω_P and Ω respectively. We allow for these light fields to be detuned against the atomic transition and include dephasing noise for all levels but the ground state. States $|s\rangle$ and $|g\rangle$ are supposed to have the same parity, preventing dipole transitions and thus spontaneous decay of the former.

excited state $|e\rangle$ by a coherent probe field with Rabi frequency Ω_P and energy ω_P. Similarly the transition between $|e\rangle$ and $|s\rangle$ is coupled to a control field with Rabi frequency Ω and energy $\omega_L^{(1)}$. In addition, we allow for decay from the excited state to $|g\rangle$ and $|s\rangle$ and include dephasing noise – for example due to collisions in the medium – in states $|e\rangle$ and $|s\rangle$. The resulting master equation in the rotating

frame, after application of the rotating wave approximation is

$$\begin{aligned}\frac{d\rho}{dt} =& -\frac{i}{\hbar}[H(t),\rho] + \frac{\gamma_{eg}}{2}\left(2|g\rangle\langle e|\rho|e\rangle\langle g| - |e\rangle\langle e|\rho - \rho|e\rangle\langle e|\right)\\ &+ \frac{\gamma_{es}}{2}\left(2|s\rangle\langle e|\rho|e\rangle\langle s| - |e\rangle\langle e|\rho - \rho|e\rangle\langle e|\right)\\ &+ \frac{\gamma_{s_{\mathrm{deph}}}}{2}\left(2|s\rangle\langle s|\rho|s\rangle\langle s| - |s\rangle\langle s|\rho - \rho|s\rangle\langle s|\right)\\ &+ \frac{\gamma_{e_{\mathrm{deph}}}}{2}\left(2|e\rangle\langle e|\rho|e\rangle\langle e| - |e\rangle\langle e|\rho - \rho|e\rangle\langle e|\right)\end{aligned} \tag{4.60}$$

with the time-dependent Hamiltonian

$$\begin{aligned}H(t) =& \hbar\left(\omega_e|e\rangle\langle e| + \omega_s|s\rangle\langle s|\right)\\ &- \hbar\left(\Omega_P \mathrm{e}^{i(\omega_e-\omega_P)t}|e\rangle\langle g| + \Omega \mathrm{e}^{i\left(\omega_e-\omega_s-\omega_L^{(1)}\right)t}|e\rangle\langle s| + \mathrm{h.c.}\right).\end{aligned} \tag{4.61}$$

Notice, that the Markovian loss terms are unaffected by the transformation to the rotating frame. We first focus on the linear susceptibility of the medium in case of a weak probe field. To linear order in Ω_P one finds

$$\chi(\omega_P) = -\frac{n\mu_{eg}^2}{\epsilon_0\hbar}\left(\omega_P - \omega_e + i\gamma_e/2 - \frac{\Omega^2}{\omega_P - \omega_s - \omega_L^{(1)} + i\gamma_s/2}\right)^{-1}, \tag{4.62}$$

with $\gamma_e = \gamma_{eg} + \gamma_{es} + \gamma_{e_{\mathrm{deph}}}$ and $\gamma_s = \gamma_{s_{\mathrm{deph}}}$ as well as the atomic number density n and dipole moment μ_{eg}. Notice, that since the steady state satisfies $\rho_{gg} \approx 1$, no distinction between decay and dephasing is possible and both effects broaden the transitions in the same way. Furthermore, we have set both Ω_P and Ω to real values, which requires both fields to be phase locked for sufficiently long times. If this is not satisfied, further losses will be induced [223]. Real and imaginary parts of the susceptibility χ are shown in Fig. 4.5. The losses experienced by the probe laser, which are determined by $\Im\chi(\omega_P)$, have a very pronounced minimum at $\omega_P = \omega_s + \omega_L^{(1)}$, while the refractive index satisfies $n_R = \sqrt{1 + \Re\chi(\omega_s + \omega_L^{(1)})} = 1$. There is thus no reflection on the surface of the material and the probe photons propagate for much longer distances, than they did without the control laser field, which led to the name electromagnetically induced transparency first coined by Harris et al. [224]. However, the slope of $\Re\chi$ is large, which implies that the propagation is much slower than in vacuum. We emphasize, that $\chi(\omega_s + \omega_L^{(1)}) = 0$ only fixes the linear refractive index to be equal to unity, while higher order susceptibilities in the EIT window are in fact large, enabling the use of EIT for highly efficient frequency up conversion [225, 226] and multiwave mixing [224, 227, 228]. As long as γ_s is negligible, all of these properties are impervious against a finite detuning $\omega_P - \omega_e \neq 0$ and losses γ_e. If on the other hand losses of the metastable state $|s\rangle$ are large enough, so that $\Omega^2 \gg \gamma_e\gamma_s$ cannot be satisfied, the EIT window is destroyed.

This strong sensitivity to dephasing indicates, that in fact the unusual behavior of the susceptibility is based on destructive interference between atoms excited from the ground state and state $|s\rangle$.

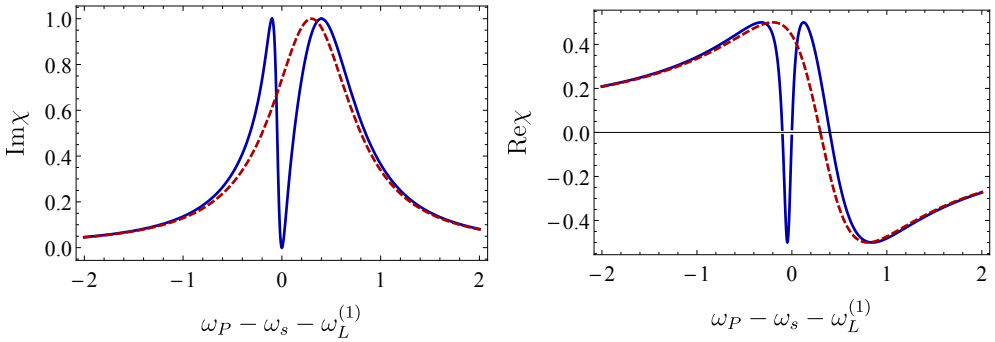

Figure 4.5: Real and imaginary part of the linear susceptibility (4.62) with (blue) and without (dashed, red) control laser $\Omega = 0.2$. Here, in the absence of decay and dephasing from the metastable state ($\gamma_s = 0$), the susceptibility vanishes at $\omega_P = \omega_s + \omega_L^{(1)}$. The remaining parameters are $\omega_e = 0.3$ and $2n\mu_{eg}^2 = \epsilon_0\hbar$ in units of $\gamma_e = 1$.

To understand this, we consider the stationary solution to Eq. (4.60) at the EIT condition $\omega_P = \omega_s + \omega_L^{(1)}$ in the ideal scenario, where $\gamma_s = 0$, and find the pure state

$$|\Psi\rangle = \frac{1}{\Omega^2 + \Omega_P^2} \left(\Omega|g\rangle - \Omega_P|s\rangle\right) \ . \tag{4.63}$$

Clearly, this state is lossless and therefore a dark state. The concept of creating these states, known as coherent population trapping (CPT), though closely related in spirit, long predates EIT [229]. As was realized by Boller et al. [222], the relative occupation and sign of the states $|s\rangle$ and $|g\rangle$ in the dark state Ψ results in a perfect destructive interference for the excited state. In other terms, the direct excitation $|g\rangle \to |e\rangle$ cancels against the indirect pathway $|g\rangle \to |e\rangle \to |s\rangle \to |e\rangle$.

With the relative population of $|s\rangle$ and $|g\rangle$ in the dark state controlled entirely by laser fields, changing these adiabatically transfers atoms between the two states. Specifically, if initially all atoms are in the ground state, Ω is switched on and then turned off while Ω_P is increased. This eventually transfers all atoms to state $|s\rangle$, without ever populating the excited state. Since the other bright eigenmodes of (4.60) are detuned to $\omega_e - \omega_P \pm \sqrt{(\omega_e - \omega_P)^2 + \Omega_P^2 + \Omega^2}$, this transfer can be performed very rapidly, if sufficiently strong lasers are available. Therefore the stimulated Raman adiabatic passage (STIRAP) [230, 231] has become an important technique in state preparation.

We now return to the propagation properties of the probe photons. When the electric field $E_P = \mathcal{E}_P\sqrt{\hbar\omega_P/(2\epsilon_0)}$ enters the medium, it transfers part of its energy into the dark state $|\Psi\rangle$ and thus hybridizes with the atomic pseudospin excitation. Indeed, using the ansatz of a mixed light-medium excitation, the so-called dark-state polariton

$$\Phi(z,t) = \cos\theta\mathcal{E}_P(z,t) - \sin\theta\sqrt{n}\rho_{eg}(z,t)\mathrm{e}^{i\Delta kz} \tag{4.64}$$

one finds the mixing angle [232]

$$\tan\theta = \sqrt{\frac{\omega_P}{2}\frac{d\Re\chi(\omega_P)}{d\omega_P}}\ . \tag{4.65}$$

Here Δk is the difference in wave-number between the control laser and the probe field, projected along the direction of propagation of the probe photons, chosen as the z-axis. At a fixed position in the medium a light pulse that passes by performs a stimulated Raman adiabatic return, i.e. a STIRAP from $|g\rangle$ to $|s\rangle$ and back. This delays its propagation and one finds the modified wave equation

$$\left[\frac{\partial}{\partial t} + c\cos^2(\theta)\frac{\partial}{\partial z}\right]\Phi(z,t) = 0\ , \tag{4.66}$$

where we identify the group velocity $v_g = c\cos^2(\theta)$. Importantly, if $\omega_e = \omega_P$, the real part of the linear susceptibility is an odd function of $\omega_P - \omega_s - \omega_L^{(1)}$ and consequently

$$\left.\frac{d^2\Re\chi(\omega_P)}{d\omega_P^2}\right|_{\omega_P=\omega_s-\omega_L^{(1)}} = 0\ , \tag{4.67}$$

which implies that a weak and sufficiently long probe pulse that is therefore tightly focused around $\omega_s + \omega_L^{(1)}$ will experience no spreading of the wave packet [233]. Clearly, the more spin-wave character the polariton has, the slower its propagation. This has famously been used to slow down light to the speed of a cyclist (8 m/s) [234] and, together with an adiabatic switch-off of the control laser, even to a complete stop [235, 236, 221]. Using counterpropagating control lasers, it has also been demonstrated, that light can be stopped and recovered without a complete rotation to spin-waves [237].

In vacuum photons do not interact and therefore need a nonlinear material to mediate their mutual interactions. Typically these nonlinear optical effects are small. The adiabatic rotation from pure photons to polaritons with a large admixture of the metastable atomic state, however, creates the opportunity to directly imprint strong interatomic interactions onto photons. Consequently, in combination with strong atomic Rydberg interactions, EIT has turned out to be a key ingredient

in achieving single-photon nonlinearities [3, 238], potentially allowing for efficient transmission, manipulation, and storage of quantum information [4]. Furthermore, single-photon nonlinearities pave the way for the study of novel quantum many-body phenomena with strongly interacting photons [3].

4.3 Diagrammatic expansion in the inverse interaction range

In the following, we will investigate the properties of polaritons in materials made of uncharged but polarizable atoms with strongly interacting excited states. This implies that the interaction between two photons is a higher order process, requiring the intermediate excitation of the atomic dipoles. Interactions between polaritons in such systems are naturally long-ranged (as the relevant electromagnetic modes typically extend over many atoms) and retarded (as the time scales of photons and atoms can be respectively tuned to be comparable). Finally, interactions inherited from atomic dipoles can be strongly dissipative due to the spontaneous decay of excited atomic levels. This feature in particular has been shown to be capable of introducing novel many-body phenomena, whereby correlations can be induced by dissipation [43, 239, 240].

We emphasize that the theoretical description of such strongly-interacting, driven-dissipative systems of photons in the many-body regime constitutes a challenging task. Specifically, the large interaction cross sections prevent a perturbative treatment, the driven-dissipative nature does not allow to exploit fluctuation-dissipation relations and prohibits, for instance, the application of Monte Carlo methods, while the long-range interactions additionally hinder an efficient employment of tensor network methods, even in one spatial dimension. Nevertheless, a few theoretical approaches have been developed for the few-body regime [241, 242, 243, 244, 245], while effective field theories have been applied in the many-body regime [246, 240, 247, 248, 249].

Here, we introduce a systematic, diagrammatic approach for the computation of non-equilibrium correlators for a many-body system of strongly interacting photons in an optically dense medium. If the characteristic photon propagation range L_P in the medium is much larger than the spacing a between the atoms, we show that a controlled diagrammatic expansion in powers of a/L_P can be performed, even if the collective light-matter coupling g_P within the mode volume of the photon is large. This perturbative expansion in a/L_P is always valid when the single-atom cooperativity $C_P^{\mathrm{sa}} = (g_P^2/\gamma\kappa)(a/L_P)$ is much smaller than unity, where γ and κ are the characteristic dissipation rates of excited atomic levels and photons, respectively. The quantitative validity of our approach can, however, even be extended to a regime of large single atom cooperativities $C_P^{\mathrm{sa}} \gtrapprox 1$, provided that the density of atomic excitations is low enough to neglect saturation effects. In such a situation, photons would not experience any nonlinearity or interactions, unless

the atoms are subjected to additional, mutual interactions which the photons can inherit. If inter-atomic interactions are present and if their range $L_E/a \gg 1$ is large, we show that the subclass of diagrams describing scattering processes with momentum transfer between photons is suppressed by a factor $\sim a/L_E$ with respect to the remaining Hartree-like diagrams. In this case we are able to perform a self-consistent resummation of the subclass of Hartree-like diagrams and obtain quantitative results in a strongly non-perturbative regime, which indeed shows important collective behavior and even phase transitions.

From a quantum-field-theory perspective, this chapter constitutes a first attempt to develop a non-relativistic version of Quantum Electrodynamics (QED) where the matter degrees of freedom are dipoles instead of charged electrons and two further important differences: i) the photons are driven and (partially) confined in space, and ii) the light-matter coupling is far away from the perturbative regime. From the applied perspective, on the other hand, we illustrate specific possible realizations in experiments involving interactions mediated through waveguide photons, for example in photonic-crystal-waveguides [17, 250], as well as Rydberg interactions [18, 19, 251, 20, 21, 238]. We moreover consider atomic level structures allowing the photons to propagate under EIT conditions [252, 233].

The basic idea underlying our diagrammatic approach can be understood in quite general terms. Let us consider a system of two completely different types of particles, which we will for later convenience call photons and atoms. For now we will keep these particles as generic as possible and only fix their mass: Photons are very light (or even massless) and therefore propagate very fast and over long distances, whereas atoms are considered as comparatively heavy, localized and thus slowly moving. Furthermore, neither atoms nor photons shall interact among themselves, that is, excited atoms can only interact via exchange photons and photons only via the nonlinear susceptibility of the atomic medium, which results in a Yukawa-type coupling. The stark contrast between the two free theories of atoms and photons allows for a controlled expansion, even in the case of strong collective light-matter interactions. This is due to the large effective mode volume of the photon, suppressing the single-atom cooperativity and thereby providing a useful expansion parameter.

To make this argument more concrete, let us for simplicity consider the specific case of photons with a group velocity c that couple with a rate g to the collection of all atoms within an effective mode volume L. We furthermore assume that the atoms are confined to fixed positions in a one-dimensional chain. Moreover, photons are lost out of the one-dimensional medium at a rate κ and the atomic transition giving rise to a dipole moment takes place between a lower stable level and an excited level decaying at a rate γ. To avoid the trivial case of the steady state being the vacuum, the atoms are additionally excited by a resonant coherent light source at a Rabi frequency Ω. For this simple model it is easy to write both the atomic and the photonic Green's functions in a perturbative expansion in the coupling strength g. Representing the photonic propagator G_{ph} with a wavy line

and its atomic counterparts G_a with a straight line, one obtains to order g^2 the diagrams depicted in Fig. 4.6.

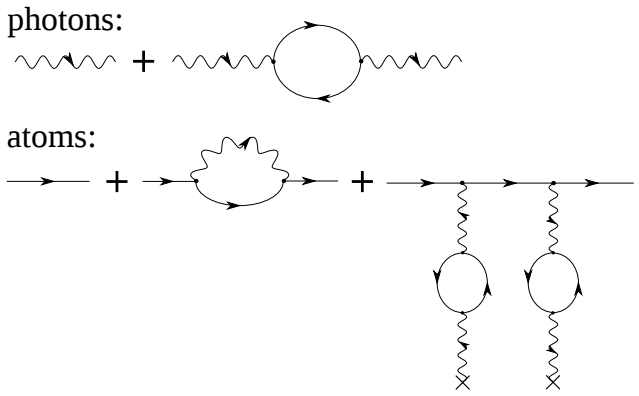

Figure 4.6: Illustration of the breakdown of the perturbative expansion of photonic and atomic propagators in second order in the coupling strength g. Wavy lines represent photons, straight lines atoms. In the case of a large collective cooperativity the self-energy correction to the photon propagator (second diagram in the first line) becomes large. The same is true for the corrections to the propagator of the atomic state in the second line due to the last contribution, which strongly couples stable and excited atomic states. Large collective cooperativities thus require an improved approach (cf. Fig. 4.15).

The leading correction to the bare photonic dispersion due to the atomic medium is given by the polarization bubble shown in Fig. 4.6a). Performing the corresponding convolutions, one immediately obtains that on-shell each correction to G_ph is proportional to g^2/γ, which implies that the expansion in powers of g breaks down if the collective cooperativity $C = g^2/(\gamma\kappa)$ becomes of order unity. Equivalently, the last term in Fig. 4.6b), which is proportional to $(\Omega g^2/\gamma\kappa)^2$, becomes larger than the bare coupling Ω^2 if $C \approx 1$. At the same time however, the other correction to the bare propagator is negligible if the cooperativity per atom $C_\mathrm{sa} = g^2/(\gamma\kappa L) \ll 1$. Here we have introduced the dimensionless effective mean free path of the photons $L = nc/\kappa$, where n is the number density of the atoms. From the point of view of the atoms this corresponds to the effective interaction range. Thus, if this dimensionless interaction range is large, the small coupling $g/\sqrt{L}$ allows for a partially perturbative treatment, where only a small subclass of diagrams (those that are not suppressed by powers of $1/L$) has to be resummed to all orders, as we illustrate below. With respect to the topology of the diagrams, this expansion is identical to a $1/N$ expansion [65], where the atoms can appear in N different degrees of freedom (flavors) which are conserved at each vertex.

While this expansion is already quite useful, as it allows to introduce controlled

interactions between polaritons, it does not immediately allow to enter the regime of strong single-atom cooperativities, where the finiteness of the Hilbert space of each atom starts to play an essential role. To correctly account for the finite polarizability of each atom, one additionally has to introduce nonlinear Feynman rules, in effect extending the theory to large single-atom cooperativities and simultaneously reducing the required set of diagrams to one that – under certain conditions – can be treated exactly (see Sec. 4.4.4).

4.4 Guided photons coupled to atomic arrays

Building on the newly gained understanding that any physical system is suitable for a $1/L$ expansion as long as it exclusively couples degrees of freedom that are well localized in position space to others that are tightly confined in the conjugate momentum space, we will now be more concrete and apply this approach to photons in optical waveguides coupled to an array of atoms. Large single-atom cooperativities in such a setup are for instance reached using atoms trapped within the evanescent-wave of photonic crystal waveguides (PCWs) [17, 250] or tapered-nanofiber waveguides (TNWs) [22, 23, 24, 25]. The concepts introduced in this section are, however, far more general and can be applied in similar ways to any system of interacting polaritons, as will be discussed by a comparison with a gas of Rydberg atoms in Sec. 4.9.

4.4.1 A microscopic model

We consider a chain of atoms trapped at fixed positions and with the internal level structure shown in Fig. 4.7a). We assume four atomic levels in an $\mathcal{N}$-configuration. The ground state is represented by $|g\rangle$ and the first excited, unstable state by $|e\rangle$. The transition between those levels is (almost) resonant with the energy of a set of propagating probe photons of the waveguide with dispersion ω_k^P. A further, metastable atomic state $|s\rangle$ can be reached from $|e\rangle$ by stimulated emission of a photon with energy $\omega_L^{(1)}$ into a laser mode, driven at Rabi amplitude Ω. Since photons can be converted into atomic excitations, the EM modes of the waveguide hybridize with the two atomic transitions and give rise to three polariton branches. The $g-e-s$ Λ-scheme has already been discussed in Sec. 4.2. Based on the results presented there, we expect a pronounced reduction of the group velocity of one of the polariton branches, which therefore becomes almost dissipationless, as described in detail in section 4.5. The direct photon-photon interaction arising from the saturation of individual atoms is extremely weak [253]. Such an interaction can be made much stronger by introducing a mechanism for the atoms to interact with one another over a distance. This is achieved via an additional set of exchange-photon modes of the waveguide with dispersion ω_k^E. These are orthogonally polarized

with respect to the P-modes introduced above and can be tuned separately. In particular, it is possible to use the exchange photons to couple a second excited state $|d\rangle$ to the state $|s\rangle$. To adjust the admixture of $|d\rangle$, we introduce a second driving laser of frequency $\omega_L^{(2)}$ and Rabi amplitude Ω_s. In the actual calculations shown here we will for concreteness choose a cosine dispersion for the P-photons and a quadratic dispersion for the E-photons, which corresponds to the situation in PCWs. The actual choice however, does not make any qualitative difference. In general the parabolic approximation to ω_k^E is justified by tuning the laser frequency in the vicinity of a dispersion minimum or maximum. In particular, tuning into the band gap creates a bound state, since the exchange photon cannot propagate and becomes localized around the atom that has emitted it. This bound state was first described by Douglas et al. [250], who also investigated the strong interactions with other atoms it facilitates within the region of its localization, that itself can be adjusted via the detuning from the band edge.

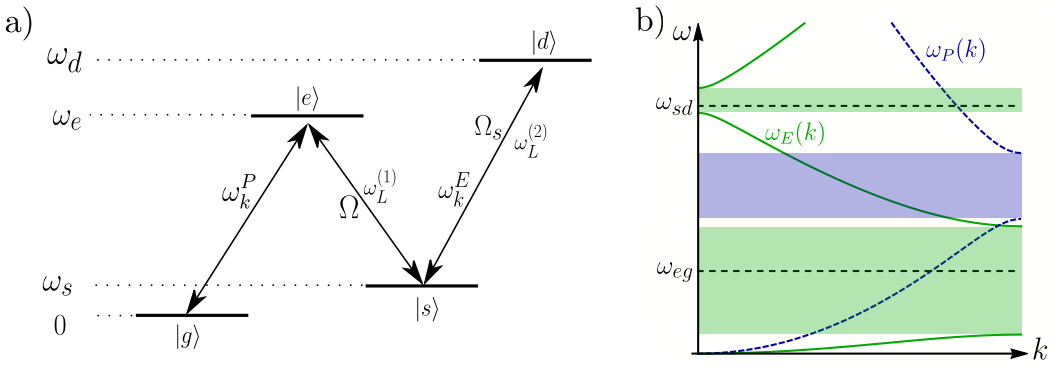

Figure 4.7: In a) the level scheme of atoms trapped near a photonic crystal waveguide is shown. External lasers with Rabi amplitudes Ω and Ω_s drive transitions between the metastable state $|s\rangle$ and decaying excited states $|e\rangle$ and $|d\rangle$. The two orthogonal polarizations of the photon modes within the PCW are (almost) resonant with the $|g\rangle - |e\rangle$ and $|s\rangle - |d\rangle$ transition respectively. Without the excited state $|d\rangle$ the system therefore reduces to the well-known Λ level scheme. In b) a scenario of propagating probe photons and localized exchange photons, realizable for example by specifically engineered Bloch bands in PCWs is illustrated.

To make this discussion more concrete, we provide in Fig. 4.8 a sketch of a possible realization of the level scheme presented in Fig. 4.7 with the help of PCWs. In these systems, the two transverse light polarizations do not mix and their band structures can be tuned independently. In fact, these engineered photon bandstructures potentially allow to control not only the photon dispersion but also both the strength and the range of interactions [250, 254, 244], as well as the coupling

with the environment [255]. It is therefore possible to trap the atoms in a chain that is commensurate with the periodicity of the PCW, have them hybridize with the propagating probe photons and simultaneously make the resulting polaritons interact via localized exchange photons of the orthogonal polarization. The letter being engineered such that the $|s\rangle - |d\rangle$-transition lies within the band gap. A possible configuration for the necessary detunings between atomic transitions and photon bands is shown in Fig. 4.7b). Alternatively, the atoms could also be held in place in the evanescent field of a tapered fiber using tweezers [256, 257]. In this case, the band gap of the exchange photons is replaced by their mass gap.

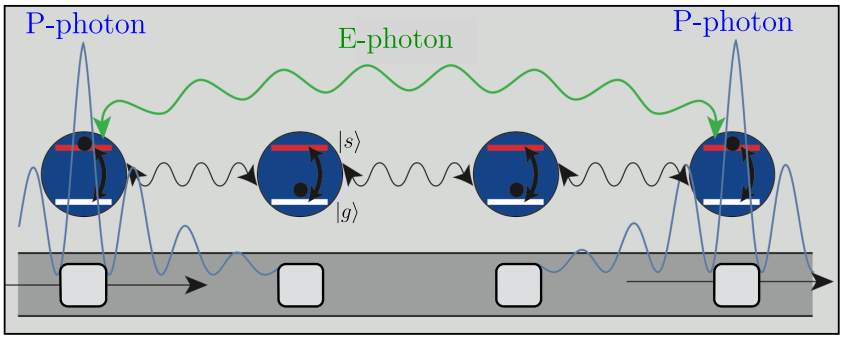

Figure 4.8: Proposed realization of IIT in a chain of atoms fixed in a periodic arrangement in the evanescent field of a photonic crystal waveguide. The probe photons propagating through the waveguide hybridize with atoms in state $|s\rangle$, which then interact dissipatively via localized exchange photons.

Our diagrammatic approach will be developed within a non-equilibrium functional-integral formalism. However, since for each atom the Hilbert space is finite, more precisely the occupation of all its states sums up to one, the representation of atomic operators in a form that is convenient for the path integral formulation has to be given some thought. Here we will restrict ourselves to the limit of a small density of excited atoms, where saturation effects of the medium can be neglected. As a result, the Schwinger boson representation without explicit restriction to the boson number of each atomic transition will suffice. In particular, the action of the Hamiltonian in the atomic Hilbert space can be broken down into a sum of spin-1/2 operators $\sigma_{\mu,\nu} = |\mu\rangle\langle\nu|$, where $|\mu\rangle, |\nu\rangle \in \{|g\rangle, |e\rangle, |s\rangle, |d\rangle\}$, which can be approximately expressed through bosonic creation and annihilation operators:

$$\sigma_{\mu,\nu} = \hat{a}^\dagger_\mu \hat{a}_\nu \,. \tag{4.68}$$

Clearly this approximation allows for an unrestricted occupation of any state of any atom – a shortcoming which will be compensated by the application of nonlinear Feynman rules and the restriction to low excitation densities. Since treating spins

within a path integral formulation is considerably more complicated than bosons [214, 258], this transformation is crucial for the tractability of the calculations that lie ahead. Within this linear regime the Hamiltonian part of the system is described by

$$\begin{aligned}\hat{H} = \hbar \sum_z \Big\{ & \omega_e \hat{a}_e^\dagger(z)\hat{a}_e(z) + \omega_s \hat{a}_s^\dagger(z)\hat{a}_s(z) + \omega_d \hat{a}_d^\dagger(z)\hat{a}_d(z) \\ & + \left(\Omega \mathrm{e}^{-i\omega_L^{(1)}t}\hat{a}_e^\dagger(z)\hat{a}_s(z) + h.c.\right) + \left(\Omega_s \mathrm{e}^{-i\omega_L^{(2)}t}\hat{a}_d^\dagger(z)\hat{a}_s(z) + h.c.\right) \\ & + \int_{-\pi}^{\pi} \frac{dk}{2\pi} \Big[\omega_k^P \left[\hat{a}_P(k)\right]^\dagger \hat{a}_P(k) + \omega_k^E \left[\hat{a}_E(k)\right]^\dagger \hat{a}_E(k) \\ & \qquad + g_P \left(\hat{a}_P(k)\mathrm{e}^{ikz} u_k^P(z)\hat{a}_e^\dagger(z)\hat{a}_g(z) + h.c.\right) \\ & \qquad + g_E \left(\hat{a}_E(k)\mathrm{e}^{ikz} u_k^E(z)\hat{a}_d^\dagger(z)\hat{a}_s(z) + h.c.\right) \Big] \Big\},\end{aligned} \tag{4.69}$$

Where $u_k^{P/E}(z)$ represents the periodic/localized part of the Bloch functions of either polarization at quasi-momentum k evaluated at the discrete positions z of the atoms. We moreover use the standard convention for the thermodynamic limit in a crystal with lattice constant $a = 1$, namely $\sum_z \mathrm{e}^{ikz} = 2\pi\delta(k)$.

We include the decay of the excited atomic states via

$$\begin{aligned}\mathcal{L}_{\gamma_e}\rho &= -\hbar \sum_z \frac{\gamma_e}{2} \left(\left\{ \hat{a}_e^\dagger(z)\hat{a}_e(z), \rho \right\} - 2\hat{a}_e(z)\rho\hat{a}_e^\dagger(z) \right) \\ \mathcal{L}_{\gamma_d}\rho &= -\hbar \sum_z \frac{\gamma_d}{2} \left(\left\{ \hat{a}_d^\dagger(z)\hat{a}_d(z), \rho \right\} - 2\hat{a}_d(z)\rho\hat{a}_d^\dagger(z) \right),\end{aligned} \tag{4.70}$$

which accounts only for independent emission from each atom, neglecting collective effects [255]. We also allow for photon losses of both polarizations into free space, such as through scattering or absorption:

$$\begin{aligned}\mathcal{L}_{\kappa_P}\rho &= -\hbar \int_k \frac{\kappa_P}{2} \left(\left\{ \left[\hat{a}_P(k)\right]^\dagger \hat{a}_P(k), \rho \right\} - 2\hat{a}_P(k)\rho \left[\hat{a}_P(k)\right]^\dagger \right) \\ \mathcal{L}_{\kappa_E}\rho &= -\hbar \int_k \frac{\kappa_E}{2} \left(\left\{ \left[\hat{a}_E(k)\right]^\dagger \hat{a}_E(k), \rho \right\} - 2\hat{a}_E(k)\rho \left[\hat{a}_E(k)\right]^\dagger \right).\end{aligned} \tag{4.71}$$

Here we have used the notation $\int_k = L \int \frac{dk}{2\pi}$. Additionally, an incoherent and homogeneous pumping of the propagating modes with a transverse light source shall drive the system out of equilibrium. Without affecting the physics of the dark-state polaritons, one could simply describe this light source by a Markovian

bath:

$$\begin{aligned}\mathcal{L}_{\kappa_s}\rho = -\hbar\int_k \frac{\kappa_s}{2}\Big(\Big\{\hat{a}_P(k)\left[\hat{a}_P(k)\right]^\dagger + \text{h.c.}, \rho\Big\} \\ -2\left[\hat{a}_P(k)\right]^\dagger \rho \hat{a}_P(k) - 2\hat{a}_P(k)\rho\left[\hat{a}_P(k)\right]^\dagger\Big)\ .\end{aligned} \tag{4.72}$$

The only disadvantage of this description is a large population of non-interacting photons propagating through the system at frequencies far detuned from any atomic resonances. In fact, a transversal light source will not couple to all modes equally well, but due to frequency dependencies of the mode matching, will predominantly couple to a certain frequency interval. To include this, we instead model the incoherent drive indirectly. First an additional Gaussian mode, with a coherence time and length much shorter than the relevant time and length scales for dark-state polaritons, is itself driven by a Markovian bath:

$$\begin{aligned}\hat{H}_b &= \omega_0 \hat{b}^\dagger \hat{b} \\ \mathcal{L}_{\text{loss}}\rho_b &= -\hbar\frac{\kappa_1}{2}\left(\left\{\hat{b}^\dagger\hat{b}, \rho_b\right\} - 2\hat{b}\rho_b\hat{b}^\dagger\right) \\ \mathcal{L}_{\text{drive}}\rho_b &= -\hbar\frac{\kappa_2}{2}\left(\left\{\hat{b}\hat{b}^\dagger, \rho_b\right\} - 2\hat{b}^\dagger\rho_b\hat{b}\right)\ ,\end{aligned} \tag{4.73}$$

where $\hat{b}^\dagger$ and $\hat{b}$ are bosonic creation and annihilation operators for the auxiliary mode with density matrix ρ_b. In a next step this mode then couples bilinearly to the propagating photons:

$$\hat{H}_{ab} = g_b\int_k (\hat{b}^\dagger\hat{a}_P(k) + \hat{a}_P^\dagger(k)\hat{b})\,. \tag{4.74}$$

In the limit of strong driving, where κ_1/κ_2 approaches unity from below, this construction, that effectively mimics a frequency dependent coupling of the system to a highly occupied incoherent bath, is described by the following addition to the Liouvillian

$$\begin{aligned}\mathcal{L}_{\kappa_s}\rho(t) = -\frac{\hbar}{2}\int_k\int_{-\infty}^{t} dt'\Big(\kappa_s(t-t')\left[\left[\hat{a}_{P,I}(k,t)\right]^\dagger, \left[\hat{a}_{P,I}(k,t'), \rho_I(t')\right]\right] \\ -\kappa_s(t'-t)\left[\hat{a}_{P,I}(k,t), \left[\left[\hat{a},_{P,I}(k,t')\right]^\dagger, \rho(t')\right]\right]\Big)\ ,\end{aligned} \tag{4.75}$$

where the additional index I indicates that operators are to be evaluated in the interaction picture, in which H as well as all Lindblad operators (except $\mathcal{L}_{\kappa_s}$) contribute to the time evolution of the operators. We note that $\kappa_s(t)$ has an exponential decay, the parameters of which can be tuned by the properties of the Gaussian mode. While this construction is rather cumbersome if written as Liouvillian, in the path integral description the Gaussian mode can be integrated out immediately giving rise to a simple, closed expression for a colored bath.

Note that, in order to control the occupation of the propagating modes, it is sufficient to choose $\kappa_1 = \kappa_2$ such that Stokes and anti-Stokes processes are equal in amplitude and then to adjust the loss rate κ_P accordingly. This construction implies that the anti-Stokes processes are at least equally likely as the Stokes processes, such that the bath is effectively at a finite positive temperature and cannot be inverted. Consequently lasing or condensation of polaritons are excluded [259]. The fact that the linearized description of decay of excited atoms violates atom number conservation is an unphysical feature of this approximation. Since a more rigorous modeling of spontaneous decay, e.g. via the Lindblad operator $\hat{a}_e\hat{a}_g^\dagger$, is diagrammatically equivalent to a two-body interaction, which significantly complicates a systematic treatment, we compensate these spurious atom losses on average by fixing the density of atoms in the ground state. As we will see later, as long as saturation effects are negligible, this description of the atoms in combination with a specific selection rule for the Feynman diagrams becomes exact (see Sec. 4.4.4).

4.4.2 Non-equilibrium functional-integral formulation on the Keldysh contour

We now have to recast our non-equilibrium problem into a functional-integral form on the Schwinger-Keldysh contour. Since there are several different bosonic modes, we introduce the retarded matrix Green's function

$$iG_{ij}^R(x,x') = \theta(t-t')\left\langle\left[\hat{a}_i(x),\hat{a}_j^\dagger(x')\right]\right\rangle , \tag{4.76}$$

and the Keldysh Green's function

$$iG_{ij}^K(x,x') = \left\langle\left\{\hat{a}_i(x),\hat{a}_j^\dagger(x')\right\}\right\rangle , \tag{4.77}$$

with $i,j = g,e,s,d,E,P$ labeling the degree of freedom, each of which is treated by means of the coherent state path integral as described in Sec. 4.1. Following the procedure detailed there, the fields $a(x)_j$ are rotated to *quantum* and *classical* fields labeled as $a_j^{\mathrm{q}}(x)$ and $a_j^{\mathrm{cl}}(x)$ respectively. Due to causality the former have identically vanishing correlations: $\langle\hat{a}_i^{\mathrm{q}}(x)[\hat{a}_j^{\mathrm{q}}]^\dagger(x')\rangle \equiv 0$ and the advanced Green's function satisfies $G_{ij}^A(x,x') = \left[G_{ij}^R\right]^*(x',x)$, where $(\cdot)^*$ denotes the complex conjugation.

For the non-interacting atoms coupled to the coherent laser fields, the inverse

retarded Green's function reads

$$\left[\bar{G}^R_{a,0}\right]^{-1}(\omega,\omega') = \begin{pmatrix} \left(\omega-\omega_d+i\frac{\gamma_d}{2}\right)\delta(\Delta) & -\Omega_s\delta\left(\Delta-\omega_L^{(2)}\right) & 0 & 0 \\ -\Omega_s\delta(\Delta+\omega_L^{(2)}) & \left(\omega-\omega_s+i\frac{\epsilon}{2}\right)\delta(\Delta) & -\Omega\delta(\Delta+\omega_L^{(1)}) & 0 \\ 0 & -\Omega\delta(\Delta-\omega_L^{(1)}) & \left(\omega-\omega_e+i\frac{\gamma_e}{2}\right)\delta(\Delta) & 0 \\ 0 & 0 & 0 & (\omega+i\frac{\epsilon}{2})\delta(\Delta) \end{pmatrix}, \tag{4.78}$$

where we used the basis

$$\mathbf{a}_a^{(\mathrm{q,cl})}(\omega,z) = \begin{pmatrix} a_d(\omega,z) \\ a_s(\omega,z) \\ a_e(\omega,z) \\ a_g(\omega,z) \end{pmatrix}^{(\mathrm{q,cl})} \tag{4.79}$$

as well as the shorthand notation $\Delta = \omega - \omega'$. As it turns out, it is far more convenient to transform into a rotating frame, where the states $|e\rangle$, $|s\rangle$ and $|d\rangle$ rotate at frequencies ω_e, $\omega_e - \omega_L^{(1)}$ and $\omega_e - \omega_L^{(1)} + \omega_L^{(2)}$ respectively. Within this frame the atomic Green's function becomes time translationally invariant, that is $G^{-1}_{a,0}(\omega,\omega') = G^{-1}_{a,0}(\omega)\delta(\omega-\omega')$ with

$$\left[G^R_{a,0}\right]^{-1}(\omega) = \begin{pmatrix} \omega-\Delta_d-\Delta_s+i\frac{\gamma_d}{2} & -\Omega_s & 0 & 0 \\ -\Omega_s & \omega-\Delta_s+i\frac{\epsilon}{2} & -\Omega & 0 \\ 0 & -\Omega & \omega+i\frac{\gamma_e}{2} & 0 \\ 0 & 0 & 0 & \omega+i\frac{\epsilon}{2} \end{pmatrix}, \tag{4.80}$$

and the fields shifted accordingly in frequency:

$$\mathbf{a}_a^{(\mathrm{q,cl})}(\omega,z) = \begin{pmatrix} a_d(\omega+\omega_e-\omega_L^{(1)}+\omega_L^{(2)},z) \\ a_s(\omega+\omega_e-\omega_L^{(1)},z) \\ a_e(\omega+\omega_e,z) \\ a_g(\omega,z) \end{pmatrix}^{(\mathrm{q,cl})}. \tag{4.81}$$

Here the detunings $\Delta_s = \omega_e - \omega_L^{(1)} - \omega_s$ and $\Delta_d = \omega_d - \omega_s - \omega_L^{(2)}$ between laser frequencies and atomic transitions have been introduced. In order to avoid confusion, throughout the remainder of this thesis we will exclusively work in the rotating frame. The corresponding Keldysh component of the inverse Green's function

within the same frame of reference is then given by

$$D^K_{a,0}(\omega) = \begin{pmatrix} i\gamma_d & 0 & 0 & 0 \\ 0 & i\epsilon & 0 & 0 \\ 0 & 0 & i\gamma_e & 0 \\ 0 & 0 & 0 & (3-2n_V)i\epsilon \end{pmatrix} . \tag{4.82}$$

It should be pointed out, that the factor $3-2n_V$ in the ground-state sector accounts for the occupation of this mode with a homogeneous number density of lattice defects or vacancies $n_V \in [0,1]$. Thus, for $n_V = 0$ the ground state is homogeneously occupied with one atom per site ($n = -1/2 + i\int \frac{d\omega}{4\pi} G^K = 1 - n_V = 1$).
A similar rotation can also be performed for the retarded and Keldysh component of the inverse photon Green's function, which then are given by

$$\left[G^R_{p,0}\right]^{-1}(\omega,k) = \begin{pmatrix} \omega - \Delta_E(k) + i\frac{\kappa_E}{2} & 0 \\ 0 & \omega - \Delta_P(k) + i\frac{\kappa_P}{2} \end{pmatrix} \tag{4.83}$$

and

$$D^K_{p,0}(\omega,k) = \begin{pmatrix} i\kappa_E & 0 \\ 0 & i\kappa_P + 2i\kappa_s(\omega) \end{pmatrix} \tag{4.84}$$

respectively. Here we expressed both functions in the basis

$$\mathbf{a}^{(\mathrm{q,cl})}_p(\omega,k) = \begin{pmatrix} a_E(\omega + \omega^{(2)}_L, k) \\ a_P(\omega + \omega_e, k) \end{pmatrix}^{(\mathrm{q,cl})} , \tag{4.85}$$

and introduced the detunings $\Delta_P(k) = \omega_P(k) - \omega_e$ and $\Delta_E(k) = \omega_E(k) - \omega^{(2)}_L$. Note that here we have already performed the Gaussian integration over the auxiliary field b, after which the inverse probe photon propagator in general is modified by the subtraction of $g_b^2 G_b(\omega)$. Assuming very strong coupling to the incoherent source, however, κ_1 and κ_2 diverge, while $\kappa_0 = 2(\kappa_1 - \kappa_2)$ and $\kappa_s = 2g_b^2\kappa_1$ are kept finite. In this limit $g_b^2 G^R_b(\omega)$ vanishes, while $\kappa_s(\omega) = -ig_b^2 G^K_b(\omega)/2 = \kappa_s/((\omega-\omega_0)^2 + \kappa_0^2)$ remains finite.
Modeling the situation in PCWs, throughout this chapter we will approximate the dispersion of the exchange photons as parabolic: $\omega^E(k) = \omega^E_0 - \alpha_E(k-k_E)^2$ around the band edge $\omega^E(k_E) = \omega^E_0$, which is assumed to be slightly detuned against the $|s\rangle - |d\rangle$ transition. With this choice the exchange photon spreads diffusively around the emitting atom with an average mode volume and therefore interaction range given by

$$L_E = \sqrt{\alpha_E/\kappa_E} . \tag{4.86}$$

On the other hand, since we are eventually interested in the interaction induced

modifications to the dispersion of the propagating photons, we will require no approximations to the dispersion ω_k^P. As already stressed above, the actual form of the photon dispersion does not play a role.

Making use of the above notation, the non-interacting part of the action $S = S_0 + S_{\rm int}$ can be fully expressed in terms of the bare atomic (subscript a) and photonic (subscript p) Green's functions as

$$S_0 = \hbar \int \frac{d\omega}{2\pi} \left(\sum_z [\mathbf{a}_a]^*(\omega, z) \mathcal{G}_{a,0}^{-1}(\omega) \mathbf{a}_a(\omega, z) + \int \frac{dk}{2\pi} [\mathbf{a}_p]^*(\omega, k) \mathcal{G}_{p,0}^{-1}(\omega, k) \mathbf{a}_p(\omega, k) \right). \tag{4.87}$$

Here the index 0 is meant to indicate the absence of self-energy corrections due to interactions (see below). Furthermore, $\mathbf{a}_\mu = \left\{ \mathbf{a}_\mu^{\rm cl}, \mathbf{a}_\mu^{\rm q} \right\}$ with $\mu \in \{a, p\}$ are the vectors of classical and quantum fields with the corresponding inverse Keldysh matrix Green's functions given by

$$\mathcal{G}_{\mu,0}^{-1} = \begin{pmatrix} 0 & \left[G_{\mu,0}^A\right]^{-1} \\ \left[G_{\mu,0}^R\right]^{-1} & D_{\mu,0}^K \end{pmatrix}. \tag{4.88}$$

Finally, the interaction part of the action reads

$$\begin{aligned} S_{\rm int} = \int \frac{d\omega}{2\pi} \int \frac{dk}{2\pi} \sum_z \\ \Bigg(\frac{1}{\sqrt{2}} g_P \mathrm{e}^{ikz} u_k^P(z) \Big[a_P^{\rm q}(k) \left(\bar{a}_e^{\rm q}(z) a_g^{\rm q}(z) + \bar{a}_e^{\rm cl}(z) a_g^{\rm cl}(z) \right) \\ + a_P^{\rm cl}(k) \left(\bar{a}_e^{\rm cl}(z) a_g^{\rm q}(z) + \bar{a}_e^{\rm q}(z) a_g^{\rm cl}(z) \right) \Big] + \text{h.c.} \\ + \frac{1}{\sqrt{2}} g_E \mathrm{e}^{ikz} u_k^E(z) \Big[a_E^{\rm q}(k) \left(\bar{a}_d^{\rm q}(z) a_s^{\rm q}(z) + \bar{a}_d^{\rm cl}(z) a_s^{\rm cl}(z) \right) \\ + a_E^{\rm cl}(k) \left(\bar{a}_d^{\rm cl}(z) a_s^{\rm q}(z) + \bar{a}_d^{\rm q}(z) a_s^{\rm cl}(z) \right) \Big] + \text{h.c.} \Bigg) \,, \end{aligned} \tag{4.89}$$

where to save space, we have introduced the notation $\bar{a}_i = a_i^*$ for the conjugate transpose of the field a_i. As the atoms are fixed at positions commensurate with the PCW, we can use the periodicity of the dimensionless Bloch functions $u_k^{P,E}(z)$ to replace them by $u_k^{P,E}(0)$. In general, careful engineering of the PCW allows some control over the momentum dependence of $u_k^{P,E}(0)$ [16, 17]. Here we will choose the simplest approximation of a constant, which we then absorb into the coupling via the replacement $g_{P,E}|u_k^{P,E}(0)| \to g_{P,E}$.

In analogy with the scalar case discussed in Sec. 4.1 one can apply Wick's theorem to find the dressed Green's function

$$\mathcal{G}_\mu^{\alpha\beta}(x, x') = \langle \mathbf{a}_\mu^\alpha(x) * \bar{\mathbf{a}}_\mu^\beta(x') \rangle_S \,, \tag{4.90}$$

with $*$ the outer product and $\mu \in \{a, p\}$ as well as $\alpha, \beta = \mathrm{cl}, \mathrm{q}$. Here, as opposed to the bare propagators, the expectation value is taken with respect to the full action S. Expanding the exponent $\mathrm{e}^{iS_{\mathrm{int}}}$ under the path integral, one once again obtains the infinite Dyson series

$$\mathcal{G} = \mathcal{G}_{\mu,0} + \mathcal{G}_{\mu,0} \circ \Sigma_\mu \circ \mathcal{G}_{\mu,0} + \mathcal{G}_{\mu,0} \circ \Sigma_\mu \circ \mathcal{G}_{\mu,0} \circ \Sigma_\mu \circ \mathcal{G}_{\mu,0} + \dots , \tag{4.91}$$

where $\circ$ denotes the convolution in space and time with a simultaneous matrix product in the Keldysh index $\{\mathrm{cl}, \mathrm{q}\}$ as well as the field components g, e, s, d or P, E for the atomic ($\mu = a$) or photonic propagators ($\mu = p$) respectively. Summation of this geometric series for the retarded Green's function gives the same structure as in Sec. 4.1:

$$\begin{aligned} G_\mu^R &= \left(G_{\mu,0}^R - \Sigma_\mu^R\right)^{-1} . \\ G_\mu^K &= G_\mu^R \circ \left(\Sigma_\mu^K - D_{\mu,0}^K\right) \circ G_\mu^A . \end{aligned} \tag{4.92}$$

As $\Sigma_\mu^{R,K}$ in general depend on Keldysh and retarded components of both photonic and atomic Green's functions, these Dyson equations are coupled and have to be solved simultaneously.

4.4.3 Kramers-Kronig relations

Due to causality, each vertex involves either one or three quantum fields. There are thus four copies of each vertex, differing only in the Keldysh index while otherwise being identical. In general, this substructure gives rise to a large amount of Feynman diagrams to be calculated, even after application of the fundamental symmetries derived in Sec. 4.1. Luckily, most of these can be related to one another using Kramers-Kronig relations. In the following we will illustrate how these relations can be exploited. For the sake of compactness of the graphical illustrations, we avoid drawing all possible diagrams so that each line we draw can be a retarded, advanced or Keldysh Green's function, as long as the vertex allows it.

In analogy to our discussion of the scalar field theory, we introduce the distribution function $F(\omega)$ defined by $G^K(\omega) = G^R(\omega)F(\omega) - F(\omega)G^A(\omega)$. Note, that the identification $G^K(\omega) = i\rho(\omega)F(\omega)$ holds only if all Green's functions can be diagonalized simultaneously. Nevertheless, in the absence of particles $F(\omega) = 1$ is always true and thus allows to express the Keldysh component through the retarded Green's function. We will denote this special case of an unoccupied degree of freedom by a subscript 0 attached to the causality index (K) as in G^{K_0}. For these empty modes, invoking Kramers-Kronig relations for the retarded Green's

function

$$\Re G^R(\omega) = \mathcal{P}\int_{-\infty}^{\infty}\frac{d\omega'}{\pi}\frac{\Im G^R(\omega')}{\omega'-\omega}$$
$$\Im G^R(\omega) = -\mathcal{P}\int_{-\infty}^{\infty}\frac{d\omega'}{\pi}\frac{\Re G^R(\omega')}{\omega'-\omega} \tag{4.93}$$

allows to find some simplifications. Indeed, any two Green's functions $G_1(\omega)$ and $G_2(\omega)$ will obey

$$\int_{-\infty}^{\infty}\frac{d\omega'}{2\pi}G_1^{K_0}(\omega')G_2^R(\omega-\omega') = \int_{-\infty}^{\infty}\frac{d\omega'}{2\pi}G_1^R(\omega')G_2^{K_0}(\omega-\omega')$$
$$\int_{-\infty}^{\infty}\frac{d\omega'}{2\pi}G_1^{K_0}(\omega')G_2^R(\omega+\omega') = -\int_{-\infty}^{\infty}\frac{d\omega'}{2\pi}G_1^A(\omega')G_2^{K_0}(\omega+\omega'), \tag{4.94}$$

which follow immediately from (4.93) by splitting the retarded Green's function into real and imaginary part. Additionally, one has

$$\int_{-\infty}^{\infty}\frac{d\omega'}{2\pi}G_1^{K_0}(\omega')G_2^{K_0}(\omega-\omega') = \int_{-\infty}^{\infty}\frac{d\omega'}{2\pi}\left(G_1^A(\omega')G_2^A(\omega-\omega')+G_1^R(\omega')G_2^R(\omega-\omega')\right)$$
$$\int_{-\infty}^{\infty}\frac{d\omega'}{2\pi}G_1^{K_0}(\omega')G_2^{K_0}(\omega+\omega') = -\int_{-\infty}^{\infty}\frac{d\omega'}{2\pi}\left(G_1^A(\omega')G_2^R(\omega+\omega')+G_1^A(\omega')G_2^R(\omega+\omega')\right), \tag{4.95}$$

which are easily proven by applying the Fourier transform to the convolution and using that

$$\mathcal{F}(\mathcal{H}(f)) = -i\,sgn(t)\mathcal{F}(f), \tag{4.96}$$

where f is any function and $\mathcal{H}$ and $\mathcal{F}$ are Hilbert and Fourier transform, respectively.

Similar identities, using the same method, can also be proven for more complicated products and higher order convolutions of Green's functions. Since the bare atomic propagators for all but the ground state, as well as that of the bare exchange photon, are unoccupied, we can use these identities to considerably simplify the following calculations.

4.4.4 Nonlinear Feynman rules

Apart from the Keldysh structure, the interaction part of the action given in (4.89) contains two different types of vertices, both depicted in Fig. 4.9, which under time reversal pairwise transform into one another. Either an atom is excited through the absorption of a photon (see Fig. 4.9a)), or, by the time-reversed process of emitting a photon, the atom returns to a stable state (c.f. Fig. 4.9b)). Using

the vertices, one can draw all Feynman diagrams order by order in the coupling constants. However, in doing so one applies bosonic Feynman rules to atoms, which due to the strong nonlinearities should instead have a restricted Hilbert space with $\sum_{j=g,e,s,d}\langle \hat{a}_j^\dagger \hat{a}_j\rangle = 1$. This implies that each atom occupies either only one level or in general a properly restricted superposition. One therefore has to be careful not to overcount diagrams by simultaneously placing an atom in the same state twice (which would be allowed for bosons). This means that, at every point in time and in every diagram, two counter propagating atomic lines belonging to the same atom have to be found in distinct levels, or must otherwise be identified with one another, i.e. their lines in the Feynman diagram have to be contracted.

In general it is very hard to fully enforce these conditions, as one would need to implement increasingly complicated restrictions in real-time on each and every perturbation to the bare scalar Green's functions. Doing so for all diagrams would eventually restore the exact, finite Fock space of the atoms. Here, we instead limit ourselves to impose restrictions allowing to exactly compute the fully dressed, single probe photon propagator in the absence of the state $|d\rangle$.

As we will see, the insertion of self-energies in the form of polarization bubbles – which are diagrams of the type shown on the right of Fig. 4.6a) – into the bare probe photon Green's function will hybridize this propagating photon mode with stationary atoms, forming polaritons in the process. Without state $|d\rangle$, and without saturation effects these polaritons will not interact among each other. When introducing polariton-polariton interactions via coupling to $|d\rangle$ it is then of paramount importance to expand around the correct limit of non-interacting polaritons, which will only by ensured by the implementation of the above restrictions imposed by nonlinear Feynman rules. In the non-interacting regime, where the polariton self-energy is given by a polarization bubble with the external laser fields mixing states $|e\rangle$ and $|s\rangle$ and the probe photons mixing $|g\rangle$ and $|e\rangle$, it suffices to demand that any two counterpropagating Green's functions of the same atom have to involve disjoint sets of states. All diagrams where this is not the case are simply set to zero.

We now show that these simplified nonlinear selection rules correctly capture the retarded polariton Green's function. The latter reads

$$G_P^R(\omega,k) = \left(G_{P_0}^R(\omega,k)^{-1} - \Sigma_P^R(\omega)\right)^{-1} , \tag{4.97}$$

with the self-energy given by

$$\Sigma_P^R(\omega) = \frac{ig_P^2}{2}\int \frac{d\omega'}{2\pi}\left(G_e^K(\omega+\omega')G_g^A(\omega') + G_e^R(\omega+\omega')G_g^K(\omega')\right) . \tag{4.98}$$

We now make use of the Kramers-Kronig relations (4.94) and realize that only

diagrams with either $F_g(\omega) \neq 1$ or $F_e(\omega) \neq 1$ are finite, and thus

$$\Sigma_P^R(\omega) = \frac{ig_P^2}{2} \int_{-\infty}^{\infty} \frac{d\omega'}{2\pi} \left(\delta G_g^K(\omega') G_e^R(\omega + \omega') + G_g^A(\omega') \delta G_e^K(\omega + \omega') \right) , \quad (4.99)$$

where $\delta G^K(\omega) = G^K(\omega) - 2i\Im G^R(\omega)$ is related to the spectral number density by $n(\omega) = i\delta G^K/2$. However, as the atomic medium without probe photons is entirely in the ground state and no atoms are being created, the only way to get $\delta G_e^K(\omega) \neq 0$ is by coupling to $\delta G_g^K(\omega)$. On the other hand, corrections to the bare ground-state propagator all inevitably have to involve the excited state $|e\rangle$.

To compare the effect of the exact and simplified nonlinear Feynman rules, consider the perturbative insertion of corrections into the bare retarded Green's functions:

$$G^R(t,t') = G_0^R(t,t') + \int dt_1 \int dt_2 G_0^R(t,t_1) \Sigma^R(t_1,t_2) G_0^R(t_2,t') + \dots , \quad (4.100)$$

which due to causality are non-zero only if $t > t_1 > t_2 > t'$. Consequently, none of the Green's functions and self-energies can be evaluated simultaneously and no cancellations due to the nonlinear Feynman rules are required. Similarly, the Keldysh component of the interacting Green's function is given by

$$\delta G^K(t,t') = \int dt_1 \int dt_2 G^R(t,t_1) (\delta \Sigma^K(t_1,t_2) - \delta D_0^K(t_1,t_2)) G^A(t_2,t'), \quad (4.101)$$

where $\delta D_0^K = D_0^K - 2i\Im\left(\left[G_0^R \right]^{-1} \right)$ and $\delta \Sigma^K(t_1,t_2) = \Sigma^K(t_1,t_2) - 2i\Im\Sigma^R(t_1,t_2)$ have been introduced. Due to the retarded and advanced Green's functions one has $t > t_1$ and $t' > t_2$. Clearly those insertions with $t_1 < t'$ have to be discarded, as then, between these times, the retarded and advanced Green's function of the same state counterpropagate. With this restriction in place $\delta \Sigma^K(t_1,t_2)$ has to be evaluated at t', which is necessarily simultaneous with the retarded Green's function of the other state in the polarization bubble, and the diagram again has to be removed. In the end, as only the ground state satisfies $\delta D_0^K \neq 0$, we are left with the simple result

$$\Sigma_P^R(\omega) = \frac{ig_P^2}{2} \int_{-\infty}^{\infty} \frac{d\omega'}{2\pi} \delta G_{g,0}^K(\omega') G_e^R(\omega + \omega') , \quad (4.102)$$

where in Σ_e^R no dependence on G_g is allowed. For the Keldysh component of the polariton self-energy one has, due to the Kramers-Kronig relations (4.95),

$$\delta \Sigma_P^K(\omega) = \frac{ig_P^2}{2} \int_{-\infty}^{\infty} \frac{d\omega'}{2\pi} \left(2G_g^{K_0} + \delta G_{g,0}^K(\omega') \right) \delta G_e^K(\omega + \omega') . \quad (4.103)$$

Following a similar argument as above, one can show that this contribution vanishes

once either the full or the simplified nonlinear selection rule is applied. As these arguments can be continued order by order in the coupling constants, we find that for non-interacting polaritons both selection rules coincide. For an alternative proof that electromagnetically induced transparency in the limit of low polariton densities is exactly recovered by the simplified nonlinear Feynman rules see Appendix B. Furthermore, we emphasize, that neglecting dephasing of the excited atomic states is no restriction to the applicability of the field theoretic description, because for low polariton densities, dephasing and decay are indistinguishable (see Sec. 4.2).

For higher order diagrams of the probe photon propagator that involve the exchange photon, as well as for the polarization bubble of the exchange photon itself, these new simplified Feynman rules do not work quite as well. The reason for this lies in the fact that both states $|s\rangle$ and $|d\rangle$ that necessarily appear in the polarization bubble of an exchange photon, have non-vanishing self-energies. In real time these insertions into the bare propagators can then partially exclude each other, meaning that the simplified nonlinear Feynman rules no longer correctly capture the polarizability of the atoms. However, if the effective coupling rate between states $|s\rangle$ and $|d\rangle$ is small compared to γ_d, the excited atom will likely have decayed before it can be transferred into another state. To ensure this, we will exclusively work in a regime of small Ω_s/γ_d. Note, however, that this condition will be significantly modified upon inclusion of strong interpolariton interactions, wherefore we will also require $\left(\Omega_s^{\text{eff}}\right)^2/(\gamma_d^{\text{eff}}\gamma_s^{\text{eff}}) \ll 1$ for the fully dressed quantities.

In order to test that the choice of the specific implementation of the nonlinear Feynman rules – of which many different versions can be constructed – does not affect the results, we compare the two extreme options. One is the most strict implementation of the Feynman rules, where all diagrams that could at least partially be forbidden are entirely excluded. The other option corresponds to the opposite choice, where all at least partially allowed diagrams are fully included. In the following, we will refer to these two options as the "strict" and "lenient" implementation of the Feynman rules. If we observe no difference between the results from both options, the ambiguity in the nonlinear Feynman rules is of no quantitative significance and either version can be used to provide a lowest order approximation to the actual (time-dependent) selection rules.

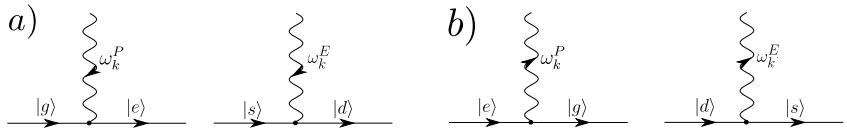

Figure 4.9: Yukawa-type interaction vertices form the fundamental building blocks of QED with neutral atoms and guided photons.

In summary, the nonlinear Feynman rules outlined here partially compensate the unphysical tendency of the bosonized atoms to bunch together with the photons.

As long as the number density of excited atoms is small compared to that of the ground state, saturation effects of the atomic medium can be neglected and no further selection rules have to be implemented. While this restriction to the selection of diagrams might seem complicated to enforce consistently, we will see that it actually simplifies the Feynman diagrams.

4.4.5 Loop reduction

Beyond the Kramers-Kronig relations, a further significant simplification can be achieved by noting that the atomic ground state has no dynamics of its own. Hence any loop involving the bare Keldysh component of the ground-state propagator can be computed trivially[1]. In and of itself this is not a particularly useful observation. In combination with the Kramers-Kronig relations and the nonlinear Feynman rules introduced in the last subsections, however, several loop integrals can be computed exactly.

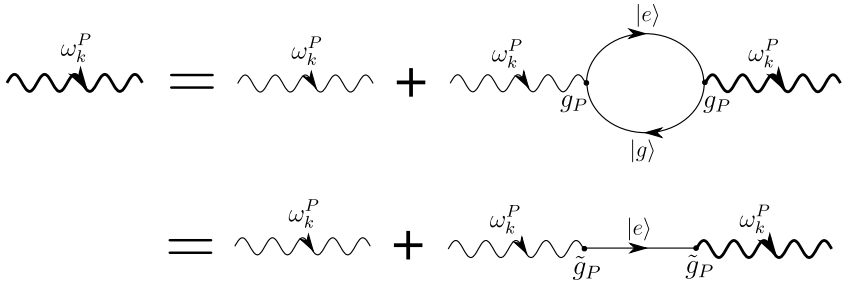

Figure 4.10: The Probe photon propagator to leading order in $1/L_P$ can be simplified significantly using the loop reduction procedure.

To better understand how all of these properties come together, let us consider the case of a probe photon propagating through any polarizable medium. This process to leading order in $1/L$ is described by the diagrammatic equation in Fig. 4.10. Here the propagator of the excited state cannot be specified further, since interactions with other excited atoms can and will dress it. The ground-state propagator on the other hand only couples to other states via the absorption of a probe photon. Employing the Feynman rules of section 4.4.4, it will thus always be described by the bare Green's function. Consequently, the diagram of Fig. 4.10 for the retarded probe photon propagator is solved by (4.97) and (4.102). Since furthermore $G^K_{g,0}(\omega) = -2\pi i(3-2n_V)\delta(\omega)$, the remaining integral can then be solved immediately, such that one finally obtains

$$\Sigma^R_P(\omega) = g_P^2(1-n_V)G^R_e(\omega)\,, \tag{4.104}$$

[1]The retarded component instead contains an Heaviside theta and is thus still time-dependent.

completely independent of the form of the interactions between excited states. A similar calculation gives the equivalent result

$$\delta\Sigma_P^K(\omega) = g_P^2(2 - n_V)\delta G_e^K(\omega) \tag{4.105}$$

for the Keldysh component of the self-energy. Hence, the result for the polarization bubble is the same as for a bilinear coupling converting a photon into an excited atomic state, albeit with the modified coupling constant $\tilde{g}_P = g_P\sqrt{2 - n_V}$. This identification changes the topology of diagrams. However, quite importantly the ordering in powers of the inverse interaction range remains unaffected. Note that, despite the extremely long lifetime of the meta-stable state $|s\rangle$, due to the static laser field coupling to states $|e\rangle$ and $|d\rangle$ the corresponding Keldysh component $G_s^K(t - t')$ explicitly depends on time and a similar identity for particle hole loops involving $|s\rangle$ is not quite as useful.

4.4.6 Self-consistence and conserving approximations

We have already mentioned in Sec. 4.1, that in a field theoretic description the integrals of motion of a system are only conserved within the so called conserving approximations, which themselves can be derived from an appropriate thermodynamic functional and always result in self-consistent theories, where all self-energy insertions are repeated in every internal Green's function. Conversely, any approximation can easily be tested for its conserving properties by contracting all self-energies with the corresponding Green's functions obtained via the Dyson equations. If the result can be written as an action with the appropriate symmetries, the dynamics are conserving.

In the present case it is unfortunately impossible to build a proper functional, since it would be incompatible with the approximate nonlinear Feynman rules introduced above. Having a conserving approximation in our case is however not crucial. This is a consequence of the incoherent, transversal drive and Markovian losses of the full, microscopic theory introduced in Sec. 4.4.1. These neither conserve energy nor quasi-momentum. Therefore, the only conserved quantity is the total number of atoms, which we approximately enforce, at least on average, by means of the nonlinear Feynman rules. While dropping these would allow to construct a self-consistent 2PI effective action, the resulting theory would not conserve the atom number either, since the approximate formulation of radiative decay in Eqs. (4.70) explicitly breaks the corresponding symmetry of the atomic sector under the $U(1)$ transformation $\hat{\mathbf{a}}_a \to \hat{\mathbf{a}}_a \mathrm{e}^{i\phi}$ and $\hat{\mathbf{a}}_a^\dagger \to \hat{\mathbf{a}}_a^\dagger \mathrm{e}^{-i\phi}$. Instead of trying to enforce conservation laws on a microscopic level, we will largely make use of self-consistent solutions of our Dyson equations in order to include the important non-perturbative effects.

4.5 Leading order: Polaritons and electromagnetically induced transparency

As was already explained in Sec. 4.4.5, if there is no interaction between different atoms, other than via the exchange of probe photons, the probe photon propagator is fully given by the solution to the diagrammatic equation in Fig. 4.10. Of course, this is only true in the case of a low excitation density in the atomic medium, since otherwise saturation effects will induce further interactions between probe photons that are not captured by the present approach (see Appendix B). In this low excitation density limit however, the retarded photon propagator G_P for $g_E = \Omega_s = 0$ can be directly obtained from Eqs. (4.97) and (4.104), where

$$\begin{aligned} G_e^R(\omega) &= G_{e,0}^R(\omega) = \frac{1}{\omega - \frac{\Omega^2}{\omega - \Delta_s + i\epsilon/2} + i\gamma_e/2} \\ G_e^K(\omega) &= G_{e,0}^K(\omega) = -2i\Im G_{e,0}^R(\omega) \end{aligned} \tag{4.106}$$

are the components of the bare propagators of the excited state $|e\rangle$ obtained by inverting $\left[G_{a,0}^R\right]^{-1}$ in Eq. (4.80). Without any coupling to state $|d\rangle$ the atomic level scheme is identical to the well-known Λ-scheme, which in the limit of vanishing excitation density has already been discussed in Sec. 4.2. One should note that the solution we give here involves no approximations beyond the linearization of the spin degree of freedom, which we showed in Sec. 4.4.4 to be fully compensated by simple nonlinear Feynman rules. As such, it is not surprising that the results will be identical with those obtained in Sec. 4.2.

In particular, one can immediately identify G_e^R with the polarizability of the medium. Hence, as pointed out earlier, G_P^R no longer describes free photons, but the eigenmodes of the system, which are photons hybridized with the medium. The dispersion of these new degrees of freedom, the polaritons, has three branches resulting from the coupling of two atomic transitions and the photonic dispersive mode, which far away from the atomic resonance Δ_e is essentially that of the free photon. Due to the vanishing losses of state $|s\rangle$, however, the central branch – the so called dark-state polariton, which is a combination of a photon and an atom in state $|s\rangle$ without any admixture of the lossy $|e\rangle$ – is very long lived. Within the path integral description, the trivial calculation leading to Eq. (4.106) thus captures the phenomenon of EIT. On a more pedagogical note, the destructive interference at the heart of EIT becomes particularly apparent upon inspection of the diagrammatic expression for G_e shown in Fig. 4.11.

Since the dark-state polariton is a linear superposition of a localized atom and propagating photon, its group velocity can be tuned by adjusting the ratio Ω/g_P. However, without losses in state $|s\rangle$, the line-width is modified at the same rate, such that the penetration depth of photons into the waveguide is not affected. This can be easily verified by comparing the group velocity of the dark-state polariton

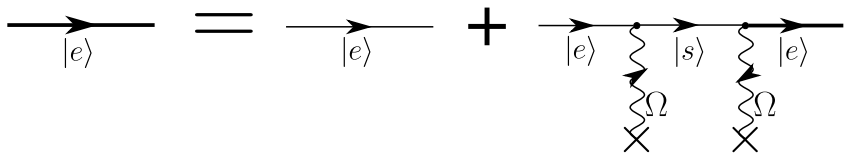

Figure 4.11: Dyson equation for G_e in the polarization bubble. The interference between the direct excitation of an atom to state $|e\rangle$ and the indirect path via $|s\rangle$ gives rise to EIT.

with its line-width. Linearizing the dispersion of the free photons, which on the energy scale of the susceptibility of the medium (set by γ_e) is typically well justified, the group velocity can be determined from the pole of the polariton Green's function $G_P^R(\omega, k)$ given by Eqs. (4.97), (4.104) and (4.106). In the limit of mostly atomic polaritons, where the ratio between atomic and photonic contributions to the polariton $\theta = g_P^2(1 - n_V)/\Omega^2$ becomes large, an expansion around the EIT window results in the condition

$$\left[G_P^R(\omega, k)\right]^{-1} = \theta^{-1}(\omega - \Delta_s) - v_P(k - k_{\mathrm{EIT}}) + i\eta(\omega - \Delta_s)^2 + i\kappa_P/2 = 0 \,, \tag{4.107}$$

where v_P is the local group velocity of the bare photon near the resonance at $k = k_{\mathrm{EIT}}$ with the laser acting on the $|s\rangle - |e\rangle$ transition. Furthermore we have introduced the convenient abbreviation $\eta = \gamma_e\theta/(2\Omega^2)$. At the center of the EIT window the group velocity is given by

$$v_g = \frac{d\omega_{\mathrm{res}}}{dk} = \frac{v_P}{\sqrt{\theta^2 + 2\eta\kappa_P}} \sim \Omega^2 \,, \tag{4.108}$$

where ω_{res} satisfies the condition (4.107). This result is clearly equivalent to the group velocity previously obtained by the ansatz (4.64). On the other hand, at k_{EIT} the line-width of the dark-state polariton is given by

$$\Delta\omega = \frac{\sqrt{-\theta^2 - \eta\kappa_P + \sqrt{\theta^4 + 2\eta\theta^2\kappa_P + 2\eta^2\kappa_P^2}}}{\sqrt{2}\eta} \sim \Omega^2 \,. \tag{4.109}$$

Expanding around large θ, we find

$$\begin{aligned} v_g &\approx v_p \frac{\Omega^2}{g_P^2(1 - n_V)} = \frac{v_p}{\theta} \\ \Delta\omega &\approx \frac{\Omega^2\kappa_P}{2g_P^2(1 - n_V)} = \frac{\omega_p}{\theta} \end{aligned} \tag{4.110}$$

and therefore

$$\frac{v_g}{\Delta\omega} = \frac{2v_P}{\kappa_P} \,, \tag{4.111}$$

which agrees with the result for the free photon. Consequently, the effective probe photon interaction range

$$L_P = v_P/\kappa_P \tag{4.112}$$

is unaffected by the formation of dark-state polaritons and the accompanying reduction of the group velocity. Independent of the mixing angle θ the inverse interaction range thus remains a small parameter suitable for a perturbative expansion. Note that at fixed g_P both the group velocity and line-width of the dark-state polariton can be conveniently tuned by adjusting the Rabi amplitude Ω. We illustrate this by showing a logarithmic density plot of the frequency and momentum resolved number density of polaritons $n_P(\omega, k)$ in Fig. 4.12, where the increase in group velocity and decay rate with growing Ω are clearly visible.

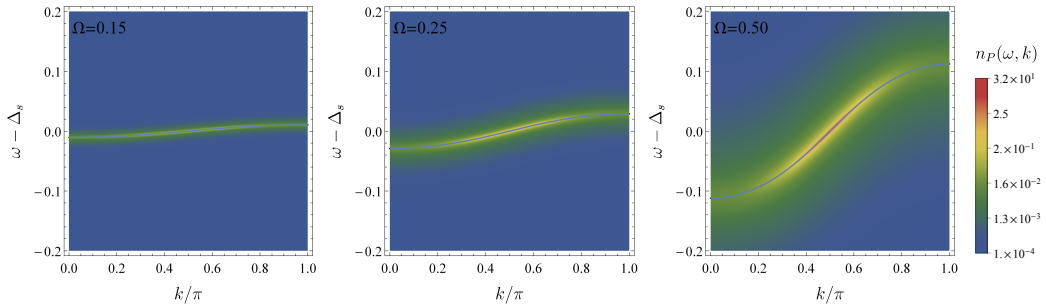

Figure 4.12: Frequency and momentum resolved number density in the vicinity of the EIT condition. The corresponding dispersion of the dark-state polariton has been added in the form of a blue line. The parameters used are $\kappa_0 = 2$, $\kappa_s = 1$, $\omega_0 = \Delta_s = \Delta_d = n_V = 0$, $g_P = 10$, $\kappa_P = 0.5$, $\gamma_e = \gamma_d = 1$ and $\Delta_P(k) = -50\cos k$.

In the absence of the fluctuation-dissipation theorem the distribution function F introduced in Sec. 4.4.3 becomes an interesting quantity as it measures the strength of the drive that a given degree of freedom experiences, independent of its actual susceptibility. As the atoms and Lindblad operators are assumed to be distributed homogeneously in space, F_P is independent of momentum. In Fig. 4.13 we illustrate that despite the broad drive by $\kappa_s(\omega)$, the distribution function of the dark-state polariton has a very sharp peak centered around the resonance with the laser on the $|e\rangle - |s\rangle$ transition, where it reaches the maximally possible value $F_P(\Delta_s) = 2\kappa_s/\kappa_P + 1$.

Let us now see how the properties of the EIT-polaritons are affected by coupling the state $|s\rangle$ to $|d\rangle$ via the laser with Rabi frequency Ω_s, but still in the absence of E photons. In this case, the Green's function G_P^R remains exactly computable in the limit of vanishing polariton density, however now the polarizability is given by the continued fraction

$$G_e^R(\omega) = \frac{1|}{|\omega + i\gamma_e/2} - \frac{\Omega^2|}{|\omega - \Delta_s + i\epsilon/2} - \frac{\Omega_s^2|}{|\omega - \Delta_s - \Delta_d + i\gamma_d/2}\,. \tag{4.113}$$

Since the admixture of $|d\rangle$ to $|s\rangle$ introduces losses $\gamma_s^{\text{eff}} \approx \Omega_s^2\gamma_d/(\Delta_d^2 + \gamma_d^2/4)$ to the metastable atomic state – and therefore to the dark-state polariton – without increasing its group velocity, the waveguide is no longer fully transparent. With slow polaritons being mostly atomic it is clear that already a very small Rabi amplitude Ω_s drastically increases the opaqueness of the waveguide. This is captured by the suppression of the peak in the distribution function in Fig. 4.13. Faster and therefore broader EIT polaritons are much less susceptible and thus the maximal value of $F_P(\omega) - 1$ once again approaches $2\kappa_s/\kappa_P + 1$ for $\Omega \to \infty$, whereas it drops to the typically much smaller value $2\kappa_s/(4g_P^2(1 - n_V)/\gamma_e + \kappa_P) + 1$ as $\Omega \to 0$ (see Fig. 4.14).

4.6 Next-to-leading order: Interactions between polaritons

The strong dependence of EIT polaritons at large θ on the properties of the metastable state $|s\rangle$ can be exploited to enhance the effect of interactions. However, one quickly realizes that to leading order in $1/L$, that is to say simultaneously in $1/L_E$ and $1/L_P$, the polaritons cannot interact. Indeed, to order $(1/L)^0$ the only interaction is a Hartree self-energy for the s-propagator of the type shown in the last diagram of Fig. 4.6b). While one can include arbitrarily many Hartree insertions (two in the above figure), as soon as a photon insertion of the type shown in the second diagram of Fig. 4.6b) appears in an atomic line, it will necessarily induce a suppression by $1/L$. Avoiding this will in particular exclude the appearance of any atomic g- or photonic P-propagators in self-energies to the s-propagator, and therefore prevent us from populating the $|s\rangle$ or the $|d\rangle$ level. The latter are not directly pumped and consequently, without $\mathcal{O}(1/L)$-insertions, empty. The distribution functions $F_{s,d}(\omega)$ are thus identical to one, which means that all particle-hole diagrams, and in particular all Hartree diagrams vanish. This is nothing else than the statement that there can be no interaction between atoms in state $|s\rangle$ if that level is not populated.

Therefore, in our expansion, interactions between polaritons only start to play a role at $\mathcal{O}(1/L)$ and the leading order investigated in the last section is indeed a theory of non-interacting polaritons. All the diagrams for the P-photon self-energy up to order $1/L$ are shown in Fig. 4.15. Note that the version of diagram c) with the E-propagator substituted by a P-propagator has to be excluded according to

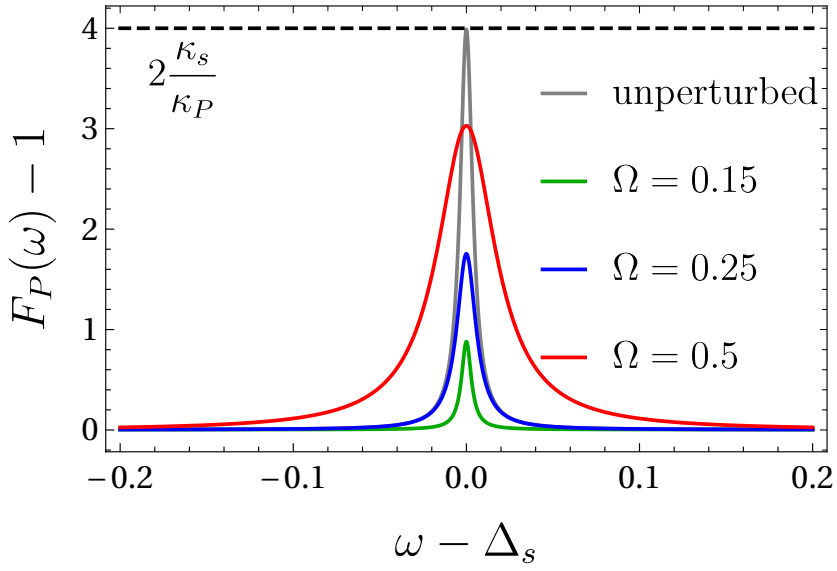

Figure 4.13: Distribution function of the perturbed dark-state polariton in the vicinity of the EIT condition at the same parameters as in Fig. 4.12 and $\Omega_s = 0.01$. Clearly the occupation of the slower polaritons is more strongly suppressed by the induced losses. For comparison we also added (in grey) the distribution function of the unperturbed EIT polaritons (i.e. $\Omega_s = 0$) for $\Omega = 0.25$.

the Feynman rules discussed in section 4.4.4. In general, the order of a diagram is given by $(1/L)^n$, where n is the number of total loops minus the number of atomic loops.

The fact that interactions take place at higher loop-order is a generic feature of polaritons formed by hybridizing probe photons with internal atomic excitations: If the atoms are initialized in the ground state and only probe photons are capable of exciting this initial configuration, then one will first need to populate the interacting atomic level, before atoms – and thus polaritons – can interact.

4.7 The limit of long-ranged atom-atom interactions

In practice quantitative simulations have predicted the interaction range to reach values of $L_E \simeq 100a$ [250] for experimentally realized parameters [260]. We therefore begin our discussion of interacting polaritons with the limit of infinite ranged exchange photons ($L_E \to \infty$), where all diagrams can be resummed completely, resulting in a fully controlled field theory of a non-equilibrium system with strong light matter interactions. In this case, no further assumptions regarding L_P are

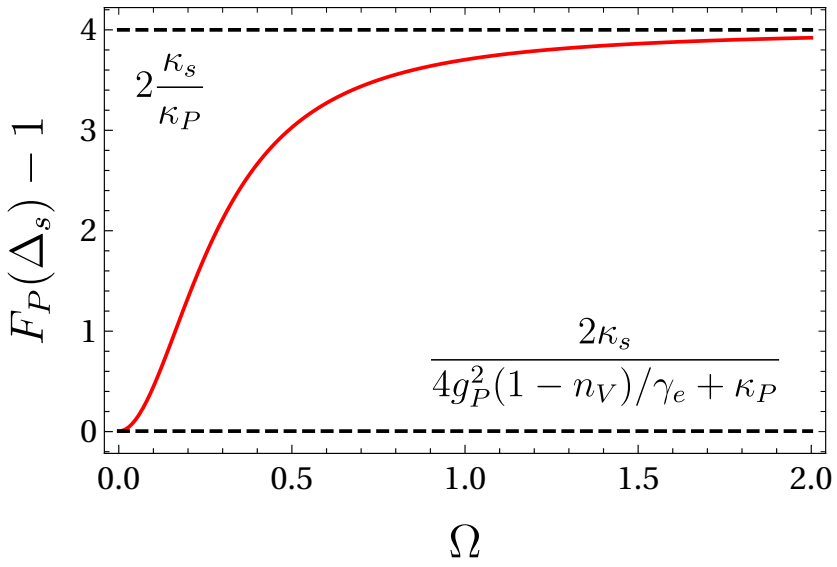

Figure 4.14: Using the same parameters as in Fig. 4.13, the EIT window is mostly destroyed for $\Omega \lesssim 0.2$, despite the very weak coupling to the lossy state $|d\rangle$. On the other hand polaritons with $\Omega \gtrsim 1$ are largely unaffected.

required. In particular, we are allowed to enter the regime of large single-atom cooperativities with respect to the propagating photons. We shall see that new phases emerge and that the corresponding phase transitions can be described in a quantitative manner. Before presenting the full theory in the $L_E \to \infty$ limit, we first demonstrate a simplified version of the diagrammatics that allows for an enhanced polariton density stabilized by dissipative interactions, which is the crucial physical ingredient for obtaining emergent new phases.

4.7.1 Reduced theory for dissipatively-interacting polaritons

In the present section we will consider only a particular subclass of the next-to-leading order interactions which does not involve momentum transfer between photons or equivalently between polaritons. In fact, we apply this restriction to all internal photon loops as well. The only diagram of this subclass contributing to the P-photon self-energy is shown in Fig. 4.15a). We will see that such a Hartree-like term can have very interesting effects on the polariton transparency window and induce a phase transition in the steady state. Importantly, while this reduced set of diagrams will not yield quantitative results for the experimentally relevant regime of slow polaritons, it helps to illustrate many useful physical concepts and provides a simple application of the techniques outlined in Sec. 4.4. We therefore employ it

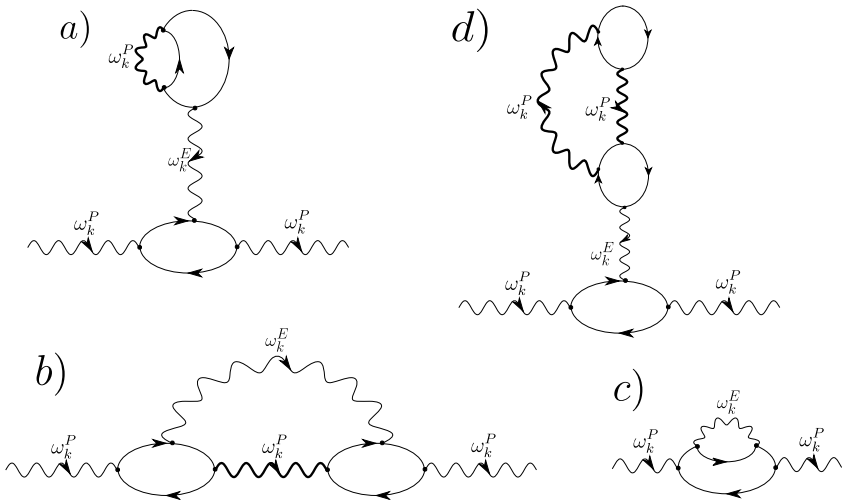

Figure 4.15: All contributions to the polariton self-energy at next-to-leading order in $1/L$. The bold lines for the probe photon indicate that all powers of the leading order polarization bubble (see Fig. 4.10) have to be inserted as well. For the purpose of clarity, we are not specifying the atomic states and also not using the loop-reduction simplification illustrated in section 4.4.5.

as an instructive introduction into the theory of strongly interacting polaritons.

Self-consistent Dyson equations

We begin with the simultaneous expansion in $1/L_E$ and $1/L_P$, which in next to leading order results in the diagrams shown in Fig. 4.15. Of these diagrams a) and d) are suppressed by $1/L_P$, c) is proportional to $1/L_E$ and b) depends on a combination of both lengths that approaches $1/\max(L_E, L_P)$ if both length scales differ a lot. Consequently, with $L_E \to \infty$ only diagrams 4.15a) and d) need to be considered. In a perturbative expansion, that is if the single-atom cooperativity obeys$C_P = g_P^2/(\kappa_P \gamma_e L_P) \ll 1$, no self-consistent treatment, apart from the resummation of all RPA diagrams that give rise to EIT, is required. At the same time, these weak interactions only sightly perturb the bare EIT and no qualitatively new effects are encountered as these require coupling strengths that are large enough to compensate for the bare $|s\rangle$ to $|d\rangle$ coupling Ω_s, thereby breaking the strict confines of the $1/L_P$-expansion (see Sec. 4.7.1). We therefore extend our analysis to strong single-atom cooperativities, where all diagrams of the same class as 4.15a) and d) have to be taken into account. As this becomes somewhat involved, we will introduce the idea of the self-consistent resummation of a class of diagrams and the resulting physical consequences first by using only the diagram in 4.15a). With

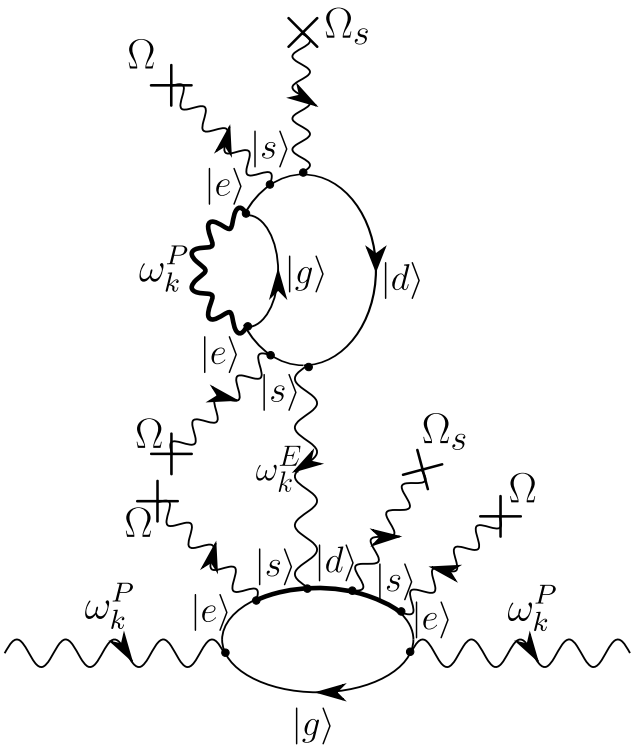

Figure 4.16: Same diagram as in Fig. 4.15a), but with all propagators and external fields labeled explicitly.

all couplings to external lasers made explicit, this diagram takes the form shown in Fig. 4.16. Clearly, every $|s\rangle - |d\rangle$ transition can either be directly driven by a laser acting on a single atom, as is the case in the second transition in the lower loop in Fig. 4.16, or by the exchange of an E-photon with another atom that in turn couples to the laser, which is realized for the excitation from $|s\rangle$ to $|d\rangle$ in the lower loop of Fig. 4.16. The interchangeability of the single- and multiple-atom processes gives rise to an infinite set of diagrams that is conveniently captured by a self-consistent treatment of the skeleton diagram.

The resulting approximation is depicted diagrammatically in Fig. 4.17. As we explain in the following, the corresponding self-consistent Dyson equations can be simplified such that they require finding only a single number χ as the solution of a nonlinear integral equation.

In close analogy to the formalism of Sec. 4.5, the probe photon Green's functions

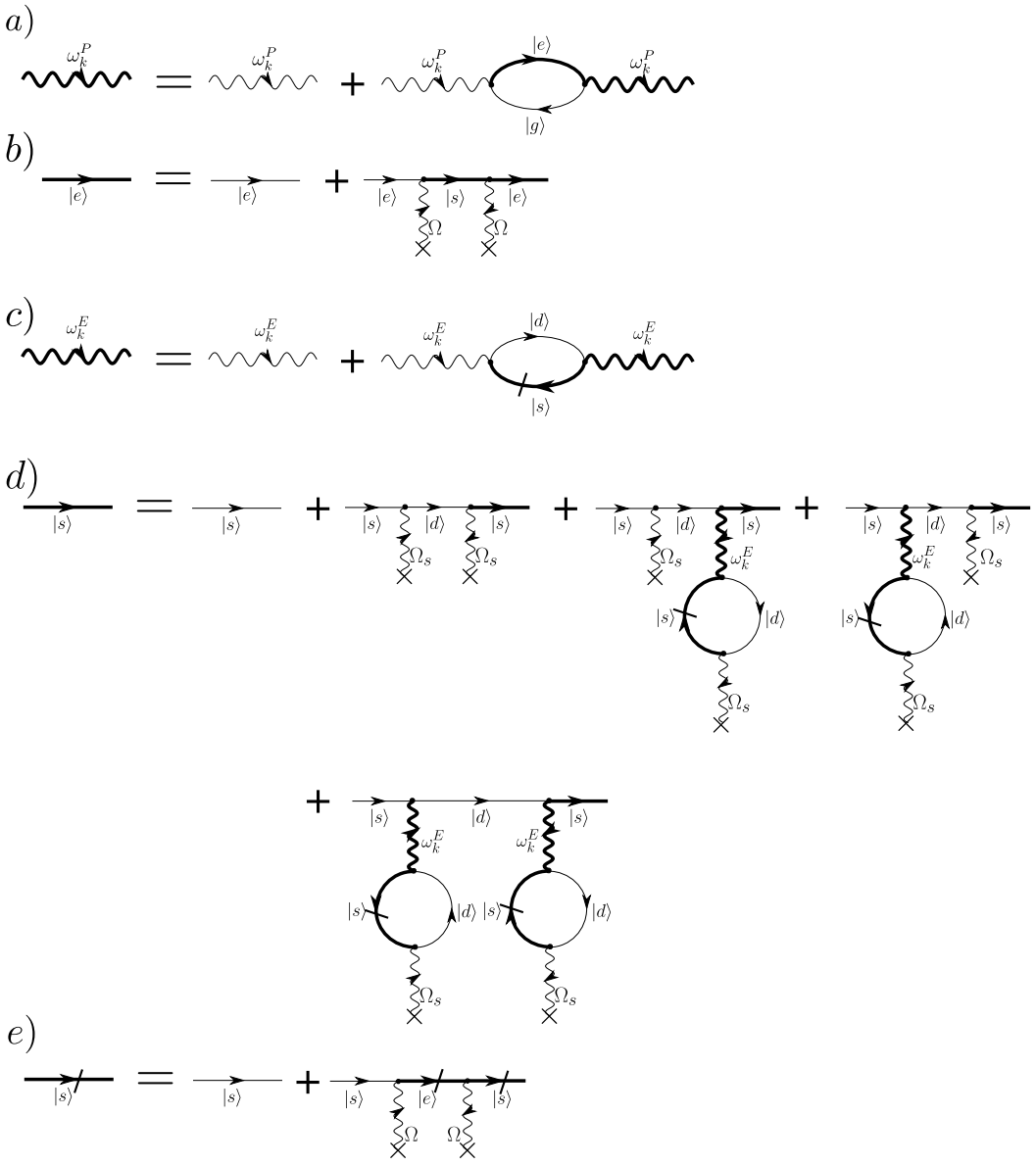

Figure 4.17: Diagrammatic representation of the Dyson equations in the reduced Hartree-like approximation. The latter neglects all interaction diagrams at next-to-leading order except that in Fig. 4.16a). For the purpose of clarity, we refrain from using the loop-reduction simplification introduced in section 4.4.5.

are dressed by excitations induced in the medium. The result

$$\begin{aligned} G_P^R(\omega,k) &= \left[G_P^A(\omega)\right]^* = \frac{1}{\omega - \Delta_P(k) - \Sigma_P^R(\omega,k) + i\kappa_P/2} \\ G_P^K(\omega,k) &= G_P^R(\omega,k)\left(\Sigma_P^K(\omega,k) - i\kappa_P - 2i\kappa_s\right) G_P^A(\omega,k) \end{aligned} \tag{4.114}$$

is therefore still fully determined by the polarization bubble, which using the Kramers-Kronig relations can again be put in the closed form

$$\begin{aligned} \Sigma_P^R(\omega,k) &= \frac{g_P^2(1-n_V)}{\omega - \Omega^2 G_s^R(\omega) + i\gamma_e/2} \\ \Sigma_P^K(\omega,k) &= 2i\Im\Sigma_P^R(\omega,k)\,. \end{aligned} \tag{4.115}$$

However now the propagator of state $|s\rangle$

$$G_s^R(\omega) = \left[G_s^A(\omega)\right]^* = \frac{1}{\omega - \Delta_s - \Sigma_s^R(\omega) + i\epsilon/2} \tag{4.116}$$

has a modified coupling to state $|d\rangle$:

$$\Sigma_s^R(\omega) = \frac{\left(\Omega_s^{\text{eff}}\right)^2}{\omega - \Delta_d - \Delta_s + i\gamma_d/2}\,, \tag{4.117}$$

where $\Omega_s^{\text{eff}} = \Omega_s\,|1+\chi|$ includes the effects of the direct coupling rate Ω_s as well as those due to the interactions. Here χ is simply a complex number, which stems from the fact that the exchange photon mediating the interaction between different polaritons carries zero momentum and – in the rotating frame – zero frequency as well.

In the polarization bubbles of the exchange photon the nonlinear Feynman rules forbid a dressing of G_s by $|d\rangle$, which thus requires the definition of a second type of s-propagator

$$G_{\not s}^R(\omega) = \left[G_{\not s}^A(\omega)\right]^* = \frac{1}{\omega - \Delta_s - \Sigma_{\not s}^R(\omega) + i\epsilon/2} \tag{4.118}$$

that couples exclusively to $|e\rangle$, which in turn can emit and reabsorb a probe photon. This is accounted for by defining

$$\Sigma_{\not s}^R(\omega) = \frac{\Omega^2}{\omega - \Sigma_e^R(\omega) + i\gamma_e/2} \tag{4.119}$$

and

$$\begin{aligned}\Sigma^K_{\not g}(\omega) &= 2i\Im\Sigma^R_{\not g}(\omega) + \delta\Sigma^K_{\not g}(\omega)\\ \delta\Sigma^K_{\not g}(\omega) &= \frac{\Omega^2\left(\Sigma^K_e(\omega) - 2i\Im\Sigma^R_e(\omega)\right)}{\left(\omega - \Re\Sigma^R_e(\omega)\right)^2 + \left(\gamma_e/2 - \Im\Sigma^R_e(\omega)\right)^2}\,.\end{aligned} \tag{4.120}$$

Here the self-consistency loop closes, as the self-energy Σ^R_e depends on the probe photon propagator via

$$\Sigma^R_e(\omega) = \frac{i}{2}g_P^2\int_{-\infty}^{\infty}\frac{d\omega'}{2\pi}\int_{-\pi}^{\pi}\frac{dk}{2\pi}\left[G^R_P(\omega-\omega',k)G^K_g(\omega') + G^K_P(\omega-\omega',k)G^R_g(\omega')\right] \tag{4.121}$$

and

$$\delta\Sigma^K_e(\omega) = \Sigma^K_e(\omega) - 2i\Im\Sigma^K_e(\omega) = \frac{i}{2}g_P^2\int_{-\infty}^{\infty}\frac{d\omega'}{2\pi}\int_{-\pi}^{\pi}\frac{dk}{2\pi}\delta G^K_P(\omega-\omega',k)\delta G^K_g(\omega')\,, \tag{4.122}$$

As announced at the beginning of this section, the self-consistent functional equations $G^R_{P,\star} = G^R_P\left[G^R_{P,\star}, G^K_{P,\star}\right]$ and $G^K_{P,\star} = G^K_P\left[G^R_{P,\star}, G^K_{P,\star}\right]$ have been reduced to a single parameter satisfying a fixed point equation $\chi_\star = \chi(\chi_\star)$. As mentioned before, this is in part due to the Hartree nature of the interactions considered here, which implies that the functional form of Σ^R_s is fixed and analytically known. On the other hand it is a consequence of the nonlinear Feynman rules, which enforce an unoccupied propagator G^K_s and therefore $\Sigma^K_s = 2i\Im\Sigma^R_s$, which reduces the number of coupled equations.

The frequency integral in the first of the two expressions in Eq. (4.121) is trivial, as $G^K_g(\omega) \propto \delta(\omega)$. Since the poles of G^R_P can be found analytically, also the frequency integral in the second term of $\Sigma_e(\omega)$ can be solved exactly via the residue theorem, such that only the momentum integration has to be evaluated numerically. After application of the residue theorem one obtains

$$\begin{aligned}\Sigma^R_e(\omega) =& -\sum_n\int\frac{dk}{2\pi}g_P^2\frac{\kappa_s}{2\Im(\omega_n(k))}\frac{1}{\omega-\omega_n(k)+i\epsilon/2}\\ &\times\frac{f(\omega_n(k))f^*(\omega_n^*(k))}{\prod_{m\neq n}(\omega_n(k)-\omega_m(k))(\omega_n(k)-\omega_m^*(k))}\\ &+\int\frac{dk}{2\pi}\frac{1}{2}g_P^2(4-2n_V)G^R_P(\omega+i\epsilon/2,k)\\ \Sigma^K_e(\omega) =& 2i\Im\Sigma^R_e(\omega) - i\kappa_s\int\frac{dk}{2\pi}g_P^2(2-2n_V)G^R_P(\omega,k)G^A_P(\omega,k)\,,\end{aligned} \tag{4.123}$$

where $n \in \{1,2,3,4\}$, $\omega_n(k)$ are the poles of $G_P^R(\omega,k)$ and

$$\begin{aligned} f(\omega) =&(\omega+i\gamma_e/2)(\omega-\Delta_s+i\epsilon/2)(\omega-\Delta_s-\Delta_d+i\gamma_d/2) \\ &-\Omega^2(\omega-\Delta_s-\Delta_d+i\gamma_d/2)-\left(\Omega_s^{\text{eff}}\right)^2(\omega+i\gamma_e/2)\,. \end{aligned} \tag{4.124}$$

With all Green's functions depending solely on the parameter χ, we are left with the task to solve for it self-consistently. The corresponding equation can again be read off from Fig. 4.17 and states

$$\chi = \frac{\Sigma_E^R(0)}{\Delta_E(0)-\Sigma_E^R(0)+i\kappa_E/2}\,. \tag{4.125}$$

So far, there is no ambiguity regarding the nonlinear Feynman rules. In the polarization bubbles of the exchange photon however, these partially forbid dressing the propagator of state $|d\rangle$ via couplings to the metastable state. Employing the strict interpretation where G_d^R remains undressed, the exchange photon self-energy reads

$$\Sigma_E^R(\omega) = \frac{i}{2}\int\frac{d\omega'}{2\pi}g_E^2 G_{\not s}^R(\omega')G_{\not s}^A(\omega')\delta\Sigma_{\not s}^K(\omega')G_d^R(\omega+\omega') \tag{4.126}$$

with

$$G_d^R(\omega) = G_{d_0}^R(\omega) = \frac{1}{\omega-\Delta_s-\Delta_d+i\gamma_d/2}\,. \tag{4.127}$$

If on the other hand the lenient rule is applied one is to use

$$G_d^R(\omega) = \left(\left[G_{d_0}^R\right]^{-1}(\omega) - \frac{\left(\Omega_s^{\text{eff}}\right)^2}{\omega-\Delta_s-\frac{\Omega^2}{\omega+i\gamma_e/2}}\right)^{-1}, \tag{4.128}$$

which includes all possible admixtures of atomic states to $|d\rangle$, as the insertion of the ground state can always be excluded by the methods introduced in Sec. 4.4.4. Furthermore, $\Sigma_{\not s}^R$ is to be complemented by

$$\Sigma_{\not s}^R \to \Sigma_{\not s}^R + \frac{\left(\Omega_s^{\text{eff}}\right)^2}{\omega-\Delta_s-\Delta_d+i\gamma_d/2}\,, \tag{4.129}$$

with the dependence of $\delta\Sigma_{\not s}^K$ on Σ_e^R and $\delta\Sigma_e^K$ remaining unaffected.

Choosing among these two ways of applying Feynman rules affects the propagation of the exchange photons and hence the light-mediated atom-atom interactions.

The photon propagator is ultimately given by

$$G_E^R(\omega,k) = \left[G_E^A(\omega)\right]^* = \frac{1}{\omega - \omega_E(k) - \Sigma_E^R(\omega,k) + i\kappa_E/2}$$
$$G_E^K(\omega,k) = G_E^R(\omega,k)\left(\Sigma_E^K(\omega,k) - i\kappa_E\right)G_E^A(\omega,k)\,, \tag{4.130}$$

with

$$\Sigma_E^K(\omega,k) = \Sigma_E^{K_0}(\omega,k) = 2i\Im\Sigma_E^R(\omega,k)\,. \tag{4.131}$$

Interestingly, the phase of χ can be adjusted via the detuning between the band-edge of the exchange photon and the laser Ω_s. Its amplitude depends on the density of atoms in the metastable state n_s and on the coupling constants, giving a great deal of control over the type and strength of backaction to be realized.

For numerical purposes, iterating equations (4.114) through (4.131) having the system previously initialized with some $\Omega_s^{\text{eff}} = \Omega_s$ is immensly inefficient, as convergence will fail when approaching a phase-transition (see also the discussion in Chap. 5). We avoid this problem by instead fixing Ω_s^{eff} and determining $\Omega_s(\Omega_s^{\text{eff}},\chi)$, which requires no iterations at all. This actually means that the value of Ω_s corresponding to the solution is not known a priori. However, for the computation of the entire phase-diagram this does not matter as eventually a result for any value of Ω_s will be produced.

Results: Non-equilibrium phase transition of the transparency window

A particularly interesting question which can be addressed with this newly developed formalism is whether the transparency window can be restored by interaction-related effects. If this was not the case one would have to limit the system to weak interactions or accept that strongly interacting polaritons in photonic crystal waveguides are necessarily very lossy. If on the other hand such a restoration of the transparency window is possible, it requires a condition similar in spirit to that of the original EIT, however with destructive interferences between the laser and the exchange photon that drastically reduce the coupling to state $|d\rangle$. As it turns out, such interferences are indeed predicted within our approach.

In fact this many-body phenomenon, that we will refer to under the name "interaction-induced transparency", as opposed to the well-known single-particle effect of "electromagnetically-induced transparency", appears in the form of a first order phase transition, as evidenced in the phase diagram Fig. 4.18. There, we find two possible steady-state phases: i) an "opaque" phase characterized by a small atomic excitation density n_s and ii) a "transparent" phase exhibiting instead a much larger n_s. Those two phases are separated by a first order phase transition that includes a bistable region and terminates in a critical point where the transition is continuous. More insight into the properties of the opaque and transparent

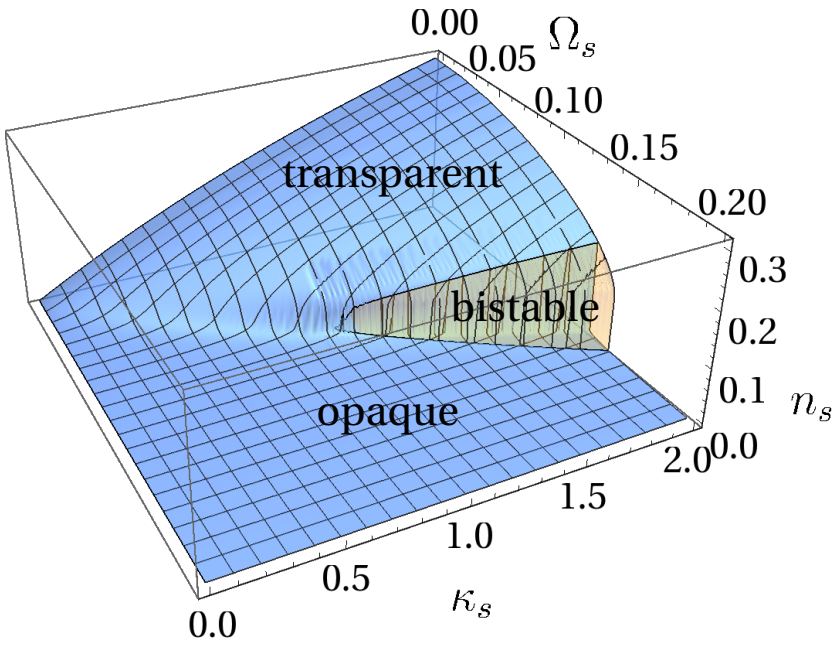

Figure 4.18: Excitation density in the atomic state s. The yellow(blue) surface corresponds to a system initialized in the "transparent"("opaque") phase with vanishing(large) values of κ_s. Parameters are the same as in Fig. 4.12, except for the previously undefined $g_E = 10$, $\kappa_E = 5$, $\Omega = 0.2$ and $\Delta_E(k) = -100k^2$

phases are obtained by examining the frequency- and momentum-resolved occupation $n_M(\omega, k)$ shown in Fig. 4.19 and normalized by $\int_{k,\omega} n_M(\omega, k) = n_M$. Far away from the narrow EIT window, the transparent and opaque solution are virtually indistinguishable (see Fig. 4.19a) and b)). However, at closer inspection the EIT window differs strongly between both cases. In the opaque phase the dark-state polariton remains broad and is only weakly populated, thus showing no signs of an EIT window. The latter is destroyed by coupling the metastable state $|s\rangle$ to the excited state $|d\rangle$, introducing an additional decay channel that is eventually inherited by the dark-state polariton.

In the transparent phase on the other hand the intensity is concentrated within a very sharp region around a specific wavenumber k_{EIT} of the dark-state polariton branch. This means that in the phase transition the system has reconstructed the transparency window. In the original non-interacting EIT effect, the window is formed due to the destructive interference in the propagator of the excited state in Fig. 4.17b). In the IIT effect, the window is also reconstructed via destructive interference, this time between the four different excitation pathways involving the state

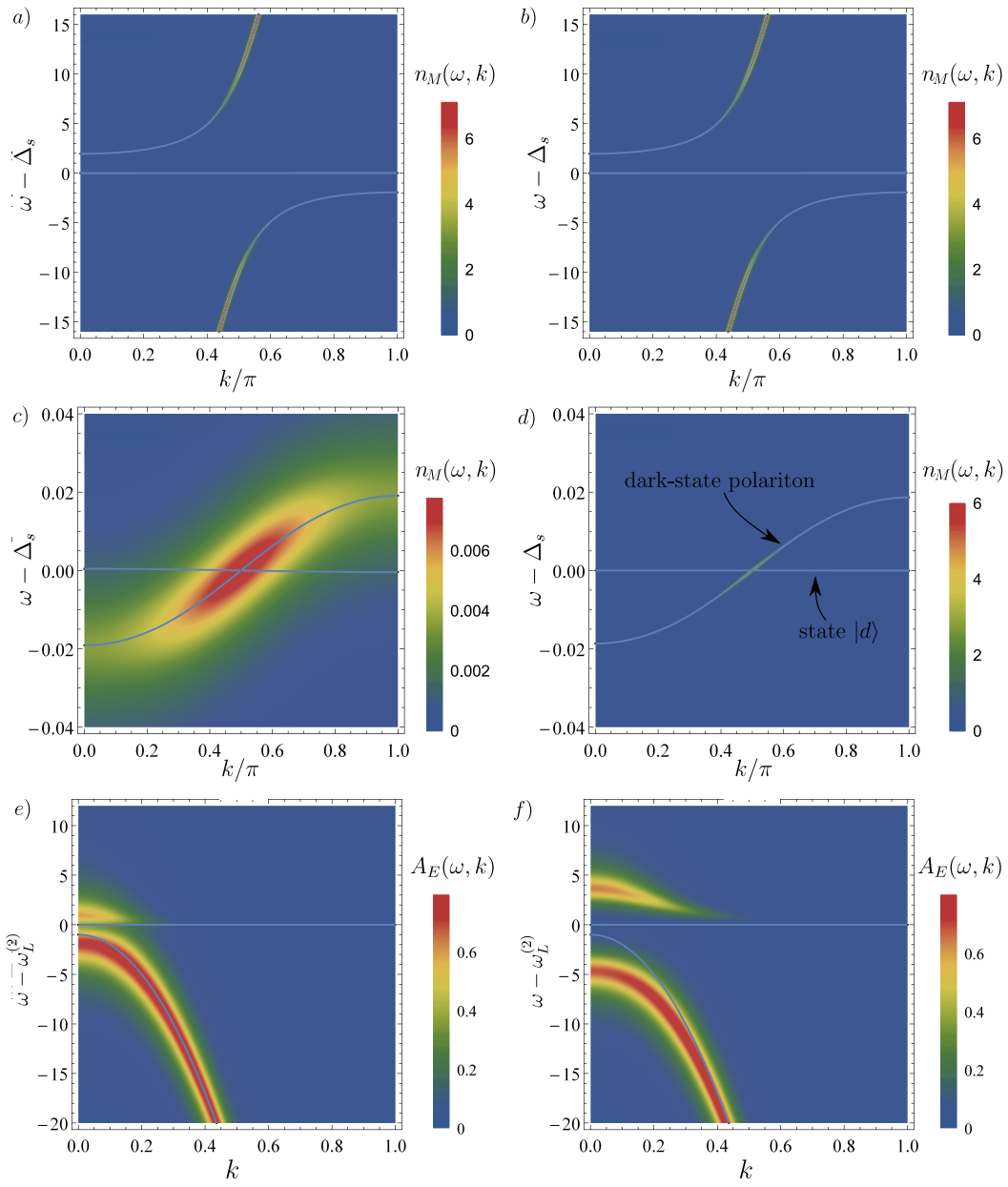

Figure 4.19: Comparison between the opaque (left) and transparent (right) solution. Top row: M-photon occupation in frequency-momentum space far away from the EIT condition is unaffected by IIT. However zoomed in on the dark-state polariton branch (middle row) the drastic difference between the two phases becomes apparent. Bottom row: spectral function of the E-photons. Solid lines correspond to the bare E-photon dispersion (inverted parabola) and the resonance frequency of the $s - d$ transition (horizontal line). The parameters are the same as in Fig. 4.18 at the bistable point $\Omega_s = 0.14$ and $\kappa_s = 2$.

$|d\rangle$ and corresponding to the last four diagrams contributing to Σ_s in Fig. 4.17d). Due to this weak coupling to level d an additional almost non-dispersive flat polariton branch exists at $\omega \approx \omega_d + \omega_L^{(1)} - \omega_L^{(2)}$ with vanishingly small occupation. Other than in the non-interacting EIT, the interfering pathways involve the E-photons i.e. interactions between polaritons, which renders IIT intrinsically nonlinear. In the lossy system this implies that IIT takes place through a first-order phase transition showing bistability. The destructive interference between the four pathways is most efficient if the self-energy of the E-photons $\Sigma_E^R(\omega_L^{(2)}+\omega_s)$ becomes purely imaginary, corresponding to strong screening of the external laser by the background of polaritons, facilitated by E-photons. This indicates that IIT is a dissipative many-body effect only accessible to systems far from thermal equilibrium.

The destruction of the transparency window in the opaque phase via coupling to a lossy state is an effect analogous to the one employed to build an optical switch in Ref. [253], whereby any two-photon state becomes strongly suppressed. If (as we do here) one uses a lossy state to induce interactions between atoms in the metastable state, the IIT additionally enables to reconstruct transparency at a tunable photon number.

The E-photons mediating the interactions between the atoms also show drastic differences between the opaque and transparent phase. As opposed to the M-photons, E-photons are not driven and can only be excited by atoms in the d level. The latter can be occupied only via laser transitions from the s level, which in turn can be populated via absorption of M-photons. Therefore, the occupation of the electrically polarized mode is suppressed by $1/L_M$ and thus typically small for realistic parameters. It is therefore more instructive to analyze the spectral function, defined as $A_E(\omega,k) = -2\Im G_E^R(\omega,k)$, which is normalized to 1 and accessible for instance by combining the waveguide output with a reference field on a beamsplitter [261]. $A_E(\omega,k)$ is shown in the bottom row of Fig. 4.19. In the opaque phase the spectral weight is mostly on the bare dispersion curve, with a width set by the losses κ_E. This is caused by the low number of atoms in state s, which makes the modification Σ_E of the photon-propagation due to the medium negligible. On the other hand, in the transparent phase we see that the bare E-photon branch hybridizes with the atomic $s-d$ excitation. In addition, in the momentum region close to the dispersion maximum, spectral weight is transferred from the photon-like branch to the atom-like branch. This screening effect is quantitatively important and reduces the strength of the E-photon-mediated interactions for polaritons in the transparency window. Since therefore retardation of the mediated interaction is very important, adiabatic elimination of the bare E-photons would largely overestimate the bright region in the phase diagram.

Following this phenomenological analysis, the remainder of this section will provide a complementary analysis focusing on the nature of the underlying non-equilibrium phase transition and discuss the fundamental mechanism from a more formal perspective as an application of our diagrammatic approach.

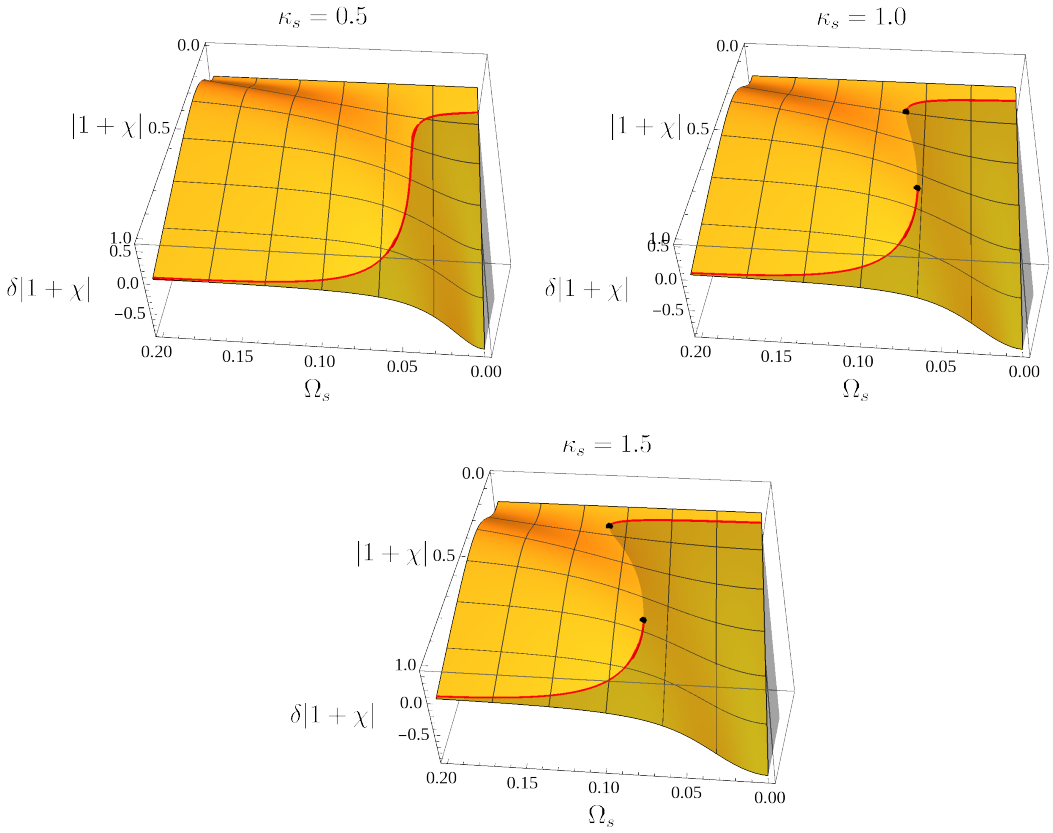

Figure 4.20: Flow diagram and stability analysis of the effective relative coupling strength $|1+\chi|$ as a function of the externally adjustable parameter Ω_s, where otherwise the same parameters as in Fig. 4.12 are used together with the lenient interpretation of the nonlinear Feynman rules as well as $\Delta_E(k=0) = -1$, $\kappa_E = 5$ and $g_E = 10$. The red line indicates stable, stationary solutions.

The reconstruction of the transparency window can be attributed to the positive feedback brought about by the dependence of χ in Eq. (4.125) on the excitation density: $\chi \propto n_s$, which stabilizes both a low density i.e. opaque phase and a high density i.e. transparent phase, separated by a first-order phase transition. The mechanism behind this can be understood by studying Figs. 4.20 and 4.21, which show the amplitude and sign of the variation in the flow of the quantity $|1+\chi|$ during the evaluation of the self-consistence equation (4.125). If the system is initialized with a certain value of χ such that $\delta|1+\chi|$ is positive, the system will flow towards the opaque phase and vice versa, if $\delta|1+\chi| < 0$, the system is unstable towards the transparent phase. Consequently, only those parameter

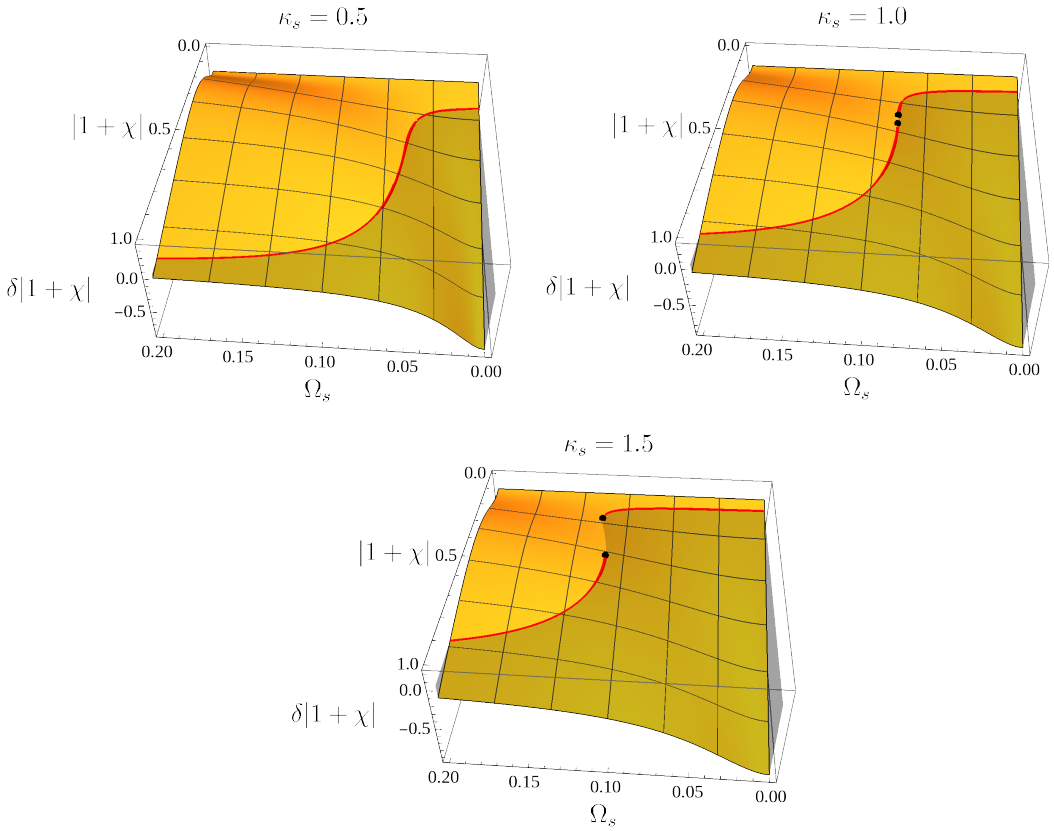

Figure 4.21: The same diagram as in Fig. 4.20 but using the strict version of the nonlinear Feynman rules.

combinations with $\delta|1+\chi| = 0$ and a negative slope in $\delta|1+\chi|$ as a function of $|1+\chi|$ are stable and therefore marked with a red line in Figs. 4.20 and 4.21. In sufficiently strongly driven systems we witness the emergence of a bistability: for a given Rabi amplitude Ω_s two stable solutions exist. They differ significantly in the effective coupling Ω_s^{eff} and in the occupation of dark-state polaritons. Quite surprisingly we find a stable transparent solution with $\Omega_s^{\text{eff}} \ll \Omega_s$, which entails significantly reduced losses compared to the non-interacting case with $g_E = 0$. Remarkably, the stable ratio $\Omega_s^{\text{eff}}/\Omega_s$ is smallest for purely dissipative interactions, that is, when $\Sigma_E^R(0)$ is purely imaginary. In this case, the phase shift between the E-photon-mediated driving of the $s-d$ transition and the direct driving via Ω_s is most destructive. This results in small losses for the dark-state polaritons, at least if there are enough to create a sufficiently large backaction in the form of $\Sigma_E^R(0)$. A comparison between Figs. 4.20 and 4.21 demonstrates that for these rather small values of Ω_s the choice of the nonlinear Feynman rules does not affect the results

appreciably. For the remainder of this section, we will therefore focus on the strict implementation of the Feynman rules.

In combination with the possibility of the simultaneous stability of an opaque and a transparent phase, a first order phase transition similar to that between a gaseous and a liquid phase emerges: above a critical bare laser strength Ω_{s_c} an increasingly strong hysteresis is observed as the source intensity κ_s is increased (see Fig. 4.22). However, at exactly the critical laser strength, the first order phase transition ends in a critical point, where the phase transition is continuous and of mean-field type. This is to be expected by a Hartree-type theory with infinitely ranged interactions and we verify it by fitting the numerical data for $n_s(\kappa_s, \Omega_{s_c}) \sim \kappa_s^{1/\delta}$ with a power law (see Fig. 4.23). This allows us to extract the critical exponent δ of the dependence of the order parameter on the external source. Our result $\delta = 3 \pm 0.01$ is in agreement with the Ising universality class where $\delta = 3$ [262].

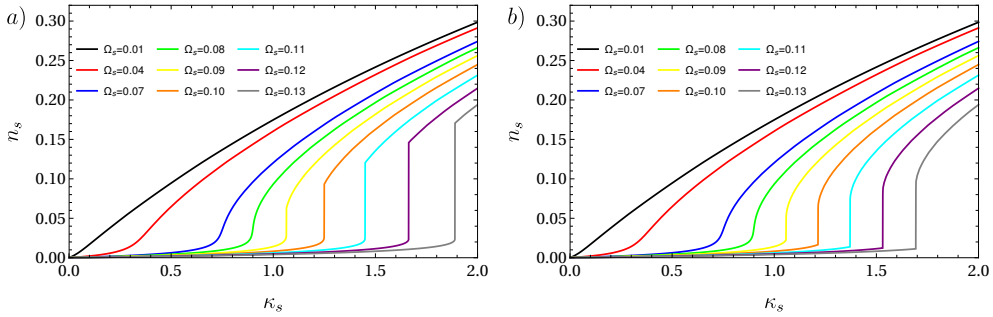

Figure 4.22: Hysteresis of the polariton density, evidenced in n_s for scans at the incoherent drive strength κ_s for different values of Ω_s. In panel a) the system is initialized in the opaque phase with $\kappa_s = 0$, whereas panel b) uses $\kappa_s = 2$ in the transparent phase as a starting point. Below the critical Rabi amplitude $\Omega_{s_c} \approx 0.0851$ both scans are identical. However above Ω_{s_c} the initial phase is stabilized against fluctuations induced by slow scans and a hysteresis curve becomes observable. The parameters used are the same as in Fig. 4.20.

We note that in the regime of the first order phase transition, the difference in polariton density between the opaque and transparent solution is typically large. This can be seen from the distribution function (see Fig. 4.24) as well as from the frequency- and momentum-resolved photonic number density of Fig. 4.25. One thus concludes that, far away from the critical point in the opaque phase the system behaves essentially as a non-interacting theory: the occupation numbers are so small that interactions via exchange photons play no role and the bare – but due to Ω_s, lossy – EIT is recovered.

In the transparent phase on the other hand an only weakly perturbed Λ-scheme

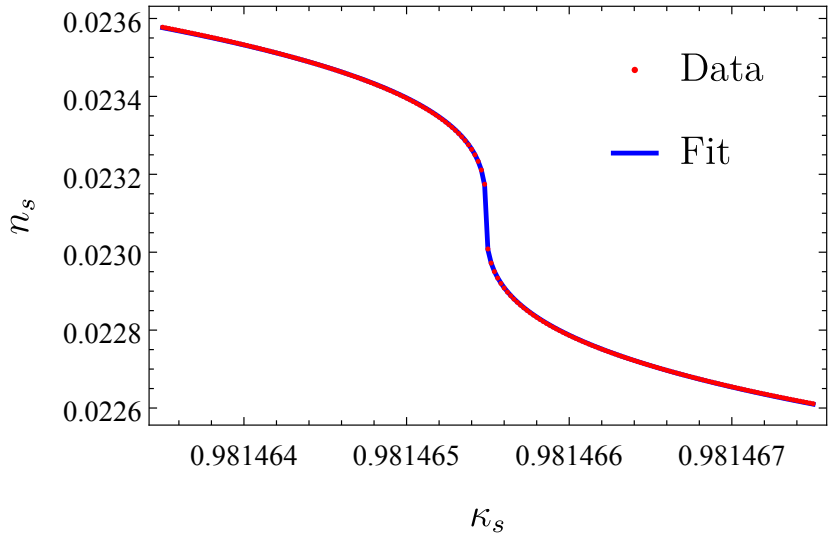

Figure 4.23: Power law fit to the density of excited atoms at the critical coupling strength $\Omega_{s_c} \approx 0.0851$ for the same parameters as in Fig. 4.20. The critical exponent of the order parameter as a function of the drive strength is determined to be $\delta = 3 \pm 0.01$.

is restored, which seems to imply that the effective degrees of freedom are again only weakly interacting. Correspondingly, many simple correlation functions can be described by an effective free theory. However, except for the limit of vanishing Ω_s, the response of the system to external perturbations will be very different compared to the free theory discussed in Sec. 4.5.

Analytic estimates and requirements of the bistable regime

Due to the simplicity of the reduced theory presented in this section, we can actually give some analytic estimates for the conditions necessary for a phase transition. Due to the typically large atomic admixture θ to the dark-state polaritons, even for relatively strong driving $\kappa_s \sim \kappa_P$, a slow group velocity gives rise to only a small photon number density

$$n_P = i \int \frac{d\omega}{4\pi} \int \frac{dk}{2\pi} \delta G_P^K(\omega, k) < \theta n_s \ll 1 \,. \tag{4.132}$$

Here the first inequality results from the fact that only photons in a narrow frequency interval actually form dark-state polaritons. Most photons instead hybridize into bright polaritons, that involve the decaying excited atomic states, resulting in even smaller occupations.

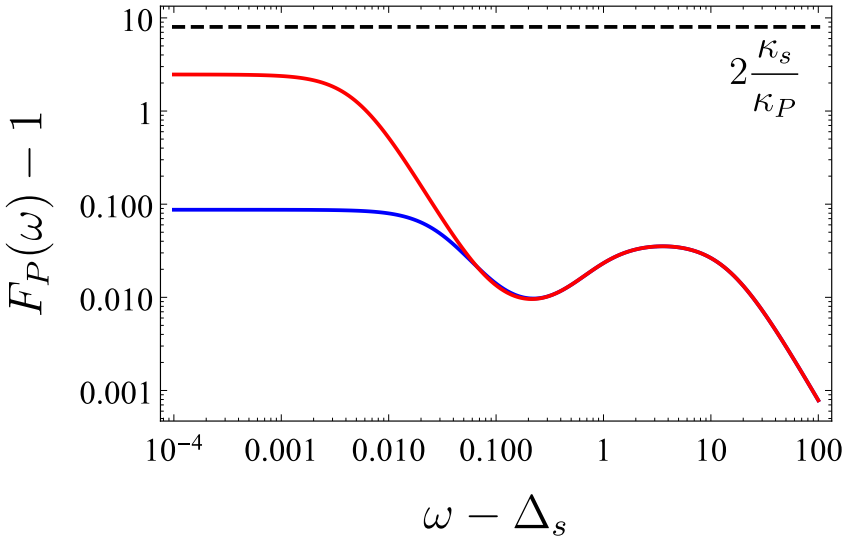

Figure 4.24: Double logarithmic plot of the distribution functions $F_P(\omega)$ of the transparent phase in red and the opaque phase in blue for the same parameters as in Fig. 4.20. Near the EIT condition $F_P - 1$ differs by more than an order of magnitude.

Of the two contributions to Σ_e^R in (4.123), the second one thus dominates. Typically, in PCW or tapered fibers, the photonic bandwidth is several orders of magnitude larger than the inverse lifetimes of all atomic states. It is therefore well justified to approximate the photon spectrum as linear. We do so by writing their retarded Green's function as a sum of left- and right-movers

$$G_P^R(\omega) = \frac{1}{\omega - \Delta_P^{(0)} - v_P k - \Sigma_P^R(\omega) + i\kappa_P} + \frac{1}{\omega - \Delta_P^{(0)} + v_P k - \Sigma_P^R(\omega) + i\kappa_P}. \tag{4.133}$$

For $L_P = \kappa_P / v_P \gg 1$ the EIT window in momentum space is much narrower than the inverse lattice constant $1/a$ and thus far away from the band edge a linearized spectrum suffices to reproduce the results obtained from any Bloch wave with the same group velocity in the EIT window.

Together with the observation that, since the atoms are fixed in space, $\Sigma_P^R(\omega)$ is momentum independent, this allows to find

$$\begin{aligned} \Sigma_e^R &\approx -i g_P^2 (2 - n_V) |u_k^P(0)|^2 / v_P \\ \delta\Sigma_e^K &\approx -g_P^2 (1 - n_V) \frac{2}{v_P} \frac{i\kappa_s}{\kappa_P/2 - \Im\Sigma_P^R(\omega)}, \end{aligned} \tag{4.134}$$

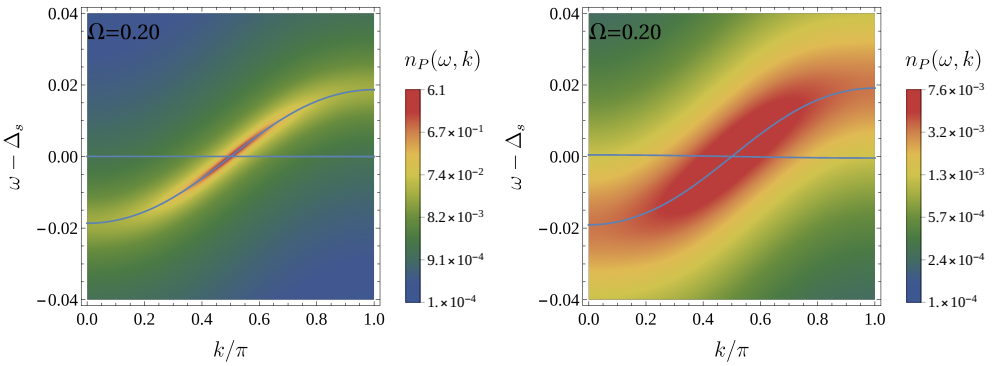

Figure 4.25: The frequency and momentum resolved photon number density $n_P(\omega,k)$ in the transparent phase (left) exhibits an almost perfect transparency window, whereas the opaque phase (right) with the same parameters shows strongly dissipative polaritons (note the difference by almost three orders of magnitude in the maximal spectral density). The almost flat blue line corresponds to the atomic level $|d\rangle$, that hybridizes with the probe photon to form a fourth, bright polariton branch. For small values of Ω_s, which is the case for the parameters of Fig. 4.20 also at use here, this hybridization remains weak and the new polariton branch consequently is essentially unoccupied.

where the momentum integral has been approximated by an integral along the entire real axis. This result can be used to approximate the number density of atoms in the metastable state by

$$\begin{aligned} n_s &= i\int_{-\infty}^{\infty}\frac{d\omega}{4\pi}|G_s^R(\omega)|^2\delta\Sigma_{\not s}^K(\omega) = i\int_{-\infty}^{\infty}\frac{d\omega}{4\pi}|G_{\not s}^R(\omega)|^2|G_e^R(\omega)|^2\delta\Sigma_e^K(\omega) \\ &\approx \int_{-\infty}^{\infty}\frac{d\omega}{2\pi}\kappa_s(\omega)\left|\frac{1}{\frac{(\omega-\Delta_s)}{\Omega^2}\left(\omega+(2-n_V)i\frac{g_P^2}{v_P}+i\gamma_e/2\right)-1}\right|^2 \\ &\qquad\times\frac{g_P^2}{\Omega^2}\frac{1-n_V}{v_P\left(\kappa_P/2-\Im\Sigma_P^R(\omega)\right)}\,. \end{aligned} \tag{4.135}$$

As can be extracted from Figs. 4.20 and 4.21 the system becomes bistable once

$$0 \overset{!}{>} \frac{d\Omega_s}{d\Omega_s^{\text{eff}}} = \frac{d}{d\Omega_s^{\text{eff}}}\frac{\Omega_s^{\text{eff}}}{|1+\chi(\Omega_s^{\text{eff}})|}\,, \tag{4.136}$$

which, using the explicit form (4.125) can be rewritten as

$$\frac{d\chi}{d\Omega_s^{\text{eff}}} \overset{!}{>} \left| \frac{-\Delta_E(0) + i\kappa_E/2}{\Omega_s^{\text{eff}}\left(-\Delta_E(0) - \Sigma_E^R(0) + i\kappa_E/2\right)} \right| . \tag{4.137}$$

In the ideal case of a resonance between the exchange photon and the corresponding laser ($\Delta_E(0) = 0$) as well as strong coupling g_E, such that $|\Sigma_E^R(0)| \gg \kappa_E$, this still requires

$$\frac{dn_s\Omega_s^{\text{eff}}}{d\Omega_s^{\text{eff}}} < 0 . \tag{4.138}$$

A condition, that can be satisfied only if

$$\Im\Sigma_P^R(0) - \Omega_s^{\text{eff}} \frac{d}{d\Omega_s^{\text{eff}}} \Im\Sigma_P^R(0) > \kappa_P/2 , \tag{4.139}$$

where we used (4.135) with the absolute value approximated by unity as an upper bound. Since the minimum of the frequency dependent loss rate

$$-\Im\Sigma_P^R(\omega) \approx \sigma + \eta(\omega - \Delta_s)^2 \tag{4.140}$$

with the abbreviations

$$\begin{aligned} \sigma &= \frac{2(\Omega_s^{\text{eff}})^2 g_P^2 (1 - n_V)|u_P^k(0)|^2}{\gamma_e(\Omega_s^{\text{eff}})^2 + \tilde{\gamma}_d\Omega^2} \\ \eta &= \frac{g_P^2(1 - n_V)|u_P^k(0)|^2\gamma_e}{2\Omega^4} \\ \tilde{\gamma}_d &= \frac{\gamma_d^2 + 4\Delta_d^2}{\gamma_d} \end{aligned} \tag{4.141}$$

for slow polaritons is tightly focused around $\omega = \Delta_s$, this is a reasonably good approximation. Using the just stated expansion of the probe photon self-energy around Δ_s, one finds the left hand side of Eq. (4.139) to be maximized for

$$\Omega_s^{\text{eff}} = \sqrt{\frac{\gamma_d\Omega^2}{3\gamma_e}} , \tag{4.142}$$

where one finds a strong collective coupling satisfying

$$g_P^2 > 2\gamma_e\kappa_P \tag{4.143}$$

or equivalently a large collective cooperativity $L_P C_P > 2$ to be a necessary condition for the emergence of a bistability. While, due to the rough approximations used here, this is only a lower bound on the collective cooperativity, it clearly

shows that the type of phase transition discussed here is not amenable to a purely perturbative approach.

Instead of calculating a lower bound for the collective cooperativity $L_P C_P$ we can also search for a rough estimate that includes all relevant scales. To do so, we approximate $n_s \approx p C_P \Omega_s^2/\Omega^2$, where $p = 2\kappa_s(0)/\kappa_P$ is the pump ratio, indicating how strongly the probe photons near the EIT condition are driven compared to their losses. Inserting this expression for n_s into $|\Im\Sigma_E^R(0)| \gtrsim \kappa_E$, which is necessary for a highly non-perturbative regime, yields the final strong coupling condition

$$p L_E C_E C_P \frac{\Omega_s^2}{\Omega^2} \gtrsim 1\,. \tag{4.144}$$

An actual bistability additionally requires an efficient backaction of the losses in the dressed state $|s\rangle$ onto the dark-state polariton density. Therefore, typical systems that exhibit a phase transition satisfy Eq. (4.144) by more than one order of magnitude. For example, for the parameters of the critical point in Fig. 4.23, one has $p L_E C_E C_P \Omega_s^2/\Omega^2 \approx 58$.

Fortunately, these strong coupling requirements are met for parameters that are expected to become experimentally viable in PCWs in the near future [17], namely $\gamma_{e,d} \sim 10\text{MHz}$, $g_{M,E} \sim 10^3\gamma_e$, $J_M \sim 10^7\gamma_e$, $\alpha_E \sim 10^6\gamma_e$ and $\kappa_{M,E} \sim 10\gamma_e$, for which our approach indeed predicts the existence of a IIT transition. Because of the highly tunable photon dispersions in PCWs this will likely be possible with $C_E \lesssim 1$, where our theory becomes quantitatively valid. It is also worth mentioning that, as we will see in the following, the additional diagrams that need to be added to the ones in Fig. 4.17 in order to render our predictions fully quantitative actually enhance the IIT-effect, which results in a parametrically larger bistable region.

4.7.2 Quantitative theory in the infinite-range limit

The reduced class of diagrams discussed in the previous section is helpful to obtain a general idea about the emergence of a phase transition between the two limits of a perfectly restored transparency window deep within the transparent phase on the one hand, and an empty system in the opaque phase on the other hand. Our main goal, however, is the quantitative description that extends all the way to the critical point and the bistable region. In order to achieve this, one has to include all diagrams that can be created self-consistently from the two diagrams in Fig. 4.15a) and d). The resulting theory is illustrated in terms of Feynman diagrams in Fig. 4.26, which differs from the reduced theory of the previous section by the addition of the Fock diagram to the Dyson equation of the exchange photon (see last diagram in the third line of Fig. 4.26). Note that at this level of the theory the exchange photon obtains a Nambu structure, which requires us to extend the Kramers-Kronig relations of Sec. 4.4.3 to anomalous Green's functions, which we will do in the following.

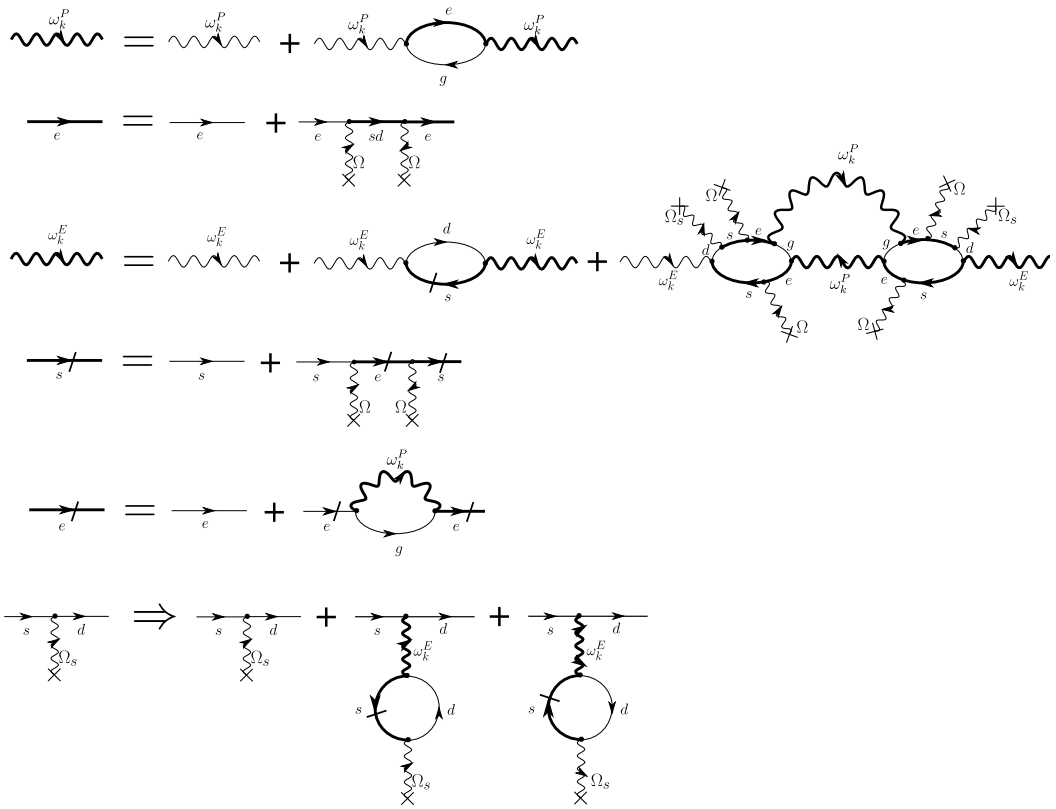

Figure 4.26: Complete diagrammatics in the limit $L_E \to \infty$. Note that we do not show the anomalous components of the self-energy for the E-photon. Those are however obtained from the last diagram in the second line upon an exchange of laser and E-photons acting on the same transition. We included the anomalous components in the calculation (see section 4.7.2).

Anomalous Green's functions

The appearance of anomalous Green's functions for the exchange photons is caused by the presence of a background coherent contribution to the E-photon field. This has to be expected from the theory presented in Sec. 4.7.1, as an E-photon can be resonantly excited by the external laser field with strength Ω_s. The net effect is that a coherent component i.e. a condensate arises in the connected part of the two-point function of the exchange photon as an addition to the background coherent laser field. This effect is described by the last diagram in the third line of Fig. 4.26, where at each atom the order in which the E-photon and the laser are coupled to a given transition can be chosen arbitrarily. While this formally creates anomalous contributions to the self-energy, it underlines the physical argument that from the

perspective of fixed atoms exchange photons and laser photons are indistinguishable if their frequency is identical.

It is important to understand that this condensation of E-photons will not be inherited by the probe photons. Consequently, no polariton condensate can be generated unless the probe photons themselves are directly coupled to an inverted bath (which we excluded from the outset). Similar to what is done in equilibrium, each component of the non-equilibrium Green's function can be augmented by a Nambu structure. For the retarded and the Keldysh part of the Green's function one typically defines the following 2×2 matrix

$$G^R(\omega,p) = -i \begin{pmatrix} \left\langle b^{\mathrm{cl}}(\omega,p)\bar{b}^{\mathrm{q}}(\omega,p)\right\rangle & \left\langle b^{\mathrm{cl}}(\omega,p)b^{\mathrm{q}}(-\omega,-p)\right\rangle \\ \left\langle \bar{b}^{\mathrm{cl}}(-\omega,-p)\bar{b}^{\mathrm{q}}(\omega,p)\right\rangle & \left\langle \bar{b}^{\mathrm{cl}}(-\omega,-p)b^{\mathrm{q}}(-\omega,-p)\right\rangle \end{pmatrix}$$

$$= -i \left(\begin{array}{cc} (\omega,p) \quad (\omega,p) & (-\omega,-p) \quad (\omega,p) \\ (\omega,p) \quad (-\omega,-p) & (-\omega,-p) \quad (-\omega,-p) \end{array} \right) \tag{4.145}$$

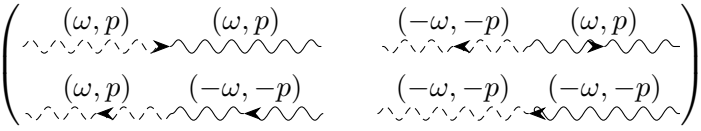

and the same for $G^K(\omega,p)$ with all quantum fields (index q) replaced by classical fields (index cl). The diagonal entries then describe ordinary Green's functions, while the off-diagonal, so-called anomalous components, are non-zero only in the presence of a condensate. For the retarded Green's function the Dyson equation takes the same form as in equilibrium

$$G^R = G_0^R + G_0^R \cdot \Sigma^R \cdot G^R\,, \tag{4.146}$$

where G_0^R is purely diagonal. Retarded, advanced and Keldysh Green's functions are once again not independent and one finds relations between them which are very similar to the case where anomalous Green's functions are absent. Specifically, the retarded and advanced components have to satisfy $G^R_{\sigma\rho}(\omega,p) = G^A_{\bar{\sigma}\bar{\rho}}(-\omega,-p)$, where $\sigma,\rho \in \{1,2\}$ and $\bar{\sigma}$ is the complement of σ. The proof follows from a direct inspection of the respective Feynman diagrams: exchanging the external legs reverses the direction of the momentum and energy flow and simultaneously reverses causality, thereby equating the off-diagonal entries of G^R and G^A. Additionally $\left[G^A\right]^\dagger = G^R$ follows immediately once the definition (4.145) is evaluated on the Keldysh contour. Therefore, the advanced Green's function never has to be calculated and the retarded Green's function can be restricted to only two independent functions:

$$G^R(\omega,p) = \begin{pmatrix} G^R_{11}(\omega,p) & G^R_{12}(\omega,p) \\ \left[G^R_{12}\right]^*(-\omega,-p) & \left[G^R_{11}\right]^*(-\omega,-p) \end{pmatrix}. \tag{4.147}$$

Furthermore, considering all self-energy diagrams order-by-order, one can prove that $G^R_{\sigma\bar{\sigma}}(\omega,p) = G^R_{\bar{\sigma}\sigma}(\omega,p)$, which is true for any uniform bosonic system in and out of equilibrium [188].

Taking the conjugate transpose of the Keldysh component can be done immediately in frequency space and a comparison of elements reveals the anti-hermitian structure, i.e. $\left[G^K\right]^\dagger = -G^K$. We can thus still use the parametrization $G^K = G^R \cdot F - F \cdot G^A$, with a hermitian matrix F. The fact that $F = \sigma_z$ for an empty system accounts for the reversed order of operators between the components of the first and the second row of G^K. Exchanging incoming and outgoing particles in G^K furthermore allows to identify $G^K_{\sigma\rho}(\omega, p) = G^K_{\bar{\sigma}\bar{\rho}}(-\omega, -p)$. By considering again all possible self-energy diagrams one finds the additional symmetry $G^K_{\sigma\bar{\sigma}}(\omega, p) = -\left[G^K_{\bar{\sigma}\sigma}\right]^*(-\omega, -p)$. The Dyson equation for the Keldysh component directly generalizes to the Nambu structure: $G^K = G^R \cdot \left(\Sigma^K - D_0^K\right) \cdot G^A$, which together with the other symmetries implies

$$\Sigma^{K_0}(\omega, p) = 2 \begin{pmatrix} i\Im\Sigma^R_{11}(\omega, p) & \Re\Sigma^R_{12}(\omega, p) \\ -\Re\Sigma^R_{12}(-\omega, -p) & i\Im\Sigma^R_{11}(-\omega, -p) \end{pmatrix} \tag{4.148}$$

for the empty system and

$$\delta\Sigma^K(\omega, p) = \Sigma^K(\omega, p) - \Sigma^{K_0}(\omega, p) = \begin{pmatrix} \delta\Sigma^K_{11}(\omega, p) & \delta\Sigma^K_{12}(\omega, p) \\ -\left[\delta\Sigma^K_{12}\right]^*(\omega, p) & \delta\Sigma^K_{11}(-\omega, -p) \end{pmatrix} \tag{4.149}$$

for excitations above the vacuum. With these definitions the Kramers-Kronig relations of section 4.4.3 remain valid without limitation. For simplicity we only provide the Kramers-Kronig relations for a single convolution with some normal Green's function labeled G_n, keeping in mind that generalizations take exactly the same form:

$$\int \frac{d\omega'}{2\pi} \left[G^K_{\sigma\rho}(\omega') G^R_n(\omega - \omega') - G^R_{\sigma\rho}(\omega') G^K_n(\omega - \omega')\right] = -\delta_{\rho 2} \int \frac{d\omega'}{\pi} G^R_{\sigma\rho}(\omega') G^R_n(\omega - \omega') \tag{4.150}$$

as well as

$$\begin{aligned} &\int \frac{d\omega'}{2\pi} \left(G^K_{\sigma\rho}(\omega') G^K_n(\omega - \omega') - G^R_{\sigma\rho}(\omega') G^R_n(\omega - \omega') - G^A_{\sigma\rho}(\omega') G^A_n(\omega - \omega')\right) \\ &= -\int \frac{d\omega'}{\pi} \left(\delta_{\rho 2} G^R_{\sigma\rho}(\omega') G^R_n(\omega - \omega') + \delta_{\sigma 2} G^A_{\sigma\rho}(\omega') G^A_n(\omega - \omega')\right) . \end{aligned} \tag{4.151}$$

Note that due to the symmetries of the diagonal entries of the Green's functions, these two relations already fully incorporate the four equations derived in section 4.4.3.

Dyson equations

Having introduced the anomalous non-equilibrium Green's functions we can now solve the self-consistent Dyson equations shown in Fig. 4.26, where in order to simplify the notation we have introduced the matrix Green's function $\mathcal{G}_{sd}$ for the states $|s\rangle$ and $|d\rangle$. In absence of any diagrams of order $1/L_E$, it is fully determined by the corresponding submatrix of $\left[G^R_{a,0}\right]^{-1}$ (see Eq. (4.80)), but with the effective Rabi amplitude $\Omega_s^{\text{eff}} = \Omega_s|1+\chi|$:

$$\mathcal{G}^{R/K}_{sd} = \begin{pmatrix} G^{R/K}_{ss} & G^{R/K}_{sd} \\ G^{R/K}_{ds} & G^{R/K}_{dd} \end{pmatrix} = \begin{pmatrix} \omega - \Delta_s + i\epsilon/2 & -\Omega_s^{\text{eff}} \\ -\Omega_s^{\text{eff}} & \omega - \Delta_d - \Delta_s + i\gamma_d/2 \end{pmatrix}^{-1} . \tag{4.152}$$

In fact, as indicated by the last line in Fig. 4.26, and in analogy to Sec. 4.7.1, Ω_s has to be replaced everywhere by Ω_s^{eff} and $G^{R/K}_{ss}$ supersedes the identical expression $G^{R/K}_s$ used in Sec. 4.7.1. Apart from these notational remarks, the only physical difference between the present theory and the one discussed in section 4.7.1 is in the propagator of the exchange photon, which acquires a new self-energy contribution $\Sigma_E^{R_2}$:

$$G^R_E = \left(\left[G^{R_0}_E\right]^{-1} - \Sigma^{R_1}_E - \Sigma^{R_2}_E \right)^{-1} . \tag{4.153}$$

While the first term $\Sigma_E^{R_1}(\omega)$ remains exactly the same as Eq. (4.126), the second, due to the Nambu structure takes the lengthy form

$$\begin{aligned} \Sigma^{R_2}_E(\omega,k) =& \frac{i}{2} g_P^4 g_E^2 \Omega^4 \Omega_s^2 |1+\chi|^2 (1-n_V)^2 \int \frac{d\omega'}{2\pi}\frac{dp}{2\pi} \left|G^R_e(\omega')G^R_{ss}(\omega')\right|^2 \delta G^K_P(\omega',p) \\ &\times \Bigg[\left[G^R_{ss}(\omega+\omega')G^R_e(\omega+\omega')\right]^2 G^R_P(\omega+\omega', p+k) \\ &\qquad \times \begin{pmatrix} \left[G^R_d(\omega+\omega')\right]^2 & G^A_d(\omega')G^R_d(\omega+\omega') \\ G^R_d(\omega')G^R_d(\omega+\omega') & \left|G^R_d(\omega')\right|^2 \end{pmatrix} \\ &+ \left[G^A_e(\omega'-\omega)G^A_{ss}(\omega'-\omega)\right]^2 G^A_P(\omega'-\omega, p-k) \\ &\qquad \times \begin{pmatrix} \left|G^R_d(\omega')\right|^2 & G^A_d(\omega'-\omega)G^A_d(\omega') \\ G^A_d(\omega'-\omega)G^R_d(\omega') & \left[G^A_d(\omega'-\omega)\right]^2 \end{pmatrix} \Bigg] . \end{aligned} \tag{4.154}$$

Some care has to be taken when it comes to determining χ: $\Sigma_E^{R_2}$ is actually indistinguishable from $\Sigma_E^{R_1}$ once one of their external legs is substituted with the laser field Ω_s. Consequently, coupling to the coherent field with $\Sigma_E^{R_2}$ would overcount

the diagrams in the last line of Fig. 4.26. Therefore, χ is given by

$$\chi = \sum_j \Sigma^{R_1}_{E_{jj}} G^R_{E_{j1}} \Big|_{k,\omega=0} . \tag{4.155}$$

Note that using the real and positive definition $\Omega_s^{\text{eff}} = \Omega_s|1+\chi|$ in the anomalous components of the exchange photon Green's function is wrong, since it leads to an incorrect behavior of G_E under a global $U(1)$ transformation $\hat{a}_{E,d} \to \hat{a}_{E,d} e^{i\phi}$ and $\hat{a}^\dagger_{E,d} \to \hat{a}^\dagger_{E,d} e^{-i\phi}$. This does not matter, however, since all observables depend only on the gauge invariant $|1+\chi|^2$, which allows us to simplify our calculations. By fixing the real value Ω_s^{eff} one can then directly determine the corresponding experimentally relevant parameter Ω_s. From a computational point of view, this makes for a very cheap calculation, as the two-dimensional convolution in Eq. (4.154) – which has to be calculated only once – only has to be evaluated at $k = \omega = 0$.

Similar to the previous section, the simplified nonlinear Feynman rules are not uniquely defined and we thus again have to choose between the strict and lenient way of implementing the rules in order to estimate the error bounds of the simplified diagrammatics. We do so in the same fashion as before, i.e. for the strict rule we use $G^{A/R}_{d_0}$ in Eqs. (4.154), and (4.126). For the lenient version we employ $G^{A/R}_{d}$ according to Eq. (4.128) together with the replacement (4.129) for the very same equations.

Before we proceed to discuss the results obtained from the set of coupled Dyson equations introduced in this section, it is instructive to view these calculations from a more conceptual point of view: despite the potentially large single-atom cooperativity experienced by the probe photons, their density is assumed to be small, such that dark-state polaritons in the absence of exchange photons are non-interacting quasiparticles. This is correctly captured by the nonlinear Feynman rules, which allow for an exact diagrammatic solution of the Yukawa theory in the $g-e-s-P$ sector. If we now consider the additional coupling to level d and include the E-photons, we can eliminate the atomic degrees of freedom to obtain an effective theory for the dressed propagating and exchange photons. Indeed, on the one hand the atomic level structure contains the microscopic details necessary for the formation of polaritons, which within the effective theory is incorporated in the dressed P-photons, and on the other hand the atoms serve as interaction vertices between one probe photon and an arbitrary number of exchange photons. While the latter may be strongly dressed with probe photons themselves, there are only two processes for this that are allowed by the atomic vertices, namely those in the third line of Fig. 4.26. The diagrammatic representation of the effective theory is shown in Fig. 4.27. We stress that this is completely equivalent to the theory presented in Fig. 4.26. In the first line of Fig. 4.27, the free polariton propagator is defined and indicated as a curly-line. In the second line the interaction vertices between the polariton and the E-photons are illustrated. Out of these, only the first

two are shown but actually and infinite number of E-lines is allowed in the vertex indicated by the dots in the last line of Fig. 4.27, where all possible interaction-corrections to the polariton self-energy are shown. Luckily all of these vertices can be conveniently resummed as a geometric series, as we have demonstrated earlier in the derivation of the self-consistent equations. Similarly, all possible contributions to the E-photon self-energy are shown in the third line. However, as every vertex has to involve exactly one probe photon, the number of diagrams here is limited to two.

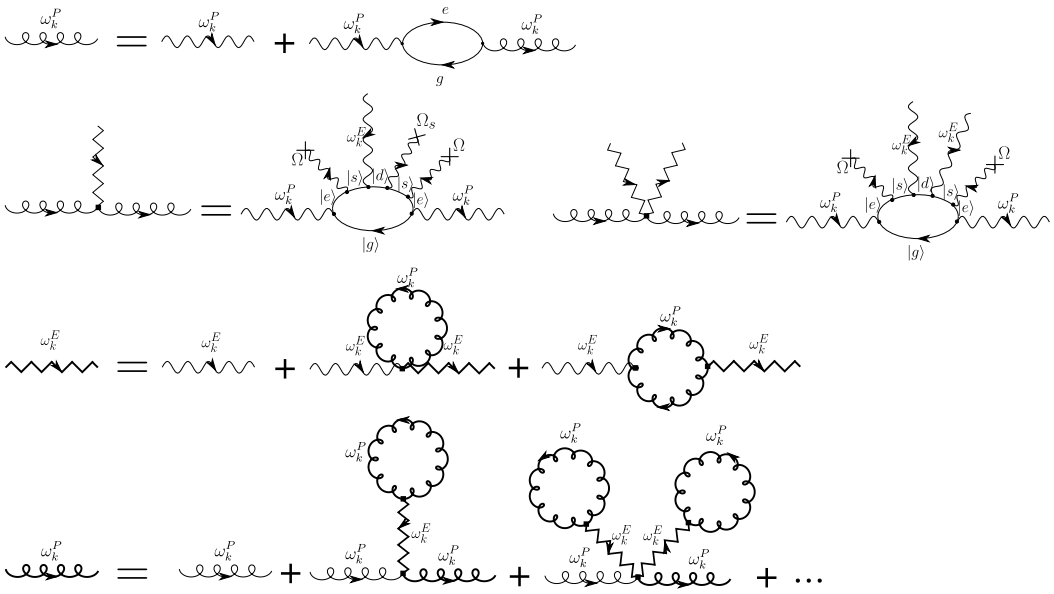

Figure 4.27: Effective theory of dark-state polaritons in the limit of infinite interaction range, i.e. $L_E \to \infty$. While there is an infinite set of vertices coupling a single probe photon to an arbitrary number of exchange photons, these are conveniently summed up in the geometric series embedded in Σ_P^R. This effective theory is completely equivalent to the one shown in Fig. 4.26.

Quantitative results and validity

With the inclusion of all effects at leading order in $1/L_E$, χ is no longer bounded from below by -1. In fact, it can achieve arbitrarily small values, which can be understood by a closer examination of the effects of $\Sigma_E^{R_2}$ in terms of the effective theory in Fig. 4.27, where it is represented as the last diagram of the third line. Within this framework one immediately realizes, that $\Sigma_E^{R_2}$ describes in fact a particle-hole excitation of a probe photon. Since, however, this photon itself is strongly dressed, its distribution $F_P(\omega)$ is sharply peaked. This allows for a

resonant reallocation of photons from highly occupied frequencies and momenta towards low-occupation regions, by means of the particle-hole excitations in $\Sigma_E^{R_2}$. Where this is possible, it will act as a locally inverted environment for G_E, thereby effectively driving the exchange photons. Since there is no other diagram to counter this effect, the exchange photon propagator can develop a divergence, resulting in $\chi \to -\infty$, which is unphysical. While in general there is nothing wrong with the inverted bath experienced by the exchange photons, one has to pay attention to its effect on $L_E = \sqrt{\alpha_E/\kappa_E^{\text{eff}}}$. The latter namely vanishes as the divergence in G_E^R is approached. Consequently, diagrams at higher order in $1/L_E$ have to be included and these will in turn prevent the unphysical instability in the exchange photon propagator. We will outline the underlying processes in the next section. Nevertheless, as long as L_E remains large enough, $-\chi$ can still become large without forcing us to include subleading orders in L_E. This can happen to such an extent, that it actually overcompensates the bare coupling Ω_s up to the point where a new, strongly interacting phase emerges. This new phase, which will be referred to as "intermediate phase", is stable, as evidenced by the flow diagrams 4.28 and 4.29, which we show again for both the lenient and the strict implementation of the Feynman rules. As there is hardly any quantitative differences between the two versions, we will in the following focus on the strict rules.

Previously, we presented an argument for the emergence of the bistability, whereby an increase in Ω_s^{eff} was met with a sufficiently fast decrease of n_s (and of χ), so that Ω_s itself was reduced, resulting in a non-unique identification $\Omega_s(\Omega_s^{\text{eff}})$, i.e. a bistability. It is exactly the opposite effect that stabilizes the intermediate phase, whereby for small Ω_s an increase of Ω_s^{eff} increases the efficiency of the drive experienced by G_E^R, such that $|\chi|$ grows until this effect is exactly balanced by the effects of increased losses discussed in Sec. 4.7.1. If this happens at $\chi \lesssim -1$ a stable intermediate phase exists.

As can be observed in Fig. 4.30, where the losses γ_d have been increased tenfold compared to Figs. 4.20 and 4.21, the stability of the transparent phase is strongly enhanced in comparison with the results of Sec. 4.7.1. This is a consequence of the slow dark-state polaritons, which require that each probe photon during its lifetime excites on average multiple atoms. As such, while the field content of the two contributions $\Sigma_E^{R_1}$ and $\Sigma_E^{R_2}$, as well as the relative detunings between atoms, lasers and guided photons, allow no distinction between these contributions, $\Sigma_E^{R_2}$ is favored combinatorically by a factor $\sim C_P$. In essence, on can think of the last diagram in the third line of Fig. 4.26 or equivalently Fig. 4.27 as an antenna increasing the amplitude of the indirect coupling beyond that of the direct laser driven transition between $|s\rangle$ and $|d\rangle$. Consequently, slow polaritons with infinitely ranged interactions are typically dominated by these diagrams. If the gain of the antenna $\sim C_P$ is large and increases sufficiently with Ω_s^{eff}, as suggested by the superficial dependence $\Sigma_E^{R_2} \sim (\Omega_s^{\text{eff}})^2$, it can counteract the reduction in polariton density, thereby stabilizing the intermediate phase.

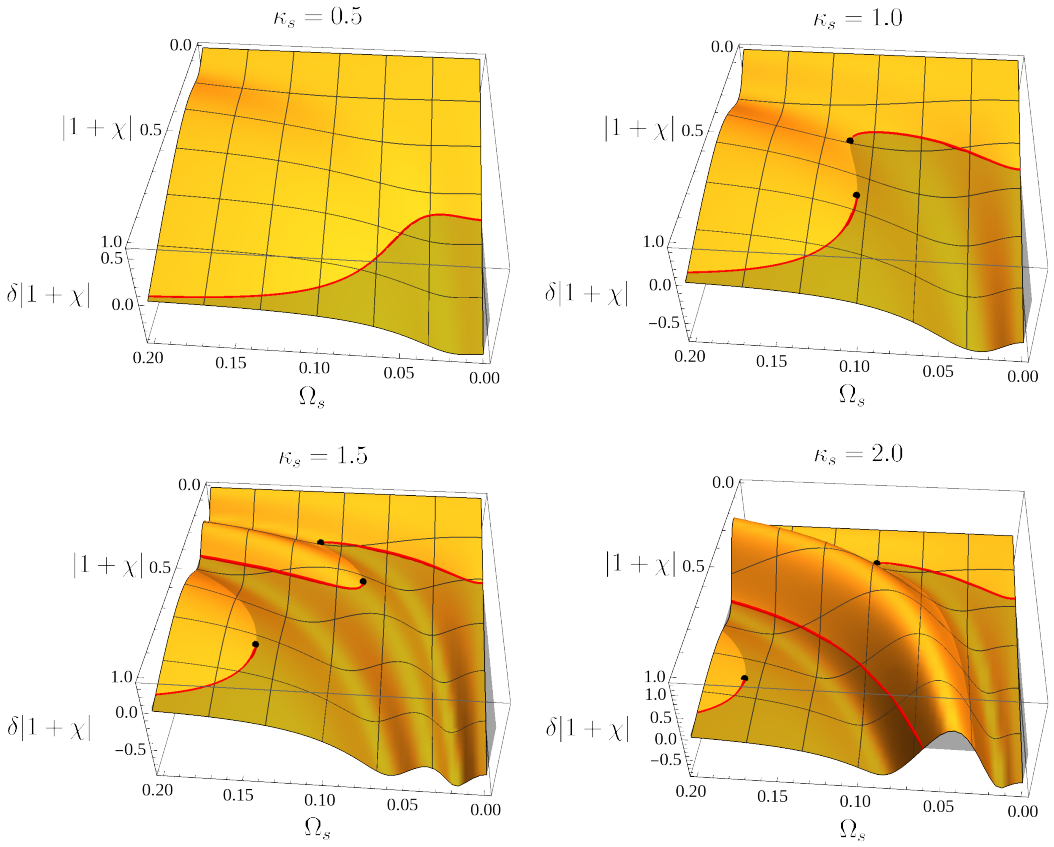

Figure 4.28: Flow diagram of the effective relative coupling strength $|1+\chi|$ as a function of the externally adjustable parameter Ω_s, where apart from $\gamma_d = 10$ the same parameters as in Fig. 4.20 are used together with the lenient interpretation of the nonlinear Feynman rules. Note the emergence of a tristable region, where in addition to the opaque and transparent phases a new, strongly interacting semi-transparent phase appears.

As is indicated by the color gradients in Fig. 4.30, the transparent and opaque phase are adiabatically connected. The same is true for the transparent and intermediate phase as the latter emerges from the former at large drive strengths κ_s. In order to more closely investigate the properties of each phase, we provide a plot of the number density of atoms in the state $|s\rangle$ (Fig. 4.31), which shows that in every phase the polariton density and therefore their lifetime decreases as Ω_s is increased. However, in case of the intermediate phase n_s and the polariton lifetime decrease also with increasing κ_s, which implies that the interaction strength is increased. This demonstrates that the intermediate phase is indeed stabilized by the overcom-

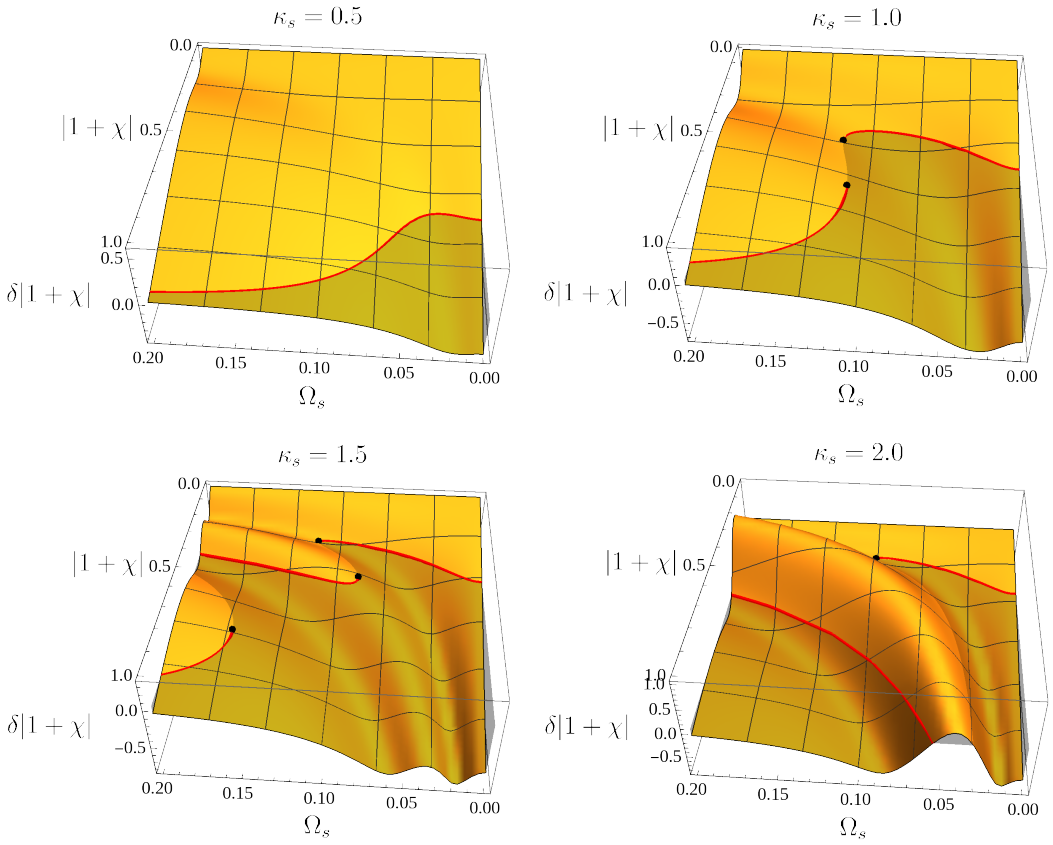

Figure 4.29: Same diagram as in Fig. 4.28 but using the strict version of the non-linear Feynman rules.

pensation of Ω_s via strong interactions and its properties are not directly linked to either the weakly interacting limit $\Omega_s/\kappa_s \to \infty$ or the unperturbed polaritons at $\kappa_s/\Omega_s \to \infty$. We therefore use the strong backaction condition of a negative slope in the polariton density $dn_s/d\kappa_s$ as the defining property to distinguish between the transparent and intermediate phase in Fig. 4.31. The relatively low density and the increased line-width of the dark-state polaritons (see Fig. 4.32) in the intermediate phase actually helps with the numerical investigation, as the discretization of momentum and frequency space can be performed at a lower resolution and saturation effects can more readily be discarded.

4.8 Controlled expansion to finite L_E

As was summarized at the end of the last section, the restriction to a theory that exclusively resums all Hartree diagrams of the effective theory in Fig. 4.27

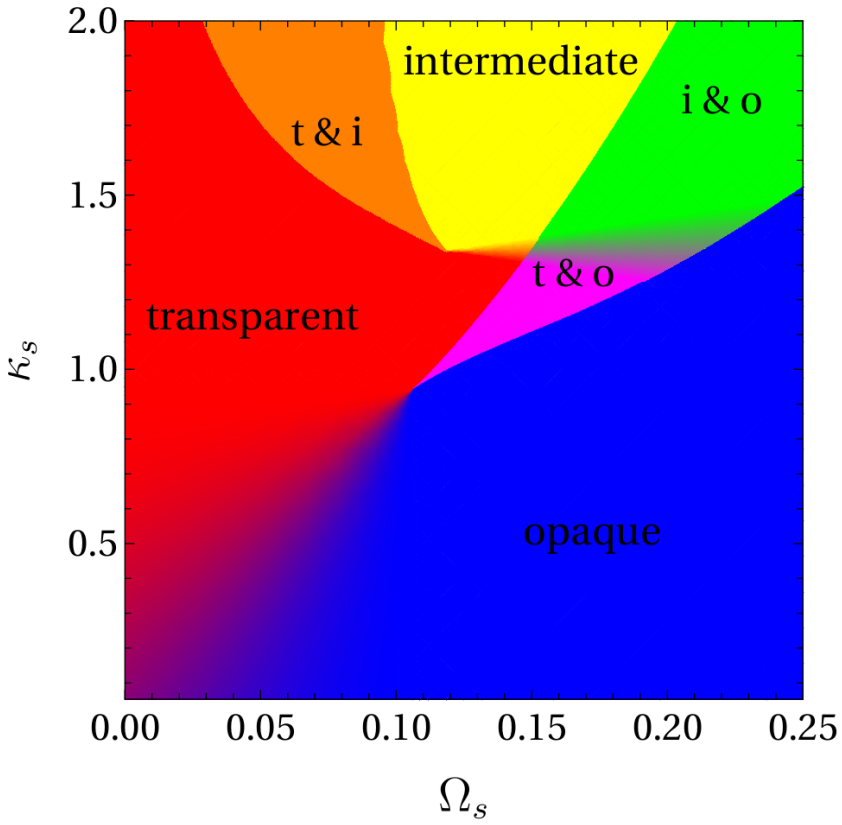

Figure 4.30: The quantitative phase diagram in the limit $L_E \to \infty$ and with the parameters of Fig. 4.28, shows three distinct phases. While the transparent and opaque phase can be adiabatically connected to free theories far away from the multistable regime, the same cannot be said for the strongly interacting intermediate phase. The region of coexistence between opaque and transparent phase is indicated in magenta, that between transparent and intermediate phase in orange, and the remaining bistable area in green. All multistable regions are labeled by the initial characters of the coexisting phases.

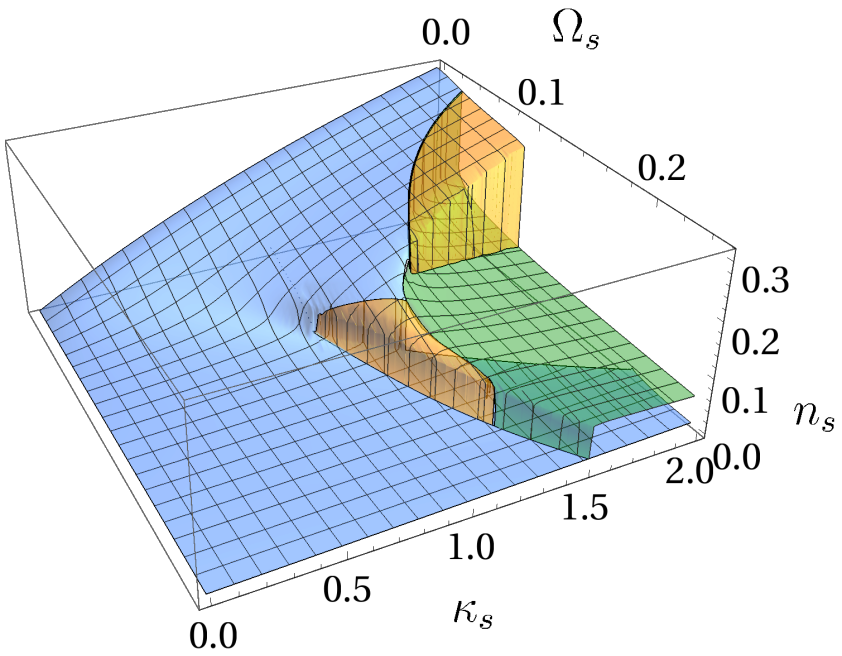

Figure 4.31: The number density of atoms in the metastable state $|s\rangle$ can be used to characterize the three distinct phases. For the slow polaritons obtained for the parameters of Fig. 4.28, that are also used here, n_s is a good estimate of the dark-state polariton density. The density of the intermediate phase is highlighted in green and those of the adiabatically connected transparent and opaque phases in blue. If these coexist the transparent solution is shown in yellow. As a testament to the overcompensation of Ω_s by χ the density of the strong coupling intermediate phase decreases as the drive intensity κ_s is increased.

is not always quantitatively justified. In particular, for current experiments with PCWs [17] the range of the exchange photons is limited due to imperfections in the fabrication that cause rather large losses κ_E. Therefore, in this section we will go one step further and include all diagrams in next-to-leading order. This allows us to include scattering between polaritons, that is, processes involving momentum transfer. In terms of the effective theory in Fig. 4.27, the only modification is the inclusion of the two diagrams in Fig. 4.33. Equivalently, in terms of the original theory including the atomic degrees of freedom, we obtain the Dyson equations shown in Fig. 4.34. One can identify these self-energies with the full set of self-consistently generated diagrams from the next-to-leading order corrections in $1/L_E$ and $1/L_P$ to the probe-photon propagator shown in Fig. 4.15.

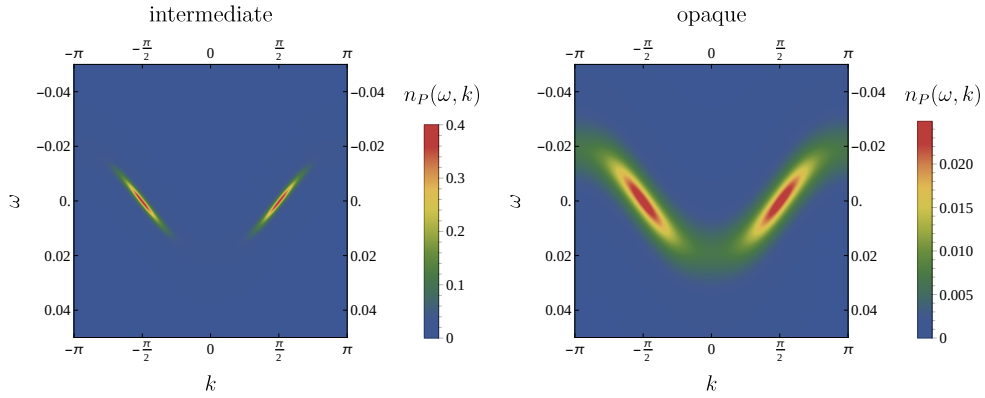

Figure 4.32: The Comparison of the EIT window for the two different stable phases shows a distinct ordering in the brightness of the dark-state polaritons. Except for $\kappa_s = 2$ and $\Omega_s = 0.21$ the parameters of Fig. 4.28 were used.

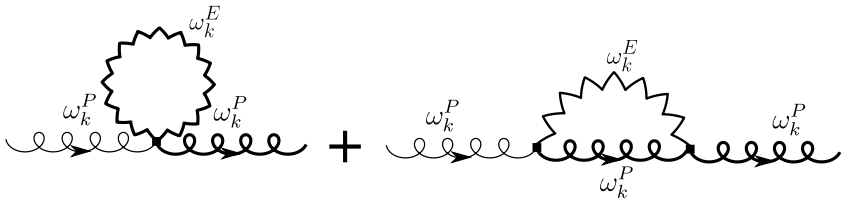

Figure 4.33: Addition to the effective theory in Fig. 4.27 at next-to-leading order in $1/L_E$.

4.8.1 Self-consistent theory at $\mathcal{O}(1/L_E)$

As can be seen in Fig. 4.34, a fully self-consistent theory involving all effects at next-to-leading order in the inverse interaction range requires to solve an even larger number of coupled integral equations than in the previous section. This task might seem daunting at first sight, however, using the Kramers-Kronig relations (see section 4.4.3) and the loop reduction procedure (see section 4.4.5), every single diagram can once again be broken down into a combination of independent one-loop effects. Due to the nonlinear Feynman rules (section 4.4.4), great care has to be taken in determining which of these single loop effects can be combined. We do so by introducing two different matrix Green's functions $\mathcal{G}_{sd}$ and $\tilde{\mathcal{G}}_{sd}$ for the states $|s\rangle$ and $|d\rangle$. To help distinguish these propagators in Feynman diagrams, we slash the propagator of $\tilde{\mathcal{G}}_{sd}$ twice. When appearing as an insertion inside the probe-photon propagator, $\mathcal{G}_{sd}$ cannot itself involve a self-energy that would return the atom to its ground state. There is thus only one contribution to the self-energy

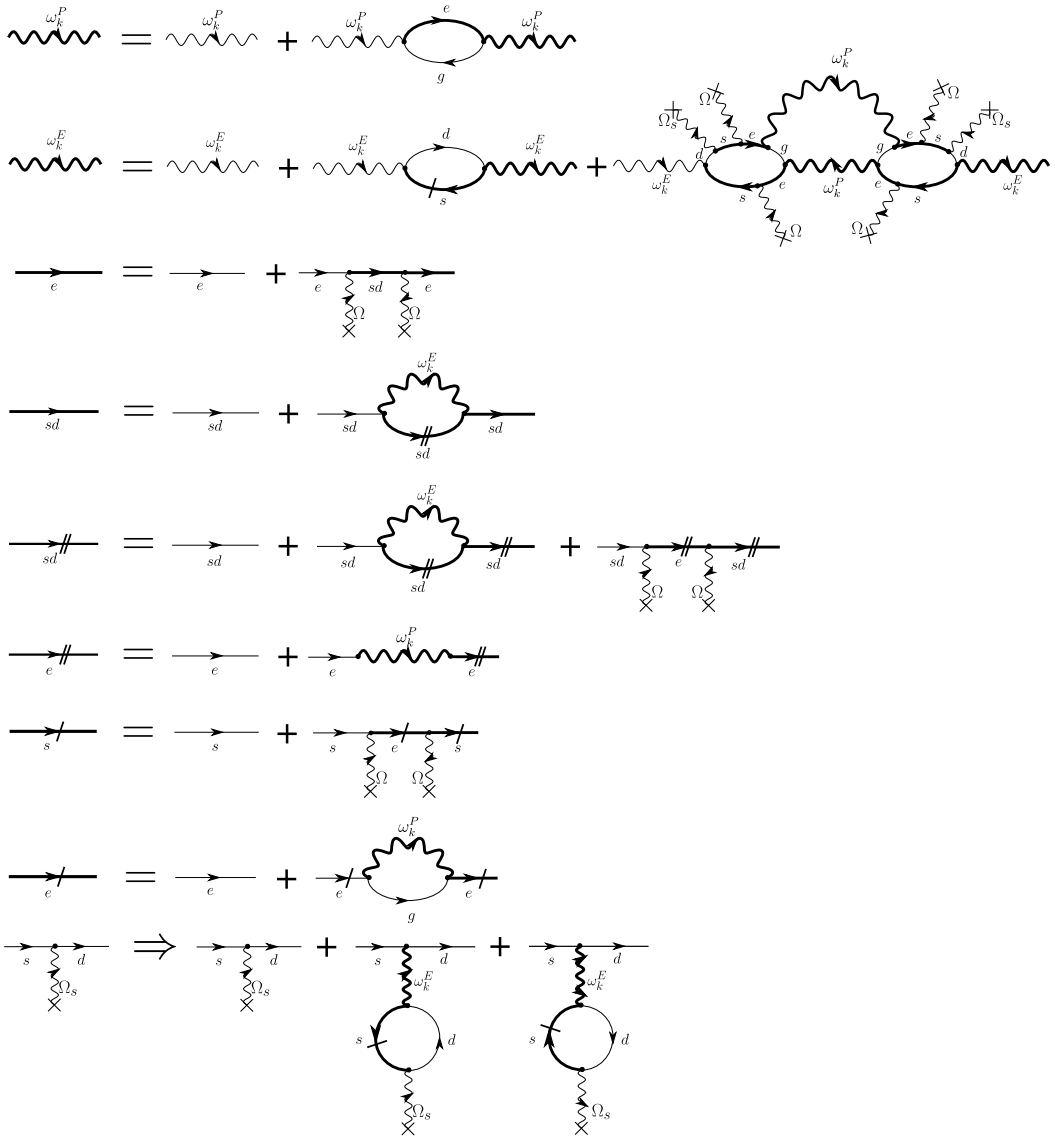

Figure 4.34: Complete set of coupled Dyson equations at next-to-leading order. The loop-reduction procedure of section 4.4.5 is employed here and, depending on the Feynman rules at use, d-propagators are either bare or given as part of G_{sd}, of which the s-propagator in the last diagram of the third line is just the (11)-component.

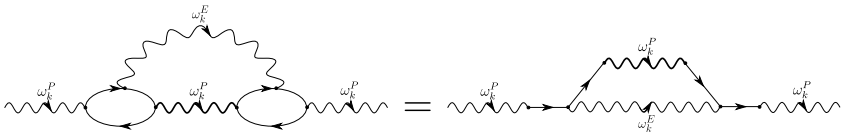

Figure 4.35: Loop reduction procedure for the Feynman diagram in Fig. 4.15b), which formally delocalizes excited atoms. Note that during this procedure the probe photon coupling strength has to be modified by $g_P \to g_P\sqrt{2-2n_V}$ to properly reflect the atom number density.

and the matrix propagator takes the fairly simple form

$$\mathcal{G}^R_{sd} = \left(\left[\mathcal{G}^R_{sd}\right]^{-1} - \Sigma^R_{sd} \right)^{-1} , \tag{4.156}$$

where

$$\Sigma^R_{sd} = \frac{i}{2} g_E^2 \begin{pmatrix} \delta G^K_{E_{22}} \star \tilde{G}^R_{dd} + G^R_{E_{22}} \star \delta\tilde{G}^K_{dd} & G^R_{E_{21}} \star \delta\tilde{G}^K_{ds} + \left(\delta G^K_{E_{21}} + 2G^{K_0}_{E_{21}}\right) \star \tilde{G}^R_{ds} \\ \delta G^K_{E_{12}} \star \tilde{G}^R_{sd} + G^R_{E_{12}} \star \delta\tilde{G}^K_{ds} & G^R_{E_{11}} \star \delta\tilde{G}^K_{ss} + \left(\delta G^K_{E_{11}} + 2G^{K_0}_{E_{11}}\right) \star \tilde{G}^R_{ss} \end{pmatrix} \tag{4.157}$$

uses $\star$ to denote the convolution in ω and k. The corresponding Keldysh component reads

$$\delta\mathcal{G}^K_{sd} = \mathcal{G}^R_{sd} \cdot \delta\Sigma^K_{sd} \cdot \mathcal{G}^A_{sd} , \tag{4.158}$$

with

$$\delta\Sigma^K_{sd} = \frac{i}{2} g_E^2 \begin{pmatrix} \left(\delta G^K_{E_{22}} + 2G^{K_0}_{E_{22}}\right) \star \delta\tilde{G}^K_{dd} & \left(\delta G^K_{E_{21}} + 2\left[G^R_{E_{12}}\right]^*\right) \star \delta\tilde{G}^K_{ds} \\ \left(\delta G^K_{E_{12}} - 2G^R_{E_{12}}\right) \star \delta\tilde{G}^K_{sd} & \delta G^K_{E_{11}} \star \delta\tilde{G}^K_{ss} \end{pmatrix} . \tag{4.159}$$

Note that $\Sigma^{R/K}_{sd}$ are allowed to depend on the quasi-momentum k, since, due to the photon admixture with momentum transfer, they effectively no longer describe a completely stationary atom. This effective delocalization of the atoms is not an actual physical process, but rather a mathematical trick to accommodate the loop reduction procedure shown in Fig. 4.35. In fact, we construct $\tilde{\mathcal{G}}_{sd}$ via

$$\tilde{\mathcal{G}}^R_{sd} = \left(\left[\mathcal{G}^R_{sd}\right]^{-1} - \begin{pmatrix} \Sigma^R_s & 0 \\ 0 & 0 \end{pmatrix} \right)^{-1} \tag{4.160}$$

with

$$\Sigma_s^R = \frac{\Omega^2}{\omega - g_P^2\left[(1-n_V)G_P^R + \frac{1}{2}G_g^R \star_\omega \delta G_P^K\right] + i\gamma_e/2}\,, \tag{4.161}$$

where $\star_\omega$ indicates a particle-hole convolution in frequency only, i.e.

$$f \star_\omega h = \int_{-\infty}^{\infty} \frac{d\omega'}{2\pi} f(\omega')h(\omega'+\omega)\,. \tag{4.162}$$

Furthermore, the related

$$\delta\tilde{\mathcal{G}}_{sd}^K = \tilde{\mathcal{G}}_{sd}^R \cdot \left(\delta\Sigma_{sd}^K + \begin{pmatrix} \delta\Sigma_s^K & 0 \\ 0 & 0 \end{pmatrix}\right) \cdot \tilde{\mathcal{G}}_{sd}^R\,, \tag{4.163}$$

where

$$\delta\Sigma_s^K = \frac{g_P^2}{\Omega^2}(1-n_V)\delta G_P^K |\Sigma_s^R|^2 \tag{4.164}$$

correctly includes all repeated scattering processes of a probe photon into a probe and an exchange photon. The loop reduction procedure therefore allows for a very cost-efficient inclusion of pairing effects between probe and exchange photons, that would otherwise require a self-consistent treatment of the corresponding T-matrix.

The Dyson equation for the probe photon propagator takes almost exactly the same form as it does for the non-interacting EIT:

$$\begin{aligned} G_P^R &= \left(\omega - \Delta_P(k) - g_P^2(1-n_V)G_e^R + i\kappa_P/2\right)^{-1} \\ \delta G_P^K &= \left(\Omega^2 g_P^2(2-n_V)\delta G_{ss}^K |G_e^R|^2 - 2i\kappa_s(\omega)\right)|G_P^R|^2\,, \end{aligned} \tag{4.165}$$

with the only difference being hidden in the more elaborate form of G_{ss}.

In order to close the set of coupled equations one has to find the full exchange photon propagator, which again has two self-energy contributions as in Eq. (4.153). The first one

$$\Sigma_E^{R_1}(\omega) = \frac{i}{2}g_E^2 \begin{pmatrix} \left[\delta G_{\not s}^K \star_\omega G_d^R\right](\omega) & 0 \\ 0 & \left(\delta G_{\not s}^K \star_\omega G_d^R\right)(-\omega) \end{pmatrix} \tag{4.166}$$

is already known from Sec. 4.7.1 and in the present notation involves the propagator $\delta G_{\not s}^K$ given by

$$\delta G_{\not s}^K(\omega) = \frac{g_P^2}{\Omega^2}(1-n_V)\kappa_s(\omega)\left|\frac{\Sigma_{\not s}^R(\omega)}{\omega - \Delta_s - \Sigma_{\not s}^R(\omega) + i\gamma_s/2}\right|^2 \int \frac{dk}{2\pi}\delta G_P^K(\omega,k). \tag{4.167}$$

For the strict interpretation of the nonlinear Feynman rules we use

$$\Sigma^R_{\not P}(\omega) = \frac{\Omega^2}{\omega + i\gamma_e/2 - g_P^2 \int \frac{dk}{2\pi} \left[(1-n_V) G_P^R + \kappa_s(\omega) G_g^R \star_\omega \delta G_P^K\right]} \tag{4.168}$$

and $G_d^R = G_{d_0}^R$. One therefore recovers exactly the same expression for $\Sigma^R_{E_1}$ as in the previous sections. In case of the lenient Feynman rules the denominator in the absolute value in Eq. (4.167) is to be replaced by

$$\omega - \Delta_s - \Sigma^R_{\not P}(\omega) + i\gamma_s/2 + \frac{\left(\Omega_s^{\rm eff}\right)^2}{\omega - \Delta_d - \Delta_s + i\gamma_d/2} + \int_{-\pi}^{\pi} \frac{dk}{2\pi} \Sigma^R_{ss}(\omega, k)\,, \tag{4.169}$$

where Σ^R_{ss} is the 11-component of Σ^R_{sd}. At the same time G_d^R is given by $\tilde{G}^R_{dd}$. This leaves $\Sigma_E^{R_2}$, which takes the same form as in Sec. 4.7.2:

$$\begin{aligned}
\Sigma_E^{R_2}(\omega, k) =& \frac{i}{2} g_P^4 g_E^2 \Omega^4 \left(\Omega_s^{\rm eff}\right)^2 (1-n_V)^2 \int \frac{d\omega'}{2\pi} \frac{dp}{2\pi} \left|G_e^R(\omega') G_s^R(\omega')\right|^2 \delta G_P^K(\omega', p) \\
&\times \Bigg[\left[G_s^R(\omega+\omega') G_e^R(\omega+\omega')\right]^2 G_P^R(\omega+\omega', p+k) \\
&\qquad \times \begin{pmatrix} \left[G_d^R(\omega+\omega')\right]^2 & G_d^A(\omega') G_d^R(\omega+\omega') \\ G_d^R(\omega') G_d^R(\omega+\omega') & \left|G_d^R(\omega')\right|^2 \end{pmatrix} \\
&+ \left[G_e^A(\omega'-\omega) G_s^A(\omega'-\omega)\right]^2 G_P^A(\omega'-\omega, p-k) \\
&\qquad \times \begin{pmatrix} \left|G_d^R(\omega')\right|^2 & G_d^A(\omega'-\omega) G_d^A(\omega') \\ G_d^A(\omega'-\omega) G_d^R(\omega') & \left[G_d^A(\omega'-\omega)\right]^2 \end{pmatrix} \Bigg] .
\end{aligned} \tag{4.170}$$

Evaluating the same diagrams for the Keldysh component, one obtains the last two pieces of the puzzle:

$$\delta\Sigma_E^{K_1} = 0\,, \tag{4.171}$$

as before, and

$$\begin{aligned}\delta\Sigma_E^{K_2}(\omega,k) =& \frac{i}{2}g_P^4 g_E^2 \Omega^4 \left(\Omega_s^{\text{eff}}\right)^2 (1-n_V)^2 \\ &\times \int \frac{d\omega'}{2\pi}\frac{dp}{2\pi} \left|G_e^R(\omega')G_e^R(\omega'+\omega)G_s^R(\omega')G_s^R(\omega'+\omega)\right|^2 \\ &\times \delta G_P^K(\omega',p)\delta G_P^K(\omega'+\omega,p+k) \\ &\times \begin{pmatrix} \left|G_d^R(\omega'+\omega)\right| & G_d^A(\omega')G_d^A(\omega+\omega') \\ G_d^R(\omega')G_d^R(\omega+\omega') & \left|G_d^R(\omega')\right|^2 \end{pmatrix} \\ -2&\begin{pmatrix} 2i\left[\Im\tilde{\Sigma}_E^R(\omega,k)\right]_{11} & \left[\tilde{\Sigma}_E^R(\omega,k)+\tilde{\Sigma}_E^R(-\omega,-k)\right]_{12} \\ -\left[\tilde{\Sigma}_E^R(\omega,k)+\tilde{\Sigma}_E^R(-\omega,-k)\right]_{12}^* & 2i\left[\Im\tilde{\Sigma}_E^R(-\omega,-k)\right]_{11} \end{pmatrix}. \end{aligned} \tag{4.172}$$

with the same choices for G_d^R in Σ_E^{R/K_2} as in $\Sigma_E^{R_1}$ and $\tilde{Sigma}_E^R$ the shorthand notation for the second term in the sum of $\Sigma_E^{R_2}$.

As always, throughout this entire theory the bare laser coupling Ω_s between states $|s\rangle$ and $|d\rangle$ has been replaced by $\Omega_s^{\text{eff}} = \Omega_s|1+\chi|$, where χ given by (4.155) describes the modified conversion rate between $|s\rangle$ and $|d\rangle$ due to the presence of other polaritons, as in section 4.7.1. Contrary to the previous renditions of the

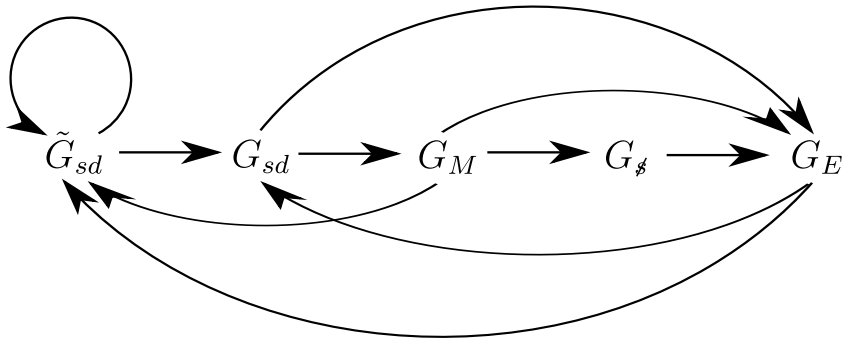

Figure 4.36: Dependency structure and ordering of updates for the self-consistent solution of the Dyson equations (4.156) through (4.172) with (4.155) iteratively updating the effective coupling Ω_s^{eff}.

self-consistent structure, with the inclusion of $1/L_E$ effects, scattering of probe photons into exchange photons becomes a possibility. Therefore, self-consistence is no longer simply a question of finding the right parameter χ, but actually involves the full frequency and momentum dependent Green's functions $G_E^{R/K}$. As such, the numerical implementation has to find the solution in an iterative manner. Since there is no direct dependence on Ω_s, one can however fix Ω_s^{eff}, initialize all Green's

functions as bare ones and iterate equations (4.156) through (4.172) together with (4.155) until χ no longer changes, see Fig. 4.36. This, once again means that the final value of Ω_s corresponding to the solution is not known a priori and has to be searched for iteratively, unless the entire phase diagram is calculated. The main advantage of this method lies again in the enhanced convergence that is unaffected by the presence of any phase transition.

As we have already discussed in Sec. 4.7.2, strictly speaking the use of the absolute value in the definition of Ω_s^{eff} in the anomalous Green's functions is wrong, since G_E no longer transforms correctly under a global $U(1)$ gauge transformation. Previously this was not a problem for the evaluation of gauge invariant observables. Despite the iterative procedure the backaction at any stage of the iteration for any observable depends only on $|1+\chi|^2$, as is required by gauge invariance. The described self-consistent calculation thus finds the correct value of $|1+\chi|$ and therefore of all normal Green's functions. To also obtain the anomalous components the correct phase of χ simply has to be restored in the final result.

4.8.2 Results

When including the effects of a finite interaction range, care has to be taken as not to break any of the assumptions underlying the quantitative validity of the approximations at use. In particular, if the interaction becomes too short-ranged, the losses in state $|d\rangle$ caused by emission of exchange photons and described by the second diagram of the fourth and fifth line of Fig. 4.34 – or equivalently the (22)-component of Eq. (4.157) – become large as a result of the narrow linewidth of state $|s\rangle$ for long lived dark-state polaritons. These effects are included in G_d^R in the lenient interpretation of the non-linear Feynman rules, but not for the strict rules. As these atomic Green's functions form the vertex of the effective theory, the differences will grow upon iteration of the self-consistency equations. The uncertainty regarding the results of the exact Feynman rules for four-level atoms thus grows with decreasing L_E. This is already observable in the comparison between Fig. 4.37 and Fig. 4.38, which qualitatively show the same phases, but with a larger discrepancy in the actual phase boundary than in the previous sections. Since the additional scattering effects that arise from the inclusion of $1/L_E$ effects into the description cannot themselves create any new instabilities and instead remedy those that could otherwise exist in G_E^R, relatively large values of C_E can be treated without much more than quantitative corrections to the previously discussed results. In particular, the parameters discussed in Figs. 4.37 and 4.38 correspond to $C_E \approx 0.22$ and $C_P = 2$. The main limitation for an extension to even smaller values of L_E or larger values of C_E lies in the discrepancy between the different interpretations of the Feynman rules, which eventually will have to be specified in more detail.

This time, for a change, we discuss our results using numerical data obtained from the lenient Feynman rules, which requires exactly the same amount of numerical effort as the strict rules. The resulting phase diagram depicted in Fig. 4.39 is

similar to that in Fig. 4.30. However, the quantitative corrections due to the finite interaction range reduce the extent of the intermediate phase. This is to be expected as the corrections in $1/L_E$ counteract the previously discussed effective drive of the exchange photons.

The restriction to large interaction ranges imposed by the discrepancy between

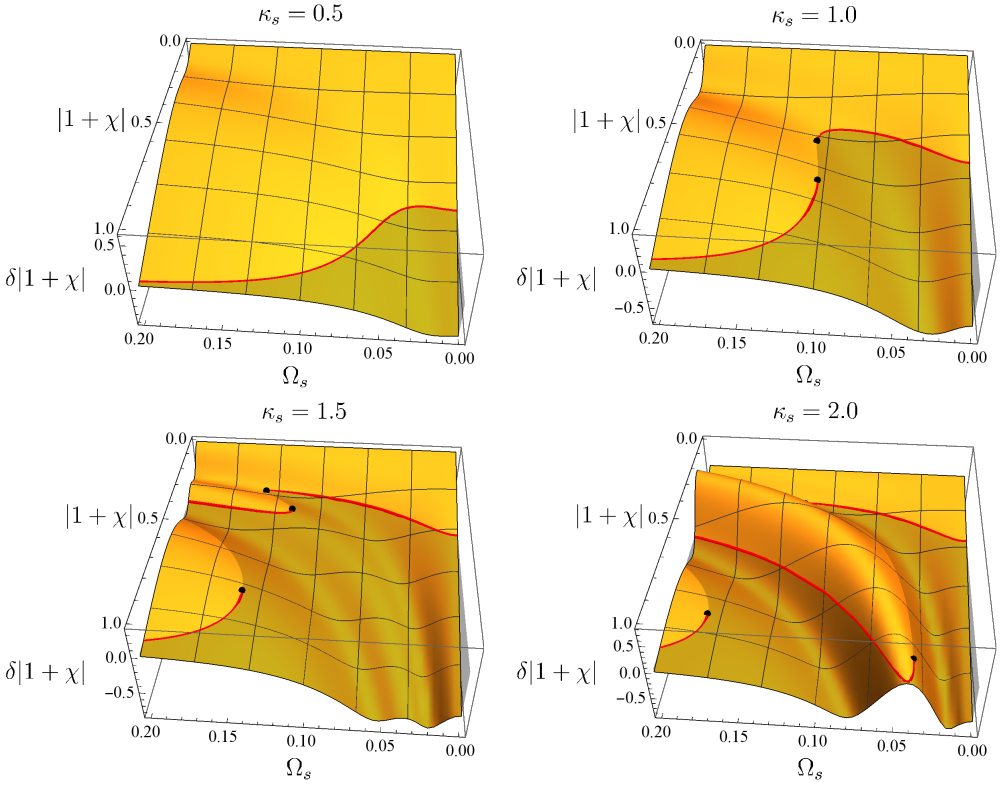

Figure 4.37: Flow diagram of the effective relative coupling strength $|1+\chi|$ as a function of the externally adjustable parameter Ω_s, using the same parameters as in Fig. 4.28, except for $\alpha_E = 400$ and $k_E = 0$, that previously did not need to be specified. Here we use the lenient interpretation of the non-linear Feynman rules. Note that the qualitative structure remains the same as in Figs. 4.28 and 4.29, however the quantitative differences compared to the strict rule in Fig. 4.38 has increased.

the approximate implementations of the Feynman rules, together with the fact that scattering between dark-state polaritons is dominated by forward scattering – the exchange photons are most efficiently coupled to at $k = 0$ – renders the effects of scattering on the probe photons actually negligible in this regime. As

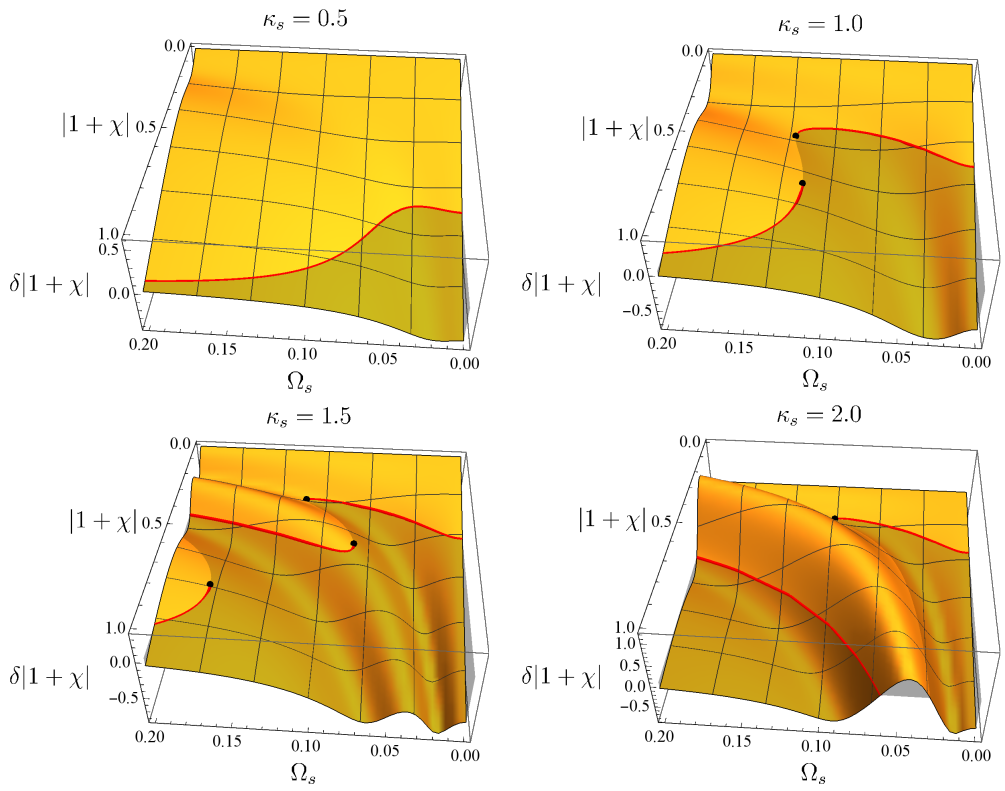

Figure 4.38: Same diagram as in Fig. 4.37 but using the strict version of the non-linear Feynman rules.

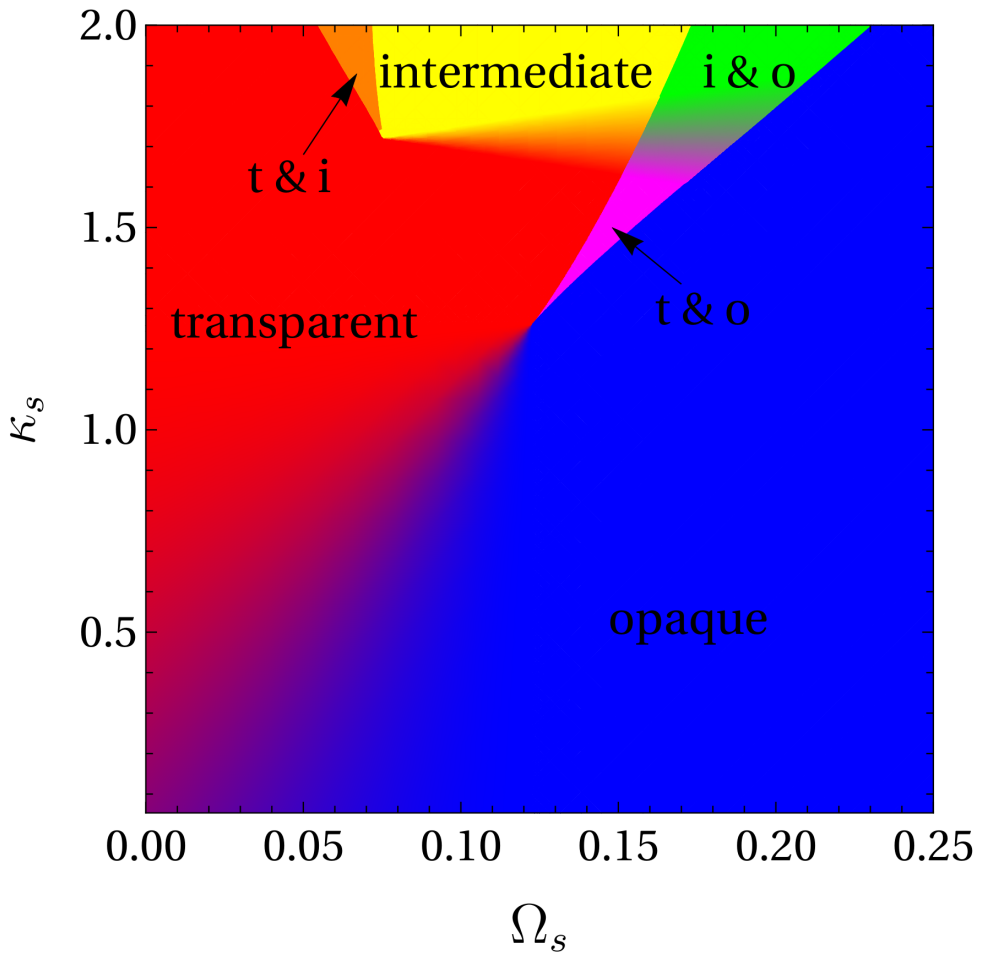

Figure 4.39: Phase diagram including corrections due to the finite interaction range. The color coding is the same as in Fig. 4.30. The bistability between transparent and intermediate phase is less pronounced and for large Ω_s the opaque phase is more prevalent. The parameters are identical to those in Fig. 4.30, except for $\alpha_E = 1000$ and $k_E = 0$ (setting the interaction range and profile) and the use of lenient Feynman rules.

a demonstration of the smallness of the redistribution due to scattering, one can examine the distribution function $F_P(\omega, k)$, which, even in the transparent phase where resonant scattering is strongest, is almost entirely momentum independent (see Fig. 4.40). Only upon subtraction of the momentum independent background a slight increase in $F_P(\omega, k)$ near the EIT window can be observed. As such, there is also no significant deformation in the dispersion of the dark-state polariton (Fig. 4.41) and the the number-density of dark-state polaritons experiences only minor corrections (Fig. 4.42).

For the present case of scattering with small momentum transfers, the most significant effect of the inclusion of $1/L_E$ corrections is the avoidance of the divergence in G_E^R appearing as an artifact of the $L_E \to \infty$ theory: while the exchange photons can still experience an effective drive due to the redistribution of energy between dark-state polaritons, this effect is significantly weakened by the increasing dissipative nature of the atomic vertex brought about by the aforementioned losses in $|d\rangle$. As the exchange photon experiences fewer and fewer losses, those of $|d\rangle$ namely increase, thereby weakening the coupling between probe and exchange photons enough to stabilize the system.

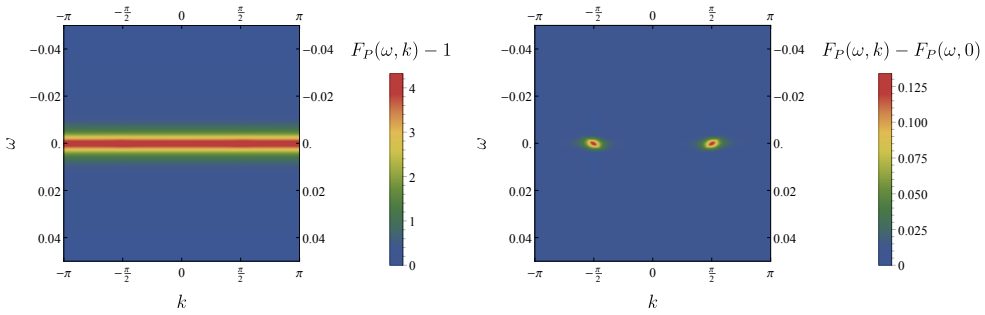

Figure 4.40: For parameters where the expansion remains quantitatively controlled, the distribution function $F_P(\omega, k)$ shows hardly any visible momentum dependence and thus only weak signatures of scattering. To make the weak momentum dependence visible, we subtracted the momentum independent background $F_P(\omega, k = 0)$. Here the transparent solution is depicted for the same parameters as in Fig. 4.37, with $\kappa_s = 1.8$, $\Omega_s = 0.07$ and $\alpha = 1000$.

4.9 Comparison with polaritons in Rydberg ensembles

Rydberg atoms exhibit essentially the same level-structure as the atoms we previously considered, but without the excited state $|d\rangle$. We will therefore mostly use the same notation as above to illustrate how interactions between Rydberg polari-

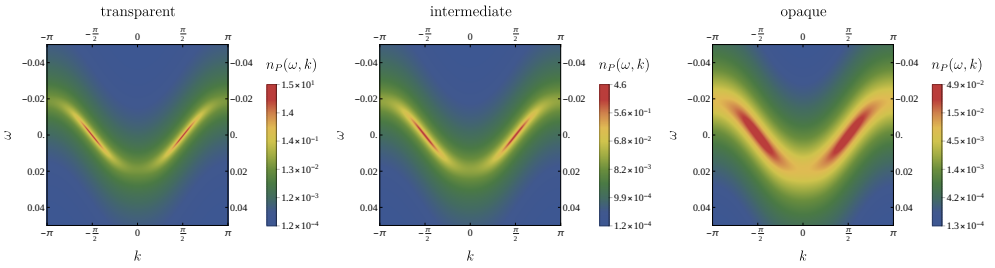

Figure 4.41: Using the same parameters as in Fig. 4.37 except for $\alpha_E = 1000$, $\kappa_s = 1.8$ and $\Omega_s = 0.07$, one again notes the pronounced difference in the overall density between the two stable phases.

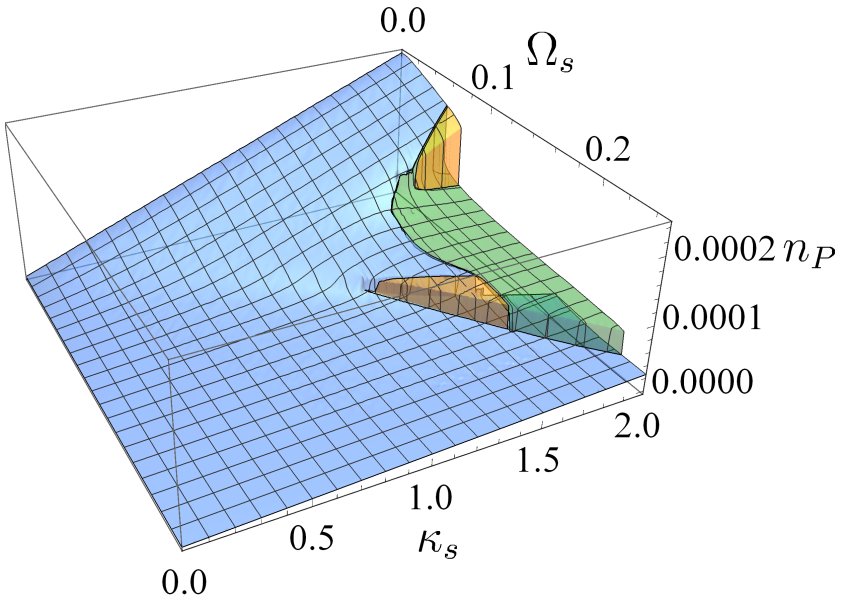

Figure 4.42: The photon density near the EIT condition is proportional to the atom density in the metastable state n_s and changes only insignificantly relative to the results for $L_E \to \infty$ if the same parameters are used (here those of Fig. 4.37).

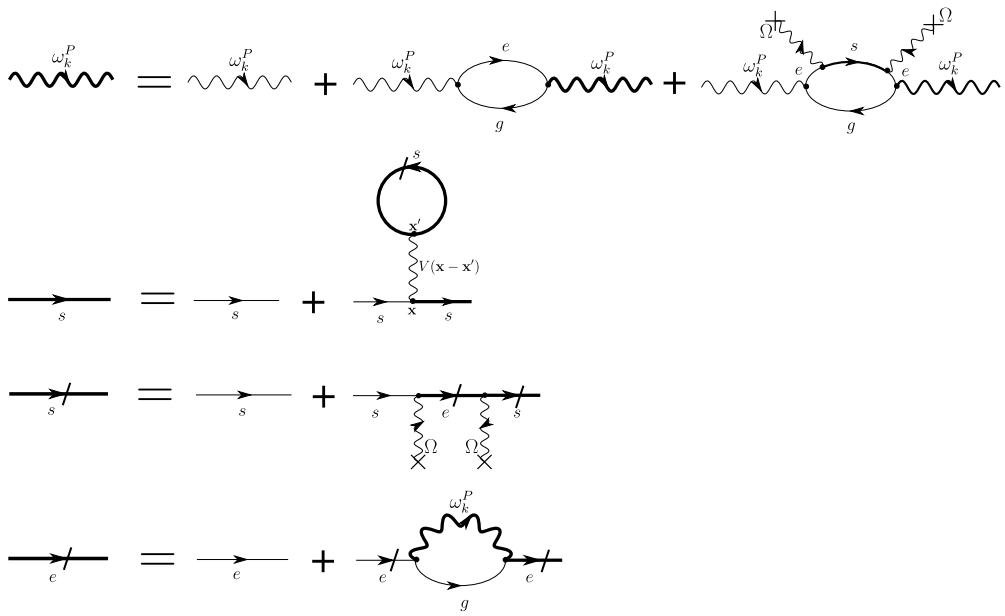

Figure 4.43: Leading order of the expansion in Feynman diagrams around the limit of infinitely ranged interactions between Rydberg polaritons. Note that, due to the use of a fixed potential, only a single interaction diagram has to be considered. Otherwise the self-consistent treatment is similar to that in Sec. 4.7.1.

tons fit into a $1/L$ expansion. Instead of driven exchange photons with significant losses and a tunable dispersion, unguided photons with low energies mediate the interactions between Rydberg atoms. In fact the quadratic Stark shift that gives rise to the interatomic van-der-Waals potential $V(\mathbf{x}) = -C/|\mathbf{x}|^6$ requires the exchange of two photons. Their dynamics however happens on timescales much shorter than those experimentally relevant and can therefore be neglected. With this knowledge it is well justified to replace the two-photon interaction by the effective potential $V(\mathbf{x}-\mathbf{x}')n_s(\mathbf{x})n_s(\mathbf{x}')$.

Diagrammatically, the resulting theory looks very similar to the one discussed in the previous sections, the only modification being the replacement of G_E^R coupling between states $|s\rangle$ and $|d\rangle$ by $V(\mathbf{x})$ acting directly on $|s\rangle$. The non-interacting Rydberg polariton theory is illustrated in the first line of Fig. 4.43 with the $|s\rangle$-propagator considered as bare. Interactions are then taken into account by dressing this state with density-density interactions that take a similar form as those considered in Sec. 4.7.1. The resulting Feynman diagram in the second line of Fig. 4.43 has to be treated self-consistently following the same procedure as in Sec. 4.7.1, with the main difference compared to Fig. 4.16 being the absence of state $|d\rangle$ and

the external source Ω_s. It is readily evaluated as

$$\Sigma_s^R(\mathbf{x},t) = \int d^3x V(\mathbf{x}-\mathbf{x}')n_s(\mathbf{x}',t) \tag{4.173}$$

with the functional dependencies $G_s^R\left[\Sigma_s^R\right]$, $G_e^R\left[G_s^R\right]$ and $G_P^R\left[G_e^R\right]$ identical to Sec. 4.7.1.

Interestingly, the leading diagrammatic contributions for the setups discussed in the previous sections actually disappear in the context of Rydberg polaritons. Self-interactions of a Rydberg atom by emission and absorption of a photon induce a Lamb shift that is already included in the bare energy of the atomic state. A repeated interaction between two Rydberg atoms on the other hand has to be treated with the nonlinear Feynman rules. By arguments identical in spirit to those of section 4.4.4 it reduces to terms already included in (4.173). Last but not least, a self-interaction of a Rydberg polariton through the interaction of two distinct atoms, similar to Fig. 4.15b), is excluded by the instantaneous nature of interactions. As such, the limit of a low Rydberg polariton density results in a less complicated, but conceptually similar expansion to that derived for PCWs and TNWs. However, the absence of an external coupling similar to Ω_s, with which the interaction can interfere destructively, prevents the emergence of phase transitions of the type discussed before.

Instead, interesting questions include the scattering of Rydberg polaritons and the stability of regular structures (i.e. n-particle bound states) or even crystals. Here we only want to give a brief idea of how these questions can be approached in terms of a $1/L$ expansion and therefore discuss the simple case of a Rydberg polariton scattering off a fixed Rydberg atom at the origin. In this case the polariton Green's function is given by

$$G_P^R(\omega,\mathbf{k},\mathbf{x}) = \left(\omega - \omega_P(k) - \frac{g_P^2(1-n_V)}{\omega - \frac{\Omega^2}{\omega-\Delta_s-V(\mathbf{x})} + i\gamma_e/2} + i\kappa_P/2\right)^{-1}, \tag{4.174}$$

where the inversion in momentum space first requires a Fourier transform from $\mathbf{x}$ to the momentum difference between incoming and outgoing polariton and is then to be understood as the inverse with respect to the convolution and thus a non-trivial operation. Nevertheless, assuming a slow, and thus well-localized, incoming Rydberg polariton of fixed frequency $\omega_{\mathrm{EIT}} = \Delta_s$ corresponding to the EIT window at $|\mathbf{x}| \to \infty$, we can calculate its losses as a function of $r = |\mathbf{x}|$ and determining the blockade radius. The losses are given by the imaginary part of the inverse propagator

$$\kappa_P^{\mathrm{eff}}(\omega,r) = \kappa_P + \frac{g_P^2(1-n_V)\gamma_e}{\left(\omega - \frac{\Omega^2}{\omega-\Delta_s-V(\mathbf{x})}\right)^2 + \gamma_e^2/4}, \tag{4.175}$$

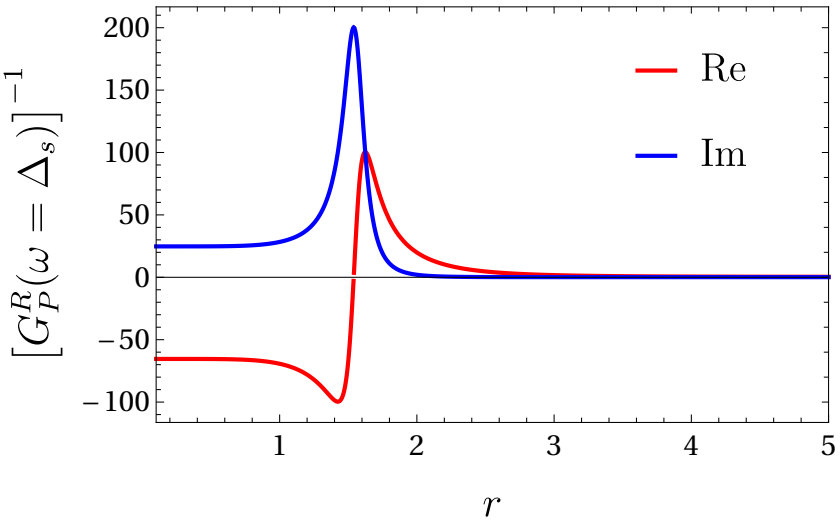

Figure 4.44: Rydberg blockade experienced by a Rydberg polariton as a function of the distance from a stationary Rydberg atom at $r = 0$. The imaginary part of the inverse propagator indicating the losses becomes very large at a distance set by the blockade radius R_b. At the same time the real part that gives rise to deflection also grows. Parameters used are $\gamma_e = 1/4$, $\kappa_P = 1/5$, $\Delta_s = 1/3$, $\Omega = 1/2$, $n_V = 0$ and $g_P = 5$.

and illustrated in Fig. 4.44. The pronounced maximum that forms at the blockade radius R_b is determined by equating the frequency shift due to Σ_e^R with the bare losses $\gamma_e/2$. As a result one finds

$$R_b = \left(\frac{C(\gamma_e + 2\Delta_s)}{2\Omega^2}\right)^{1/6}, \tag{4.176}$$

which agrees with existing work [241]. Finally, an expansion of $\kappa_P^{\text{eff}}(\Delta_s, r)$ around $r \to \infty$ reproduces the related result $\kappa_P^{\text{eff}}(\Delta_s, r) \propto r^{-12}$.

Chapter 5

Critical relaxation with overdamped quasiparticles in open quantum systems

Following a short review of the quantum kinetic equation and its most common approximations, we study the late-time relaxation in the open Dicke model. We show that the dynamical phase transition at a critical atom-light coupling is characterized by the interplay between reservoir-driven and intrinsic relaxation processes in the absence of number conservation. Above the critical coupling, small fluctuations in the occupation of the dominant quasiparticle mode start to grow in time while the quasiparticle lifetime remains finite due to losses. Near the critical interaction strength we observe a crossover between exponential and power-law $1/\tau$ relaxation, the latter driven by collisions between quasiparticles. For a quench exactly to the critical coupling, the power-law relaxation extends to infinite times, but the finite lifetime of quasiparticles prevents aging to appear in two-times response and correlation functions. We predict our results to be accessible to quench experiments with ultracold bosons in optical resonators and possibly also with trapped ions. This chapter is based on the publication Ref. [264].

5.1 Dynamics – From the quantum kinetic equation to the linearized Boltzmann equation

In chapter 4 we have discussed the steady state of a driven-dissipative system with long-range light-matter interactions. We now want to go a step further and investigate the corresponding late-time dynamics in a related setting. We begin with a short overview of dynamics far from equilibrium and its classical limit with a focus on frequently applied approximations and their respective conditions of applicability. We also discuss scenarios for how the steady state can be approached.

Independent of the choice of time-contour, the equations of motion for the Green's functions are given by the Dyson equations

$$\begin{aligned} G^R(x,x') &= \left(\left[G_0^R\right]^{-1}(x,x') - \Sigma^R(x,x') \right)^{-1} \\ G^K(x,x') &= \int dy \int dz\, G^R(x,y)\Sigma^K(y,z)G^A(z,x') \,. \end{aligned} \tag{5.1}$$

The latter of which is typically written in terms of the distribution function F defined in (4.18). For a scalar complex field, the bare Green's function in the presence of an external classical potential coupling to the density via a term in the action $V_{\rm ext}(x)\hat{\phi}^\dagger_{\rm cl}(x)\hat{\phi}_{\rm q}(x)$ is given by

$$\left[G_0^R(x,x')\right]^{-1} = \delta(x-x')\left(i\partial_t + \frac{\nabla^2_{\mathbf{r}}}{2m} - V_{\rm ext}(x)\right) \ . \tag{5.2}$$

Note that this potential can be complex if particles are exchanged with the environment. We will discuss this situation later and for the moment restrict ourselves to real valued functions $V_{\rm ext}$. The Dyson equation for the Keldysh component then becomes

$$-\left[i\partial_t + \frac{1}{2m}\nabla^2_{\rm r} - V_{\rm ext}\overset{\star}{,}F\right](x,x') = \Sigma^K(x,x') - \left(\Sigma^R \star F - F \star \Sigma^K\right)(x,x') \ , \tag{5.3}$$

where we have introduced $\star$ as the convolution operator in time and space, which satisfies the property $[\partial_t, F](x,x') = (\partial_t + \partial_{t'})F(x,x')$ [192]. Equation (5.3) is known as the quantum kinetic equation, the left hand side of which describes the evolution of a single massive particle in an external potential. It is therefore known as the kinetic term. The right hand side, however, contains interactions between multiple particles and is thus referred to as collision term.

We note, that the quantum kinetic equation is in general very difficult to solve, as it requires the forward evolution of an integro-differential equation in $2(d+1)$ dimensions. However often simplifications are possible. In particular, it is useful to separate between fast and slow degrees of freedom. There are many closely related methods, summarized as wavelet transforms [265], that are suited for this task. One analytically particularly simple – but numerically less suitable – similar method is the Wigner transform defined by

$$A(x,p) = \int dx' \ \mathrm{e}^{-ipx} A\left(x + \frac{x'}{2}, x - \frac{x'}{2}\right) \tag{5.4}$$

with the inverse

$$A(x,x') = \int \frac{dp}{(2\pi)^{d+1}} \mathrm{e}^{ip(x-x')} A\left(\frac{x+x'}{2}, p\right) \ . \tag{5.5}$$

Here we employ the notation $px = \mathbf{p}\cdot\mathbf{x} - \omega t$ as well as $dx = dt\, d\mathbf{x}^d$ and $dp = d\omega\, d\mathbf{p}^d$. The Wigner transform simplifies convolutions into a series of derivatives and turns

products into convolutions:

$$\begin{aligned}\int dy\; A(x,y)B(y,x') &\xrightarrow{\text{WT}} A(x,p)\mathrm{e}^{\frac{i}{2}\left(\overleftarrow{\partial_x}\overrightarrow{\partial_p}-\overleftarrow{\partial_p}\overrightarrow{\partial_x}\right)}B(x,p)\\ &\approx A(x,p)B(x,p)\\ &\quad+\frac{i}{2}\left(\partial_x A(x,p)\partial_p B(x,p)-\partial_p A(x,p)\partial_x B(x,p)\right)\\ A(x,x')B(x,x') &\xrightarrow{\text{WT}} \int\frac{dq}{(2\pi)^{d+1}}A(x,p-q)B(x,q)\;.\end{aligned} \tag{5.6}$$

In a system with well-defined quasiparticles, the spectral function $\rho(x,p) = i(G^R(x,p)-G^A(x,p)) = -2\Im(G^R(x,p))$ becomes sharply peaked in ω with a width given by the inverse quasiparticle lifetime $1/\tau_{\text{qp}}$. If the characteristic length (time) scale δx on which $F(x,x')$ varies as a function of the center of mass coordinate $(x+x')/2$ is much longer than the microscopic inverse momentum (energy) scale set by the dependence of the spectral function on the relative coordinate, an expansion in the derivatives in Eq. (5.4) is possible. Technically we require, that the evolution in the center of mass coordinate takes place on scales large compared to the characteristic scales of the eigenmodes of the system. In more physical terms this translates to the requirement that the length and time scale on which the system is forced out of equilibrium is much longer than the inverse quasiparticle lifetime and size. To linear order in the expansion in derivatives we find

$$\left[Z^{-1}\partial_t + \mathbf{v}_g\nabla_{\mathbf{r}} + (\partial_t V)\,\partial_\omega - (\nabla_{\mathbf{r}}V)\,\nabla_{\mathbf{k}}\right]F(x,p) = I_{\text{coll}}[F] \tag{5.7}$$

with a renormalized quasiparticle weight $Z = 1/\left(1-\partial_\omega\Re\Sigma^R\right)$, group velocity $\mathbf{v}_g(x,p) = \nabla_{\mathbf{k}}\left(\omega(\mathbf{k})+\Re\Sigma^R(x,p)\right)$ and external potential $V(x,p) = V_{\text{ext}}(x) + \Re\Sigma^R(x,p)$. The collision integral now is a simple product

$$I_{\text{coll}}[F] = i\Sigma^K(x,p) + 2F(x,p)\Im\Sigma^R(x,p)\;, \tag{5.8}$$

where the self-energies implicitly depend on F and ρ and for explicit calculations requires some approximation as well. Having restricted our discussion for the moment to an isolated system, the collision integral satisfies the condition $I_{\text{coll}}[F_{\text{eq}}] = 0$, where $F_{\text{eq}}(\omega) - 1 = \coth(\beta\omega)$ is the Bose-Einstein distribution[1].

$F_{\text{eq}}(\omega)$ already hints towards the fact, that in general the energy scale on which F varies does not depend on $1/\tau_{\text{qp}}$, but rather the (effective) temperature of the system or some mean energy density. In the collision integral F appears only if a diagram with an internal Keldysh propagator contributes. Consequently, it always appears in a product with the sharply peaked spectral function. As a result the energy dependence of F can be neglected by restricting the distribution function

[1] Similar statements are also true for fermionic and classical collision integrals with the Bose-Einstein distribution replaced by either Fermi-Dirac or Boltzmann distributions.

to the self-consistent mass shell

$$\tilde{F}(\mathbf{r},\mathbf{k},t) = F(x,\mathbf{k},\omega=\omega(\mathbf{k})+V(x,p)) \;, \tag{5.9}$$

which is nothing else than the local density approximation. Thus, on-shell and within the quasiparticle approximation we find for slowly varying distributions the quantum Boltzmann equation

$$\left[Z^{-1}\partial_t + \mathbf{v}_g\nabla_{\mathbf{r}} - (\nabla_{\mathbf{r}}V)\,\nabla_{\mathbf{k}}\right]\tilde{F}(\mathbf{r},\mathbf{k},t) = I_{\rm coll}[\tilde{F}] \;, \tag{5.10}$$

where to second order in the coupling strength the collision integral for the s-wave scattering introduced in Eq. (4.35) is given by

$$\begin{aligned} I_{\rm coll}[F] =& \frac{g^2}{2}\int\frac{dp}{(2\pi)^{d+1}}\int\frac{dq}{(2\pi)^{d+1}}\rho(x,p-q)\rho(x,k-q)\rho(x,p) \\ &\times\{[F(x,p)F(x,k-q)+1]\,[F(x,p-q)+F(x,k)] \\ &\quad -[F(x,k)F(x,p-q)+1]\,[F(x,k-q)+F(x,p)]\} \;, \end{aligned} \tag{5.11}$$

which using the mass-shell set by the bare spectral function $\rho(x,p) = 2\pi\delta(\omega-\omega(\mathbf{p}))$ becomes

$$\begin{aligned} I_{\rm coll}[\tilde{F}] =& \pi g^2\int\frac{d\mathbf{p}}{(2\pi)^d}\int\frac{d\mathbf{q}}{(2\pi)^d}\delta\left(\omega(\mathbf{p})+\omega(\mathbf{k}-\mathbf{q})-\omega(\mathbf{k})-\omega(\mathbf{p}-\mathbf{q})\right) \\ &\times\left\{\left[\tilde{F}(x,\mathbf{p})\tilde{F}(x,\mathbf{k}-\mathbf{q})+1\right]\left[\tilde{F}(x,\mathbf{p}-\mathbf{q})+\tilde{F}(x,\mathbf{k})\right]\right. \\ &\quad\left.-\left[\tilde{F}(x,\mathbf{k})\tilde{F}(x,\mathbf{p}-\mathbf{q})+1\right]\left[\tilde{F}(x,\mathbf{k}-\mathbf{q})+\tilde{F}(x,\mathbf{p})\right]\right\} \;. \end{aligned} \tag{5.12}$$

Substituting the distribution function by the occupation number $\tilde{F}(x,\mathbf{k}) = 2n(x,\mathbf{k})+1$ this turns into the well-known result for the collision term of a weakly interacting Bose gas with contact interactions [266]:

$$I_{\rm coll}[n] = 8\pi g^2\int\frac{d\mathbf{p}}{(2\pi)^d}\int\frac{d\mathbf{q}}{(2\pi)^d}\delta\left(\omega(\mathbf{p})+\omega(\mathbf{k}-\mathbf{q})-\omega(\mathbf{k})-\omega(\mathbf{p}-\mathbf{q})\right) \tag{5.13}$$

$$\times\{n(x,\mathbf{p})n(x,\mathbf{k}-\mathbf{q})\,[n(x,\mathbf{k})+1]\,[n(x,\mathbf{p}-\mathbf{q})+1] \tag{5.14}$$

$$-n(x,\mathbf{k})n(x,\mathbf{p}-\mathbf{q})\,[n(x,\mathbf{p})+1]\,[n(x,\mathbf{k}-\mathbf{q})+1]\} \;. \tag{5.15}$$

Note, that the on-shell distribution function is nothing else than the classical time-dependent probability distribution in phase space[2]. One has to be careful however, that only for non-interacting particles the spectral function satisfies $\rho(x,p) = 2\pi\delta(\omega-\omega(\mathbf{p}))$, which allows to identify $\tilde{F}$ with the equal time Keldysh

[2] In fact, quantum mechanically the simultaneous determination of position and momentum is limited by the Heisenberg uncertainty, which therefore limits the resolution, providing yet another reason for the breakdown of (5.10) once the deviation from the steady state becomes too sharply peaked in phase space [267].

Green's function and thus the occupation number. For interacting systems, even in equilibrium, the occupation number can in fact deviate significantly from the local Bose distribution. On-shell, $\tilde{F}_{\mathrm{eq}}$ is still the local thermodynamic equilibrium that satisfies $I_{\mathrm{coll}}[\tilde{F}_{\mathrm{eq}}] = 0$, but the kinetic term has non-vanishing contributions $\sim 1/(\delta\tilde{\omega}\tau_{\mathrm{qp}})$ and $\tilde{F}_{\mathrm{eq}}$ is not the full solution to the Boltzmann equation. Nevertheless, it is typically a useful lowest order approximation. We have already used that the deviation from the stationary solution varies slowly in Wigner space. It is thus only logical to go one step further and perform a gradient expansion around $\tilde{F}_{\mathrm{eq}}$. Close to the stationary solution in equilibrium field theory one can furthermore linearize the collision integral in the deviation from $\tilde{F}_{\mathrm{eq}}$ as well. This linear Boltzmann equation has a long history and has proven very useful to determine transport coefficients [268, 266]. Indeed, most condensed matter systems are surprisingly well described by this approximation to the quantum kinetic equation. One reason for this success lies in the non-perturbative nature of the collision integral, which involves scattering between self-consistently evolved distribution functions. In this regard the Boltzmann equation differs significantly from (non)-linear response theory, where expectation values are always calculated with respect to the unperturbed equilibrium distribution. Therefore, the Boltzmann equation can describe relaxation of the system as a whole, whereas (non)-linear response theory describes perturbations that are small enough for the system to remain in the steady state. The relaxation of excitations is then fully determined by the quasiparticles or eigenmodes of the stationary state.

We emphasize, that the Boltzmann equation directly results from the on-shell quantum kinetic equation for slowly varying deviations from the stationary distribution. If this approximation cannot be made, the Wigner transform is of no use and the Boltzmann equation is invalid. Nevertheless more flexible wavelet transforms will probably still provide a useful decomposition between fast and slow modes, opening the possibility to integrate over the former. Despite the success wavelets enjoy in related problems in signal processing [269, 270], the extent to which they can be utilized for analytical or numerical approximations to the quantum kinetic equation is still an open question.

So far, we have entirely neglected the dynamics of G^R, arguing, that the quasiparticles simply provide a restriction to the mass-shell, but that their lifetime is large compared to typical energy scales in the distribution function. As soon as this changes, a relation between linear response theory and the Boltzmann equation close to the steady state can emerge, connecting the late-time dynamics of the distribution function to the quasiparticles. This is typically the case for phase transitions in equilibrium, where Bosons satisfy $F_{\mathrm{eq}}(x,p) = \coth(\beta\omega)$. Consider, for example, the instability of a system towards the formation of a condensate, which close to the thermal state can only happen if the spectrum involves non-positive frequencies. Consequently the retarded Green's function that determines the linear response to a source of single particles also contributes the longest time scale to the Boltzmann equation.

5.2 Relaxation in open systems

In a closed system, the relaxation toward the equilibrium state is governed by processes which break integrability, allowing for an efficient redistribution of energy and momentum between the degrees of freedom. In this respect, important differences arise between classical and quantum systems [271, 272]. By contrast, in an open system the relaxation toward the stationary state is driven by exchange of energy and momentum with an external reservoir, so that the integrability-breaking intrinsic to the system does not necessarily play a role in the late-time dynamics close to the stationary state. Formally, this is reflected in the fact, that far from equilibrium the single-particle potential V_{cl} can be complex, which adds further terms that break detailed balance to the Boltzmann equation, which is then no longer solved by $F_{\mathrm{eq}}(x,p)$. In fact, no general solution is known and the additional freedom in the stationary state has several interesting consequences. Among others, the presence of quantum correlations allows for the existence of entangled stationary pure states determined by the reservoir [273]. The scenario becomes even richer if one considers the relaxation dynamics close to a phase transition. Already for classical systems the standard theory of critical dynamics near equilibrium phase transitions [274] does not fully characterize the relaxation after quenches, since aging-like behavior violates detailed-balance [275]. The extension of these concepts to quantum *and* open systems constitutes a challenging task which has recently received much attention both for the near-steady-state [276, 277, 50, 278, 279, 280, 281, 282, 283, 284, 285, 286, 287, 288, 289, 47] and quench [290, 291, 292, 293, 294, 295, 185, 296, 297, 298, 299] dynamics, also due to remarkable experimental advances in the control of hybrid systems involving phonons/photons coupled to ions [12, 13], excitons [5], superconducting circuits [6, 14, 15], mechanical modes [300], or neutral atoms [22, 32, 17, 250].

For the current discussion, we consider an open quantum many-body system close to a phase transition, where the interplay between dissipation and integrability breaking in absence of number conservation gives rise to a novel scenario for the post-quench relaxation dynamics. In particular the presence of bath terms destroys the quasiparticle character of the low-lying excitations. Consequently the quantum kinetic equation cannot be simplified and may predict an evolution vastly different from that of the quasiparticles. In particular, we will discuss a scenario, where the transition to a superradiant phase in a driven-dissipative system occurs without a related signature in the low-lying excitations. In this highly counterintuitive regime, evolution in the center-of-mass coordinate $(x+x')/2$ and the propagation distance $x-x'$ in the two-time Green's function $\mathcal{G}(x,x')$ are independent and the proliferation of excitations during the late-time evolution of the system are not related to an instability of the quasiparticles.

To be more precise, we will treat an open version [301, 302, 303, 304, 305, 306, 307, 308, 309, 310, 311] of the paradigmatic Dicke model [312], describing N two-level atoms equally coupled to a single, lossy mode of the electromagnetic field

[175, 176, 313, 314, 315, 316, 177, 317], recently realized experimentally with atoms in optical cavities [29, 30, 31, 32, 318, 319, 320]. Due to the infinite range of the atom-photon interactions (0-dimensionality), this model is integrable in the thermodynamic limit: $N = \infty$, corresponding to non-interacting polaritonic quasiparticles. Despite the absence of local degrees of freedom (typically used to characterize equilibration [321]), integrability breaking in the Dicke model at finite N has been shown to lead to chaotic behavior [322, 323] and thermalization [324] in the closed-system case. Thermalization can also be achieved at $N = \infty$ via disorder [261]. Here we describe the late-time dynamics following a quench of the atom-light coupling strength in the open system at finite N. We show that quantum non-equilibrium fluctuations induced by quasiparticle interactions trigger a dynamical phase transition, which causes the occupation of the dominant quasiparticle-mode to become unstable and grow in time. The quasiparticle lifetime, on the other hand, remains finite in presence of the Markovian losses. In the critical regime, we predict a crossover between exponential and power-law $1/\tau$ relaxation. The latter is driven by quasiparticle collisions and extends to infinite times for a quench exactly to the critical point. However, since the quasiparticles involved retain a finite lifetime throughout the transition, the equilibration time does not diverge, thus aging is not observed in two-times functions.

We emphasize, that the algebraic dynamics with overdamped quasiparticles is a genuine out-of-equilibrium many-body effect, *not* related to critical slowing down since the system size N is finite. The description of the relaxation driven by quasiparticle collisions requires non-perturbative many-body techniques. In particular, it cannot be described using mean-field approaches.

Quench experiments performed recently in the open Dicke model [320] have started exploring the dynamical phase transition, for which our theory provides the quantum description of the critical relaxation. Our predictions will be observable in the late-time behavior of response and correlation functions after small quenches near the critical point (see Sec. 5.7).

5.3 The open Dicke model

After the adiabatic elimination of the excited state, bosons in optical resonators are described by the Hamiltonian (3.7). For the current discussion, we will simplify this system to involve only a single cavity, thus fixing $i = 1$, with a mode function $\eta_1(\mathbf{r}) = \cos(k_0 z)$. Furthermore, we will simplify the geometry to one dimension, by choosing the laser mode function $\eta_L(\mathbf{r}) = 1$. Clearly an atom that absorbs or emits a photon will experience a kick with momentum $\pm k_0$. At low temperatures, where the atoms form a weakly interacting Bose-Einstein condensate, we can thus replace the continuous spatial coordinate of the atomic cloud by a discrete set of momenta. Upon truncation of the single-particle Hilbert space to $\{|0\rangle, |k_0\rangle\}$ one

finds (for $\hbar = 1$) [29, 177]

$$\hat{H} = \delta_c \hat{a}^\dagger \hat{a} + E_R \sum_{i=1}^{N} \sigma_i^z + g\sqrt{2}\frac{\Omega}{\Delta_A}\sigma_i^x \left(\hat{a}^\dagger + \hat{a}\right) , \tag{5.16}$$

with the effective spin-1/2 operators

$$\sigma_i^z = \frac{1}{2}\left(|k_0\rangle_i\langle k_0|_i - |0\rangle_i\langle 0|_i\right) \quad \text{and} \quad \sigma_i^x = \frac{1}{2}\left(|0\rangle_i\langle k_0|_i + |k_0\rangle_i\langle 0|_i\right) . \tag{5.17}$$

Given the infinite interaction range, one can identify the collective spin operators $\hat{S}_{z,x} = \frac{1}{2}\sum_{i=1}^{N}\sigma_i^{z,x}$ with the spin projections of a spin-$N/2$ rotor and rewrite Eq. (5.16) as

$$\hat{H} = \omega_0 \hat{a}^\dagger \hat{a} + \omega_z \hat{S}_z + \frac{2g}{\sqrt{N}}\hat{S}_x \left(\hat{a}^\dagger + \hat{a}\right) , \tag{5.18}$$

where we have relabeled the frequencies and coupling constants according to

$$\delta_c \to \omega_0 \quad , \quad E_R \to \omega_z \quad \text{and} \quad \frac{g\Omega}{\Delta_A} \to g\sqrt{\frac{2}{N}} . \tag{5.19}$$

The truncated Hamiltonian (5.18) is nothing else than the Dicke model [312], which therefore describes the coupling of N two-level atoms to a single mode of the electromagnetic field.

As opposed to the discussion in Chap. 3, we will consider an open version of this model by introducing Markovian photon losses with a rate κ. The non-unitary time evolution is described by the Lindblad master equation for the density matrix ρ,

$$\partial_t \rho = -i\left[\hat{H}, \rho\right] + \kappa\left(2\hat{a}\rho\hat{a}^\dagger - \left\{\hat{a}^\dagger\hat{a}, \rho\right\}\right) . \tag{5.20}$$

Since we will be interested in systems with large atom numbers N, we perform a Holstein-Primakoff transformation: $S_z = -N/2 + \hat{b}^\dagger\hat{b}$ and $S^+ = \hat{b}^\dagger\sqrt{N - \hat{n}} \approx \sqrt{N}\hat{b}^\dagger\left(1 - \hat{n}/(2N)\right)$, while $S_x = \frac{1}{2}\left(S^+ + S^-\right)$ and $S^- = S^{+\dagger}$, yielding the following Hamiltonian

$$\begin{aligned} \hat{H} &= \hat{H}_0 + \hat{H}' \\ \hat{H}_0 &= \omega_0\hat{a}^\dagger\hat{a} + \omega_z\hat{b}^\dagger\hat{b} + g\left(\hat{a} + \hat{a}^\dagger\right)\left(\hat{b} + \hat{b}^\dagger\right) \\ \hat{H}' &= -\frac{g}{2N}\left(\hat{a} + \hat{a}^\dagger\right)\left(\hat{b}^\dagger\hat{b}^\dagger\hat{b} + \hat{b}^\dagger\hat{b}\hat{b}\right) + \mathrm{O}\left(\frac{1}{N^2}\right) . \end{aligned} \tag{5.21}$$

For $N = \infty$ the interaction Hamiltonian $\hat{H}'$ vanishes and the Hamiltonian (5.21) becomes that of two linearly coupled harmonic oscillators where the oscillator $\hat{a}$

is damped by the Markov reservoir. Hence the model is integrable i.e. describes non-interacting quasiparticles corresponding to polaritonic collective modes mixing atomic and photonic excitations. These are the normal modes of the coupled-oscillator system, which can be computed using the coupled equations of motion for the averages $\langle \hat{a} \rangle$ and $\langle \hat{b} \rangle$. This quadratic model has a phase transition in the steady state at a critical coupling strength [301, 305, 304]

$$g_{c,0} = \sqrt{\frac{\omega_0^2 + \kappa^2}{4\omega_0}\omega_z}, \tag{5.22}$$

where the system spontaneously breaks the $\mathbb{Z}_2$ symmetry $\hat{S}_x \to -\hat{S}_x, \hat{a} \to -\hat{a}$ by taking a finite average polarization $\langle \hat{b} \rangle \propto \sqrt{N}$ and a finite coherent light field component $\langle \hat{a} \rangle \propto \sqrt{N}$. This superradiant transition of mean-field type [175, 176] is caused by a soft mode (see also Fig. 5.5) with zero characteristic frequency ω_{qp}, which switches from being damped to growing in time, i.e. the damping rate κ_{qp} crosses zero at $g_{c,0}$. We emphasize, that the transition is purely dissipative, i.e. characterized by completely overdamped quasiparticles $\kappa_{\mathrm{qp}} \geq 0$ and $\omega_{\mathrm{qp}} = 0$. This is due to the presence of Markovian losses while the transition is driven by the Hamiltonian sector [307].

The Hamiltonian (5.21) does not conserve the excitation-number since it contains counterrotating terms. This has the same effect as a driving term, which can indeed compensate the effect of losses, resulting in a steady state with a finite excitation number [301, 303, 304, 307]. Moreover, as is the case in driven-dissipative systems, the coexistence of counterrotating terms and Markov losses violates the detailed balance characterizing global equilibrium (see [307] and section 5.6).

We conclude this section by pointing out that the absence of a continuum (or extensive number) of degrees of freedom does not prevent the system to show many-body behavior. The Dicke model, due to the infinite range of atom-light interactions, is 0-dimensional i.e. the spatial structure is lost. It therefore describes many quasiparticle excitations occupying the 4 possible polaritonic collective modes. The non-integrable model $N < \infty$ includes interactions between these quasiparticles. Given the unlimited Hilbert space in every mode and since the occupation numbers are generically large ($O(N^{1/2})$) in the scaling regime, see [307] and Section 5.6), there is no notion by which the system describes a few-body or impurity problem. In particular, for the critical late-time dynamics of the system the relaxation i.e. redistribution of energy between the modes is strongly affected by quasiparticle collisions. This behavior cannot be described using mean-field approaches and instead requires many-body techniques like the non-perturbative diagrammatics introduced next.

5.4 The self-consistent Hartree-Fock approximation

The non-equilibrium critical properties of the open Dicke model have been recently investigated near the steady state [31, 325, 326] and in quench experiments [320, 303]. Here we want to go beyond these semiclassical studies and describe the critical post-quench late-time relaxation including quantum fluctuations due to quasiparticle interactions at finite system sizes as well as classical fluctuations from the Markov reservoir. We adopt a diagrammatic technique based on the real-time Keldysh functional-integral formulation of the Dyson equation [197, 44], extending the steady state approach developed in [307] to include the relaxation induced by quasiparticle collisions as well as the breaking of time-translation invariance. An introduction into the Keldysh formalism and the construction of the Keldysh action from a master equation is presented in Sec. 4.1 and a detailed account of its application to the Dicke model is given in Ref. [307]. We therefore only state the result.

Due to the loss of particle number conservation it is convenient to symmetrize the action through the identification of terms between advanced and retarded contributions. The symmetrized action of $\hat{H}_0$ in the absence of coherent fields then reads [307]

$$S_0 = \int \frac{d\omega}{2\pi} V^\dagger(\omega) \begin{pmatrix} 0 & \left[G_0^A\right]^{-1}(\omega) \\ \left[G_0^R\right]^{-1}(\omega) & D^K(\omega) \end{pmatrix} V(\omega), \tag{5.23}$$

because retarded and advanced Green's functions interchange under $\omega \to -\omega$. The bare inverse Green's functions $\left[G_0^R\right]^{-1}(\omega)$ and D_0^K are given by

$$\left[G_0^R\right]^{-1}(\omega) = \begin{pmatrix} \omega - \omega_0 + i\kappa & 0 & -g & -g \\ 0 & -\omega - \omega_0 - i\kappa & -g & -g \\ -g & -g & \omega - \omega_z & 0 \\ -g & -g & 0 & -\omega - \omega_z \end{pmatrix} \tag{5.24}$$

and

$$D_0^K = \begin{pmatrix} 2i\kappa & 0 & 0 & 0 \\ 0 & 2i\kappa & 0 & 0 \\ 0 & 0 & 0 & 0 \\ 0 & 0 & 0 & 0 \end{pmatrix}. \tag{5.25}$$

Here the verbose notation with the eight-component field

$$V(\omega) = \begin{pmatrix} a_{\mathrm{cl}}(\omega) \\ a^*_{\mathrm{cl}}(-\omega) \\ b_{\mathrm{cl}}(\omega) \\ b^*_{\mathrm{cl}}(-\omega) \\ a_{\mathrm{q}}(\omega) \\ a^*_{\mathrm{q}}(-\omega) \\ b_{\mathrm{q}}(\omega) \\ b^*_{\mathrm{q}}(-\omega) \end{pmatrix} \tag{5.26}$$

is necessary, since each – Keldysh $(\mathrm{cl}, \mathrm{q})$ and Nambu $(\omega, -\omega)$ structure – double the number of fields compared to the quantum mechanical representation.

For $N < \infty$ the terms of the quartic interaction Hamiltonian $\hat{H}'$ in Eq. (5.21) have to be added to the action in (5.23). Considering the possibility of interactions on the forward and the backward branch of the Keldysh contour, the corresponding part of the action reads

$$\begin{aligned} S_{\mathrm{int}} = \frac{g}{4N} \Big[& \left[(a_{cl} + a^*_{cl}) \star \left(b_q + b^*_q \right) + \left(a_q + a^*_q \right) \star (b_{cl} + b^*_{cl}) \right] \star \left[b^*_{cl} \star b_{cl} + b^*_q \star b_q \right] \\ & + \left[(a_{cl} + a^*_{cl}) \star (b_{cl} + b^*_{cl}) + \left(a_q + a^*_q \right) \star \left(b_q + b^*_q \right) \right] \star \left[b^*_{cl} \star b_q + b^*_q \star b_{cl} \right] \Big] (\omega), \end{aligned} \tag{5.27}$$

where "$\star$" denotes the convolution in ω (normalized by $1/(2\pi)$).

Our aim in the following is to investigate the effects of S_{int} on the steady state and the late-time dynamics near the superradiant transition.

The quantum dynamics of the system is described by the coupled Dyson equations:

$$G^K = G^R \circ \left(\Sigma^K - D^K_0 \right) \circ G^A \tag{5.28}$$

$$\left(\left[G^R_0 \right]^{-1} - \Sigma^R \right) \circ G^R = \delta(t - t'), \tag{5.29}$$

where $G^{(K,R)}$ is the interacting Green's function and "$\circ$" indicates the convolution in real time. The equations (5.28) and (5.29) need to be solved for the two independent (but coupled) Green's functions G^K and G^R. This approach thus allows to independently determine correlation functions through G^K and response functions through G^R, which is essential to describe systems out of thermal equilibrium.

The self-energies $\Sigma^{(K,R)}$ in general depend self-consistently on the Green's functions. In a stationary state, all two-point functions depend only on the difference between initial time t and final time t' and thus their Fourier transform is a function of only a single frequency. Otherwise they also depend on the sum of these times. Therefore, we need in general an additional pair of equations which is time-reversed

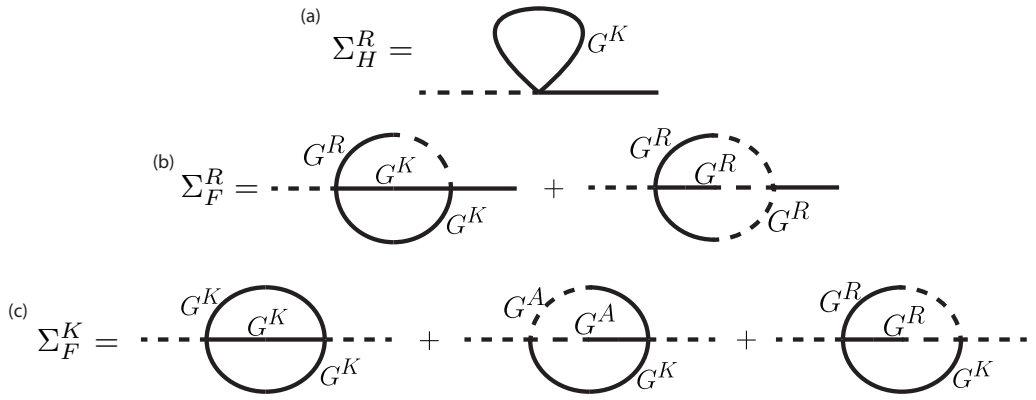

Figure 5.1: Self-energy diagrams used in the SCHF calculations: (a) leading-order $1/N$ corrections amount to nothing more than a Hartree shift in the retarded Green's function. (b) and (c) are therefore the leading frequency-dependent corrections to the bare retarded and Keldysh Green's function respectively. Following the same notation as in Chap. 4, the solid (dashed) line correspond to a "classical" ("quantum") field attached to the vertex.

with respect to Eqs. (5.28) and (5.29), as discussed in App. C.3.

The main results presented here are obtained within a self-consistent Hartree-Fock (SCHF) approximation, corresponding to the selection of diagrams for the self-energies shown in Fig. 5.1. The self-consistent Hartree (SCH) approach has already been treated by Dalla Torre et al in [307] for the steady state. As we illustrate next, the inclusion of the Fock processes we perform here is required to describe the effect of quasiparticle collisions breaking integrability. Despite the presence of a Markov reservoir these collisions are essential ingredients in the steady state and late-time relaxation dynamics of the system close to the superradiant transition.

Self-consistency is achieved by calculating the self-energies $\Sigma^{(K,R)}$ as functionals of the dressed, rather than the bare Green's functions:

$$\Sigma^{(K,R)} = \Sigma^{(K,R)}\big[G^R, G^K\big] .$$

In order to highlight the novelties introduced by our SCHF approach, we now briefly discuss the main features of the SCH theory. Within the Hartree approximation only one skeleton diagram contributes to the self-energies. Futhermore, because $G^R(0) + G^A(0) = 0$ only the retarded/advanced self-energy is non-zero

$$(\Sigma^R_{\rm H})_{i,j} = -\frac{ig}{4N} M_{i,k,l,j} \left(i\delta_{k,l} - \int \frac{d\omega}{2\pi} G^K_{k,l}(\omega) \right) , \tag{5.30}$$

which is the first diagram in Fig. 5.1. Since each Green's function is a 4×4 matrix, the vertex tensor M has $4^4 = 256$ entries. But these are nonzero only for the combinations allowed by the interaction (5.27). In the Hartree self-energy the tensor M thus contains only the 16 nonzero entries that include only one "quantum" field. The omission of vertices with three "quantum" fields is justified, because it is impossible to contract such a vertex with G^K. Since the Hartree self-energy is frequency independent the integral in (5.30) can be solved exactly, which entails that the self-consistency condition can also be solved (mostly) analytically. We give some of the details of this calculation, as well as the derivation of (5.30) in appendix C.1.

The theory becomes more involved within the SCHF approach we employ here. First of all, the Fock self-energy of Fig. 5.1 is frequency-dependent as opposed to its Hartree counterpart (5.30). This enriches the problem by the inclusion of memory effects and allows for a more detailed description of fluctuations in the excitation number, that become important near the Dicke transition, as will be discussed in section 5.5. Additionally, the Keldysh component of the Fock self-energy is nonzero and the retarded component has an imaginary part. This implies that the inclusion of the Fock processes in our theory allows us to describe relaxation through redistribution of energy via collisions between quasiparticles.

As expected, the interaction includes both classical and quantum vertices (see Sec. 4.1. Near the phase transition, a bare scaling analysis of the model (5.23), (5.27) correctly indicates that the latter are of higher order in $1/N$ compared to the more classical former subset of diagrams [307]. Yet, in order to improve our quantitative results for intermediate values of N, we keep those diagrams. Independent of this, the self-consistent resummation of two-loop diagrams cannot be performed analytically, forcing us to rely heavily on numerical methods for the calculation of quantitative results. However, all the analytical expression presented here are completely independent of the numerics, that can therefore be used for an independent confirmation (see for example Fig. 5.6).

To deal with all possible contractions resulting from the tensorial structure of the vertex we follow the same procedure that was used for the Hartree diagrams. There are however some differences which we illustrate in appendix C.2 together with the computational methods employed.

5.5 Steady state

In this section we consider the steady state of the coupled Dyson equations (5.28) and (5.29). We will show how the integrability-breaking through quasiparticle interactions leads to intrinsic equilibration, which adds to the one induced by the coupling to the external reservoir.

5.5.1 Superradiant instability

Since the integrability-breaking term (5.27) of the action is suppressed like $1/N$, one would naively expect the Hartree and Fock processes of Fig. 5.1 to provide perturbative corrections at any fixed large N. In the absence of transition points this is in general true, but only within an equilibrium formulation of the problem. Otherwise, as explained in Sec. 4.1, if we are not allowed to assume *a priori* the validity of a fluctuation-dissipation theorem, even perturbatively-small integrability-breaking terms need to be treated self-consistently in order to properly describe the emergent steady state as well as the late-time relaxation dynamics [197]. However, for an open system, the perturbative treatment can still be employed for the description of the late-time behavior if an external reservoir – macroscopic and unperturbed by the system – takes care of the relaxation process. This is indeed the case for the open Dicke model, where the Markov bath of electromagnetic modes is coupled to the light mode $\hat{a}$ and the latter is linearly coupled to the atomic mode $\hat{b}$, so that all degrees of freedom are externally damped. Yet, already within the integrable theory, the model shows a phase transition at the critical coupling $g_{c,0}$ at which the external damping of the collective quasiparticles vanishes, so that the relaxation and late-time dynamics can still be dominated by the effect of the integrability-breaking terms, which then become non-perturbative. In particular, as we shall see, during the late-time dynamics in this critical regime the Fock processes are crucial, being the only ones beyond the bare damping that lead to relaxation due to integrability-breaking.

The growing importance of the integrability-breaking processes compared to the integrable dynamics, as well as the relative importance of Fock compared to Hartree, is illustrated in Fig. 5.2, where we plot the occupation number of the photonic mode

$$\langle n_a \rangle = \langle \hat{a}^\dagger \hat{a} \rangle = -\frac{1}{2} + i \int \frac{d\omega}{4\pi} \left(G^K(\omega) \right)_{1,1} \tag{5.31}$$

as a function of the coupling strength.

The comparison of the photon numbers provides an estimate of the distance from the transition point below which we enter a non-perturbative regime. While for Fock terms to become relevant one needs to be even closer to $g_{c,0}$ than for important Hartree terms. However, for $N \gg 1$ both contributions to the self-energy are significant for coupling strengths g that satisfy $(g - g_{c,0})/g_{c,0} \sim 1/\sqrt{N}$ [307]. Therefore, there is no finite particle number beyond which Hartree corrections are sufficient to describe dynamics near $g_{c,0}$. Once in the fully non-perturbative regime we thus resort to the SCHF approach to solve the coupled Dyson Eqs. (5.28) and (5.29).

After having analyzed the photon number, we now consider the modification of the quasiparticle spectrum, which is obtained from the poles of the retarded Green function $G^R(\omega)$. The real and imaginary part of the poles correspond to the os-

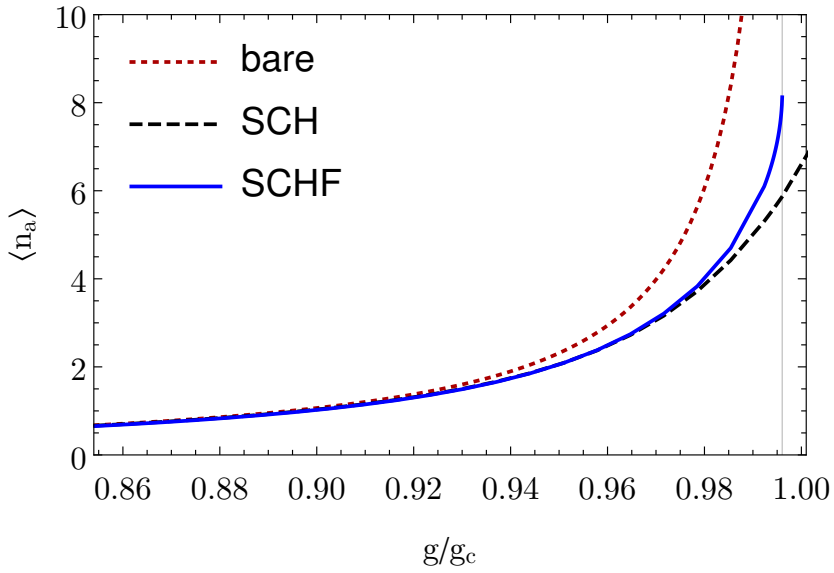

Figure 5.2: Comparison of the photon number (c.f. Eq. (5.31)) calculated within the integrable theory (red dotted), in Hartree approximation (black dashed) and Hartree-Fock approximation (blue) as a function of the coupling strength. While the non-interacting result, representing the $N \to \infty$ limit shows a second order phase transition at $g = g_{c,0}$, the Hartree calculation continues smoothly through $g_{c,0}$ and shows no instability. Contrary to that, the Hartree-Fock steady state becomes unstable at the gray line. Note, however, that at the critical point $g_c(N)$ the photon number remains finite and $\sim N^{1/2}$. The parameters used are $\kappa = 2$, $\omega_0 = 2$, $\omega_z = 2.1$ and $N = 1000$, resulting in $g_{c,0} \approx 1.4491$.

cillation frequency and damping of the quasiparticles i.e. the collective polaritonic modes. The Hartree self-energy simply provides a frequency-independent shift of the spectrum, preventing the collective mode frequency from vanishing. Therefore, for any finite N, the dynamical instability triggering the superradiant phase transition is absent within the SCH approach. On the other hand, the Fock self-energy is frequency-dependent and also has an imaginary part, as discussed in section 5.4. A closer investigation of the perturbative effects of the diagrams in Fig. 5.1 shows that for strong enough coupling g, where the system has weakly damped excitations at zero energy, Fock processes take place almost on-shell. These processes therefore efficiently induce fluctuations in the low energy mode. In the self-consistent calculation this happens to an increased extent, such that the normal steady state eventually becomes unstable at a coupling strength

$$g_c(N) < g_{c,0}$$

smaller than the critical coupling $g_{c,0}$ for the integrable model.

5.5.2 Steady state distribution function

The non-perturbative effects of the integrability-breaking terms are measurable from several observables. Quantitative effects are observed in the spectral response of the system $\rho(\omega)$, defined by Eq. (4.17). Here it is a 4×4 matrix which, however, in the SCHF approximation has only 5 independent entries, each of which is normalized to the corresponding commutator:

$$\int \frac{d\omega}{2\pi} \left(\rho(\omega)\right)_{i,j} = \langle [\hat{V}_i, \hat{V}_j^\dagger] \rangle.$$

For instance, the entries normalized to one correspond to pump-probe measurements involving the creation of an excitation $\hat{a}^\dagger$ or $\hat{b}^\dagger$ and its annihilation after a variable time t, the latter being related to ω via a Fourier transform. In particular, for the photonic sector one would need to measure the probe transmission spectrum of the cavity [301], as has already been done experimentally in the ultracold-atom realisation of the Dicke model [327].

Quantitative effects are also observed in the correlation function

$$C(\omega) = iG^K(\omega), \tag{5.32}$$

whose entries are the Fourier transform of the symmetrized averages

$$\left(C(t)\right)_{i,j} = \langle \{\hat{V}_i(t), \hat{V}_j^\dagger(0)\} \rangle.$$

For instance, $\left(C(t)\right)_{1,1}$ corresponds to the measurement of the fluorescence spectrum of the cavity [301]. Examples of the modification of the spectral and correlation function due to integrability breaking terms are presented in Fig. 5.3. As anticipated, these observables show only quantitative but no qualitative modifications.

Qualitative effects are instead observed in the distribution function $F(\omega)$ which determines the link between the response and correlation functions. In a more intuitive phrasing one can say that $F(\omega)$ describes the boundary conditions emergent in the steady state for each degree of freedom of the system. One can thus expect $F(\omega)$ to be sensitive to the different drive and relaxation mechanisms, both external and intrinsic to the system.

In order to analyze the distribution function for the photonic and atomic degrees of freedom separately, we first project the full set of 4×4 Green's functions onto the respective 2×2 sectors. Within each sector we then solve (4.18) for $F_a(\omega)$ and $F_b(\omega)$, respectively, where the subscript a refers to photonic and b to atomic degrees of freedom. In Fig. 5.4, we plot the eigenvalues $F_a^{\pm}(\omega)$ of $F_a(\omega)$, which, due to the hermitian structure of $F(\omega)$, are purely real.

In the open Dicke model and in the integrable limit $N = \infty$, external driving

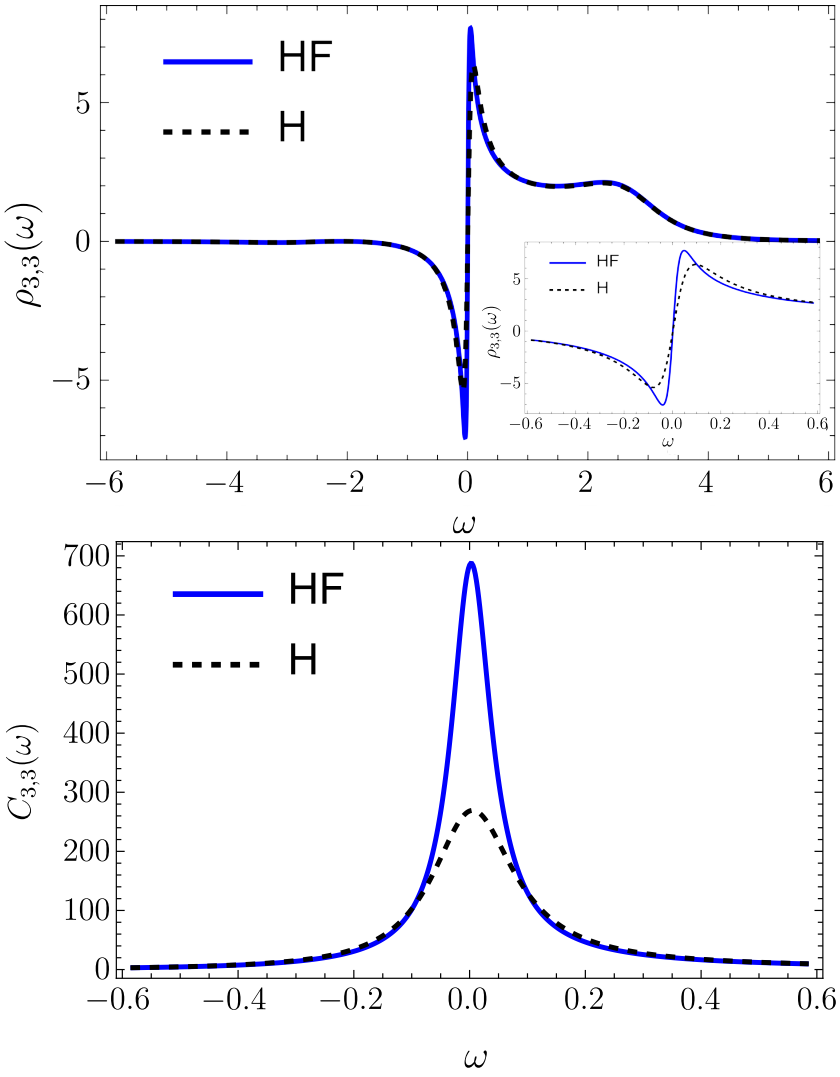

Figure 5.3: Examplary comparison of quantitative differences between SCH and SCHF results for the atomic spectral response function $\rho_{3,3}(\omega)$ and correlation function $C_{3,3}(\omega)$. Note that appreciable differences appear only close to $\omega = 0$, where correlations are significantly increased by resonant (but damped) Fock processes efficiently reducing losses and thereby increasing the number of excitations. The parameters used are the same as in Fig. 5.2 and $g = g_c(N)$.

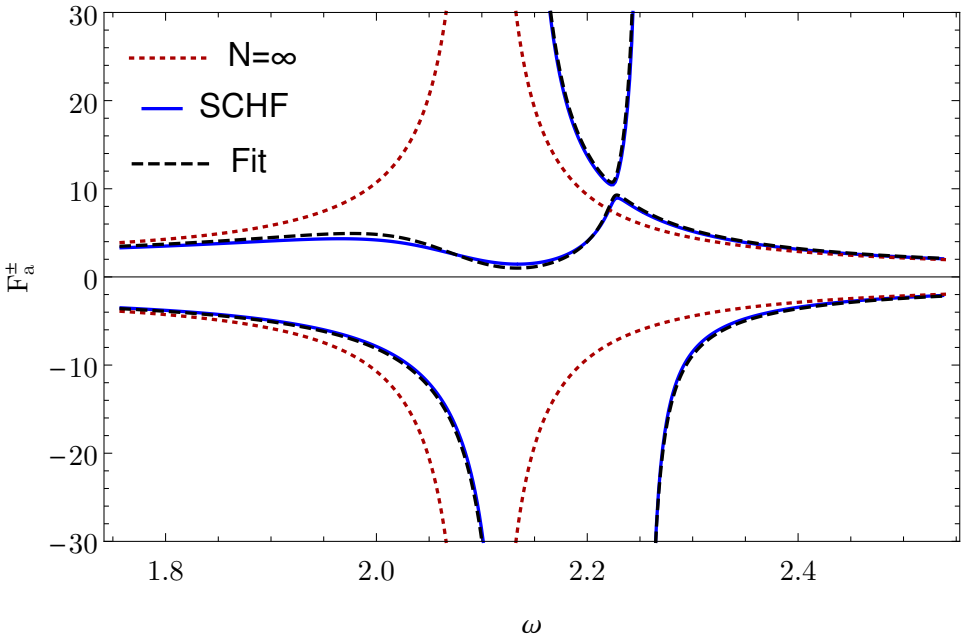

Figure 5.4: Behavior of the two eigenvalues of the photonic distribution function. The red-dotted line corresponds to the integrable theory: $N = \infty$. The blue solid line is the result obtained from full SCHF theory, where qualitatively new features appear. These can be well described by an effective linearised theory Eq. (5.33) (black-dashed line) that shifts the atomic resonance in the complex plane and therefore contains only a single (complex) fit parameter κ_b. The parameters used are the same as in Fig. 5.2, resulting in $\kappa_b \approx 0.0335 + 0.0009i$.

is effectively present due to the bilinear coupling between photonic and atomic degrees of freedom which does not conserve the excitation number, while relaxation is induced externally by photon losses. As has previously been discussed in [307], the corresponding distribution function for the photonic degree of freedom shows singularities at zero frequency and at the bare atomic resonance frequencies $\pm\omega_z$. These singularities appear on top of the frequency-independent Markov background and result from the effective drive via the atoms. These singularities are of thermal nature, behaving like T_{eff}/ω, with the effective temperature emerging due to the combination of the Markov reservoir and the driving. This temperature is different for the photonic and atomic degrees of freedom, indicating the violation of detailed balance arising from the fact that the whole system is driven but dissipates only through the photons (see also section 5.6.4).

Within our SCHF approach, we are able to include the equilibration mechanism

intrinsic to the system, which is governed by the integrability-breaking terms. In particular, as already discussed, the Fock processes allow to include the intrinsic equilibration induced by quasiparticle collisions. In the strong coupling regime: $(g_c(N) - g)/g_c(N) \lesssim N^{-1/2}$, this introduces large qualitative and quantitative changes in $F(\omega)$, as illustrated in Fig. 5.4 for the photonic degree of freedom. Here we compare the prediction of the integrable theory: $N = \infty$ with our SCHF results. Apart from a shift of the singularities from their bare value ω_z, the important qualitative change introduced by collisions is the splitting of these singularities via an avoided crossing. This splitting of the singularities at the (shifted) atomic resonances can be reproduced ad hoc by adding to the integrable theory a second Markov reservoir, this time for the atomic degree of freedom. This corresponds to the steady state of the following master equation

$$\partial_t \rho = -i \left[\hat{H}_0, \rho\right] + \kappa \left(2\hat{a}\rho\hat{a}^\dagger - \left\{\hat{a}^\dagger\hat{a}, \rho\right\}\right) + \kappa_b \left(2\hat{b}\rho\hat{b}^\dagger - \left\{\hat{b}^\dagger\hat{b}, \rho\right\}\right). \tag{5.33}$$

where $\hat{H}_0$ indicates the integrable Hamiltonian of Eq. (5.21). By choosing the effective atomic dissipation κ_b appropriately (including the shift of the resonance frequency), we can simulate the extent to which the quasiparticle collisions result in an enhanced decay of atomic excitations into multiple photons. This demonstrates how the integrability-breaking leads to faster equilibration by creating effectively a further bath for the the system.

While $F(\omega)$ contains a lot of information encoded in its functional form, its measurement requires knowledge of both the spectral response and the correlation functions. The former gives direct access to the retarded (and by complex conjugation the advanced) Green's function while the latter directly corresponds to the Keldysh Green's function. The matrix generalization of Eq. (4.18) would then allow to compute the distribution function.

5.6 Late-time dynamics

Starting from an initial atom-photon coupling g_i, we consider a sudden quench to a value $g > g_i$. We solve the coupled Dyson Eqs. (5.28) and (5.29) in the SCHF approximation in the limit of large absolute times $\tau = (t+t')/2$, i.e. for small relative deviations from the steady state, by means of an iterative numerical procedure. This approximate time evolution is explained in detail in the appendix C.3. In the limit of relative times t_{rel} long compared to the quasiparticle lifetime $1/\kappa_{\mathrm{qp}}$, that is, including only the dominant contribution from low-frequency quasiparticles, the

solutions take the following form

$$\begin{aligned}
&\left(G^K(t_{\rm rel},\tau)\right)_{\rm i,j} \simeq e^{-\kappa_{\rm qp}|t_{\rm rel}|} \\
&\times\left(G^K(0,\infty)+\frac{\delta G^K(0,0)}{e^{\kappa_{\rm kin}\tau}+\frac{\lambda_{\rm kin}}{\kappa_{\rm kin}}\delta G^K(0,0)\left(e^{\kappa_{\rm kin}\tau}-1\right)}\right), \\
&\left(G^R(t_{\rm rel},\tau)\right)_{\rm i,j} \simeq \theta\left(t_{\rm rel}\right) e^{-\kappa_{\rm qp}t_{\rm rel}} \\
&\times\left(G^R(0,\infty)+\frac{\delta G^R(0,0)}{e^{\kappa_{\rm kin}\tau}+\frac{\lambda_{\rm kin}}{\kappa_{\rm kin}}\delta G^K(0,0)\left(e^{\kappa_{\rm kin}\tau}-1\right)}\right),
\end{aligned} \tag{5.34}$$

where we used the notation $\delta G^{R/K}(0,0) = G^{R/K}(0,0) - G^{R/K}(0,\infty)$. Every com-

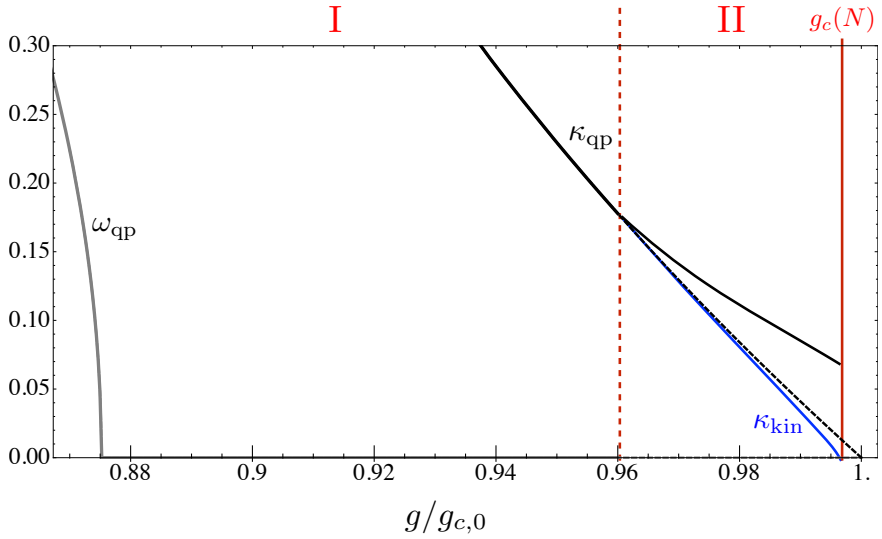

Figure 5.5: Qualitative behavior of the quasiparticle characteristic frequency $\omega_{\rm qp}$ (gray) and inverse lifetime $\kappa_{\rm qp}$ (black), together with the system's damping rate $\kappa_{\rm kin}$ (blue), as a function of the final value g of the light-matter coupling after a sudden quench from $g_i < g$. The dashed line corresponds to the prediction of the non-interacting theory $\hat{H}' = 0$, where $\kappa_{\rm kin} = \kappa_{\rm qp}$. For $\omega_{\rm qp}$ there is no difference between interacting and non-interacting predictions at large enough N.

ponent i,j $= 1, ..., 4$ of both retarded and Keldysh Green's functions follows the functional form (5.34) since the latter is determined by the least-damped quasiparticle mode corresponding to the dominant eigenvector of the 4×4 matrices[3].

[3]Note that the single-mode approximation, implicit in the results presented here, breaks down for small coupling constants, where $\omega_{\rm qp} \neq 0$ and the two most relevant modes have degenerate

The solutions depend only on three parameters whose behavior is shown in Fig. 5.5 and 5.6 as a function of the coupling strength g: the inverse quasiparticle lifetime $\kappa_{\rm qp}$ (damping rate of the relative-time dynamics), the system-damping $\kappa_{\rm kin}$ in the absolute time, and the nonlinear coefficient $\lambda_{\rm kin}$.

5.6.1 Dynamical phase transition at finite N

Let us first consider the integrable case: $N = \infty$. Since the quasiparticle interactions are absent, the system's damping is equal to the quasiparticle damping: $\kappa_{\rm kin} = \kappa_{\rm qp}$ and $\lambda_{\rm kin} = 0$. Therefore $G^K(t_{\rm rel}, \tau) \simeq e^{-\kappa_{\rm qp}|t_{\rm rel}|}(G^K(0,\infty) + \delta G^K(0,0)e^{-\kappa_{\rm qp}\tau})$ and analogously for the retarded Green's function. For $\tau \to \infty$ the steady state Green's function $G^K_{\rm ss}(t_{\rm rel}) \simeq G^K(0,\infty)e^{-\kappa_{\rm qp}|t_{\rm rel}|}$ is reached. As shown in Fig. 5.5 by the black-dashed line, for $N = \infty$ the inverse lifetime $\kappa_{\rm qp}$ vanishes linearly at the transition point $g_{c,0}$. In the non-integrable $N < \infty$ case (solid lines in Fig. 5.5), we find the phase transition to occur instead at a critical coupling

$$g = g_c(N) < g_{c,0}, \text{ with } \frac{|g_c(N) - g_{c,0}|}{g_{c,0}} \lesssim N^{-1/2}, \tag{5.35}$$

where the inverse quasiparticle lifetime $\kappa_{\rm qp}$ remains finite, while the damping $\kappa_{\rm kin}$ vanishes according to:

$$\kappa_{\rm kin} \sim \kappa_{\rm qp} N^{3/4} \sqrt{|g - g_c(N)|/g_c(N)}\,, \tag{5.36}$$

as shown in Fig. 5.6. Above the critical point: $g > g_c(N)$ the system's damping rate $\kappa_{\rm kin}$ becomes imaginary, with the magnitude again given by (5.36), indicating an instability of the steady state of Eqs. (5.34).

This peculiar dynamical phase transition characterized by a vanishing system-damping at finite quasiparticle lifetime is triggered by quasiparticle collisions in the presence of both Markovian losses and violation of number conservation, the latter effectively working as a drive. In the following, we illustrate how this critical point affects the system's dynamics after the quench.

5.6.2 Criticality and scaling laws

At any given $1 \ll N < \infty$, sufficiently far away from the critical point: $(g_c(N) - g)/g_c(N) \gtrsim N^{-1/2}$, we are in a weak-coupling regime (region I in Fig. 5.5) where the quasiparticle interactions from $\hat{H}'$ are always perturbative, so that, to order $1/N$, the Green's functions follow the integrable dynamics illustrated above: $\kappa_{\rm kin} \simeq \kappa_{\rm qp} \gg \lambda_{\rm kin}$. Instead, for a quench to strong coupling $(g_c(N) - g)/g_c(N) \lesssim N^{-1/2}$ (region II in Fig. 5.5) the interactions appreciably renormalize the dampings such that $\kappa_{\rm kin} < \kappa_{\rm qp}$. Within this region, even closer to the critical point:

lifetimes.

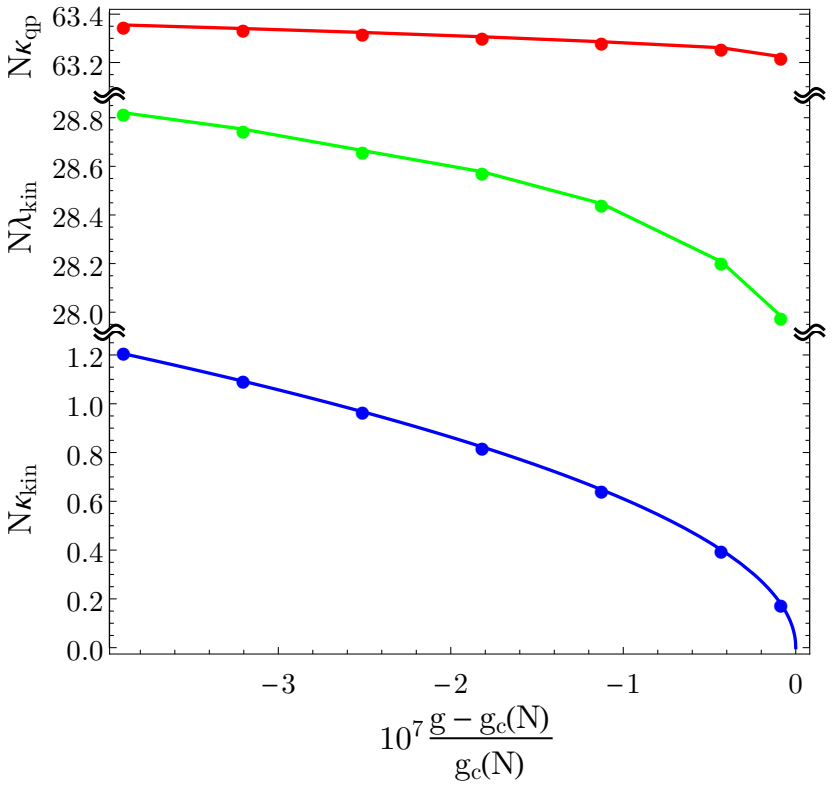

Figure 5.6: Numerical values of the kinetic parameters $\kappa_{\rm kin}$, $\lambda_{\rm kin}$ together with the inverse quasiparticle lifetime $\kappa_{\rm qp}$. $\kappa_{\rm kin}$ is fitted with the scaling law (5.36) (blue line). The parameters used are $\kappa = 2$, $\omega_0 = 2$, $\omega_z = 2.1$ and $N = 1000$, resulting in $g_{c,0} \approx 1.4491$. In the Appendix C.4 we present results for $\kappa = 0.2, 1.0$.

$(g_c(N) - g)/g_c(N) \lesssim N^{-3/2}$, we find $\kappa_{\rm qp} \sim N^{-1/2}$ such that $\lambda_{\rm kin}$ cannot be neglected any more (see also Fig. 5.6). In general, the latter depends only weakly on the coupling g and is also of order $N^{-1/2}$. The role of $\lambda_{\rm kin}$ is to introduce algebraic relaxation characteristic for non-integrable dynamics. In this model without conserved quantities [307] algebraic dynamics emerges due to criticality, but is in general not necessarily a signature of the latter, for instance in systems with conservation laws [274]. At a given N-independent coupling g, the integrable limit of the late-time dynamics is reached for $N \to \infty$, since we enter the weak coupling regime as soon as $(g_c(N) - g)/g_c(N) \gtrsim N^{-1/2}$. If instead we pin the system to criticality $(g_c(N) - g)/g_c(N) \lesssim N^{-3/2}$, the integrable limit is never approached, since according to (5.36) $\kappa_{\rm qp} \simeq \kappa_{\rm kin} \sim N^{-1/2} \to 0$ and $\lambda_{\rm kin} \sim N^{-1/2} \to 0$, so that the non-integrable character is always important. This is related to the fact that at

criticality the limits $N \to \infty$ and $\tau \to \infty$ do not commute. As a side remark, the fact that quasiparticle collisions breaking integrability become important at criticality can be seen also by analyzing the steady state. In particular, as shown in Fig. 5.4 and the accompanying discussion, integrability breaking effectively creates a bath for the spin (atomic) degree of freedom.

5.6.3 Algebraic vs. exponential dynamics

An example depicting the generic behavior of the absolute-time evolution is sketched in Fig. 5.7 using the occupation of the quasiparticle mode $n(\tau) = iG^K(0,\tau)/2 - 1/2$ as observable. The corresponding numerical results, together with a fit of the dynamical parameters in the scaling ansatz (5.34), are shown in Fig. 5.8. It is these long-time evolutions, that allow to determine $\kappa_{\rm kin}$ and $\lambda_{\rm kin}$ with sufficient accuracy to confirm their scaling as done in Fig. 5.6.

Immediately after the quench the system has to become sufficiently populated and correlated for interactions to become important. This requires a time $\tau_{\rm alg} \sim 1/\kappa_{\rm qp}$, after which the initial, exponential, integrable dynamics goes over into a non-integrable $1/\tau$ behavior. Deep inside the strong coupling regime: $|g_c(N) - g|/g_c(N) \lesssim N^{-3/2}$, a second crossover takes place on a scale $\tau_{\rm exp} \sim 1/\kappa_{\rm kin}$, where for $g < g_c(N)$ the algebraic relaxation goes back to exponential, as predicted by Eqs. (5.34). Using the result (5.36) we get the following scaling

$$\tau_{\rm exp} \sim 1/\kappa_{\rm kin} \sim N^{-1/4}(|g - g_c(N)|/g_c(N))^{-1/2} \,. \tag{5.37}$$

The transcritical time evolution with $g > g_c(N)$ is also shown in Fig. 5.7. For times later than $\tau_{\rm alg}$ the system first approaches the steady state $G^{K,R}_{\rm ss}(t_{\rm rel})$ of Eq. (5.34) algebraically ($\sim 1/\tau$). However, beyond the time-scale $\tau_{\rm exp}$ the system then evolves linearly past this unstable state with a characteristic rate given by $\partial_\tau \delta O \simeq \kappa^2_{\rm kin} O_{\rm ss} / \left(4\lambda_{\rm kin} G^K_{\rm ss}(0)\right)$ for any observable O. After the linear regime, the evolution accelerates again, becomes algebraic and would eventually converge toward the symmetry-broken steady state. The description of such a state, however, requires the expansion around a symmetry-broken saddle point, including (self-consistent) finite field expectation values $\langle \hat{a} \rangle$ and $\langle \hat{b} \rangle$, which is described by a more general version of Hamiltonian (5.21). The new steady state is therefore inaccessible to the presented dynamics. The sudden switch in the dynamical behavior at $g = g_c(N)$ characterizing the phase transition is triggered by quasiparticle collisions in presence of both Markovian losses and effective driving. In particular, since the system has weakly damped quasiparticles at $\omega_{\rm qp} = 0$ (which is possible due to Markovian losses), collisions take place almost on-shell and therefore efficiently increase the mode occupation. The drive (breaking of the number conservation) provides the source of quasiparticles allowing the latter process to induce an instability.

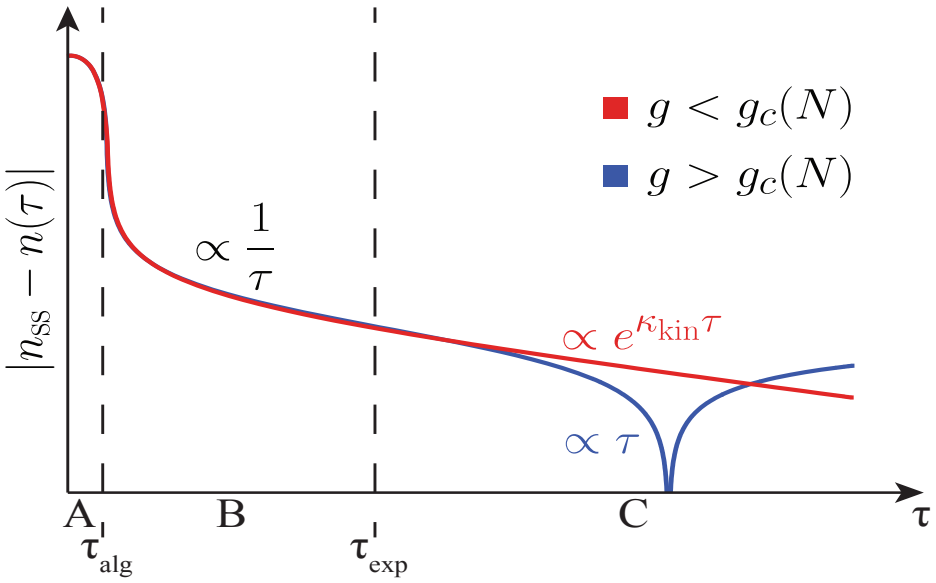

Figure 5.7: Sketch of a log-plot of the time evolution of the particle number near $g_c(N)$, separated into three regions. Starting from the vacuum, the system is for short time-scales described by the evolution according to the bare Green's function (region A), which will then cross over into an algebraic decay (region B), that continues to infinite times for $g = g_c(N)$. For $g < g_c(N)$ the final relaxation is exponential, as depicted in region C, whereas for $g > g_c(N)$ the population instead evolves linearly through that of the unstable steady state.

5.6.4 Absence of aging

For a quench exactly to the critical point $g = g_c(N)$, the power-law $1/\tau$ dynamics extends down to the steady state. Due to the breaking of time-translation invariance and the presence of critical algebraic relaxation even as $\tau \to \infty$ one might expect aging to characterize the late-time behavior of two-times functions [275]. Such behavior has been predicted to appear after quenches to critical points both in closed [328, 55, 329] and open [295] quantum sytems. In order to explore this possiblity we employ the fluctuation-dissipation ratio [275] $\chi_{\mathcal{O}}(t_1, t_2) = (G^R_{\mathcal{O}}(t_1, t_2) - G^A_{\mathcal{O}}(t_1, t_2))/\partial_{t_1} G^K_{\mathcal{O}}(t_1, t_2)$ with $t_1 < t_2$, which allows to address possible violations of detailed balance and define effective temperatures for non-equilibrium systems, where the fluctuation-dissipation theorem cannot be relied on. In $\chi_{\mathcal{O}}(t_1, t_2)$ the index $\mathcal{O}$ means that the quotient is to be taken between expectation values corresponding to the most highly occupied eigenvector of some operator $\mathcal{O}$. The limit $\lim_{t_1\to\infty} \lim_{t_2\to\infty} \chi_{\mathcal{O}}(t_1, t_2) \equiv 1/T_{\text{eff}}$ defines an effective temperature. In systems exhibiting aging after a quench to the critical point the equilibration time diverges.

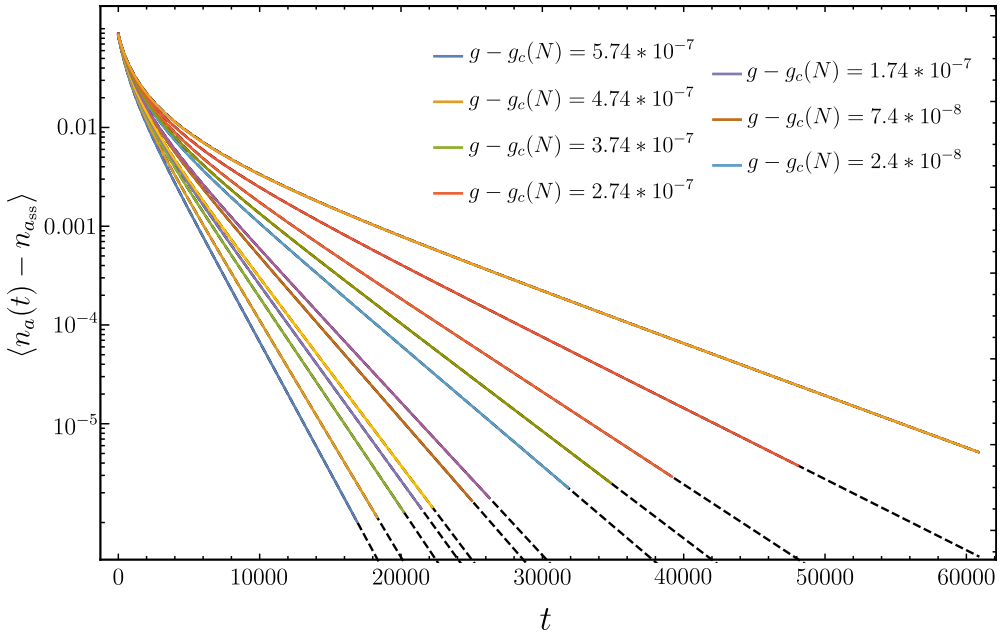

Figure 5.8: Time evolution of the deviation of the photon number $n_a(t)$ from its steady state for long times in the vicinity of $g_c(N)$ as a log-plot. The solid lines represent numerical data obtained from the iterative pseudo time evolution detailed in App. C.3, while the dashed lines are a two parameter fit (κ_{kin} and λ_{kin}) with the function (5.34). The parameters used are once again the same as in Fig. 5.2.

As a consequence, the effective temperature defined through the above limit will not be equal to the value of the effective temperature obtained directly from the steady state, even if the system is in contact with a thermal reservoir. Using our late-time Green's functions (5.34) it is easy to see that the fluctuation-dissipation ratio is independent of the relative time:

$$\chi(t_{\text{rel}}, \tau) = \frac{1}{T_{\text{eff}}} \frac{1}{1 + \frac{1}{\lambda_{\text{kin}} \kappa_{\text{qp}} \tau^2}}. \tag{5.38}$$

Therefore, for absolute times larger than the equilibration scale

$$\tau_{\text{eq}} = 1/\sqrt{\lambda_{\text{kin}} \kappa_{\text{qp}}} \tag{5.39}$$

it relaxes to the inverse effective temperature T_{eff}. Since at $g_c(N)$ the quasiparticle lifetime remains finite $1/\kappa_{\text{qp}} < \infty$, the equilibration scale τ_{eq} is also finite and thus no aging takes place. $1/\kappa_{\text{qp}} < \infty$ also implies that the initial-slip exponent θ describing the $(t_2/t_1)^\theta$ scaling of two-times functions [275] is irrelevant, since the

dynamics is exponential in the relative-time direction (see Eq. (5.34)). However, due to the driven-dissipative nature of the system, the steady state is not in global equilibrium, implying that the effective temperature obtained from (5.38) depends in general on the particular degree of freedom considered, consistent with what was found in [307] by extracting T_{eff} directly from the steady state (see also Sec. 5.5.2).

5.6.5 Absence of quasi-stationary states

As anticipated above, the fact that we must be close to the superradiant transition in order to observe the non-integrable dynamics implies the absence of quasi-stationary or prethermal plateaus. Those correspond to intermediate quasi-stationary states where the system can remain for long times before the true fully relaxed steady state is reached. At a distance $N^{-3/2} \lesssim |g - g_c(N)|/g_c(N) \lesssim N^{-1/2}$ from the transition, the reason for the absence of these plateaus is obvious, since both τ_{alg} and τ_{exp} scale like $N^{1/2}$. Thus the necessary separation of time scales is not achieved. On the other hand, at a distance $|g - g_c(N)|/g_c(N) \lesssim N^{-3/2}$, τ_{alg} and τ_{exp} scale differently and hence can be well separated, as shown in the previous section. Yet, this implies also that the relative deviation of the candidate quasi-stationary state from the steady state at τ_{exp} is correspondingly very small, preventing the observation of a plateau. Most importantly, we cannot slow down the characteristic time-scale $\tau_{\text{alg}} \sim N^{1/2}$ since it essentially does not depend on the transition. Therefore the relaxation rate of the algebraic dynamics remains finite even at the transition point and the plateau would in turn exhibit a finite slope.

A clear (but trivial) separation of time-scales is always present in the open Dicke model far away from the transition, for the simple reason that the integrability-breaking terms are suppressed like $1/N$ in the Hamiltonian. However, this again does not imply the appearance of quasi-stationary states since the relaxation due to the non-integrable terms is then perturbative and thus overshadowed from the relaxation due to external damping. Consequently, the open Dicke model shows no prethermalization. The situation is different in the system studied in [185, 296], where the relaxation in the particle sector is achieved only due to non-integrable terms, thus their effect is always non-perturbative for the particles. This allows to observe quasi-stationary states in the particle sector even in the presence of interactions with infinite range, as demonstrated in [296].

5.7 Predictions for the experiment

The dynamical phase transition of the open Dicke model has been investigated in recent quench experiments performed with a Bose-Einstein condensate (BEC) in an optical cavity [320]. We expect our predictions to be observable in response and correlation functions of the cavity output, once the wait-time τ_{w} after the quench satisfies $\tau_{\text{w}} \gtrsim \tau_{\text{alg}} \sim 1/\kappa_{\text{qp}} \sim N^{1/2}$ (see Section 5.6). Generically, the smallest value of τ_{alg} is reached when ω_z (corresponding to the recoil frequency $\omega_{\text{rec}} \sim$ KHz in the

BEC experiments) is of the same order as κ. This can be seen by comparing the value of $\kappa_{\rm qp}$ for the values of $\kappa = 2, 1, 0.2$ shown in Fig. 5.6 and Fig. C.1, at a given $\omega_z = 2.1$. The largest $\kappa_{\rm qp}$ is reached indeed for $\kappa \simeq \omega_z$, while for even larger κ (not shown) the quasiparticle damping decreases. For instance, in the experimental setup of [320] the cavity is of very high quality: $\kappa \simeq \omega_{\rm rec}$, so that $\kappa_{\rm qp} \sim \kappa N^{-1/2}$ that is $\tau_{\rm w} \gtrsim$ ms $\times (10^5)^{1/2} \sim 300$ms. While this is below typical BEC-lifetimes, it is currently not achieved in the experiments [320], but in principle possible in the new-generation setups.

While the measurement of response functions require cavity probe-transmission experiments [301, 307], the behavior of the correlation function in Fig. 5.7 will be directly observable from the cavity output intensity.

Alternatively, these critical dynamics could possibly be observed with two trapped ions in a harmonic trap that realize the open quantum Rabi model [330, 331]. In the limit of a large ratio between the sum and the difference of the detunings on the red and blue sideband, which plays the role of N in the Dicke model, both models satisfy the same scaling relations [330, 331]. It is thus likely, that critical dynamics, similar to those described here, are also observable there.

Chapter 6

Conclusion

In this thesis we have discussed phase transitions in bosonic systems with long range interactions that typically arise in quantum optical many-body systems, where they are mediated by photons, which experience unavoidable losses. We have thus considered various different non-equilibrium scenarios as well as various types of order. Focusing mainly on the example of the infinite range transverse Ising chain, we have demonstrated, that the proper extension of the ground state Loschmidt echo to finite temperatures is given by the fidelity return rate r_{F}. Due the numerical complexity of this quantity, the equivalent, but more easily accessible quantum return rate r_{q} was defined and the phase diagram obtained by an analysis of its non-analyticities was compared to that determined from the infinite time magnetization. Using a thorough finite size scaling for very large systems with up to $N = 64001$ spins, it was shown, that both methods produce quantitatively the same dynamical phase diagrams. An intuitive, physical understanding of these results was provided in form of a semiclassical analysis of the return rate, built on the dynamics of the spin WKB wave function. The ensuing geometric interpretation of cusps in the return rate of interacting systems, has allowed us to make a connection to an effective Ginzburg-Landau functional and pave the way for the analysis of dynamical phase transitions in non-integrable systems.

We have provided a thorough investigation of the symmetries and low energy excitations of a recent experiment on supersolid-like behavior in cold atoms trapped inside two crossed optical resonators. In particular, we have demonstrated that higher order intercavity scattering processes break the accidental $U(1)$ symmetry, whereby the Goldstone mode becomes gapped. Our estimate of the corresponding mass is in agreement with the experimental observations [1, 2].

Using the Keldysh path integral formalism, we have developed a controlled, non-perturbative description of strongly interacting EIT-polaritons with long interaction range. The application to photonic crystal waveguides has led us to the prediction of interaction induced transparency (IIT), which is characterized by the appearance of a transparency window in the presence of strong interactions due to nonlinear interference effects. In the context of nonlinear quantum optics, IIT constitutes a novel, genuine quantum many-body effect in an open, driven system. From the more fundamental perspective of many-body physics, the IIT phenomenon is a non-equilibrium phase transition in the driven-dissipative steady state

which has no analogue so far in condensed matter, as it stems from the dissipative and retarded nature of the interactions between polaritons. Including corrections, resulting from a finite interaction range, we were able to demonstrate the stability of IIT against scattering with finite momentum transfer.

Finally, the dynamics of the open Dicke model near the critical coupling strength was investigated by means of a self-consistent Hartree-Fock theory. Upon the inclusion of finite size effects close to the critical point, a highly counter intuitive picture emerges: The evolution in absolute time decouples from the low-energy excitation spectrum and the condensation transition arises not as the consequence of undamped quasiparticles, but due to a proliferation of overdamped excitations driven by efficient scattering in the absence of particle number conservation. Near the critical interaction strength we have demonstrated the corresponding crossover between exponential and algebraic relaxation, which at the critical coupling continues indefinitely, and have found an analytic expression for the late-time Green's functions.

Appendix A

Solutions to the self-consistent mean-field theory with two crossed cavities

This appendix focuses on the solutions to Eqs. (3.27). These coupled equations determine the exact phase diagram Fig. 3.2 of the experiment [1]. We will first deal with the case of empty cavities, where the wave function can be found analytically. Building on this solution the critical coupling strength U_p for the emergence of superradiance can be found from perturbation theory. Finally, deep within the superradiant phase, a fully numerical solution for the emergence of supersolidity is required.

A.1 Empty cavities

With $\alpha_i = 0$ the Schrödinger equation for the atoms simplifies to

$$\left(-\frac{\nabla^2}{2m} + \frac{\Omega^2}{\Delta_A}\cos^2(k_0 y)\right)\psi_{n,\mathbf{k}}(\mathbf{r}) = E_{n,\mathbf{k}}\psi_{n,\mathbf{k}}(\mathbf{r}) \,, \tag{A.1}$$

where we neglected the slowly varying trapping potential. Moreover n is the band index and $\mathbf{k}$ the quasi-momentum. Eq. (A.1) is solved by Mathieu sine and cosine functions C and S

$$\psi_{n,\mathbf{k}}(\mathbf{r}) = c_1 C\left(\frac{\tilde{E}}{E_R} + \frac{U_p}{2\epsilon_R}, -\frac{U_p}{4\epsilon_R}, k_0 y\right) + c_2 S\left(\frac{2\tilde{E}}{k_0^2} + \frac{U_p}{2\epsilon_R}, -\frac{U_p}{4\epsilon_R}, k_0 y\right) \,, \tag{A.2}$$

with the notation $\tilde{E} = E - (k_x^2 + k_z^2)/(2m)$. Without loss of generality we can choose the wave function even and find

$$\psi_{n,\mathbf{k}} = \sqrt{2} e^{ik_x x + ik_z z} C\left(\frac{\tilde{E}}{E_R} + \frac{U_p}{2\epsilon_R}, -\frac{U_p}{4\epsilon_R}, k_0 y\right) \,, \tag{A.3}$$

which is periodic and therefore an allowed solution, if the characteristic value a_s with $s = \frac{k_y}{k_0}$ satisfies

$$a_s\left(\frac{U_p}{4\epsilon_R}\right) = \frac{\tilde{E}}{E_R} + \frac{U_p}{2\epsilon_R} \,. \tag{A.4}$$

The corresponding eigenenergy is then given by

$$E_{n,\mathbf{k}} = \frac{k_0^2 a_s\left(\frac{U_p}{4\epsilon_R}\right) + (k_x^2 + k_z^2) - m\delta_c U_p}{2m} \,. \tag{A.5}$$

It is typically more convenient to perform integrals in quasi-momentum over the extended zone scheme, instead of the reduced representation. To avoid confusion we label the eigenenergy in the extended picture by $E(\mathbf{k})$. The thermal occupation is then simply given by integrating the Bose distribution over the available eigenstates. Performing the integrals in k_x and k_z analytically one finds

$$n(\beta) = \int \frac{d^3k}{(2\pi)^3} n_B(\beta E(\mathbf{k})) = -\int_0^\infty \frac{dk_y}{2\pi} \frac{m \ln\left(1 - e^{\beta\mu_{\text{eff}}}\right)}{2\pi\beta\hbar^2} \tag{A.6}$$

with effective chemical potential

$$\mu_{\text{eff}}(k_y) = \mu - \frac{k_0^2 a_s\left(\frac{U_p}{4\epsilon_R}\right) - m\delta_c U_p}{2m} \,. \tag{A.7}$$

For $\Omega^2/(E_R\Delta_A) \to 0$ this reproduces the result of a three-dimensional non-interacting Bose gas with the critical density

$$n(\beta)\big|_{\mu=0} = \zeta(3/2)\Gamma(3/2)\frac{m^{3/2}}{\sqrt{2}\hbar^3\pi^2\beta^{3/2}} \,. \tag{A.8}$$

More importantly Bose-Einstein condensation takes place independent of the lattice potential for $\mu_{\text{eff}}(0) = 0$. From this condition the critical temperature can be determined numerically.

A.2 Weak superradiance

Small cavity occupations can be treated perturbatively. In particular, for the onset of superradiance such a description becomes exact. Instead of using stationary perturbation theory for $\psi_{n,\mathbf{k}}$, we use the more convenient expansion of the Green's function in powers of V_{sp}

$$G(\mathbf{k},\alpha) = G_0(\mathbf{k}) - \int \frac{d^3k'}{(2\pi)^3} G_0(\mathbf{k}) V_{\text{sp}}(\mathbf{k}',\alpha) G_0(\mathbf{k}'-\mathbf{k}) + \mathcal{O}(V_{\text{sp}}^2) \,. \tag{A.9}$$

This is then inserted into the cavity field equation

$$-\Delta_i\alpha_i + V\sum_n \int_{\mathrm{BZ}} \frac{d^3k}{(2\pi)^3} G_{ml}(\omega_n,k)\frac{\partial V_{\mathrm{sp}}^{lm}}{\partial\alpha_i} = 0\ , \tag{A.10}$$

where V is the volume of the atomic cloud and the band indices m and l are being summed over. Insertion of the linear expansion of the Green's function in V_{sp} yields

$$-\Delta_i\alpha_i + \frac{Ng^2}{2\Delta_A}\alpha_i - \frac{V\Omega^2 g^2}{8\Delta_A^2}\Re(\alpha_i)\int \frac{d^3k}{(2\pi)^3}\sum_{i,n} G_0(\omega_n,\mathbf{k})G_0(\omega_n,\mathbf{k}_i+\mathbf{k}) = 0\ . \tag{A.11}$$

The remaining Matsubara sum can be performed analytically:

$$\begin{aligned}\sum_{n'} G_0(\omega_{n'},\mathbf{k})G_0(\omega_{n'}+\omega_n,\mathbf{k}_i+\mathbf{k}) &= \sum_{n'}\frac{1}{i\omega_{n'}-E(\mathbf{k})}\frac{1}{i\left(\omega_n+\omega_{n'}\right)-E(\mathbf{k}+\mathbf{k}')}\\ &= -\frac{n_B(\beta E(\mathbf{k}))-n_B(\beta E(\mathbf{k}+\mathbf{k}'))}{E(\mathbf{k})-E(\mathbf{k}+\mathbf{k}')+i\omega_n}\ .\end{aligned} \tag{A.12}$$

However the momentum integral in the thermal Lindhard function

$$\Pi(\omega_n,\mathbf{k}) = -\int\frac{d^3k'}{(2\pi)^3}\frac{n_B(\beta E(\mathbf{k}'))-n_B(\beta E(\mathbf{k}+\mathbf{k}'))}{E(\mathbf{k}')-E(\mathbf{k}+\mathbf{k}')+i\omega_n} \tag{A.13}$$

cannot be solved analytically. Moreover $\Pi(\omega_n,\mathbf{k})$ is missing the contribution of the possibly macroscopically occupied ground state. Including the condensate shifts $\Pi(\omega_n=0,\mathbf{k}_i)$ by $2m\rho_{\mathrm{BEC}}/k_i^2$, with ρ_{BEC} the density of the condensate. The linearized cavity field equation allows solutions with finite α_i beyond the critical coupling strength

$$\lambda_c = \left(\frac{8}{\sum_{i=1,2}\left(\frac{\rho_{\mathrm{BEC}}}{n}\frac{1}{\epsilon_R}+\frac{1}{m^{3/2}\delta_c^{1/2}}\Pi(0,\mathbf{k}_i)\right)}\right)^{1/2}\ . \tag{A.14}$$

Below the critical temperature T_c set by $\mu_{\mathrm{eff}}(0)=0$, this condition marks the phase transition to a supersolid-like phase.

A.3 Supersolid solution

Deep within the superradiant phase, no contribution to the single-particle potential V_{sp} can be treated perturbatively. Consequently the wave functions solving the

Schrödinger equation of the mean-field Hamiltonian

$$\hat{H}_{\mathrm{MF}} = -\frac{\nabla^2}{2m} + V_{\mathrm{sp}}(\mathbf{r}) \tag{A.15}$$

are no longer analytically known and a purely numerical approach has to be chosen. We thus discretize one half of the hexagonal first Brillouin zone on a triangular grid of 694 points and, working in the extended representation, include the neighboring $N_k = 361$ copies. These large grids are necessary, as a deep lattice scatters the wave function across many Brillouin zones and at low temperatures the thermal cloud will be tightly focused around the Γ-points. Note, that due to the $\mathbf{Z}_2$ symmetry along the k_y direction it suffices to use half of each Brillouin zone. In quasi-momentum space the Hamiltonian couples only states differing by short reciprocal lattice vectors. One thus has to diagonalize 694 sparse matrices, each of which has size $N_k \times N_k$. Since the Hamiltonian depends on the cavity fields α_i, which have to be found self-consistently, this calculation has to be repeated a lot. We therefore only find the $N_n \approx 10 - 30$ smallest eigenvalues of each matrix using a Krylov subspace method. With these eigenenergies of the N_n lowest bands, we find the thermal filling fraction f_{th} as a function of the chemical potential. The k_z direction is unaffected by the two-dimensional lattice and can be integrated over. This gives rise to the Polylogarithm $\mathrm{Li}_{1/2}$ in

$$\begin{aligned} f_{\mathrm{th}}(\mu) =& \frac{\sqrt{3\theta}\epsilon_R}{2(2\pi)^2 f N_k N_n} \left(\frac{f}{\zeta(3/2)}\right)^{1/3} \\ & \times \sum_{n,\mathbf{k}\in \mathrm{BZ}} \mathrm{Li}_{1/2}\left(\exp\left(\frac{1}{2\pi\theta}\left(\frac{\zeta(3/2)}{f}\right)^{2/3}(\mu - E_{n,\mathbf{k}})\right)\right) , \end{aligned} \tag{A.16}$$

where $\theta = T/T_c^{\mathrm{ideal}}$ is the dimensionless temperature. Furthermore we define the atomic density matrix in momentum space

$$\begin{aligned} \Xi_{\mathbf{G},\mathbf{G}'}(\mu) = \sum_{n,\mathbf{k}\in \mathrm{BZ}} \psi_n^*(\mathbf{k}+\mathbf{G})\psi_n(\mathbf{k}+\mathbf{G}') \Bigg\{ & \frac{\sqrt{3\theta}\epsilon_R}{2(2\pi)^2 f N_k N_n} \left(\frac{f}{\zeta(3/2)}\right)^{1/3} \theta(E_{n,\mathbf{k}} - \mu) \\ & \times \mathrm{Li}_{1/2}\left[\exp\left(\frac{1}{2\pi\theta}\left(\frac{\zeta(3/2)}{f}\right)^{2/3}(\mu - E_{n,\mathbf{k}})\right)\right] \\ & + f_0[1 - \theta(E_{n,\mathbf{k}} - \mu)] \Bigg\} . \end{aligned} \tag{A.17}$$

Here we choose the convention that $\theta(0) = 0$ for the Heaviside theta function and since the integral over the Brillouin zone has already been performed $\mathbf{G}$ and $\mathbf{G}'$ are vectors of the reciprocal lattice. Moreover, $\psi_n(\mathbf{k})$ is the eigenfunction of the

Hamiltonian (A.15) with quasi-momentum k in the n-th Bloch band. Evaluating $f_{\mathrm{th}}(\mu)$ for some guess of α_i, one can find the chemical potential $\mu < \min_k E(k)$, that satisfies $f_{\mathrm{th}}(\mu) = f$. If no such value exists the chemical potential is fixed to $\mu = \min_k E(\mathbf{k})$. The gas is then partially in a BEC with a condensate fraction $f_0 = f - f_{\mathrm{th}}(\min_k E(k))$. The updated cavity fields are then found via the matrix equation

$$\begin{aligned}\begin{pmatrix}\alpha_1\\ \alpha_2\end{pmatrix} = \Bigg[&\left(\frac{\Delta_1}{\delta_c} - \sum_{\mathbf{G},\mathbf{G}'}\Xi_{\mathbf{G},\mathbf{G}'}(\mu)V_{\mathrm{sp}}^{(1)}(\delta\mathbf{G})\right)\left(\frac{\Delta_2}{\delta_c} - \sum_{\mathbf{G},\mathbf{G}'}\Xi_{\mathbf{G},\mathbf{G}'}(\mu)V_{\mathrm{sp}}^{(2)}(\delta\mathbf{G})\right)\\ &- \left(\sum_{\mathbf{G},\mathbf{G}'}\Xi_{\mathbf{G},\mathbf{G}'}(\mu)V_{\mathrm{sp}}^{\mathrm{mix}}(\delta\mathbf{G})\right)^2\Bigg]^{-1}\\ &\times\begin{pmatrix}\frac{\Delta_2}{\delta_c} - \sum_{\mathbf{G},\mathbf{G}'}\Xi_{\mathbf{G},\mathbf{G}'}(\mu)V_{\mathrm{sp}}^{(2)}(\delta\mathbf{G}) & \sum_{\mathbf{G},\mathbf{G}'}\Xi_{\mathbf{G},\mathbf{G}'}(\mu)V_{\mathrm{sp}}^{\mathrm{mix}}(\delta\mathbf{G})\\ \sum_{\mathbf{G},\mathbf{G}'}\Xi_{\mathbf{G},\mathbf{G}'}(\mu)V_{\mathrm{sp}}^{\mathrm{mix}}(\delta\mathbf{G}) & \frac{\Delta_1}{\delta_c} - \sum_{\mathbf{G},\mathbf{G}'}\Xi_{\mathbf{G},\mathbf{G}'}(\mu)V_{\mathrm{sp}}^{(1)}(\delta\mathbf{G})\end{pmatrix}\\ &\cdot\begin{pmatrix}\sum_{\mathbf{G},\mathbf{G}'}\Xi_{\mathbf{G},\mathbf{G}'}(\mu)\frac{\partial V_{\mathrm{sp}}(\delta\mathbf{G})}{\partial\alpha_1}\Big|_{\alpha_2\to 0}\\ \sum_{\mathbf{G},\mathbf{G}'}\Xi_{\mathbf{G},\mathbf{G}'}(\mu)\frac{\partial V_{\mathrm{sp}}(\delta\mathbf{G})}{\partial\alpha_2}\Big|_{\alpha_1\to 0}\end{pmatrix},\end{aligned} \tag{A.18}$$

where we use the shorthand notation $\delta\mathbf{G} = \mathbf{G} - \mathbf{G}'$. For completeness we have furthermore introduced the dimensionless intercavity potentials

$$\begin{aligned}V_{\mathrm{sp}}^{(i)} &= \frac{1}{\alpha_i\delta_c}\frac{\partial V_{i,i}\big|_{\hat{a}_i\to\alpha_i}}{\partial\alpha_i}\\ V_{\mathrm{sp}}^{\mathrm{mix}} &= \sum_{\sigma=1,2}\frac{1}{\alpha_{\bar{\sigma}}\delta_c}\frac{\partial V_{1,2}\big|_{\hat{a}_i\to\alpha_i}}{\partial\alpha_\sigma}\end{aligned} \tag{A.19}$$

proportional to the dimensionless strength $U_0 = g^2N/(\Delta_A\delta_c)$. In agreement with the experimental parameters, we only keep the linear, homogeneous contribution

$$\frac{\Delta_i}{\delta_c} - \sum_{\mathbf{G}=\mathbf{G}'}\Xi_{\mathbf{G},\mathbf{G}'}(\mu)V_{\mathrm{sp}}^{(2)}(\delta\mathbf{G}) = -\frac{\delta_{c_i}}{\delta_c} \tag{A.20}$$

throughout the calculations in Sec. 3.2. In this approximation the quadratic and off-diagonal terms $\propto V_{\mathrm{sp}}^{\mathrm{mix}}$ disappear completely. If the actual self-consistent solution of the coupled mean-field equations is to be determined, the update procedure has to be repeated until no significant change of μ and α_i occurs between updates. Close to the critical point this can take a long time. However, for the phase diagram no iteration is needed at all. Instead, the initial guess is chosen with some small $\alpha_i^{\mathrm{init}} \simeq 10^{-4}$ and only a single iteration is performed. Depending

on the direction of the update, the i-th cavity is either empty ($\alpha_i^{\text{new}} < \alpha_i^{\text{init}}$) or superradiant ($\alpha_i^{\text{new}} > \alpha_i^{\text{init}}$). With f_0 necessarily determined during the update all four phases in Fig. 3.2 can be distinguished.

Appendix B

Alternative derivation of nonlinear Feynman rules

In section 4.4.4 we argued that in order to capture the properties of non-interacting polaritons giving rise to electromagnetically induced transparency, it is not actually necessary to implement nonlinear Feynman rules in real time. Instead, it suffices to simply exclude all self-energy insertions into the ground-state propagator and to forbid any of the excited states to repeatedly couple to the ground state. By these means we then derived the (exact) polarizability of the atomic medium in 4.5. It is instructive to rederive this result directly from the coupled Lindblad equations of the spin operators $\sigma_{\mu,\nu}$ introduced in Sec. 4.4.1.
The retarded polarizability of each atom in the ground state is given by

$$P(t) = \theta(t) \left[\mathrm{Tr}(\sigma_{g,e}(t)\sigma_{e,g}\rho) - \mathrm{Tr}(\sigma_{e,g}\sigma_{g,e}(t)\rho) \right] . \tag{B.1}$$

The latter of these contributions vanishes identically as $\rho = \sigma_{g,g}$. The time evolution of $\sigma_{g,e}(t)$ is given by

$$-i\dot{\sigma}_{g,e}(t) = [H, \sigma_{g,e}(t)] + i\gamma_e \left(\sigma_{g,e}\sigma_{g,e}(t)\sigma_{e,g} - \frac{1}{2} \left\{ \sigma_{e,g}\sigma_{g,e}, \sigma_{g,e}(t) \right\} \right) , \tag{B.2}$$

which very nicely simplifies, if one uses $\sigma_{e,g}\sigma_{g,e} = \sigma_{e,e}$, as well as the observation that H in the limit of low polariton densities acts trivially on the ground state, which implies $\sigma_{g,e}\sigma_{g,e}(t) = 0$ and $H\sigma_{g,e}(t) = 0$. One thus ends up with

$$i\dot{\sigma}_{g,e}(t) = \sigma_{g,e}(t)H - i\frac{\gamma_e}{2}\sigma_{g,e}(t)\sigma_{e,e} , \tag{B.3}$$

which has the solution

$$\sigma_{g,e}(t) = \sigma_{g,e}e^{-i\tilde{H}t} , \tag{B.4}$$

where $\tilde{H} = H + i\frac{\gamma_e}{2}\sigma_{e,e}$ is the non-hermitian effective Hamiltonian governing the time evolution of the three level system in the presence of losses. Inserting this

result back into the polarizability, we obtain

$$P(t) = \theta(t) \left(e^{i\tilde{H}t} \right)_{22} . \tag{B.5}$$

Upon Fourier transformation this turns into

$$P(\omega) = \frac{i}{\omega - \frac{\Omega^2}{\omega - \Delta_s} + i\gamma_d/2} , \tag{B.6}$$

which coincides with the result obtained by means of the simplified nonlinear Feynman rules in (4.106). We thus have seen that, due to the absence of laser coupling between the atomic ground state and the excited state, nonlinear Feynman rules are easily implemented. As is mentioned in Sec. 4.4.4, the dynamics of the other excited state of the $\mathcal{N}$-scheme is not as simple. Thus a similar derivation for the susceptibility of the medium from the perspective of the exchange photon fails.
We can now go beyond the limit of low polariton densities and consider the effect of a finite density of excited atoms. In this case, there is a finite fraction of atoms for which $\rho \neq \sigma_{g,g}$. In particular, due to EIT, excited atoms will predominantly occupy the metastable state ($\rho = \sigma_{s,s}$). This, however, implies that $\sigma_{e,g}\rho$ and $\rho\sigma_{e,g}$ both vanish. The main effect of a finite density of polaritons will thus simply result in a reduced susceptibility of the atoms, which is easily included via a finite density of defects n_V in the chain of atoms. If the number density of excited atoms remains small, this effect can be neglected all together, as it will have no effect on the stability of phases reported in chapter 4.

Appendix C

Dicke model

C.1 Keldysh formulation of the self-consistent Hartree theory

In this appendix, we provide some details on the self-consistent Hartree theory introduced in section 5.4. First, note that the Kronecker delta in Eq. ((5.30)) is necessary, as the product of operators in the interaction is normal-ordered, whereas the Keldysh Green's function is time-ordered (in terms of the "classical" fields). Therefore the normal-ordered product evaluated on the closed-time contour reads

$$\langle \hat{b}^\dagger(t)\hat{b}(t)\rangle = \langle b_+(t)b_+^*(t+0^+)\rangle = \langle b_-(t+0^+)b_-^*(t)\rangle \tag{C.1}$$

while the Keldysh Green's function can be expressed as

$$iG^K(t,t') = \langle b_+(t)b_+^*(t')\rangle + \langle b_-(t)b_-^*(t')\rangle. \tag{C.2}$$

The difference between $iG^K(t,t+)$ and twice the particle number can therefore be compensated by

$$\langle b_-(t)b_+^*(t+0^+)\rangle - \langle b_+(t)b_-^*(t+0^+)\rangle = -1. \tag{C.3}$$

To account for all possible diagrams at one loop level with the correct symmetry factors it is sufficient to include all permutations (irrespective of the possibility of two subscripts being identical) and multiply by the symmetry factor 1/2, to account for the starting- and end-point of G^K being identical. For example the vertex $\hat{a}_q\hat{b}_{cl}\hat{b}_{cl}\hat{b}_{cl}^*$ translates to the subscript $(5,3,3,4)$ and its 23 permutations. In this labeling system numbers refer to entries in the vector V, in accordance with this, the subscripts in G^K both run from 1 to 4. Before actually contracting M with G^K, care has to be taken whether an index is contracted with an incoming or an outgoing particle, or in other terms, whether a given field is part of V or $V^\dagger$. As even positions (counting from left to right) in each subscript are contracted into the left side of a Green's function they are to be interpreted as part of $V^\dagger$, which translates to the need of shifting even indices at even positions by -1 and odd indices at even positions by +1. On the other hand, as indices at odd positions of V are always contracted into the right side of a Green's function they are part of

V, which calls for no change in those subscripts.

Integrating over G^K in Eq. ((5.30)), since there is no frequency dependence in the self-energy, can actually be done analytically, as all integrals can be performed using the residue theorem, where we have the ambiguity of closing the integration contour in the upper or lower ω-plane. In any case only a maximum of 4 poles of the retarded *or* advanced Green's function contribute. Eventually one has to solve an equation depending on products of roots of polynomials of degrees ≤ 4, which can be done to arbitrary precision using numerical methods. Note, even though it seems like one has to solve an equation for 4×4 matrices, these coupled equations boil down to just two linearly independent ones. This is a consequence of the symmetry in the interaction, that allows to parametrize the retarded self energy as

$$\Sigma_H^R = \begin{pmatrix} 0 & 0 & \Sigma_1 & \Sigma_1 \\ 0 & 0 & \Sigma_1 & \Sigma_1 \\ \Sigma_1 & \Sigma_1 & 2\Sigma_2 & \Sigma_2 \\ \Sigma_1 & \Sigma_1 & \Sigma_2 & 2\Sigma_2 \end{pmatrix}. \tag{C.4}$$

The solution of the remaining self-consistency equations

$$\Sigma_1 = \frac{g}{4N}\left[2 - \int \frac{d\omega}{2\pi} \Im\Big(G^K_{(3,3)} + G^K_{(3,4)} + G^K_{(4,4)}\Big)\right] \tag{C.5}$$

$$\Sigma_2 = -\frac{g}{4N} \int \frac{d\omega}{2\pi} \Im\Big(G^K_{(1,3)} + G^K_{(2,3)} + G^K_{(4,1)} + G^K_{(4,2)}\Big) \tag{C.6}$$

evaluated within a small interval (scaling like $g_{c,0}/\sqrt{N}$) of the critical coupling strength (the coupling strength, at which in the limit $N \to \infty$ the phase transition occurs) yields the scaling of the largest eigenvalue of the matrix $\langle n \rangle = -\frac{1}{2} + i \int \frac{d\omega}{4\pi} G^K(\omega)$ that is discussed in the main text.

C.2 Details on the self-consistent Hartree-Fock approach and computational techniques

Within the SCHF approach introduced in section 5.4, we follow the same procedure illustrated above for the Hartree diagrams to deal with all possible contractions resulting from the tensorial structure of the vertex. There are, however, some minor differences

- The two vertices involved are being contracted with different combinations of incoming and outgoing fields. We take care of this by shifting all but the first index of the vertex contracted with the outgoing particle according to the rules that were already used in the Hartree calculation.
- For the vertex that acts on the incoming particle only the last index is treated

this way.

- Afterwards the n-th index of the left vertex is connected via a Green's function with the n+1-th index of the right vertex (for a particle propagating from right to left). The remaining indices are externally exhibited by the self-energy.
- Finally, one has to compensate for the over-counting due to identical contractions. This is to say that one has to divide by the factorial of the number of retarded Green's functions multiplied with the factorial of the number of Keldysh Green's functions. We distinguish between those Green's functions internally by limiting the intervals over which the indices in all contractions run. This is necessary to achieve adequate speeds in the numerical calculations and easily compensated for by the symmetry factors. Additionally one has to include a factor of 1/2 due to the expansion of the exponential.

To numerically tackle the self-consistency equations we again start by noting some symmetries of the self-energies:

$$\Sigma^R = \begin{pmatrix} \Sigma_1^R & \Sigma_1^R & \Sigma_3^R & \left[\Sigma_3^R\right]^* \\ \Sigma_1^R & \Sigma_1^R & \Sigma_3^R & \left[\Sigma_3^R\right]^* \\ \Sigma_2^R & \Sigma_2^R & \Sigma_4^R & \Sigma_5^R \\ \left[\Sigma_2^R\right]^* & \left[\Sigma_2^R\right]^* & \Sigma_5^R & \left[\Sigma_4^R\right]^* \end{pmatrix} \tag{C.7}$$

and

$$\Sigma^K(t) = \begin{pmatrix} \Sigma_1^K(t) & \Sigma_1^K(t) & -\left[\Sigma_2^K(-t)\right]^* & \Sigma_2^K(-t) \\ \Sigma_1^K(t) & \Sigma_1^K(t) & -\left[\Sigma_2^K(-t)\right]^* & \Sigma_2^K(-t) \\ \Sigma_2^K(t) & \Sigma_2^K(t) & \Sigma_4^K(t) & \Sigma_3^K(t) \\ -\left[\Sigma_2^K(t)\right]^* & -\left[\Sigma_2^K(t)\right]^* & -\left[\Sigma_3^K(t)\right]^* & -\left[\Sigma_4^K(t)\right]^* \end{pmatrix}. \tag{C.8}$$

However, now the expressions involved are far to cumbersome to show them here (each consisting of several thousand convolutions). As these convolutions can no longer be treated analytically we perform fast Fourier transforms including about 10^5 to 10^7 points for each Green's function and calculate the convolutions in the time domain, where they are nothing but simple products. Finally, we transform the resulting self-energy in time back to the frequency domain. While this calculation is conceptionally straightforward, there are some technicalities which significantly increase precision and reduce computation time:

- As the frequency-dependence of the self-energy emerges from convolutions of Green's functions we can conclude that $\lim_{\omega\to\infty}\Sigma^R(\omega) \to \Sigma_H^R + \mathcal{O}(1/\omega)$ and $\lim_{\omega\to\infty}\Sigma^K(\omega) \to \mathcal{O}\left(1/\omega^2\right)$, while all off-diagonal entries fall of even faster. This allows to choose the frequency interval for the Fourier transform much smaller, as only these next to leading corrections have to be treated

numerically. The contributions from the high-frequency tail in Hartree approximation are then added after the Fourier transform.

- To allow for the long-time tails of the possibly very sharp peaks of the Green's functions in the vicinity of the the scale invariant point, we optimize the scale s in the numerical implementation of $f(st) = (2\pi\delta\omega)\sum f(\omega)\exp is\omega t$ for $t \in \mathbb{N}$ and where the sum runs through $\omega = -\omega_{\max}, -\omega_{\max} + \delta\omega, ...$ In other words the interval in the time domain has to be chosen according to the physical parameters, but independent of the interval in the frequency domain.

Finally, one has to find a method by which convergence of the self-consistency equation can be achieved quickly. While it is always possible to use an extremely small update parameter c in the interaction procedure:

$$\Sigma_{\text{new}} = (1-c)\Sigma_{\text{old}} + c\Sigma[G[\Sigma_{\text{old}}]], \tag{C.9}$$

it is quite frequently possible to reach convergence much faster by using Newton's method for root searching. However Σ is a functional and the update will never do this justice. Instead it only uses a rough estimate based on the amplitude of $G(\omega)$ to calculate the purely local update parameter $c(\omega)$. This, together with the opposing effects that Hartree and Fock diagrams take on a partially converged Green's function, forces the use of a conventional, small update constant c near the phase transition.

C.3 Approximate kinetic theory

Starting from the Dyson Eqs. (5.28) and (5.29) , we consider the relaxation dynamics of the system in the SCHF approach of section 5.4. Due to the self-consistency of the approach and the non-trivial dynamics of both retarded and Keldysh Green's functions (and self-energies) one obtains strongly nonlinear differential equations far from the steady state. To make progress, we limit ourselves to the late-time dynamics where only small deviations from the steady state are left. In this regime, one can expand in the time-derivatives to linear order. However, as we will see, there is a regime close to the phase transition where a linearization in the deviations from the steady state fails and nonlinearities lead to algebraic relaxation.

To each Dyson equation we actually need to add the time-reversed counterpart, since in general the Green's functions depend on two times (two frequencies). We thus have the following four matrix-valued equations, formulated in the time do-

main:

$$\left(\left[G_0^R\right]^{-1} - \Sigma_H^R - \Sigma_F^R\right) \circ G^K = \left(\Sigma_F^K - D_0^K\right) \circ G^A$$
$$G^K \circ \left(\left[G_0^A\right]^{-1} - \Sigma_H^A - \Sigma_F^A\right) = G^R \circ \left(\Sigma_F^K - D_0^K\right) \tag{C.10}$$
$$\left(\left[G_0^R\right]^{-1} - \Sigma_H^R - \Sigma_F^R\right) \circ G^R = \delta(t - t')$$
$$G^R \circ \left(\left[G_0^R\right]^{-1} - \Sigma_H^R - \Sigma_F^R\right) = \delta(t - t') \tag{C.11}$$

where the first time-reversed pair of equations determines the 4 by 4 Keldysh Green's function and the second determines the 4 by 4 retarded Green's function. Note, that we explicitly separated the contribution to the self-energies coming from Hartree and Fock processes.

We now change coordinates and switch from t, t' to absolute time τ and relative frequency ω via the Wigner transformation (see Sec. 5.1). In many situations, the dependence on the absolute time is slow and only a finite number of these derivatives are actually relevant, allowing for the expansion of the exponential. Since we are interested in the relaxation close to the steady state, it will be sufficient to keep only first order derivatives in τ. This is the case because, as we shall see, near $g_c(N)$ the effective damping κ_{kin} of the dynamics in τ will disappear without a diverging quasiparticle lifetime. Otherwise the derivatives in ω would cancel out the suppression in powers of derivatives in τ. After taking the Wigner transform of the two pairs of equations (C.10) and (C.11), it is convenient to take the sum and the difference of each pair. One of the two resulting equations for each pair will then contain only products of derivatives with respect to ω and τ. While this obscures the physics to some extent, it can nonetheless be treated on the same footing as the other equation. This would be necessary if we found solutions for the Green's functions in the kernel of the latter equation, a complication that our algorithm will avoid by design[1]. We thus disregard this equation and for each pair $\{G^K, G^R\}$ keep only the one containing the unrenormalized derivative with respect to τ and end up with one equation stemming from the Keldysh pair (C.10) and one from the retarded pair (C.11). After explicitly separating the deviations of Green's functions $\delta G^{R,A,K} = G^{R,A,K} - G_{\text{ss}}^{R,A,K}$ and self-energies $\Sigma^{R,A,K} = \Sigma_{\text{ss}}^{R,A,K} + \delta\Sigma^{R,A,K}$

[1] Since we use equation (C.14) only to extract the kinetic parameters for the most slowly decaying eigenvector δG^K, but not to actually find this eigenvector, both kinetic equations contain the same information and are therefore redundant.

from their steady state values, we obtain the two rather complicated equations

$$\begin{aligned}
i\partial_\tau \delta G^K &= \delta G^K \left(\left[G_0^A(\omega=0) \right]^{-1} - \Sigma_{\mathrm{ss}}^A \right) P - G_{\mathrm{ss}}^K \delta\Sigma^A P \\
&\quad - P \left(\left[G_0^R(\omega=0) \right]^{-1} - \Sigma_{\mathrm{ss}}^R \right) \delta G^K + P \delta\Sigma^R G_{\mathrm{ss}}^K \\
&\quad + \frac{i}{2} \partial_\tau \delta G^K \partial_\omega \left(\Sigma_{\mathrm{ss}}^A + \delta\Sigma^A \right) P - \frac{i}{2} \partial_\omega \left(\delta G^K + G_{\mathrm{ss}}^K \right) \partial_\tau \delta\Sigma^A P \\
&\quad - \frac{i}{2} P \partial_\tau \delta\Sigma^R \partial_\omega \left(G_{\mathrm{ss}}^K + \delta G^K \right) + \frac{i}{2} P \partial_\omega \left(\Sigma_{\mathrm{ss}}^R + \delta\Sigma^R \right) \partial_\tau \delta G^K \\
&\quad + P \left(\Sigma^K - D_0^K \right) \delta G^A + P \delta\Sigma^K G_{\mathrm{ss}}^A - \delta G^R \left(\Sigma_{\mathrm{ss}}^K - D_0^K \right) P \\
&\quad - G_{\mathrm{ss}}^R \delta\Sigma^K P - \frac{i}{2} P \partial_\tau \delta\Sigma^K \partial_\omega G_{\mathrm{ss}}^A + \frac{i}{2} P \partial_\omega \Sigma_{\mathrm{ss}}^K \partial_\tau \delta G^A \\
&\quad - \frac{i}{2} \partial_\tau \delta G^R \partial_\omega \Sigma_{\mathrm{ss}}^K P + \frac{i}{2} \partial_\omega G_{\mathrm{ss}}^R \partial_\tau \delta G^K \\
i\partial_\tau \delta G^R &= \delta G^R \left(\left[G_0^R(\omega=0) \right]^{-1} - \Sigma_{\mathrm{ss}}^R \right) P - P \left(\left[G_0^R(\omega=0) \right]^{-1} - \Sigma_{\mathrm{ss}}^R \right) \delta G^R \\
&\quad - G_{\mathrm{ss}}^R \delta\Sigma^R P + P \delta\Sigma^R G_{\mathrm{ss}}^R + \frac{i}{2} \partial_\tau \delta G^R \partial_\omega \Sigma_{\mathrm{ss}}^R P - \frac{i}{2} \partial_\omega G_{\mathrm{ss}}^R \partial_\tau \delta\Sigma^R P \\
&\quad - \frac{i}{2} P \partial_\tau \delta\Sigma^R \partial_\omega G_{\mathrm{ss}}^R + \frac{i}{2} P \partial_\omega \Sigma_{\mathrm{ss}}^R \partial_\tau \delta G^R ,
\end{aligned} \tag{C.12}$$

where

$$P = \mathrm{diag}(1, -1, 1, -1) \tag{C.13}$$

accounts for the sign of ω in $\left[G_0^R \right]^{-1}$, which itself is a consequence of the Nambu structure. The nonlinearity of these equations comes from the fact that in a self-consistent theory the self-energies $\delta\Sigma^{R,A,K}$ in turn depend on the deviations $\delta G^{R,A,K}$ via the Dyson equations. The next step is to expand the equations in powers of the deviations from the steady state. Eq. (C.10) then generically takes the following form:

$$\partial_\tau \delta G^K \approx - \sum_{\sigma \in \{R,A,K\}} \kappa_{\mathrm{kin}\sigma} \delta G^\sigma - \sum_{\sigma,\sigma'} \lambda_{\mathrm{kin}\sigma,\sigma'} \delta G^\sigma \delta G^{\sigma'} + \mathcal{O}\left(\delta^3\right), \tag{C.14}$$

where the renormalization of the τ-derivative due to products with derivatives with respect to ω has been omitted, since it can be shown that the term must be invariant under a rescaling of the system size and $\mathcal{O}(1)$. Consequently, apart from this renormalization, the damping rate $\kappa_{\mathrm{kin}\sigma}$ of the exponential relaxation can be expressed as the eigenvalues of linear operators.

We will instead proceed along a shortcut to obtain an estimate of the relaxation rate κ_{kin}. We exploit the iterative procedure required for the convergence of the self-consistent resummation used to find the steady state in section 5.5. For a

sufficiently small update parameter c (see Appendix C.2) it resembles indeed a simplified time evolution, where in each "time step"/iteration the past is always assumed to be completely time independent. For long times and small values of $\kappa_{\mathrm{kin}}/\kappa_{\mathrm{qp}}$ this is a good approximation and the convergence is reached along the eigenvector of the Fredholm integral operator with eigenvalue κ_{kin}. This procedure allows for an a posteriori justification of the use of the Iterative Pseudo (IP) time evolution to compute κ_{kin}.
In the IP time evolution the overall time scale is not fixed. However, we note that by mapping one iteration to a time difference τ, the IP time evolution predicts (after linearization around the steady state and subtraction of the latter)

$$\delta G^R(t+\tau) = \delta G^R(t) + c\left(G^R_{\mathrm{ss}}\Sigma^R(\delta G^R(t))G^R_{\mathrm{ss}} - \delta G^R(t)\right). \tag{C.15}$$

Since including the dynamics for the Keldysh component contributes only further additive terms with the same global prefactors, we simplify the expressions here to depend solely on the retarded Green's function. By comparison with (C.14), we realize that $\tau = c/\kappa_{\mathrm{qp}}$ and conclude that the condition for a trustworthy description of the late-time evolution by the iterative procedure requires $c\kappa_{\mathrm{kin}} \ll \kappa_{\mathrm{qp}}$, which allows the choice $c = 1$ in the regime where the time-dependence of the past may be neglected. This simplification is crucial for our ability to deal with long times, as otherwise Fock diagrams would require an integral over the entire past, causing the computational cost for a time-step to grow linearly with the simulated time.
The fact that the leading nonlinearity in Eq. (C.14) is of second order in the deviation from the steady state is a general feature of self-consistency, which makes our result in this section applicable to a wide range of systems close to criticality. It is worth noting that in the system the kinetic Eq. (C.14) cannot be formulated on-shell, that is, the frequency convolutions contained in $\Sigma^{R,A,K}(\tau,\omega)$ cannot be eliminated assuming a long quasiparticle lifetime with respect to inverse characteristic excitation energies. This indeed typically fails in an overdamped system, where no quasiparticles exist and therefore both quantities scale equally and are of similar size. It is also worth mentioning that, because of the $1/\omega$ divergence in the distribution function $F(\omega)$ discussed in 5.5.2, the commonly used formulation of kinetic equations in terms of $F(\omega)$ [197] is not an option here.

C.4 Role of the photon loss rate κ

In this section we complement the results presented in the main text by computing the dynamical parameters κ_{qp}, κ_{kin}, λ_{kin} for smaller values of the photon loss rate κ. The goal is to illustrate the qualitative behavior of the system in the isolated limit $\kappa \to 0$. In Fig. C.1 we show the results for $\kappa = 1$ and $\kappa = 0.2$, to be compared with Fig. 5.6 of the main text, computed for $\kappa = 2$. Two main observations emerge: i) since all the dynamical parameters (κ_{qp}, κ_{kin} , λ_{kin}) decrease for decreasing κ, the global timescale becomes slower; ii) since κ_{qp} and κ_{kin} approach one another,

it becomes more difficult (i.e. one has to tune the system even closer to $g_c(N)$) to reach the dynamical critical regime where $\kappa_{\text{kin}} \ll \kappa_{\text{qp}}$. Ultimately, in the $\kappa = 0$ limit, we expect κ_{kin} to become coupled to κ_{qp}, in the sense that the former cannot be made arbitrarily small compared to the latter, at any given N. The numerical computation leading to a set of results as the one in Fig. C.1 is very demanding and becomes more so a $\kappa \to 0$, since the global timescale becomes slower and $\kappa_{\text{kin}} \to \kappa_{\text{qp}}$ (see previous section). Our approach is not applicable in the case $\kappa = 0$.

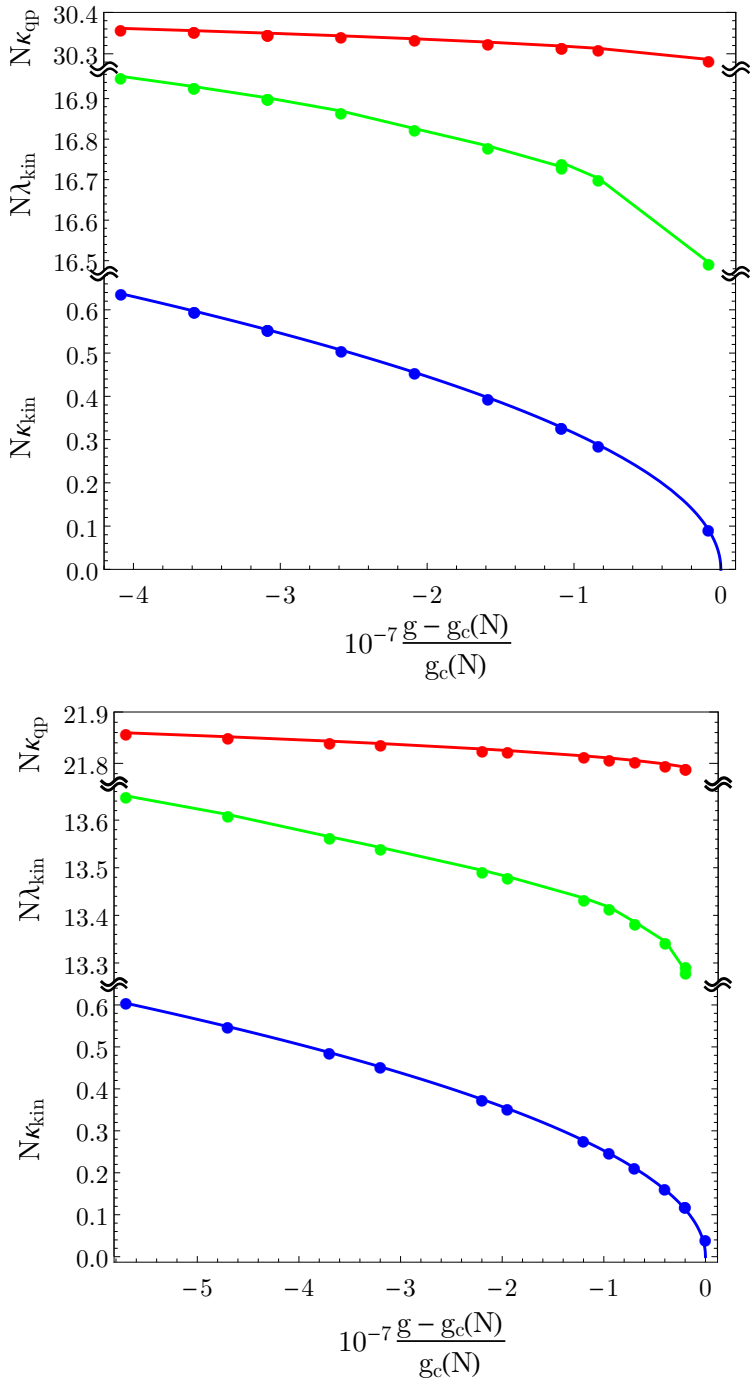

Figure C.1: Numerical values of the kinetic parameters κ_{kin}, λ_{kin} as well as the inverse quasiparticle lifetime κ_{qp}. The parameters used are the same as in the main text, apart from $\kappa = 1$ (upper panel) and $\kappa = 0.2$ (lower panel), which result in $g_{c,0} \approx 1.1420$ and $g_{c,0} \approx 1.0298$ respectively.

List of Publications

J. Lang and F. Piazza "Critical relaxation with overdamped quasiparticles in open quantum systems" *Phys. Rev. A* **94**, 033628 (2016)

J. Lang, F. Piazza, and W. Zwerger Collective excitations and supersolid behavior of bosonic atoms inside two crossed optical cavities *New Journal of Physics*, **19**(12), 123027 (2017)

J. Lang, B. Frank, and J. C. Halimeh "Concurrence of dynamical phase transitions at finite temperature in the fully connected transverse-field ising model" *Phys. Rev. B* **97**, 174401 (2018)

B. Frank, J. Lang, and W. Zwerger "Universal phase diagram and scaling functions of imbalanced Fermi gases", *ArXiv e-prints* arXiv:1804.03035 *JETP*, **127** (5), 812 (2018) (special issue in honor of L. P. Pitaevskii's 85^{th} birthday)
For the extended abstract see: *JETP* **154** (5), 953 (2018)

J. Lang, B. Frank, and J. C. Halimeh "Dynamical quantum phase transitions: A geometric picture" *Phys. Rev. Lett.* **121**, 130603 (2018)

J. Lang, D. E. Chang, and F. Piazza "Interaction-induced transparency for strong-coupling polaritons" *ArXiv e-prints*, arXiv:1810.12912 (2018)

J. Lang, D. E. Chang, and F. Piazza "Non-equilibrium diagrammatic approach to strongly interacting photons" *ArXiv e-prints*, arXiv:1810.12921 (2018)

J. Lang and B. Frank "Fast logarithmic Fourier-Laplace transform of nonintegrable functions" *ArXiv e-prints*, arXiv:1812.09575 (2018)

References

[1] J. Léonard, A. Morales, P. Zupancic, T. Esslinger, and T. Donner. Supersolid formation in a quantum gas breaking a continuous translational symmetry. *Nature*, 543(7643):87–90, 03 2017.

[2] J. Léonard, A. Morales, P. Zupancic, T. Donner, and T. Esslinger. Monitoring and manipulating Higgs and Goldstone modes in a supersolid quantum gas. *Science*, 358(6369):1415–1418, 2017.

[3] D. E. Chang, V. Vuletic, and M. D. Lukin. Quantum nonlinear optics – photon by photon. *Nat Photon*, 8(9):685–694, 09 2014.

[4] H. J. Kimble. The quantum internet. *Nature*, 453(7198):1023–1030, 06 2008.

[5] I. Carusotto and C. Ciuti. Quantum fluids of light. *Rev. Mod. Phys.*, 85:299–366, Feb 2013.

[6] M. J. Hartmann, F. G. S. L. Brandão, and M. B. Plenio. Quantum many-body phenomena in coupled cavity arrays. *Laser & Photonics Reviews*, 2(6):527–556, 2008.

[7] M. Hafezi, P. Adhikari, and J. M. Taylor. Chemical potential for light by parametric coupling. *Phys. Rev. B*, 92:174305, Nov 2015.

[8] J. Lebreuilly, A. Biella, F. Storme, D. Rossini, R. Fazio, C. Ciuti, and I. Carusotto. Stabilizing strongly correlated photon fluids with non-Markovian reservoirs. *Phys. Rev. A*, 96:033828, Sep 2017.

[9] R. Ma, B. Saxberg, C. Owens, N. Leung, Y. Lu, J. Simon, and D. I. Schuster. A Dissipatively Stabilized Mott Insulator of Photons. *ArXiv e-prints arXiv:1807.11342*, July 2018.

[10] T. Ozawa, H. M. Price, A. Amo, N. Goldman, M. Hafezi, L. Lu, M. Rechtsman, D. Schuster, J. Simon, O. Zilberberg, and I. Carusotto. Topological Photonics. *ArXiv e-prints arXiv:1802.04173*, February 2018.

[11] J. Zhang, G. Pagano, P. W. Hess, A. Kyprianidis, P. Becker, H. Kaplan, A. V. Gorshkov, Z.-X. Gong, and C. Monroe. Observation of a many-body dynamical phase transition with a 53-qubit quantum simulator. *Nature*, 551:601, November 2017.

[12] R. Blatt and C. Roos. Quantum simulations with trapped ions. *Nature Physics*, 8(4):277–284, 2012.

[13] J. W. Britton, B. C. Sawyer, A. C. Keith, C.-C. J. Wang, J. K. Freericks, H. Uys, M. J. Biercuk, and J. J. Bollinger. Engineered two-dimensional Ising interactions in a trapped-ion quantum simulator with hundreds of spins. *Nature*, 484(7395):489–492, 2012.

[14] A. A. Houck, H. E. Türeci, and J. Koch. On-chip quantum simulation with superconducting circuits. *Nature Physics*, 8(4):292–299, 2012.

[15] S. Schmidt and J. Koch. Circuit QED lattices: towards quantum simulation with superconducting circuits. *Annalen der Physik*, 525(6):395–412, 2013.

[16] C.-L. Hung, S. M. Meenehan, D. E. Chang, O. Painter, and H. J. Kimble. Trapped atoms in one-dimensional photonic crystals. *New Journal of Physics*, 15(8):083026, 2013.

[17] A. Goban, C. L. Hung, S. P. Yu, J. D. Hood, J. A. Muniz, J. H. Lee, M. J. Martin, A. C. McClung, K. S. Choi, D. E. Chang, O. Painter, and H. J. Kimble. Atom–light interactions in photonic crystals. *Nat Commun*, 5, 05 2014.

[18] V. Parigi, E. Bimbard, J. Stanojevic, A. J. Hilliard, F. Nogrette, R. Tualle-Brouri, A. Ourjoumtsev, and P. Grangier. Observation and Measurement of Interaction-Induced Dispersive Optical Nonlinearities in an Ensemble of Cold Rydberg Atoms. *Phys. Rev. Lett.*, 109:233602, Dec 2012.

[19] Y. O. Dudin and A. Kuzmich. Strongly Interacting Rydberg Excitations of a Cold Atomic Gas. *Science*, 336(6083):887–889, 2012.

[20] O. Firstenberg, T. Peyronel, Q.-Y. Liang, A. V. Gorshkov, M. D. Lukin, and V. Vuletić. Attractive photons in a quantum nonlinear medium. *Nature*, 502:71–75, 09 2013.

[21] C. Carr, R. Ritter, C. G. Wade, C. S. Adams, and K. J. Weatherill. Nonequilibrium Phase Transition in a Dilute Rydberg Ensemble. *Phys. Rev. Lett.*, 111:113901, Sep 2013.

[22] E. Vetsch, D. Reitz, G. Sagué, R. Schmidt, S. T. Dawkins, and A. Rauschenbeutel. Optical Interface Created by Laser-Cooled Atoms Trapped in the Evanescent Field Surrounding an Optical Nanofiber. *Phys. Rev. Lett.*, 104:203603, May 2010.

[23] H. L. Sørensen, J.-B. Béguin, K. W. Kluge, I. Iakoupov, A. S. Sørensen, J. H. Müller, E. S. Polzik, and J. Appel. Coherent Backscattering of Light Off One-Dimensional Atomic Strings. *Phys. Rev. Lett.*, 117:133604, Sep 2016.

[24] N. V. Corzo, B. Gouraud, A. Chandra, A. Goban, A. S. Sheremet, D. V. Kupriyanov, and J. Laurat. Large Bragg Reflection from One-Dimensional Chains of Trapped Atoms Near a Nanoscale Waveguide. *Phys. Rev. Lett.*, 117:133603, Sep 2016.

[25] Y. Meng, A. Dareau, P. Schneeweiss, and A. Rauschenbeutel. Near-Ground-State Cooling of Atoms Optically Trapped 300 nm Away from a Hot Surface. *Phys. Rev. X*, 8:031054, Sep 2018.

[26] D. E. Chang, A. H. Safavi-Naeini, M. Hafezi, and O. Painter. Slowing and stopping light using an optomechanical crystal array. *New Journal of Physics*, 13(2):023003, 2011.

[27] J. Chan, A. H. Safavi-Naeini, J. T. Hill, S. Meenehan, and O. Painter. Optimized optomechanical crystal cavity with acoustic radiation shield. *Applied Physics Letters*, 101(8):081115, 2012.

[28] M. Kalaee, T. K. Paraïso, H. Pfeifer, and O. Painter. Design of a quasi-2D photonic crystal optomechanical cavity with tunable, large x^2-coupling. *Opt. Express*, 24(19):21308–21328, Sep 2016.

[29] K. Baumann, C. Guerlin, F. Brennecke, and T. Esslinger. Dicke quantum phase transition with a superfluid gas in an optical cavity. *Nature*, 464(7293):1301–1306, April 2010.

[30] K. Baumann, R. Mottl, F. Brennecke, and T. Esslinger. Exploring Symmetry Breaking at the Dicke Quantum Phase Transition. *Phys. Rev. Lett.*, 107:140402, Sep 2011.

[31] F. Brennecke, R. Mottl, K. Baumann, R. Landig, T. Donner, and T. Esslinger. Real-time observation of fluctuations at the driven-dissipative Dicke phase transition. *Proceedings of the National Academy of Sciences*, 110(29):11763–11767, 2013.

[32] H. Ritsch, P. Domokos, F. Brennecke, and T. Esslinger. Cold atoms in cavity-generated dynamical optical potentials. *Rev. Mod. Phys.*, 85:553–601, Apr 2013.

[33] H. Bernien, S. Schwartz, A. Keesling, H. Levine, A. Omran, H. Pichler, S. Choi, A. S. Zibrov, M. Endres, M. Greiner, V. Vuletić, and M. D. Lukin. Probing many-body dynamics on a 51-atom quantum simulator. *Nature*, 551:579, November 2017.

[34] S. Baur, D. Tiarks, G. Rempe, and S. Dürr. Single-Photon Switch Based on Rydberg Blockade. *Phys. Rev. Lett.*, 112:073901, Feb 2014.

[35] D. Tiarks, S. Schmidt-Eberle, T. Stolz, G. Rempe, and S. Dürr. A photonÂ–photon quantum gate based on Rydberg interactions. *Nature Physics*, Oct 2018.

[36] S. Sun, H. Kim, Z. Luo, G. S. Solomon, and E. Waks. A single-photon switch and transistor enabled by a solid-state quantum memory. *Science*, 361(6397):57–60, 2018.

[37] M. Heyl. Dynamical quantum phase transitions: a review. *Reports on Progress in Physics*, 81(5):054001, 2018.

[38] D. Fausti, R. I. Tobey, N. Dean, S. Kaiser, A. Dienst, M. C. Hoffmann, S. Pyon, T. Takayama, H. Takagi, and A. Cavalleri. Light-Induced Superconductivity in a Stripe-Ordered Cuprate. *Science*, 331(6014):189–191, 2011.

[39] S. Giovanazzi, D. O'Dell, and G. Kurizki. Density Modulations of Bose-Einstein Condensates via Laser-Induced Interactions. *Phys. Rev. Lett.*, 88:130402, Mar 2002.

[40] N. Henkel, R. Nath, and T. Pohl. Three-Dimensional Roton Excitations and Supersolid Formation in Rydberg-Excited Bose-Einstein Condensates. *Phys. Rev. Lett.*, 104:195302, May 2010.

[41] Y. Li, G. I. Martone, L. P. Pitaevskii, and S. Stringari. Superstripes and the Excitation Spectrum of a Spin-Orbit-Coupled Bose-Einstein Condensate. *Phys. Rev. Lett.*, 110:235302, Jun 2013.

[42] S. Ostermann, F. Piazza, and H. Ritsch. Spontaneous Crystallization of Light and Ultracold Atoms. *Phys. Rev. X*, 6:021026, May 2016.

[43] I. Carusotto, D. Gerace, H. E. Tureci, S. De Liberato, C. Ciuti, and A. Imamoğlu. Fermionized Photons in an Array of Driven Dissipative Nonlinear Cavities. *Phys. Rev. Lett.*, 103:033601, Jul 2009.

[44] L. M. Sieberer, M. Buchhold, and S. Diehl. Keldysh field theory for driven open quantum systems. *Reports on Progress in Physics*, 79(9):096001, 2016.

[45] M. Heyl, A. Polkovnikov, and S. Kehrein. Dynamical Quantum Phase Transitions in the Transverse-Field Ising Model. *Phys. Rev. Lett.*, 110:135704, Mar 2013.

[46] D. Trapin and M. Heyl. Constructing effective free energies for dynamical quantum phase transitions in the transverse-field Ising chain. *Phys. Rev. B*, 97:174303, May 2018.

[47] J. Marino and S. Diehl. Driven Markovian Quantum Criticality. *Phys. Rev. Lett.*, 116:070407, Feb 2016.

[48] I. Homrighausen, N. O. Abeling, V. Zauner-Stauber, and J. C. Halimeh. Anomalous dynamical phase in quantum spin chains with long-range interactions. *Phys. Rev. B*, 96:104436, Sep 2017.

[49] M. Eckstein, M. Kollar, and P. Werner. Thermalization after an Interaction Quench in the Hubbard Model. *Phys. Rev. Lett.*, 103:056403, Jul 2009.

[50] S. Diehl, A. Tomadin, A. Micheli, R. Fazio, and P. Zoller. Dynamical Phase Transitions and Instabilities in Open Atomic Many-Body Systems. *Phys. Rev. Lett.*, 105:015702, Jul 2010.

[51] P. Smacchia, M. Knap, E. Demler, and A. Silva. Exploring dynamical phase transitions and prethermalization with quantum noise of excitations. *Phys. Rev. B*, 91:205136, May 2015.

[52] M. Schiró and M. Fabrizio. Time-Dependent Mean Field Theory for Quench Dynamics in Correlated Electron Systems. *Phys. Rev. Lett.*, 105:076401, Aug 2010.

[53] B. Sciolla and G. Biroli. Quantum Quenches and Off-Equilibrium Dynamical Transition in the Infinite-Dimensional Bose-Hubbard Model. *Phys. Rev. Lett.*, 105:220401, Nov 2010.

[54] B. Sciolla and G. Biroli. Dynamical transitions and quantum quenches in mean-field models. *Journal of Statistical Mechanics: Theory and Experiment*, 2011(11):P11003, 2011.

[55] B. Sciolla and G. Biroli. Quantum quenches, dynamical transitions, and off-equilibrium quantum criticality. *Phys. Rev. B*, 88:201110, Nov 2013.

[56] A. Maraga, P. Smacchia, and A. Silva. Linear ramps of the mass in the $O(N)$ model: Dynamical transition and quantum noise of excitations. *Phys. Rev. B*, 94:245122, Dec 2016.

[57] B. Žunkovič, A. Silva, and M. Fabrizio. Dynamical phase transitions and Loschmidt echo in the infinite-range XY model. *Philosophical Transactions of the Royal Society of London A: Mathematical, Physical and Engineering Sciences*, 374(2069), 2016.

[58] M. Kitagawa and M. Ueda. Squeezed spin states. *Phys. Rev. A*, 47:5138–5143, Jun 1993.

[59] L. Pezzè, A. Smerzi, M. K. Oberthaler, R. Schmied, and P. Treutlein. Quantum metrology with nonclassical states of atomic ensembles. *Rev. Mod. Phys.*, 90:035005, Sep 2018.

[60] O. E. Barndorff-Nielsen and R. D. Gill. Fisher information in quantum statistics. *Journal of Physics A: Mathematical and General*, 33(24):4481, 2000.

[61] T.-L. Wang, L.-N. Wu, W. Yang, G.-R. Jin, N. Lambert, and F. Nori. Quantum Fisher information as a signature of the superradiant quantum phase transition. *New Journal of Physics*, 16(6):063039, 2014.

[62] J. Lang, B. Frank, and J. C. Halimeh. Concurrence of dynamical phase transitions at finite temperature in the fully connected transverse-field Ising model. *Phys. Rev. B*, 97:174401, May 2018.

[63] J. Lang, B. Frank, and J. C. Halimeh. Dynamical Quantum Phase Transitions: A Geometric Picture. *Phys. Rev. Lett.*, 121:130603, Sep 2018.

[64] S. Ma and M. Fung. *Statistical Mechanics*. World Scientific, 1985.

[65] S. Sachdev. *Quantum Phase Transitions*. Cambridge University Press, 2001.

[66] H. Touchette. The large deviation approach to statistical mechanics. *Physics Reports*, 478(1):1 – 69, 2009.

[67] M. Greiner, O. Mandel, T. W. Hänsch, and I. Bloch. Collapse and revival of the matter wave field of a Bose-Einstein condensate. *Nature*, 419:5154, Sep 2002.

[68] M. Heyl. Dynamical Quantum Phase Transitions in Systems with Broken-Symmetry Phases. *Phys. Rev. Lett.*, 113:205701, Nov 2014.

[69] P. Jurcevic, H. Shen, P. Hauke, C. Maier, T. Brydges, C. Hempel, B. P. Lanyon, M. Heyl, R. Blatt, and C. F. Roos. Direct Observation of Dynamical Quantum Phase Transitions in an Interacting Many-Body System. *Phys. Rev. Lett.*, 119:080501, Aug 2017.

[70] B. Žunkovič, M. Heyl, M. Knap, and A. Silva. Dynamical Quantum Phase Transitions in Spin Chains with Long-Range Interactions: Merging Different Concepts of Nonequilibrium Criticality. *Phys. Rev. Lett.*, 120:130601, Mar 2018.

[71] S. A. Weidinger, M. Heyl, A. Silva, and M. Knap. Dynamical quantum phase transitions in systems with continuous symmetry breaking. *Phys. Rev. B*, 96:134313, Oct 2017.

[72] C. Jarzynski. Nonequilibrium Equality for Free Energy Differences. *Phys. Rev. Lett.*, 78:2690–2693, Apr 1997.

[73] C. Jarzynski. Equilibrium free-energy differences from nonequilibrium measurements: A master-equation approach. *Phys. Rev. E*, 56:5018–5035, Nov 1997.

[74] G. E. Crooks. Nonequilibrium Measurements of Free Energy Differences for Microscopically Reversible Markovian Systems. *Journal of Statistical Physics*, 90(5):1481–1487, Mar 1998.

[75] G. E. Crooks. Path-ensemble averages in systems driven far from equilibrium. *Phys. Rev. E*, 61:2361–2366, Mar 2000.

[76] A. Silva. Statistics of the Work Done on a Quantum Critical System by Quenching a Control Parameter. *Phys. Rev. Lett.*, 101:120603, Sep 2008.

[77] E. Freitag and R. Busam. *Complex Analysis*. Lecture notes in mathematics. Springer, 2005.

[78] M. Schmitt and S. Kehrein. Dynamical quantum phase transitions in the kitaev honeycomb model. *Phys. Rev. B*, 92:075114, Aug 2015.

[79] T. D. Lee and C. N. Yang. Statistical Theory of Equations of State and Phase Transitions. II. Lattice Gas and Ising Model. *Phys. Rev.*, 87:410–419, Aug 1952.

[80] S. Vajna and B. Dóra. Topological classification of dynamical phase transitions. *Phys. Rev. B*, 91:155127, Apr 2015.

[81] S. Vajna and B. Dóra. Disentangling dynamical phase transitions from equilibrium phase transitions. *Phys. Rev. B*, 89:161105, Apr 2014.

[82] J. M. Hickey, S. Genway, and J. P. Garrahan. Dynamical phase transitions, time-integrated observables, and geometry of states. *Phys. Rev. B*, 89:054301, Feb 2014.

[83] Z. Huang and A. V. Balatsky. Dynamical Quantum Phase Transitions: Role of Topological Nodes in Wave Function Overlaps. *Phys. Rev. Lett.*, 117:086802, Aug 2016.

[84] S. Pancharatnam. Generalized theory of interference, and its applications. Part I. Coherent pencils. *Proc. Indian Acad. Sci. A*, 44:247, Nov 1956.

[85] J. C. Budich and M. Heyl. Dynamical topological order parameters far from equilibrium. *Phys. Rev. B*, 93:085416, Feb 2016.

[86] F. Andraschko and J. Sirker. Dynamical quantum phase transitions and the Loschmidt echo: A transfer matrix approach. *Phys. Rev. B*, 89:125120, Mar 2014.

[87] J. C. Halimeh and V. Zauner-Stauber. Dynamical phase diagram of quantum spin chains with long-range interactions. *Phys. Rev. B*, 96:134427, Oct 2017.

[88] V. Zauner-Stauber and J. C. Halimeh. Probing the anomalous dynamical phase in long-range quantum spin chains through Fisher-zero lines. *Phys. Rev. E*, 96:062118, Dec 2017.

[89] Q. Wang and H. T. Quan. Probing the excited-state quantum phase transition through statistics of Loschmidt echo and quantum work. *Phys. Rev. E*, 96:032142, Sep 2017.

[90] N. Fläschner, D. Vogel, M. Tarnowski, B. S. Rem, D.-S. Lühmann, M. Heyl, J. C. Budich, L. Mathey, K. Sengstock, and C. Weitenberg. Observation of dynamical vortices after quenches in a system with topology. *Nature Physics*, 14(3):265–268, March 2018.

[91] K. Wang, X. Qiu, L. Xiao, X. Zhan, Z. Bian, W. Yi, and P. Xue. Simulating dynamic quantum phase transitions in photonic quantum walks. *ArXiv e-prints arXiv:1806.10871*, June 2018.

[92] X.-Y. Xu, Q.-Q. Wang, M. Heyl, J. C. Budich, W.-W. Pan, Z. Chen, M. Jan, K. Sun, J.-S. Xu, Y.-J. Han, C.-F. Li, and G.-C. Guo. Measuring a Dynamical Topological Order Parameter in Quantum Walks. *ArXiv e-prints arXiv:1808.03930*, August 2018.

[93] T. Tian, Y. Ke, L. Zhang, S. Lin, Z. Shi, P. Huang, C. Lee, and J. Du. Observation of dynamical phase transitions in a topological nanomechanical system. *ArXiv e-prints arXiv:1807.04483*, July 2018.

[94] X.-Y. Guo, C. Yang, Y. Zeng, Y. Peng, H.-K. Li, H. Deng, Y.-R. Jin, S. Chen, D. Zheng, and H. Fan. Observation of dynamical quantum phase transition by a superconducting qubit simulation. *arXiv e-print arXiv:1806.09269*, June 2018.

[95] N. O. Abeling and S. Kehrein. Quantum quench dynamics in the transverse field Ising model at nonzero temperatures. *Phys. Rev. B*, 93:104302, Mar 2016.

[96] M. Heyl and J. C. Budich. Dynamical topological quantum phase transitions for mixed states. *Phys. Rev. B*, 96:180304, Nov 2017.

[97] U. Bhattacharya, S. Bandyopadhyay, and A. Dutta. Mixed state dynamical quantum phase transitions. *Phys. Rev. B*, 96:180303, Nov 2017.

[98] P. Zanardi, H. T. Quan, X. Wang, and C. P. Sun. Mixed-state fidelity and quantum criticality at finite temperature. *Phys. Rev. A*, 75:032109, Mar 2007.

[99] L. Campos Venuti, N. T. Jacobson, S. Santra, and P. Zanardi. Exact Infinite-Time Statistics of the Loschmidt Echo for a Quantum Quench. *Phys. Rev. Lett.*, 107:010403, Jul 2011.

[100] N. Sedlmayr, M. Fleischhauer, and J. Sirker. Fate of dynamical phase transitions at finite temperatures and in open systems. *Phys. Rev. B*, 97:045147, Jan 2018.

[101] M. Kac, G. E. Uhlenbeck, and P. C. Hemmer. On the van der Waals Theory of the Vapor-Liquid Equilibrium. I. Discussion of a One-Dimensional Model. *Journal of Mathematical Physics*, 4(2):216–228, 1963.

[102] A. Das, K. Sengupta, D. Sen, and B. K. Chakrabarti. Infinite-range Ising ferromagnet in a time-dependent transverse magnetic field: Quench and ac dynamics near the quantum critical point. *Phys. Rev. B*, 74:144423, Oct 2006.

[103] J. Wilms, J. Vidal, F. Verstraete, and S. Dusuel. Finite-temperature mutual information in a simple phase transition. *Journal of Statistical Mechanics: Theory and Experiment*, 2012(01):P01023, 2012.

[104] H. Lipkin, N. Meshkov, and A. Glick. Validity of many-body approximation methods for a solvable model: (I). Exact solutions and perturbation theory. *Nuclear Physics*, 62(2):188 – 198, Feb 1965.

[105] N. Meshkov, A. Glick, and H. Lipkin. Validity of many-body approximation methods for a solvable model: (II). Linearization procedures. *Nuclear Physics*, 62(2):199 – 210, Feb 1965.

[106] A. Glick, H. Lipkin, and N. Meshkov. Validity of many-body approximation methods for a solvable model: (III). Diagram summations. *Nuclear Physics*, 62(2):211 – 224, Feb 1965.

[107] R. Botet, R. Jullien, and P. Pfeuty. Size Scaling for Infinitely Coordinated Systems. *Phys. Rev. Lett.*, 49:478–481, Aug 1982.

[108] R. Botet and R. Jullien. Large-size critical behavior of infinitely coordinated systems. *Phys. Rev. B*, 28:3955–3967, Oct 1983.

[109] S. Morrison and A. S. Parkins. Dynamical Quantum Phase Transitions in the Dissipative Lipkin-Meshkov-Glick Model with Proposed Realization in Optical Cavity QED. *Phys. Rev. Lett.*, 100:040403, Jan 2008.

[110] R. Islam, C. Senko, W. C. Campbell, S. Korenblit, J. Smith, A. Lee, E. E. Edwards, C.-C. J. Wang, J. K. Freericks, and C. Monroe. Emergence and Frustration of Magnetism with Variable-Range Interactions in a Quantum Simulator. *Science*, 340(6132):583–587, 2013.

[111] B. Neyenhuis, J. Zhang, P. W. Hess, J. Smith, A. C. Lee, P. Richerme, Z.-X. Gong, A. V. Gorshkov, and C. Monroe. Observation of prethermalization in long-range interacting spin chains. *Science Advances*, 3(8), 2017.

[112] P. W. Hess, P. Becker, H. B. Kaplan, A. Kyprianidis, A. C. Lee, B. Neyenhuis, G. Pagano, P. Richerme, C. Senko, J. Smith, W. L. Tan, J. Zhang, and C. Monroe. Non-thermalization in trapped atomic ion spin chains. *Philosophical Transactions of the Royal Society of London A: Mathematical, Physical and Engineering Sciences*, 375(2108), 2017.

[113] P. Ribeiro, J. Vidal, and R. Mosseri. Exact spectrum of the Lipkin-Meshkov-Glick model in the thermodynamic limit and finite-size corrections. *Phys. Rev. E*, 78:021106, Aug 2008.

[114] B. Dóra, F. Pollmann, J. Fortágh, and G. Zaránd. Loschmidt Echo and the Many-Body Orthogonality Catastrophe in a Qubit-Coupled Luttinger Liquid. *Phys. Rev. Lett.*, 111:046402, Jul 2013.

[115] E. Canovi, P. Werner, and M. Eckstein. First-Order Dynamical Phase Transitions. *Phys. Rev. Lett.*, 113:265702, Dec 2014.

[116] T. Fogarty, A. Usui, T. Busch, A. Silva, and J. Goold. Dynamical phase transitions and temporal orthogonality in one-dimensional hard-core bosons: from the continuum to the lattice. *New Journal of Physics*, 19(11):113018, 2017.

[117] N. D. Mermin and H. Wagner. Absence of Ferromagnetism or Antiferromagnetism in One- or Two-Dimensional Isotropic Heisenberg Models. *Phys. Rev. Lett.*, 17:1133–1136, Nov 1966.

[118] W. P. Su, J. R. Schrieffer, and A. J. Heeger. Solitons in Polyacetylene. *Phys. Rev. Lett.*, 42:1698–1701, Jun 1979.

[119] A. P. Schnyder, S. Ryu, A. Furusaki, and A. W. W. Ludwig. Classification of topological insulators and superconductors in three spatial dimensions. *Phys. Rev. B*, 78:195125, Nov 2008.

[120] T. Bzdušek and M. Sigrist. Robust doubly charged nodal lines and nodal surfaces in centrosymmetric systems. *Phys. Rev. B*, 96:155105, Oct 2017.

[121] K. Gottfried and T. Yan. *Quantum Mechanics: Fundamentals*. Graduate Texts in Contemporary Physics. Springer New York, 2003.

[122] A. Messiah. *Quantum Mechanics*. Dover books on physics. Dover Publications, 1999.

[123] J. L. van Hemmen and A. Sütő. Tunneling of quantum spins. *Physica B+C*, 141(1):37 – 75, 1986.

[124] P. A. Braun. Discrete semiclassical methods in the theory of Rydberg atoms in external fields. *Rev. Mod. Phys.*, 65:115–161, Jan 1993.

[125] J. L. van Hemmen and A. Sütő. WKB for quantum spins. *Physica A: Statistical Mechanics and its Applications*, 321(3):493 – 497, 2003.

[126] A. Polkovnikov. Phase space representation of quantum dynamics. *Annals of Physics*, 325(8):1790 – 1852, 2010.

[127] Video of an anomalous quench at $T = 0$. `https://youtu.be/gE72RBlWZ-c`, 2018.

[128] Video of a regular quench at $T = 0$. `https://youtu.be/fUueTOyI2S4`, 2018.

[129] Video of an anomalous quench at finite temperature. `https://youtu.be/e8JhRAY-qbg`, 2018.

[130] Video of a quench at zero temperature in the XX model. `https://youtu.be/IcRo4hnX_iI`, 2018.

[131] M. Heyl. Scaling and Universality at Dynamical Quantum Phase Transitions. *Phys. Rev. Lett.*, 115:140602, Oct 2015.

[132] T. D. Ladd, F. Jelezko, R. Laflamme, Y. Nakamura, C. Monroe, and J. L. O'Brien. Quantum computers. *Nature*, 464:45 EP –, Mar 2010. Review Article.

[133] J. I. Cirac and P. Zoller. Goals and opportunities in quantum simulation. *Nature Physics*, 8:264, Apr 2012.

[134] I. M. Georgescu, S. Ashhab, and F. Nori. Quantum simulation. *Rev. Mod. Phys.*, 86:153–185, Mar 2014.

[135] B. M. Escher, R. L. d. Matos Filho, and L. Davidovich. General framework for estimating the ultimate precision limit in noisy quantum-enhanced metrology. *Nature Physics*, 7:406–411, 2011.

[136] L. Pezzè and A. Smerzi. Quantum theory of phase estimation. In G. M. Tino and M. A. Kasevich, editors, *Atom Interferometry, Proceedings of the International School of Physics 'Enrico Fermi', Course 188, Varenna, July 2013*, pages 691 – 741. IOS Press, Amsterdam, 2014.

[137] R. Islam, R. Ma, P. M. Preiss, M. Eric Tai, A. Lukin, M. Rispoli, and M. Greiner. Measuring entanglement entropy in a quantum many-body system. *Nature*, 528:77 EP –, Dec 2015. Article.

[138] P. Hauke, M. Heyl, L. Tagliacozzo, and P. Zoller. Measuring multipartite entanglement through dynamic susceptibilities. *Nature Physics*, 12:778–782, August 2016.

[139] P. Hyllus, W. Laskowski, R. Krischek, C. Schwemmer, W. Wieczorek, H. Weinfurter, L. Pezzé, and A. Smerzi. Fisher information and multiparticle entanglement. *Phys. Rev. A*, 85:022321, Feb 2012.

[140] G. Tóth. Multipartite entanglement and high-precision metrology. *Phys. Rev. A*, 85:022322, Feb 2012.

[141] A. Holevo. *Probabilistic and Statistical Aspects of Quantum Theory*. Publications of the Scuola Normale Superiore. Scuola Normale Superiore, 2011.

[142] D. Leibfried, M. D. Barrett, T. Schaetz, J. Britton, J. Chiaverini, W. M. Itano, J. D. Jost, C. Langer, and D. J. Wineland. Toward Heisenberg-Limited Spectroscopy with Multiparticle Entangled States. *Science*, 304(5676):1476–1478, 2004.

[143] B. L. Higgins, D. W. Berry, S. D. Bartlett, H. M. Wiseman, and G. J. Pryde. Entanglement-free Heisenberg-limited phase estimation. *Nature*, 450:393 EP –, Nov 2007.

[144] T. Nagata, R. Okamoto, J. L. O'Brien, K. Sasaki, and S. Takeuchi. Beating the Standard Quantum Limit with Four-Entangled Photons. *Science*, 316(5825):726–729, 2007.

[145] L. J. Fiderer and D. Braun. Quantum metrology with quantum-chaotic sensors. *Nature Communications*, 9(1351), 2018.

[146] S. L. Braunstein and C. M. Caves. Statistical distance and the geometry of quantum states. *Phys. Rev. Lett.*, 72:3439–3443, May 1994.

[147] J. Lang, F. Piazza, and W. Zwerger. Collective excitations and supersolid behavior of bosonic atoms inside two crossed optical cavities. *New Journal of Physics*, 19(12):123027, 2017.

[148] M. Boninsegni and N. V. Prokof'ev. Colloquium: Supersolids: What and where are they? *Reviews of Modern Physics*, 84:759–776, April 2012.

[149] O. Penrose and L. Onsager. Bose-Einstein Condensation and Liquid Helium. *Phys. Rev.*, 104:576–584, Nov 1956.

[150] E. P. Gross. Unified Theory of Interacting Bosons. *Phys. Rev.*, 106:161–162, Apr 1957.

[151] E. Gross. Classical theory of boson wave fields. *Annals of Physics*, 4(1):57 – 74, 1958.

[152] M. W. Ray and R. B. Hallock. Observation of unusual mass transport in solid hcp ^{4}He. *Phys. Rev. Lett.*, 100:235301, Jun 2008.

[153] M. W. Ray and R. B. Hallock. Observation of mass transport through solid ^{4}He. *Phys. Rev. B*, 79:224302, Jun 2009.

[154] P. Fulde and R. Ferrell. Superconductivity in a Strong Spin-Exchange Field. *Phys. Rev.*, 135:A550, 1964.

[155] A. Larkin and Y. Ovchinnikov. Inhomogeneous state of superconductors. *Zh. Eksp. Teor. Fiz.*, 47:1136, 1964.

[156] A. F. Andreev and I. M. Lifshitz. Quantum Theory of Defects in Crystals. *Sov. Phys. JETP*, 29:1107, Dec 1969.

[157] G. V. Chester. Speculations on Bose-Einstein Condensation and Quantum Crystals. *Phys. Rev. A*, 2:256–258, Jul 1970.

[158] A. Leggett. *Quantum Liquids: Bose Condensation and Cooper Pairing in Condensed-matter Systems*. Oxford graduate texts in mathematics. Oxford University Press, 2006.

[159] M. W. Meisel. Supersolid ^{4}He: an overview of past searches and future possibilities. *Physica B: Condensed Matter*, 178(1):121 – 128, 1992. Proceedings of the Körber Symposium on Superfluid ^{3}He in Rotation.

[160] E. Kim and M. H. W. Chan. Probable observation of a supersolid helium phase. *Nature*, 427:225–227, 2004.

[161] E. Kim and M. H. W. Chan. Observation of Superflow in Solid Helium. *Science*, 305(5692):1941–1944, 2004.

[162] A. J. Leggett. Can a Solid Be "Superfluid"? *Phys. Rev. Lett.*, 25:1543–1546, Nov 1970.

[163] M. Boninsegni, A. B. Kuklov, L. Pollet, N. V. Prokof'ev, B. V. Svistunov, and M. Troyer. Fate of Vacancy-Induced Supersolidity in ^{4}He. *Phys. Rev. Lett.*, 97:080401, Aug 2006.

[164] E. Burovski, E. Kozik, A. Kuklov, N. Prokof'ev, and B. Svistunov. Superfluid Interfaces in Quantum Solids. *Phys. Rev. Lett.*, 94:165301, Apr 2005.

[165] E. Kim and M. H. W. Chan. Supersolid Helium at High Pressure. *Phys. Rev. Lett.*, 97:115302, Sep 2006.

[166] A. S. C. Rittner and J. D. Reppy. Observation of Classical Rotational Inertia and Nonclassical Supersolid Signals in Solid ^{4}He below 250 mK. *Phys. Rev. Lett.*, 97:165301, Oct 2006.

[167] A. Penzev, Y. Yasuta, and M. Kubota. Annealing Effect for Supersolid Fraction in ^{4}He. *Journal of Low Temperature Physics*, 148(5):677–681, Sep 2007.

[168] B. Spivak and S. A. Kivelson. Phases intermediate between a two-dimensional electron liquid and Wigner crystal. *Phys. Rev. B*, 70:155114, Oct 2004.

[169] J.-R. Li, J. Lee, W. Huang, S. Burchesky, B. Shteynas, F. Ç. Top, A. O. Jamison, and W. Ketterle. A stripe phase with supersolid properties in spin–orbit-coupled Bose–Einstein condensates. *Nature*, 543(7643):91–94, 03 2017.

[170] I. Dimitrova, W. Lunden, J. Amato-Grill, N. Jepsen, Y. Yu, M. Messer, T. Rigaldo, G. Puentes, D. Weld, and W. Ketterle. Observation of two-beam collective scattering phenomena in a Bose-Einstein condensate. *Phys. Rev. A*, 96:051603, Nov 2017.

[171] F. Mivehvar, S. Ostermann, F. Piazza, and H. Ritsch. Driven-Dissipative Supersolid in a Ring Cavity. *Phys. Rev. Lett.*, 120:123601, Mar 2018.

[172] S. Ostermann, H.-W. Lau, H. Ritsch, and F. Mivehvar. Cavity-induced emergent topological spin textures in a Bose Einstein condensate. *ArXiv e-prints arXiv:1807.03316*, July 2018.

[173] A. T. Black, H. W. Chan, and V. Vuletić. Observation of Collective Friction Forces due to Spatial Self-Organization of Atoms: From Rayleigh to Bragg Scattering. *Phys. Rev. Lett.*, 91:203001, Nov 2003.

[174] R. H. Dicke. Coherence in Spontaneous Radiation Processes. *Phys. Rev.*, 93:99–110, Jan 1954.

[175] K. Hepp and E. H. Lieb. On the superradiant phase transition for molecules in a quantized radiation field: the dicke maser model. *Annals of Physics*, 76(2):360 – 404, 1973.

[176] Y. K. Wang and F. T. Hioe. Phase Transition in the Dicke Model of Superradiance. *Phys. Rev. A*, 7:831–836, Mar 1973.

[177] D. Nagy, G. Kónya, G. Szirmai, and P. Domokos. Dicke-Model Phase Transition in the Quantum Motion of a Bose-Einstein Condensate in an Optical Cavity. *Phys. Rev. Lett.*, 104:130401, Apr 2010.

[178] F. Piazza, P. Strack, and W. Zwerger. Bose-Einstein condensation versus Dicke-Hepp-Lieb transition in an optical cavity. *Annals of Physics*, 339:135 – 159, 2013.

[179] A. U. J. Lode and C. Bruder. Fragmented Superradiance of a Bose-Einstein Condensate in an Optical Cavity. *Phys. Rev. Lett.*, 118:013603, Jan 2017.

[180] H. Wagner. Long-wavelength excitations and the Goldstone theorem in many-particle systems with "broken symmetries". *Zeitschrift fur Physik*, 195:273–299, June 1966.

[181] M. Liu. Two possible types of superfluidity in crystals. *Phys. Rev. B*, 18:1165–1176, Aug 1978.

[182] S. Safaei, C. Miniatura, and B. Grémaud. Triangular and honeycomb lattices of cold atoms in optical cavities. *Phys. Rev. A*, 92:043810, Oct 2015.

[183] S. Gopalakrishnan, Y. E. Shchadilova, and E. Demler. Intertwined and vestigial order with ultracold atoms in multiple cavity modes. *Phys. Rev. A*, 96:063828, Dec 2017.

[184] D. Pekker and C. Varma. Amplitude/Higgs Modes in Condensed Matter Physics. *Annual Review of Condensed Matter Physics*, 6(1):269–297, 2015.

[185] F. Piazza and P. Strack. Quantum kinetics of ultracold fermions coupled to an optical resonator. *Phys. Rev. A*, 90:043823, Oct 2014.

[186] J. Lang, D. Chang, and F. Piazza. Interaction-induced transparency for strong-coupling polaritons. *ArXiv e-print arXiv:1810.12912*, 2018.

[187] J. Lang, D. Chang, and F. Piazza. Non-equilibrium diagrammatic approach to strongly interacting photons. *ArXiv e-print arXiv:1810.12921*, 2018.

[188] A. Fetter and J. Walecka. *Quantum Theory of Many-particle Systems*. Dover Books on Physics. Dover Publications, 2003.

[189] A. Abrikosov. *Fundamentals of the Theory of Metals*. North-Holland, 1988.

[190] J. Schwinger. Brownian Motion of a Quantum Oscillator. *Journal of Mathematical Physics*, 2(3):407–432, 1961.

[191] O. V. Konstantinov and V. I. Perel'. A Diagram Technique for Evaluating Transport Quantities. *Journal of Experimental and Theoretical Physics*, 12(1):142, 1961.

[192] L. Kadanoff and G. Baym. *Quantum statistical mechanics: Green's function methods in equilibrium and nonequilibrium problems*. Frontiers in physics. W.A. Benjamin, 1962.

[193] L. V. Keldysh. Diagram Technique for Nonequilibrium Processes. *Journal of Experimental and Theoretical Physics*, 20(4):1018, 1965.

[194] T. Matsubara. A New Approach to Quantum-Statistical Mechanics. *Progress of Theoretical Physics*, 14(4):351–378, 1955.

[195] R. Kubo. Statistical-Mechanical Theory of Irreversible Processes. I. General Theory and Simple Applications to Magnetic and Conduction Problems. *Journal of the Physical Society of Japan*, 12(6):570–586, 1957.

[196] I. Bloch, J. Dalibard, and W. Zwerger. Many-body physics with ultracold gases. *Rev. Mod. Phys.*, 80:885–964, Jul 2008.

[197] A. Kamenev. *Field Theory of Non-Equilibrium Systems*. Cambridge University Press, 2011.

[198] M.-A. Lemonde and A. A. Clerk. Real photons from vacuum fluctuations in optomechanics: The role of polariton interactions. *Phys. Rev. A*, 91:033836, Mar 2015.

[199] M.-A. Lemonde, N. Didier, and A. A. Clerk. Enhanced nonlinear interactions in quantum optomechanics via mechanical amplification. *Nature Communications*, 7(11338), 2016.

[200] S. Jeon. Hydrodynamic transport coefficients in relativistic scalar field theory. *Phys. Rev. D*, 52:3591–3642, Sep 1995.

[201] S. Jeon and L. G. Yaffe. From quantum field theory to hydrodynamics: Transport coefficients and effective kinetic theory. *Phys. Rev. D*, 53:5799–5809, May 1996.

[202] J. Berges. Introduction to Nonequilibrium Quantum Field Theory. *AIP Conference Proceedings*, 739(1):3–62, 2004.

[203] J. M. Deutsch. Quantum statistical mechanics in a closed system. *Phys. Rev. A*, 43:2046–2049, Feb 1991.

[204] M. Srednicki. Chaos and quantum thermalization. *Phys. Rev. E*, 50:888–901, Aug 1994.

[205] H. Mori. Transport, Collective Motion, and Brownian Motion. *Progress of Theoretical Physics*, 33(3):423–455, 1965.

[206] P. Degenfeld-Schonburg and M. J. Hartmann. Self-consistent projection operator theory for quantum many-body systems. *Phys. Rev. B*, 89:245108, Jun 2014.

[207] M. Wagner. Expansions of nonequilibrium Green's functions. *Phys. Rev. B*, 44:6104–6117, Sep 1991.

[208] R. K. Bryan. Maximum entropy analysis of oversampled data problems. *European Biophysics Journal*, 18(3):165–174, Apr 1990.

[209] M. Jarrell and J. Gubernatis. Bayesian inference and the analytic continuation of imaginary-time quantum Monte Carlo data. *Physics Reports*, 269(3):133 – 195, 1996.

[210] J. Maciejko. *An Introduction to Nonequilibrium Many-Body Theory.* North-Holland, Oct. 2007.

[211] P. C. Martin and J. Schwinger. Theory of Many-Particle Systems. I. *Phys. Rev.*, 115:1342–1373, Sep 1959.

[212] R. Feynman and F. Vernon. The theory of a general quantum system interacting with a linear dissipative system. *Annals of Physics*, 24:118 – 173, 1963.

[213] N. Janssen and W. Zwerger. Quantum Brownian motion in a one-dimensional disordered system. *Zeitschrift für Physik B Condensed Matter*, 83(3):441–446, Oct 1991.

[214] E. G. Dalla Torre, Y. Shchadilova, E. Y. Wilner, M. D. Lukin, and E. Demler. Dicke phase transition without total spin conservation. *Phys. Rev. A*, 94:061802, Dec 2016.

[215] J. M. Luttinger and J. C. Ward. Ground-State Energy of a Many-Fermion System. II. *Phys. Rev.*, 118:1417–1427, Jun 1960.

[216] M. Potthoff. Non-perturbative construction of the Luttinger-Ward functional. *Condensed Matter Physics*, 9:557, Feb 2006.

[217] G. Baym and L. P. Kadanoff. Conservation Laws and Correlation Functions. *Phys. Rev.*, 124:287–299, Oct 1961.

[218] G. Baym. Self-Consistent Approximations in Many-Body Systems. *Phys. Rev.*, 127:1391–1401, Aug 1962.

[219] L. Onsager and S. Machlup. Fluctuations and irreversible processes. *Phys. Rev.*, 91:1505–1512, Sep 1953.

[220] P. C. Martin, E. D. Siggia, and H. A. Rose. Statistical Dynamics of Classical Systems. *Phys. Rev. A*, 8:423–437, Jul 1973.

[221] A. V. Turukhin, V. S. Sudarshanam, M. S. Shahriar, J. A. Musser, B. S. Ham, and P. R. Hemmer. Observation of Ultraslow and Stored Light Pulses in a Solid. *Phys. Rev. Lett.*, 88:023602, Dec 2001.

[222] K.-J. Boller, A. Imamoğlu, and S. E. Harris. Observation of electromagnetically induced transparency. *Phys. Rev. Lett.*, 66:2593–2596, May 1991.

[223] B. Dalton and P. Knight. Population trapping and ultranarrow Raman lineshapes induced by phase-fluctuating fields. *Optics Communications*, 42(6):411 – 416, 1982.

[224] S. E. Harris, J. E. Field, and A. Imamoğlu. Nonlinear optical processes using electromagnetically induced transparency. *Phys. Rev. Lett.*, 64:1107–1110, Mar 1990.

[225] G. Z. Zhang, K. Hakuta, and B. P. Stoicheff. Nonlinear optical generation using electromagnetically induced transparency in atomic hydrogen. *Phys. Rev. Lett.*, 71:3099–3102, Nov 1993.

[226] G. Z. Zhang, M. Katsuragawa, K. Hakuta, R. I. Thompson, and B. P. Stoicheff. Sum-frequency generation using strong-field coupling and induced transparency in atomic hydrogen. *Phys. Rev. A*, 52:1584–1593, Aug 1995.

[227] M. Jain, H. Xia, G. Y. Yin, A. J. Merriam, and S. E. Harris. Efficient Nonlinear Frequency Conversion with Maximal Atomic Coherence. *Phys. Rev. Lett.*, 77:4326–4329, Nov 1996.

[228] K. Hakuta, M. Suzuki, M. Katsuragawa, and J. Z. Li. Self-Induced Phase Matching in Parametric Anti-Stokes Stimulated Raman Scattering. *Phys. Rev. Lett.*, 79:209–212, Jul 1997.

[229] G. Alzetta, A. Gozzini, L. Moi, and G. Orriols. An experimental method for the observation of r.f. transitions and laser beat resonances in oriented Na vapour. *Il Nuovo Cimento B*, 36:5–20, Nov 1976.

[230] J. R. Kuklinski, U. Gaubatz, F. T. Hioe, and K. Bergmann. Adiabatic population transfer in a three-level system driven by delayed laser pulses. *Phys. Rev. A*, 40:6741–6744, Dec 1989.

[231] U. Gaubatz, P. Rudecki, S. Schiemann, and K. Bergmann. Population transfer between molecular vibrational levels by stimulated Raman scattering with partially overlapping laser fields. A new concept and experimental results. *The Journal of Chemical Physics*, 92(9):5363–5376, 1990.

[232] M. Fleischhauer and M. D. Lukin. Dark-State Polaritons in Electromagnetically Induced Transparency. *Phys. Rev. Lett.*, 84:5094–5097, May 2000.

[233] M. Fleischhauer, A. Imamoglu, and J. P. Marangos. Electromagnetically induced transparency: Optics in coherent media. *Rev. Mod. Phys.*, 77:633–673, Jul 2005.

[234] D. Budker, D. F. Kimball, S. M. Rochester, and V. V. Yashchuk. Nonlinear Magneto-optics and Reduced Group Velocity of Light in Atomic Vapor with Slow Ground State Relaxation. *Phys. Rev. Lett.*, 83:1767–1770, Aug 1999.

[235] C. Liu, Z. Dutton, C. H. Behroozi, and L. V. Hau. Observation of coherent optical information storage in an atomic medium using halted light pulses. *Nature*, 409:490, January 2001.

[236] D. F. Phillips, A. Fleischhauer, A. Mair, R. L. Walsworth, and M. D. Lukin. Storage of Light in Atomic Vapor. *Phys. Rev. Lett.*, 86:783–786, Jan 2001.

[237] M. Bajcsy, A. S. Zibrov, and M. D. Lukin. Stationary pulses of light in an atomic medium. *Nature*, 426:638–641, 2003.

[238] O. Firstenberg, C. S. Adams, and S. Hofferberth. Nonlinear quantum optics mediated by Rydberg interactions. *Journal of Physics B: Atomic, Molecular and Optical Physics*, 49(15):152003, 2016.

[239] M. Kiffner and M. J. Hartmann. Dissipation-induced correlations in one-dimensional bosonic systems. *New Journal of Physics*, 13(5):053027, 2011.

[240] E. Zeuthen, M. J. Gullans, M. F. Maghrebi, and A. V. Gorshkov. Correlated Photon Dynamics in Dissipative Rydberg Media. *Phys. Rev. Lett.*, 119:043602, Jul 2017.

[241] A. V. Gorshkov, J. Otterbach, M. Fleischhauer, T. Pohl, and M. D. Lukin. Photon-Photon Interactions via Rydberg Blockade. *Phys. Rev. Lett.*, 107:133602, Sep 2011.

[242] P. Bienias, S. Choi, O. Firstenberg, M. Maghrebi, M. Gullans, M. D. Lukin, A. V. Gorshkov, and H. Büchler. Scattering resonances and bound states for strongly interacting Rydberg polaritons. *Physical Review A*, 90(5):053804, 2014.

[243] T. Caneva, M. T. Manzoni, T. Shi, J. S. Douglas, J. I. Cirac, and D. E. Chang. Quantum dynamics of propagating photons with strong interactions: a generalized input–output formalism. *New Journal of Physics*, 17(11):113001, 2015.

[244] T. Shi, D. E. Chang, and J. I. Cirac. Multiphoton-scattering theory and generalized master equations. *Physical Review A*, 92(5):053834, 2015.

[245] M. Moos, M. Höning, R. Unanyan, and M. Fleischhauer. Many-body physics of Rydberg dark-state polaritons in the strongly interacting regime. *Phys. Rev. A*, 92:053846, Nov 2015.

[246] M. J. Gullans, J. D. Thompson, Y. Wang, Q.-Y. Liang, V. Vuletić, M. D. Lukin, and A. V. Gorshkov. Effective Field Theory for Rydberg Polaritons. *Phys. Rev. Lett.*, 117:113601, Sep 2016.

[247] P. Bienias, J. Douglas, A. Paris-Mandoki, P. Titum, I. Mirgorodskiy, C. Tresp, E. Zeuthen, M. J. Gullans, M. Manzoni, S. Hofferberth, D. Chang, and A. Gorshkov. Photon propagation through dissipative Rydberg media at large input rates. *ArXiv e-print arXiv:1807.07586*, July 2018.

[248] G. Nikoghosyan and M. Fleischhauer. Photon-Number Selective Group Delay in Cavity Induced Transparency. *Phys. Rev. Lett.*, 105:013601, Jun 2010.

[249] S. Mahmoodian, M. Čepulkovskis, S. Das, P. Lodahl, K. Hammerer, and A. S. Sørensen. Strongly Correlated Photon Transport in Waveguide Quantum Electrodynamics with Weakly Coupled Emitters. *Phys. Rev. Lett.*, 121:143601, Oct 2018.

[250] J. S. Douglas, H. Habibian, C. L. Hung, A. V. Gorshkov, H. J. Kimble, and D. E. Chang. Quantum many-body models with cold atoms coupled to photonic crystals. *Nat Photon*, 9(5):326–331, 05 2015.

[251] C. S. Hofmann, G. Günter, H. Schempp, M. Robert-de Saint-Vincent, M. Gärttner, J. Evers, S. Whitlock, and M. Weidemüller. Sub-Poissonian Statistics of Rydberg-Interacting Dark-State Polaritons. *Phys. Rev. Lett.*, 110:203601, May 2013.

[252] M. Fleischhauer and M. D. Lukin. Quantum memory for photons: Dark-state polaritons. *Phys. Rev. A*, 65:022314, Jan 2002.

[253] M. Bajcsy, S. Hofferberth, V. Balic, T. Peyronel, M. Hafezi, A. S. Zibrov, V. Vuletic, and M. D. Lukin. Efficient All-Optical Switching Using Slow Light within a Hollow Fiber. *Phys. Rev. Lett.*, 102:203902, May 2009.

[254] J. S. Douglas, T. Caneva, and D. E. Chang. Photon Molecules in Atomic Gases Trapped Near Photonic Crystal Waveguides. *Phys. Rev. X*, 6:031017, Aug 2016.

[255] A. Asenjo-Garcia, M. Moreno-Cardoner, A. Albrecht, H. J. Kimble, and D. E. Chang. Exponential Improvement in Photon Storage Fidelities Using Subradiance and "Selective Radiance" in Atomic Arrays. *Phys. Rev. X*, 7:031024, Aug 2017.

[256] J. D. Thompson, T. G. Tiecke, N. P. de Leon, J. Feist, A. V. Akimov, M. Gullans, A. S. Zibrov, V. Vuletić, and M. D. Lukin. Coupling a Single Trapped Atom to a Nanoscale Optical Cavity. *Science*, 340(6137):1202–1205, 2013.

[257] M. Endres, H. Bernien, A. Keesling, H. Levine, E. R. Anschuetz, A. Krajenbrink, C. Senko, V. Vuletic, M. Greiner, and M. D. Lukin. Atom-by-atom assembly of defect-free one-dimensional cold atom arrays. *Science*, 2016.

[258] Y. Shchadilova, M. M. Roses, E. G. Dalla Torre, M. D. Lukin, and E. Demler. Fermionic formalism for driven-dissipative multi-level systems. *ArXiv e-prints arXiv:1804.03543*, April 2018.

[259] T. Byrnes, N. Y. Kim, and Y. Yamamoto. Exciton-polariton condensates. *Nature Physics*, 10:803, October 2014.

[260] S.-P. Yu, J. D. Hood, J. A. Muniz, M. J. Martin, R. Norte, C.-L. Hung, S. M. Meenehan, J. D. Cohen, O. Painter, and H. J. Kimble. Nanowire photonic crystal waveguides for single-atom trapping and strong light-matter interactions. *Applied Physics Letters*, 104(11):111103, 2014.

[261] M. Buchhold, P. Strack, S. Sachdev, and S. Diehl. Dicke-model quantum spin and photon glass in optical cavities: Nonequilibrium theory and experimental signatures. *Phys. Rev. A*, 87:063622, Jun 2013.

[262] S. Ma. *Modern Theory Of Critical Phenomena*. Advanced Books Classics. Avalon Publishing, 2000.

[263] J. Lang and F. Piazza. Critical relaxation with overdamped quasiparticles in open quantum systems. *Phys. Rev. A*, 94:033628, Sep 2016.

[264] A. Graps. An Introduction to Wavelets. *IEEE Comput. Sci. Eng.*, 2(2):50–61, June 1995.

[265] H. Smith and H. Jensen. *Transport Phenomena*. Oxford science publications. Clarendon Press, 1989.

[266] A. Altland and F. Haake. Equilibration and macroscopic quantum fluctuations in the Dicke model. *New Journal of Physics*, 14(7):073011, 2012.

[267] J. Jäckle. *Einführung in die Transporttheorie*. Vieweg, Braunschweig, 1978.

[268] O. Rioul and M. Vetterli. Wavelets and signal processing. *IEEE Signal Processing Magazine*, 8(4):14–38, Oct 1991.

[269] S. Broughton and K. Bryan. *Discrete Fourier Analysis and Wavelets: Applications to Signal and Image Processing*. Wiley, 2009.

[270] A. Polkovnikov, K. Sengupta, A. Silva, and M. Vengalattore. *Colloquium* : Nonequilibrium dynamics of closed interacting quantum systems. *Rev. Mod. Phys.*, 83:863–883, Aug 2011.

[271] J. Eisert, M. Friesdorf, and C. Gogolin. Quantum many-body systems out of equilibrium. *Nat Phys*, 11(2):124–130, 02 2015.

[272] S. Diehl, A. Micheli, A. Kantian, B. Kraus, H. Büchler, and P. Zoller. Quantum states and phases in driven open quantum systems with cold atoms. *Nature Physics*, 4(11):878–883, 2008.

[273] P. C. Hohenberg and B. I. Halperin. Theory of dynamic critical phenomena. *Reviews of Modern Physics*, 49(3):435, 1977.

[274] P. Calabrese and A. Gambassi. Ageing properties of critical systems. *Journal of Physics A: Mathematical and General*, 38(18):R133, 2005.

[275] A. Mitra, S. Takei, Y. B. Kim, and A. J. Millis. Nonequilibrium Quantum Criticality in Open Electronic Systems. *Phys. Rev. Lett.*, 97:236808, Dec 2006.

[276] D. Patanè, A. Silva, L. Amico, R. Fazio, and G. E. Santoro. Adiabatic Dynamics in Open Quantum Critical Many-Body Systems. *Phys. Rev. Lett.*, 101:175701, Oct 2008.

[277] E. G. Dalla Torre, E. Demler, T. Giamarchi, and E. Altman. Quantum critical states and phase transitions in the presence of non-equilibrium noise. *Nat Phys*, 6(10):806–810, 10 2010.

[278] J. Klaers, J. Schmitt, F. Vewinger, and M. Weitz. Bose-Einstein condensation of photons in an optical microcavity. *Nature*, 468(7323):545–548, 11 2010.

[279] E. M. Kessler, G. Giedke, A. Imamoglu, S. F. Yelin, M. D. Lukin, and J. I. Cirac. Dissipative phase transition in a central spin system. *Phys. Rev. A*, 86:012116, Jul 2012.

[280] P. Kirton and J. Keeling. Nonequilibrium model of photon condensation. *Physical review letters*, 111(10):100404, 2013.

[281] L. M. Sieberer, S. D. Huber, E. Altman, and S. Diehl. Dynamical Critical Phenomena in Driven-Dissipative Systems. *Phys. Rev. Lett.*, 110:195301, May 2013.

[282] U. C. Täuber and S. Diehl. Perturbative Field-Theoretical Renormalization Group Approach to Driven-Dissipative Bose-Einstein Criticality. *Phys. Rev. X*, 4:021010, Apr 2014.

[283] L. Bonnes, D. Charrier, and A. M. Läuchli. Dynamical and steady-state properties of a Bose-Hubbard chain with bond dissipation: A study based on matrix product operators. *Phys. Rev. A*, 90:033612, Sep 2014.

[284] M. Marcuzzi, E. Levi, S. Diehl, J. P. Garrahan, and I. Lesanovsky. Universal Nonequilibrium Properties of Dissipative Rydberg Gases. *Phys. Rev. Lett.*, 113:210401, Nov 2014.

[285] M. Hoening, W. Abdussalam, M. Fleischhauer, and T. Pohl. Antiferromagnetic long-range order in dissipative Rydberg lattices. *Phys. Rev. A*, 90:021603, Aug 2014.

[286] M. V. Medvedyeva, M. T. Čubrović, and S. Kehrein. Dissipation-induced first-order decoherence phase transition in a noninteracting fermionic system. *Phys. Rev. B*, 91:205416, May 2015.

[287] R. Labouvie, B. Santra, S. Heun, and H. Ott. Bistability in a Driven-Dissipative Superfluid. *Phys. Rev. Lett.*, 116:235302, Jun 2016.

[288] M. F. Maghrebi and A. V. Gorshkov. Nonequilibrium many-body steady states via Keldysh formalism. *Phys. Rev. B*, 93:014307, Jan 2016.

[289] J. Marino and A. Silva. Relaxation, prethermalization, and diffusion in a noisy quantum Ising chain. *Phys. Rev. B*, 86:060408, Aug 2012.

[290] N. Sedlmayr, J. Ren, F. Gebhard, and J. Sirker. Closed and Open System Dynamics in a Fermionic Chain with a Microscopically Specified Bath: Relaxation and Thermalization. *Phys. Rev. Lett.*, 110:100406, Mar 2013.

[291] Z. Cai and T. Barthel. Algebraic versus Exponential Decoherence in Dissipative Many-Particle Systems. *Phys. Rev. Lett.*, 111:150403, Oct 2013.

[292] B. Horstmann, J. I. Cirac, and G. Giedke. Noise-driven dynamics and phase transitions in fermionic systems. *Phys. Rev. A*, 87:012108, Jan 2013.

[293] M. Foss-Feig, K. R. A. Hazzard, J. J. Bollinger, and A. M. Rey. Nonequilibrium dynamics of arbitrary-range Ising models with decoherence: An exact analytic solution. *Phys. Rev. A*, 87:042101, Apr 2013.

[294] P. Gagel, P. P. Orth, and J. Schmalian. Universal Postquench Prethermalization at a Quantum Critical Point. *Phys. Rev. Lett.*, 113:220401, Nov 2014.

[295] S. Schütz and G. Morigi. Prethermalization of Atoms Due to Photon-Mediated Long-Range Interactions. *Phys. Rev. Lett.*, 113:203002, Nov 2014.

[296] S. Schütz, S. B. Jäger, and G. Morigi. Thermodynamics and dynamics of atomic self-organization in an optical cavity. *Phys. Rev. A*, 92:063808, Dec 2015.

[297] B. Sciolla, D. Poletti, and C. Kollath. Two-Time Correlations Probing the Dynamics of Dissipative Many-Body Quantum Systems: Aging and Fast Relaxation. *Phys. Rev. Lett.*, 114:170401, Apr 2015.

[298] M. Buchhold and S. Diehl. Nonequilibrium universality in the heating dynamics of interacting Luttinger liquids. *Phys. Rev. A*, 92:013603, Jul 2015.

[299] M. Ludwig and F. Marquardt. Quantum many-body dynamics in optomechanical arrays. *Physical review letters*, 111(7):073603, 2013.

[300] F. Dimer, B. Estienne, A. S. Parkins, and H. J. Carmichael. Proposed realization of the Dicke-model quantum phase transition in an optical cavity QED system. *Phys. Rev. A*, 75:013804, Jan 2007.

[301] J. Keeling, M. J. Bhaseen, and B. D. Simons. Collective Dynamics of Bose-Einstein Condensates in Optical Cavities. *Phys. Rev. Lett.*, 105:043001, Jul 2010.

[302] M. J. Bhaseen, J. Mayoh, B. D. Simons, and J. Keeling. Dynamics of nonequilibrium Dicke models. *Phys. Rev. A*, 85:013817, Jan 2012.

[303] B. Öztop, M. Bordyuh, O. E. Müstecaplioglu, and H. E. Türeci. Excitations of optically driven atomic condensate in a cavity: theory of photodetection measurements. *New Journal of Physics*, 14(8):085011, 2012.

[304] G. Kónya, D. Nagy, G. Szirmai, and P. Domokos. Finite-size scaling in the quantum phase transition of the open-system Dicke model. *Phys. Rev. A*, 86:013641, Jul 2012.

[305] D. Nagy, G. Szirmai, and P. Domokos. Critical exponent of a quantum-noise-driven phase transition: The open-system Dicke model. *Phys. Rev. A*, 84:043637, Oct 2011.

[306] E. G. D. Torre, S. Diehl, M. D. Lukin, S. Sachdev, and P. Strack. Keldysh approach for nonequilibrium phase transitions in quantum optics: Beyond the Dicke model in optical cavities. *Phys. Rev. A*, 87:023831, Feb 2013.

[307] M. Tomka, D. Baeriswyl, and V. Gritsev. Dynamically generated reduction of the mean photon number in the Dicke model. *Phys. Rev. A*, 88:053801, Nov 2013.

[308] S. Genway, W. Li, C. Ates, B. P. Lanyon, and I. Lesanovsky. Generalized Dicke Nonequilibrium Dynamics in Trapped Ions. *Phys. Rev. Lett.*, 112:023603, Jan 2014.

[309] D. Nagy and P. Domokos. Nonequilibrium Quantum Criticality and Non-Markovian Environment: Critical Exponent of a Quantum Phase Transition. *Phys. Rev. Lett.*, 115:043601, Jul 2015.

[310] O. L. Acevedo, L. Quiroga, F. J. Rodríguez, and N. F. Johnson. Robust quantum correlations in out-of-equilibrium matter–light systems. *New Journal of Physics*, 17(9):093005, 2015.

[311] R. H. Dicke. Coherence in Spontaneous Radiation Processes. *Phys. Rev.*, 93:99–110, Jan 1954.

[312] N. Lambert, C. Emary, and T. Brandes. Entanglement and the Phase Transition in Single-Mode Superradiance. *Phys. Rev. Lett.*, 92:073602, Feb 2004.

[313] J. Vidal and S. Dusuel. Finite-size scaling exponents in the Dicke model. *EPL (Europhysics Letters)*, 74(5):817, 2006.

[314] T. Liu, Y.-Y. Zhang, Q.-H. Chen, and K.-L. Wang. Large-N scaling behavior of the ground-state energy, fidelity, and the order parameter in the Dicke model. *Phys. Rev. A*, 80:023810, Aug 2009.

[315] J. Larson and M. Lewenstein. Dilute gas of ultracold two-level atoms inside a cavity: generalized Dicke model. *New Journal of Physics*, 11(6):063027, 2009.

[316] J. Mumford, J. Larson, and D. H. J. O'Dell. Impurity in a bosonic Josephson junction: Swallowtail loops, chaos, self-trapping, and Dicke model. *Phys. Rev. A*, 89:023620, Feb 2014.

[317] M. P. Baden, K. J. Arnold, A. L. Grimsmo, S. Parkins, and M. D. Barrett. Realization of the Dicke Model Using Cavity-Assisted Raman Transitions. *Phys. Rev. Lett.*, 113:020408, Jul 2014.

[318] H. Keßler, J. Klinder, M. Wolke, and A. Hemmerich. Steering Matter Wave Superradiance with an Ultranarrow-Band Optical Cavity. *Phys. Rev. Lett.*, 113:070404, Aug 2014.

[319] J. Klinder, H. Keßer, M. Wolke, L. Mathey, and A. Hemmerich. Dynamical phase transition in the open Dicke model. *Proceedings of the National Academy of Sciences*, 112(11):3290–3295, 2015.

[320] M. Fagotti and F. H. L. Essler. Reduced density matrix after a quantum quench. *Phys. Rev. B*, 87:245107, Jun 2013.

[321] C. Emary and T. Brandes. Chaos and the quantum phase transition in the Dicke model. *Phys. Rev. E*, 67:066203, Jun 2003.

[322] L. Bakemeier, A. Alvermann, and H. Fehske. Dynamics of the Dicke model close to the classical limit. *Phys. Rev. A*, 88:043835, Oct 2013.

[323] A. Altland and F. Haake. Quantum Chaos and Effective Thermalization. *Phys. Rev. Lett.*, 108:073601, Feb 2012.

[324] M. Kulkarni, B. Öztop, and H. E. Türeci. Cavity-Mediated Near-Critical Dissipative Dynamics of a Driven Condensate. *Phys. Rev. Lett.*, 111:220408, Nov 2013.

[325] G. Kónya, G. Szirmai, and P. Domokos. Damping of quasiparticles in a Bose-Einstein condensate coupled to an optical cavity. *Phys. Rev. A*, 90:013623, Jul 2014.

[326] R. Mottl, F. Brennecke, K. Baumann, R. Landig, T. Donner, and T. Esslinger. Roton-type mode softening in a quantum gas with cavity-mediated long-range interactions. *Science*, 336(6088):1570–1573, 2012.

[327] L. Foini, L. F. Cugliandolo, and A. Gambassi. Fluctuation-dissipation relations and critical quenches in the transverse field Ising chain. *Phys. Rev. B*, 84:212404, Dec 2011.

[328] A. Chiocchetta, M. Tavora, A. Gambassi, and A. Mitra. Short-time universal scaling in an isolated quantum system after a quench. *Phys. Rev. B*, 91:220302, Jun 2015.

[329] R. Puebla, M.-J. Hwang, J. Casanova, and M. B. Plenio. Protected ultrastrong coupling regime of the two-photon quantum Rabi model with trapped ions. *Phys. Rev. A*, 95:063844, Jun 2017.

[330] M.-J. Hwang, P. Rabl, and M. B. Plenio. Dissipative phase transition in the open quantum Rabi model. *Phys. Rev. A*, 97:013825, Jan 2018.

Acknowledgments

First and foremost I would like to thank Prof. Zwerger for his supervision during my time in his group. I am very thankful for being given the freedom to always work on the topics I was most interested in. Your frequent, invaluable advice and helpful comments were of the utmost importance for my understanding of the specific subjects I was working on and their various connections to other fields.
I feel very much indebted to Francesco Piazza for his advise and supervision. During the countless hours we spent in discussions you always knew how to ask the right questions, that helped the projects to proceed. Your emotional support and sheer endless optimism during times of failure were often what kept me going. Thank you for teaching me a more relaxed and productive attitude towards physics. You went far beyond your official role as my mentor and became a good friend.
I also want to thank all the scientific group members Marcus Barth, Christian Langmack, Félix Rose, Johannes Oberreuther and Simon Weidinger as well as Peter Degenfeld-Schonburg for many debates on topics in physics and beyond, ranging from the entertaining to the insightful. These conversations, that often took place over lunch, were an important contribution to the positive, free thinking atmosphere in the group.
In this context I especially have to thank my office mate Bernhard Frank. The countless hours we spent in discussions and your endless demand for more in-depth explanations were the driving force for much of the progress we made on our joint projects. Who thought, that simply sharing an office would result in a friendship, that extends far beyond physics? See you in Dresden, where I hope to finally win at least a single match of table soccer.
I am very grateful to my collaborators Jad Halimeh and Darrick Chang for the interesting topics they exposed me to. Your physical intuition and knowledge was an important test and validation for my calculations.
I also want to extend my gratitude to Michael Hartmann for interesting discussions on the scope of C-MOP and for agreeing to co-examine this thesis.
Furthermore, I have to thank Daniela Neufang for her support in administrative matters, especially regarding the arduous topic of travel reimbursement, and Stefan Recksiegel for his highly professional and swift IT support, that made my duties as group admin a lot easier.
Thank you to Gerry for always wearing glasses when driving his car.
My parents Barbara and Franz and my sister Katharina deserve a lot of gratitude for their support over many years. Thank you for standing by me, even when I screwed up in school. Nobody could tell, where I would be today, if it was not for

your defense and support, that I had not earned. But most of all I want to thank you for teaching me to value education, even when my experiments threatened to blow up the house.
Finally and most importantly, I want to thank my wife Silvia for her endless patience, when I came home late at night or worked during the weekends. Thank you for taking care of me and for all the love you make me feel.